The Effects of Fuel Stratification and Heat Release Rate Shaping in Reactivity Controlled Compression Ignition (RCCI) Combustion

by

Dan A. DelVescovo

A dissertation submitted in partial fulfillment of
the requirements for the degree of

Doctor of Philosophy
(Mechanical Engineering)

at the

University of Wisconsin-Madison

2016

Date of final oral examination: June 1st, 2016

The dissertation is approved by the following members of the Final Oral Committee:
Rolf D. Reitz, Emeritus Professor, Mechanical Engineering
Jaal B. Ghandhi, Professor, Mechanical Engineering
David A. Rothamer, Associate Professor, Mechanical Engineering
Sage L. Kokjohn, Assistant Professor, Mechanical Engineering
James J. Schauer, Professor, Civil and Environmental Engineering

ABSTRACT

Low temperature combustion strategies have demonstrated high thermal efficiency with low emissions of pollutants, including oxides of nitrogen and particulate matter. One such combustion strategy, called Reactivity Controlled Compression Ignition (RCCI), which involves the port injection of a low reactivity fuel such as gasoline, ethanol, or natural gas, and a direct injection of a high reactivity fuel, such as diesel, has demonstrated excellent control over the heat release event due to the introduction of in-cylinder stratification of equivalence ratio and reactivity.

The RCCI strategy is inherently fuel flexible, however the direct injection strategy needs to be tailored to the combination of premixed and direct injected fuels. Experimental results demonstrate that, when comparing different premixed fuels, matching combustion phasing with premixed mass percentage or SOI timing is not sufficient to retain baseline efficiency and emissions results. If the bulk characteristics of the heat release event can be matched, however, then the efficiency and emissions can be maintained.

A 0-D methodology for predicting the required fuel stratification for a desired heat release for kinetically-controlled stratified-charge combustion strategies is proposed and validated with 3-D reacting and non-reacting CFD simulations performed with KIVA3Vr2 in this work. Various heat release rate shapes, phasing, duration, and premixed and DI fuel chemistries are explored using this analysis. This methodology provides a means by which the combustion process of a stratified-charge, kinetically-controlled combustion strategy could be optimized for any fuel combination, assuming that the fuel chemistry is well characterized.

ACKNOWLEDGEMENTS

First and foremost, I would like to thank my advisor, Professor Rolf Reitz, for giving me the opportunity to participate in his research group. Throughout my time in graduate school, he has been a tremendous source of insight, knowledge, guidance, and support. I could not have asked for a better advisor. I would also like to thank Professor Sage Kokjohn for his insight, advice, and support, both academic and financial, throughout this work. I am grateful to the members of my thesis committee for taking the time to read and critique my work. Their comments, criticisms, and advice on my preliminary thesis defense helped to shape this work.

There are a number of ERC students and staff, past and present, without whose help this work would not have been possible. Truly, all the students I have interacted with in my 6 years at the University of Wisconsin-Madison have contributed in some way, however large or small, to my knowledge, my capabilities, or my sanity. I had the great fortune to learn all about RCCI, and the finer points of operating and maintaining an engine test cell, from Derek Splitter. He was a great source of knowledge and experience that helped me tremendously. I need to thank Martin Wissink for his role in building and upgrading the lab infrastructure, and for his tremendous MATLAB expertise, particularly in writing the lab post-processor. I also need to thank John Roberts for his positively, and abilities in all things mechanical, Flavio Chuahy for all his help with engine simulations, and Ryan Walker for his help in the laboratory, and our many coffee breaks.

I cannot thank my friends and family enough for their continuing support of my personal and professional life. I would never have made it this far without their support and selflessness. I need to thank my girlfriend Kelly for having the patience and understanding to deal with me as I spent all of my time writing this tome. I look forward to discovering what stories we may write together.

TABLE OF CONTENTS

LIST OF TABLES

LIST OF FIGURES

NOMENCLATURE

Abbreviations

AFR	Air-Fuel Ratio
AFR_c	Air-Fuel Ratio (Based on Emissions Bench Carbon)
AFR_m	Air Fuel Ratio (Based on Direct Mass Flows)
AFR_{stoich}	Stoichiometric Air-Fuel Ratio
AHRR	Apparent Heat Release Rate
AKI	Anti-Knock Index, Defined as (RON+MON)/2
ATDC	After Top Dead Center
BDC	Bottom Dead Center
BTDC	Before Top Dead Center
CA	Crank Angle
CA10-90	Crank Angle Degrees from 10% to 90% Mass Fraction Burned
CA50	Crank Angle at 50% Mass Fraction Burned
CDC	Conventional Diesel Combustion
CDF	Cumulative Density Function
CI	Compression Ignition
COV	Coefficient of Variation
CP	Constant Pressure
CV	Constant Volume
DI	Direct Injection
DOE	Department of Energy
DPF	Diesel Particulate Filter
E##	##% Ethanol + (100-##)% Gasoline by Volume
ECR	Effective Compression Ratio
EEE	EPA Tier II Certification Gasoline
EGR	Exhaust Gas Recirculation
EPA	Environmental Protection Agency
ERC	Engine Research Center
EVO	Exhaust Valve Open
FID	Flame Ionization Detector
FSA	Fuel Stratification Analysis
FSN	Filter Smoke Number
GA	Genetic Algorithm
GTE	Gross Thermal Efficiency
H/C	Atomic Hydrogen to Atomic Carbon Ratio
HCCI	Homogeneous Charge Compression Ignition
HD	Heavy-Duty
HRF	High Reactivity Fuel Mass Fraction
HRR	Heat Release Rate
HTHR	High Temperature Heat Release
HX	Heat Transfer

ICE	Internal Combustion Engine
IMEP	Indicated Mean Effective Pressure
$IMEP_g$	Indicated Mean Effective Pressure, Gross
$IMEP_n$	Indicated Mean Effective Pressure, Net
ITHR	Intermediate Temperature Heat Release
IVC	Intake Valve Closure
LDEF	Lagrangian-Drop Eulerian-Fluid
LHV	Lower Heating Value
LRF	Low Reactivity Fuel Mass Fraction
LTC	Low Temperature Combustion
LTHR	Low Temperature Heat Release
MEP	Mean Effective Pressure
MFB	Mass Fraction Burned
MON	Motored Octane Number
O/C	Atomic Oxygen to Atomic Carbon Ratio
ON	Octane Number
P	Pressure
PCCI	Premixed Charge Compression Ignition
PDF	Probability Density Function
PFI	Port Fuel Injection
PFS	Partial Fuel Stratification
PID	Proportional Integral Derivative
PM	Particulate Matter
PON	Pump Octane Number
PP	Peak Pressure
PPC	Partially Premixed Combustion
PPRR	Peak Pressure Rise Rate
PRE	Premixed Mass Fraction
PRF	Primary Reference Fuel
RANS	Reynolds-Averaged Navier-Stokes
r_c	Compression Ratio
RCCI	Reactivity Controlled Compression Ignition
RCM	Rapid Compression Machine
RON	Research Octane Number
SCOTE	Single Cylinder Oil Test Engine
SI	Spark Ignition
SOI	Start of Injection
T	Temperature
TDC	Top Dead Center
TSA	Thermal Stratification Analysis
UHC	Unburned Hydrocarbons
VI	Virtual Instrument

Elements and Molecules

C	Carbon
C_1	Atomic Carbon
CO	Carbon Monoxide
CO_2	Carbon Dioxide
DTBP	Di-Tert-Butyl Peroxide
EHN	2-Ethylhexyl Nitrate
H	Atomic Hydrogen
H_2	Molecular Hydrogen
H_2O	Water
H_2O_2	Hydrogen Peroxide
HC	Hydrocarbons
HO_2	Hydroperoxy Radical
N	Atomic Nitrogen
N_2	Molecular Nitrogen
NO_x	Oxides of Nitrogen
O	Atomic Oxygen
O_2	Molecular Oxygen
O_3	Ozone
OH	Hydroxl Radical
PTFE	Polytetrafluoroethylene
SO_2	Sulfur Dioxide

Symbols and Units

$\%_m$	Percentage by Mass
$\%_v$	Percentage by Volume
$\%_\varepsilon$	Percentage by Energy
cm	Centimeter
deg	Degree
g	Gram
hP	Horse Power
Hz	Hertz
J	Joule
K	Degrees Kelvin
kg	Kilogram
kPa	Kilopascal
kWh	Kilo-Watt Hour
L	Liter
min	Minute
^oC	Degrees Celsius
rev	Revolution
T^*	1000/Temperature in Kelvin

Δ	Change, or Difference
η_c	Combustion Efficiency
η_g	Gross Indicated Thermal Efficiency
η_n	Net Indicated Thermal Efficiency
η_t	Turbocharger Efficiency
η_v	Volumetric Efficiency
σ	Standard deviation
φ	Equivalence Ratio
φ_c	Charge Based Equivalence Ratio (Fresh Air Equivalence Ratio Only)
φ_{global}	Global Equivalence Ratio
φ_{local}	Local Equivalence Ratio
φ_m	Mass Based Equivalence Ratio (Includes EGR in Calculation)
φ_{pre}	Premixed Equivalence Ratio

1 *INTRODUCTION*

1.1 Motivation and Background

The internal combustion engine (ICE) has been the predominant power generation source used in transportation applications for over 100 years [1], and projects to continue to be the predominant power source well into the foreseeable future due to its reliability, high power to weight ratio, and low up front cost. ICEs can be found in automobiles, boats, trains, and aircraft, but are not limited strictly to the transportation sector. ICEs are used in recreational equipment, tools, heavy machinery, and in stationary power generation applications of all sizes.

From a historical perspective, as the use of the internal combustion engine increased, so too did the amount of urban air pollution caused by incomplete combustion and pollutant formation. While the ideal products of combustion include only carbon dioxide (CO_2) and water (H_2O), typical combustion exhaust emissions can include varying quantities of carbon monoxide (CO) and unburned hydrocarbons (UHC) due to incomplete combustion of the fuel molecules, nitrogen oxides (NO_x) which are formed due to high temperatures or as a result fuel borne nitrogen, sulfur dioxide (SO_2) which is formed from sulfur compounds contained within the fuel and lubricants, and particulate matter (PM) emissions.

These pollutant emissions from non-ideal combustion have both direct and indirect impacts on human health and quality of life. CO binds preferentially with hemoglobin in the human bloodstream, and can be deadly in high enough concentrations. PM emissions have been directly connected to various respiratory and cardiovascular illnesses and contribute to global climate change in a positive or negative direction, depending on the composition, by absorbing or

reflecting radiative emissions from the sun. Photochemical smog and ground level ozone (O_3), which are formed when NO_x reacts with volatile organic compounds in the atmosphere, such as UHCs in the presence of sunlight, have been linked to respiratory illness. NO_x and SO_2 emissions are oxidized in the upper atmosphere and then combined with water to form acid rain, which is detrimental to crops, livestock, forests, buildings, and infrastructure and contributes to acidification of lakes, rivers, and oceans, which harm aquatic ecosystems.

In addition to these emissions affecting local air quality, the anthropogenic emissions of greenhouse gases (GHG) such as carbon dioxide (CO_2) have increased dramatically over the past 100 years, contributing significantly to global climate change. CO_2, however, is a product of even ideal combustion, implying that the only way to reduce CO_2 emissions from combustion processes for a constant energy output is to increase the efficiency of the combustion process.

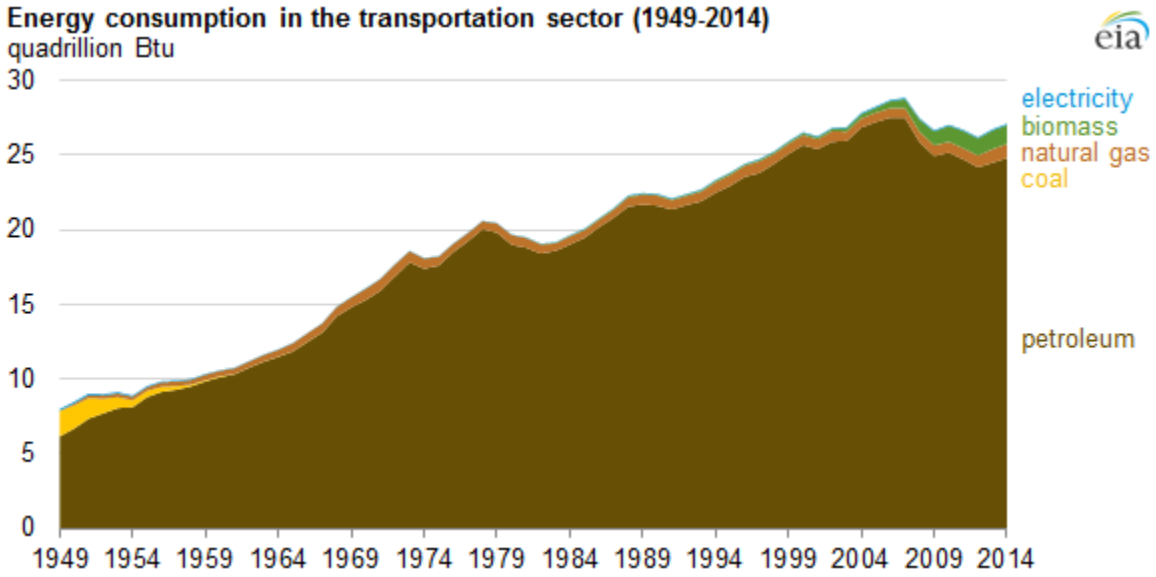

Figure 1.1: United States transportation energy consumption and source from 1949-2014. Reproduced from www.eia.gov [2]

Traditionally, the majority of ICEs have operated on hydrocarbon fuels derived from fossil fuels such as petroleum and natural gas, as can be seen in the historic trend shown in Figure 1.1. These

fuels are considered non-renewable due to the long geological time scales from which they are formed relative to human time scales, meaning that these fuel sources exist in finite supply as far as modern society is concerned. Estimations of the reserves of these fuels has varied widely over time and region as new reserves are found and costly-to-reach reserves become more economically viable, as can be seen in Figure 1.2.

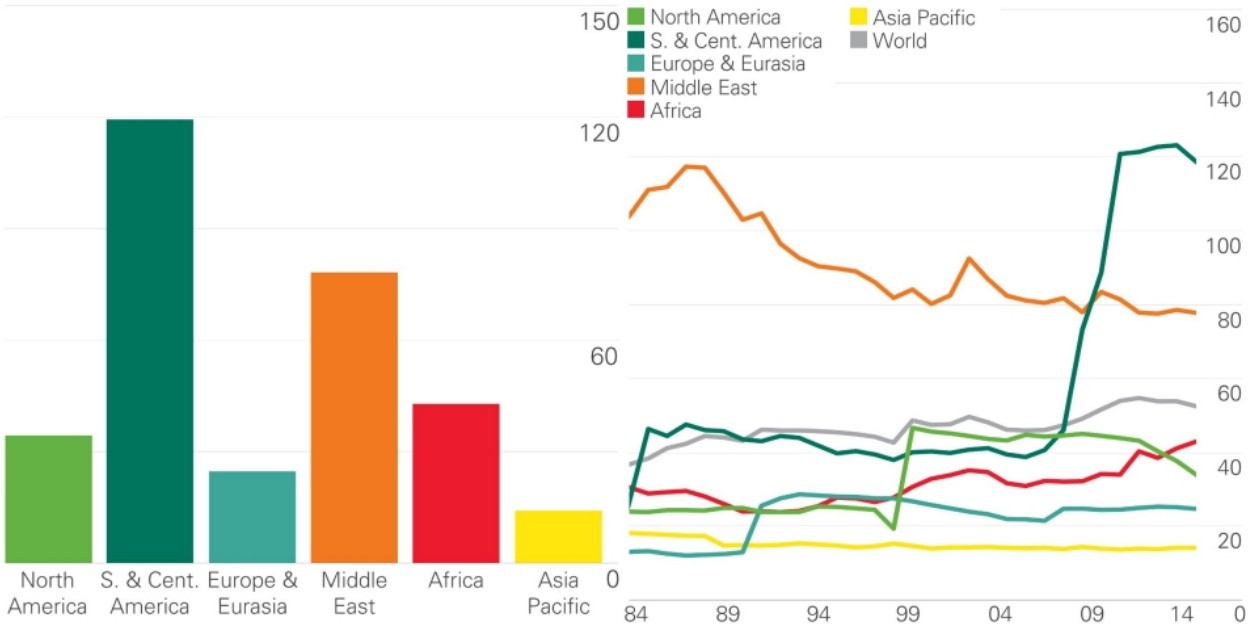

Figure 1.2: Global reserves to production (R/P) ratio, an estimation of the number of years of oil reserves assuming constant production rate by region (left), and over time from 1984 to 2014 (right). Reproduced from www.bp.com/statisticalreview [3]

Owing to the lack of certainty regarding global oil reserves, and a desire to shift to renewable energy sources for sustainability and energy security reasons, alternative and bio-derived renewable fuels have gained significant research interest over the past few decades. World biofuel production has increased significantly over the past decade, as shown in Figure 1.3, and production of biofuels is projected to grow significantly in the future, as can be seen in Figure 1.4.

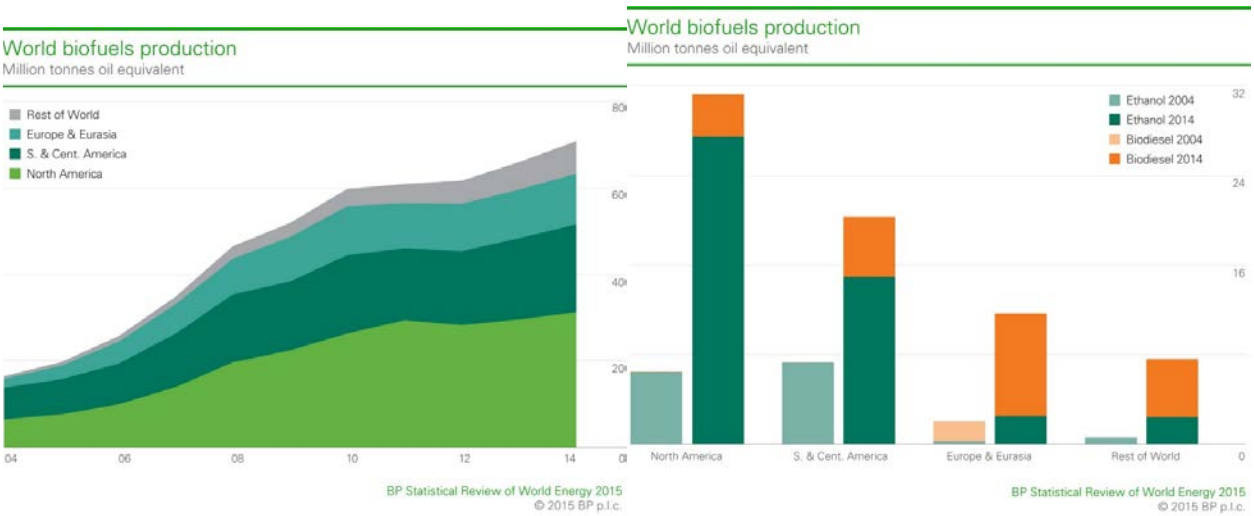

Figure 1.3: World biofuel production from 2004-2014. Reproduced from www.bp.com/statisticalreview [3]

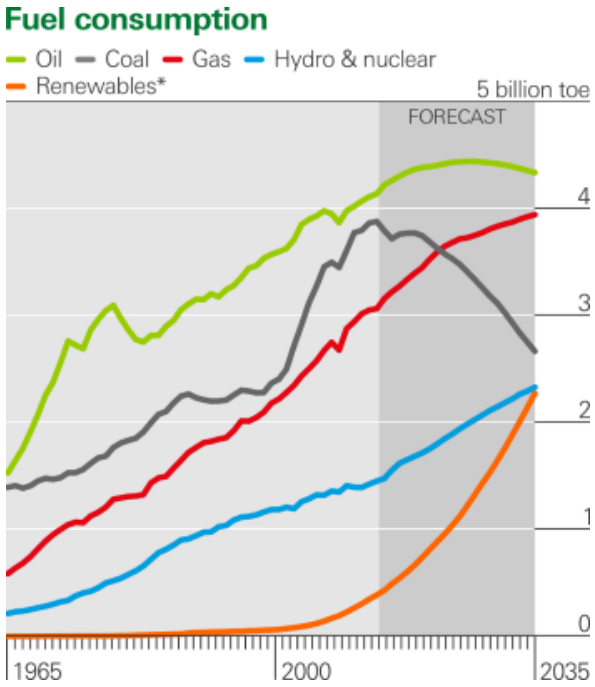

Figure 1.4: Historical and forecasted fuel consumption by source in tonnes of oil equivalent. Reproduced from www.bp.com/energyoutlook [4]

In addition to these concerns regarding fossil fuel supplies, rising concerns over smog and urban air quality resulted in the formation of emissions legislation, which mandated reductions in the pollutant emissions from vehicles [1]. A historical perspective of the emissions regulations in the United States and the European Union can be seen in Figure 1.5.

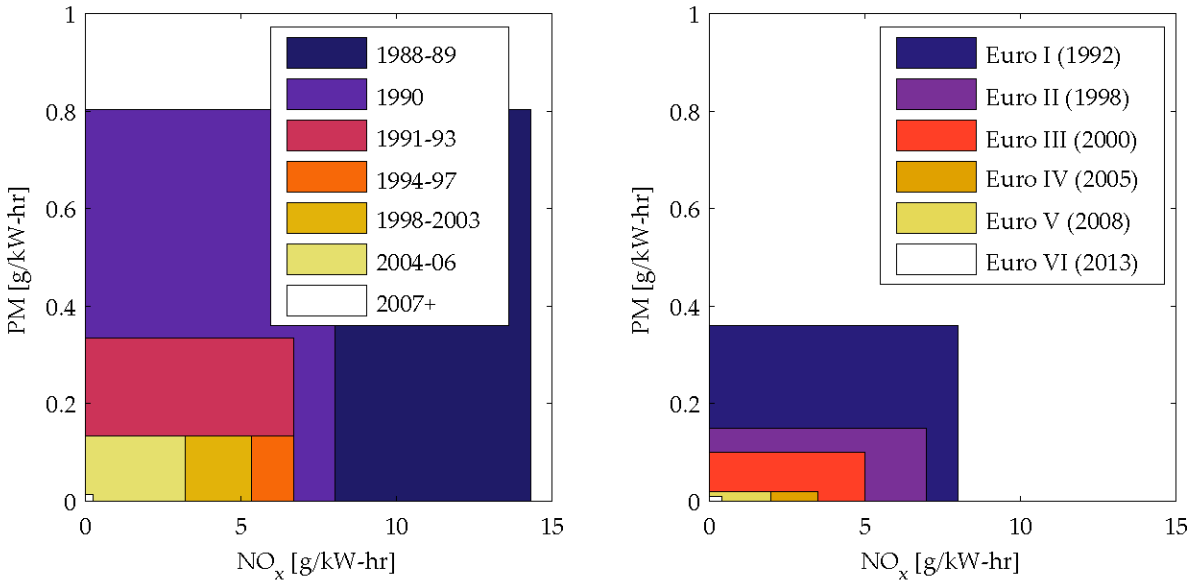

Figure 1.5: Historic Heavy-Duty PM and NO_x regulations for the United States Environmental Protection Agency (EPA) (left) and the European Union (EU) (right). Reproduced from Wissink [5]

It is clear from the global trends regarding emissions regulations, as well as fuel production projections that future engines may be required to operate efficiently on multiple alternative fuel sources with ever stricter emissions regulations. Concerns over strict emissions regulations and rising concerns over global CO_2 emissions have spawned significant research over the past 40 years to establish pathways for the development of low emission, high efficiency combustion strategies. One such group of strategies, collectively referred to as low temperature combustion (LTC) modes, includes strategies such as homogeneous charge compression ignition (HCCI), partially premixed combustion (PPC), partial fuel stratification (PFS), gasoline compression ignition (GCI), and reactivity controlled compression ignition (RCCI). These strategies all seek to take advantage of a low temperature, kinetically controlled combustion regime characterized by low pollutant emissions resulting from lean air-fuel mixtures and high thermal efficiencies from reduced heat transfer losses.

1.2 Research Objectives

The main objectives of this work are to:

- Experimentally assess the performance of alternative fuel sources in RCCI combustion with matched combustion metrics compared to baseline cases.
- Establish a method for determining fuel stratification requirements based solely on heat release data and ignition delay predictions to reduce the number of experiments and simulations required to optimize LTC strategies.
- Validate this method with reacting and non-reacting CFD simulations across a range of conditions to assess its ability to adequately predict known fuel distributions.
- Use this methodology to predict fuel stratification requirements for generated thermodynamically-favorable heat releases.
- Analyze the effect of DI and premixed fuel chemistry on fuel stratification requirements using fuels including PRF blends, methane, and syngas.

1.3 Research Method and Tools

The research presented in this work utilizes experimental engine data taken in an instrumented heavy-duty single cylinder engine test cell, 3-D CFD using KIVA-3Vr2 reacting and non-reacting engine simulations validated with the experimental engine data, and a 0-D post-processing methodology developed in MATLAB to predict fuel stratification requirements based on engine cycle heat release data.

2 *LITERATURE REVIEW*

2.1 Conventional Combustion Strategies

Internal combustion engines operate by converting the chemical energy stored between the bonds of atoms in fuel molecules into mechanical work through some combustion process. Conventional engines utilize a slider-crank mechanism, which converts this mechanical work into rotational work. The nature of the combustion processes, and mechanisms by which the combustion process proceeds, varies between combustion strategies, but engine architectures are broadly defined by their ignition mechanism. In the case of spark-ignited (SI) engines, a mixture of fuel and air is introduced into the engine and compressed in a piston-cylinder device. This mixture is then ignited by an electric spark typically located near the center of the cylinder at some predetermined timing, and a flame propagates outwards towards the periphery of the cylinder, thereby converting the fuel and air into combustion products and energy. In the case of compression ignition (CI) engines, the fuel-air mixture is compressed until the fuel auto-ignites, converting the fuel and air into products and energy.

The ideal thermodynamic cycles defining the SI and CI combustion processes are named after their respective inventors, the Otto cycle named after Nicolaus Otto, and the Diesel cycle named after Rudolf Diesel, respectively [1]. The cycles are characterized by an isentropic compression and expansion process with heat addition corresponding to the combustion process. In the case of the Otto cycle, the heat addition occurs at constant volume at top dead center (TDC) of the compression process when the cylinder volume is at its minimum. This process by assumption occurs instantaneously. The heat addition process in the Diesel cycle by contrast is assumed to occur at constant pressure. The Otto cycle has a higher maximum theoretical thermal efficiency

for a given compression ratio (r_c), alternatively for a given peak pressure, the Diesel cycle has a higher thermal efficiency [1]. The Otto cycle is limited in practice to lower r_c in order to prevent premature auto-ignition of the fuel, referred to as knock, which can result in excessive combustion noise and engine damage [1]. For this reason, SI engines require fuels with a high resistance to auto-ignition, as measured by the fuel's octane number [1], in order to achieve relatively high thermal efficiencies and engine load. These fuels are also referred to as low reactivity fuels. CI engines require very reactive fuels as measured by the fuel's cetane number, which are prone to auto-ignition. These fuels have very low octane numbers. CI engines are able to operate at higher compression ratios because they are not knock-limited, thereby offering higher thermal efficiency than conventional SI engines. These engines are commonly used in large heavy-duty vehicles and in stationary power generation where increases in fuel efficiency are very valuable [1].

Conventional CI engines utilize direct injection of high reactivity fuel in a high-temperature, mixing-controlled strategy referred to as conventional diesel combustion (CDC). The CDC strategy has the potential for high thermodynamic efficiency and low fuel consumption, made possible by the use of high compression ratios; however, due to the nature of the strategy, CDC suffers from high NO_x and PM emissions at many operating conditions, and struggles to meet strict emissions regulations without significant and costly exhaust aftertreatment [1].

2.2 Low-Temperature Combustion (LTC) Strategies

In response to stricter regulations of pollutant emissions placed on light-duty and heavy-duty vehicles by governmental agencies [6, 7] due to concerns over local air pollution and the depletion of fuel stocks over the past 40 years, researchers have sought new and novel combustion strategies to avoid the typical pollutant emissions issues associated with conventional diesel and spark

ignited engine platforms, while simultaneously searching for methods by which to increase fuel economy [1]. Compression ignition strategies, in particular, have garnered significant interest due to their potential for high thermodynamic efficiency and low fuel consumption. Figure 2.1 shows the operating region of select LTC strategies in equivalence ratio and temperature space, along with soot and NO formation regions [8]. The shaded regions for each combustion strategy represent the operating window for that particular combustion regime.

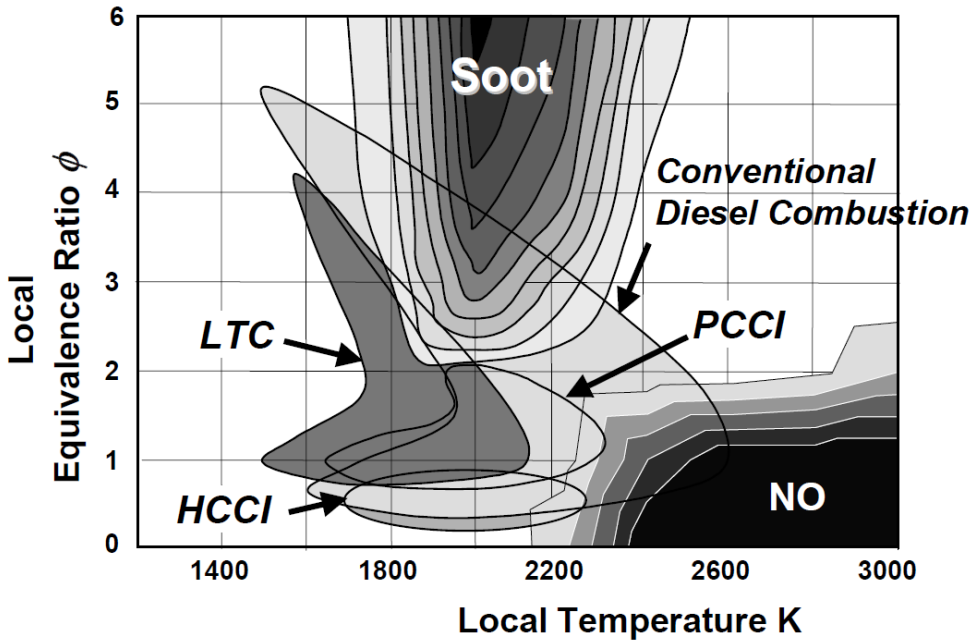

Figure 2.1: Conventional diesel and low temperature combustion strategies (LTC Diesel, HCCI, PCCI) in local φ and temperature space with NO and Soot formation contours. Reproduced from Neely, et al. [8]

Combustion strategies which are able to avoid locally rich and high temperature regions can simultaneously avoid the formation of soot and NO; however those combustion strategies that avoid high temperature regions often result in high carbon monoxide and unburned hydrocarbon emissions. Figure 2.2 shows the tradeoff between the pollutant emissions of particular interest in combustion applications.

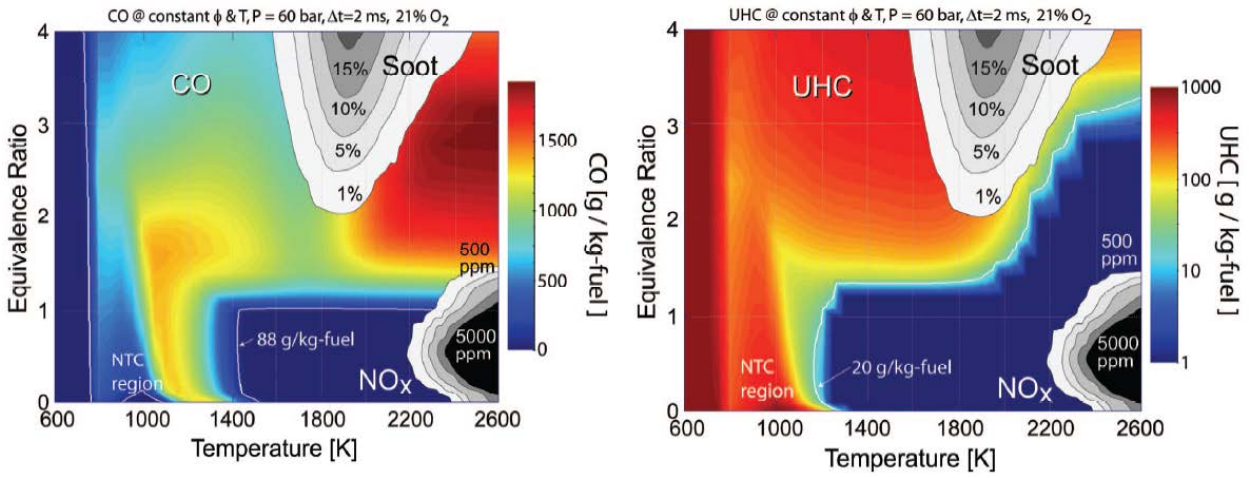

Figure 2.2: Local φ and temperature space with NO_x and Soot contours (greyscale) and CO (left) and UHC (right) contours for constant volume reactor simulations with n-Heptane/Air mixtures. Adapted from Kim, et al. [9]

As can be seen from the figure, there exists a very narrow region within the operating space where low CO, UHC, NO_x, and soot are all possible simultaneously. This operating region characterized by uniformly low emissions is where all LTC strategies optimally seek to operate within. The injection strategy must avoid locally rich regions to prevent the formation of soot; however, the equivalence ratio must remain high enough to fully oxidize CO and unburned hydrocarbons while simultaneously remaining at temperatures lower than about 2200K where NO_x formation occurs. It is not a trivial challenge to remain within this narrow desirable operating region everywhere within the combustion chamber across an entire speed/load map, especially in an engine operating under transient conditions.

A number of low temperature combustion strategies have been developed to take advantage of this low emissions operating regime, primarily differing by the amount of in-cylinder fuel stratification induced by the direct injection strategy. Figure 2.3 depicts these LTC strategies and where they lie on a fuel stratification spectrum. Fuels in blue are typically high reactivity fuels with high cetane numbers, such as conventional fuels like diesel, alternative fuels like di-methyl ether (DME), or reference fuels such as n-heptane. Fuels in orange are typically low reactivity fuels with high

octane numbers such as conventional fuels like gasoline, or ethanol blends, alternative fuels like natural gas, methanol, butanol, or syngas, or reference fuels such as iso-octane or methane. A more detailed description of some of the advanced combustion strategies of interest in the presented research can be found in the subsequent sections.

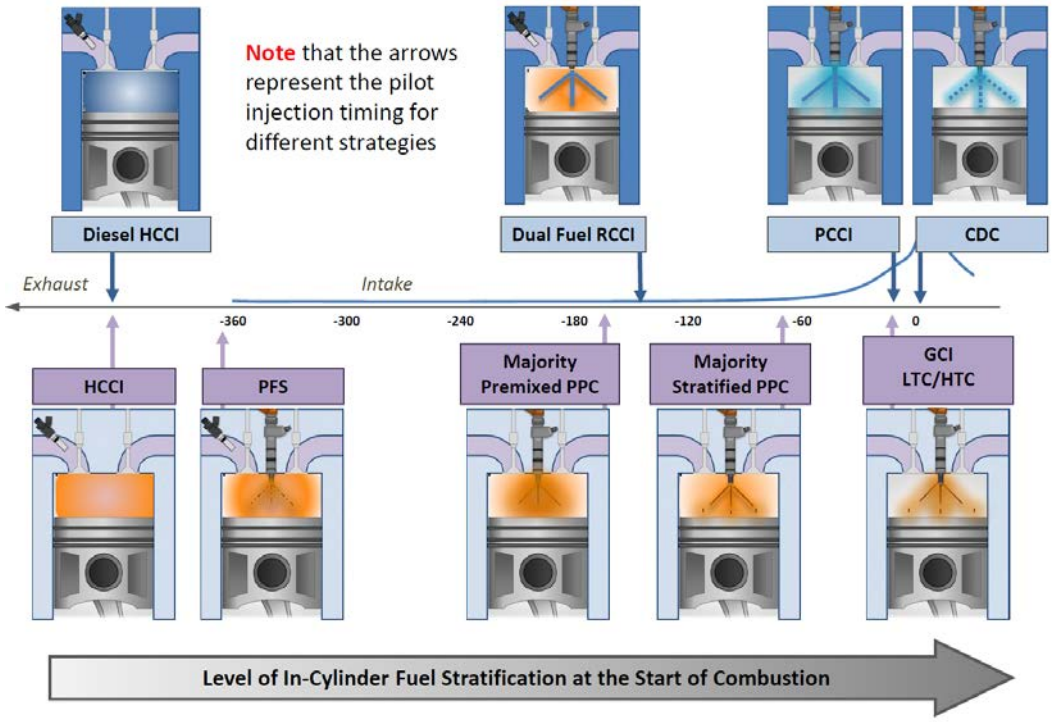

Figure 2.3: LTC strategies from least to most fuel stratification. Reproduced from Wagner, et al. [10]

2.2.1 Homogeneous Charge Compression Ignition (HCCI)

The earliest form of low temperature combustion studied was homogeneous charge compression ignition (HCCI), which utilizes a fully premixed charge of fuel and air at lean equivalence ratios ($\varphi<1.0$), which is compressed until autoignition occurs. The strategy relies on long ignition delays, which are achieved by operating with high levels of dilution either by increasing intake pressure, resulting in a decrease in equivalence ratio (φ), or by adding exhaust gas recirculation (EGR). High levels of dilution reduce peak in-cylinder temperatures, thereby reducing NO_x formation, and

operating at globally lean conditions typically results in lower PM formation and emissions. The earliest HCCI research performed on four stroke engines was performed by Najt and Foster [11] who found that the response of the combustion process of HCCI to operating parameters could be explained by the fuel chemical kinetics. HCCI has been demonstrated to achieve very high thermal efficiencies, resulting from decreased heat transfer losses and short combustion durations relative to conventional strategies, while simultaneously achieving near zero soot and NO_x emissions.

The kinetically controlled nature of the combustion strategy means that the combustion phasing is very sensitive to the in-cylinder temperature distribution, the intake pressure, global equivalence ratio and the fuel properties, while the early injection strategy provides no direct means of controlling the combustion process. Significant research on HCCI has focused on the role of thermal stratification in HCCI combustion [12-21], and the results have shown that ignition tends to propagate following the thermal gradients in the cylinder, starting in the highest temperature regions [22]. However, the HCCI strategy tends to suffer from high cycle-to-cycle variability due to its sensitivity to variations in the charge composition and in-cylinder thermal stratification, and while thermodynamically attractive, HCCI combustion is limited to a narrow operable load range that is a function of the particular fuel properties. Excessive pressure rise rates can occur at high load, which can result in engine damage, and high CO and UHC emissions and poor combustion stability is seen at low load [23].

2.2.2 Partially Premixed Combustion (PPC) and Partial Fuel Stratification (PFS)

In an effort to better control pressure rise rates and combustion phasing in HCCI combustion, strategies utilizing direct injection of a fraction of the total fuel were developed to provide equivalence ratio stratification in the cylinder. These strategies include partially premixed

combustion (PPC), and partial fuel stratification (PFS). The two strategies differ primarily by the fraction of the total fueling that is stratified (~10-20% for PFS and ~25%-50% for PPC) [10]. The equivalence ratio stratification induced by the direct injection event has been shown by researchers to provide significantly improved control over the heat release event compared to fully-premixed HCCI combustion [12, 24-29]. Figure 2.4 shows the effect of direct injection timing on peak pressure rise rate (PPRR) and ringing intensity for a fixed direct injected fraction in a PFS combustion approach.

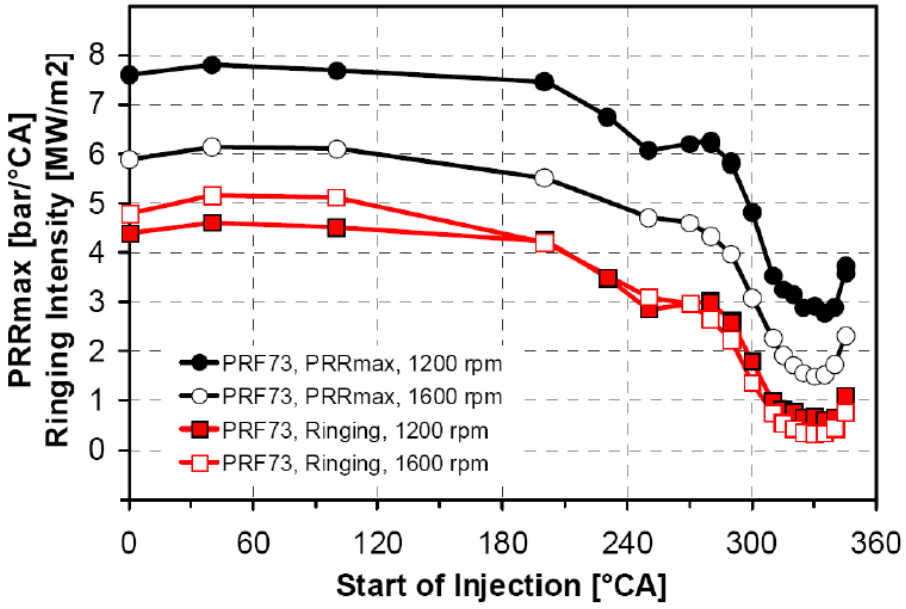

Figure 2.4: PPRR and ringing intensity as a function of DI timing for a constant CA50 of 11°ATDC for two different engine speeds with a fixed DI fraction of 14%. Reproduced from Yang et al. [28]

Between bottom dead center (BDC), corresponding to 0°CA in this figure, and about 160°CA, the start of injection (SOI) timing had virtually no effect on pressure rise rate as the mixing time between the injection and ignition timings was sufficient to negate the stratification induced by the direct injection event. As SOI was further retarded, increasing the degree of equivalence ratio stratification, the pressure rise rate decreased significantly. This fuel stratification allowed for the extension of the load range relative to a single fuel fully-premixed HCCI strategy at low loads [25,

30, 31] and high loads [31-34], though high peak pressure rise rates and limited direct control over combustion are still a challenge for PPC and PFS strategies.

2.2.3 Reactivity Controlled Compression Ignition (RCCI)

Work by Bessonette et al. [23] showed that the optimal fuel for HCCI combustion had an octane number between that of diesel and gasoline, and that the desired octane number was a function of engine load. Inagaki et al. [35] demonstrated that in-cylinder fuel blending of fuels with different properties could provide good combustion control with low emissions. Motivated by this, Kokjohn et al. [36] outlined the RCCI strategy, which involved port injection of a low reactivity fuel and multiple direct injections of a high reactivity fuel to provide coupled equivalence ratio and reactivity gradients in the cylinder. Figure 2.5 depicts the RCCI injection process.

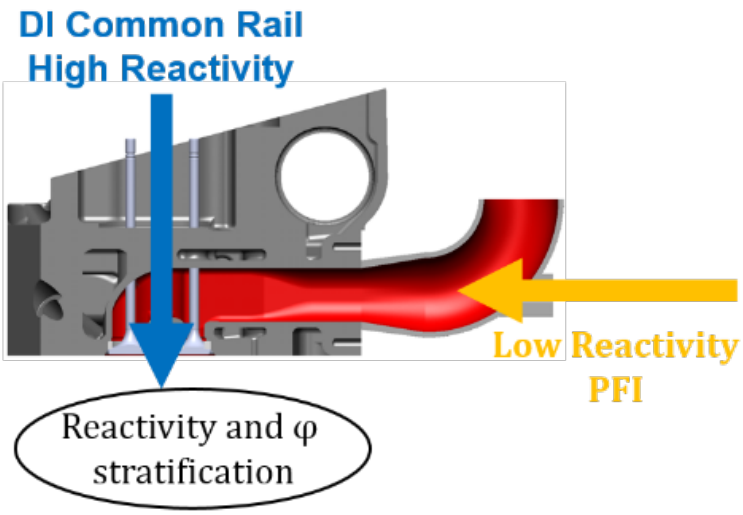

Figure 2.5: Depiction of the RCCI fuel injection process for the purposes of developing coupled reactivity and equivalence ratio stratification

Reactivity gradients provide good control over the combustion phasing and heat release rate as the injection timing and ratio of premixed to direct injected fuel can be adjusted independently, providing a range of operable conditions for a given speed/load point. Figure 2.6 shows the effect of premixed mass fraction on combustion phasing and heat release rate behavior for a fixed

injection strategy. The authors showed that the introduction of more high reactivity fuel, in this case diesel, advanced combustion phasing relative to cases with higher fractions of premixed fuel.

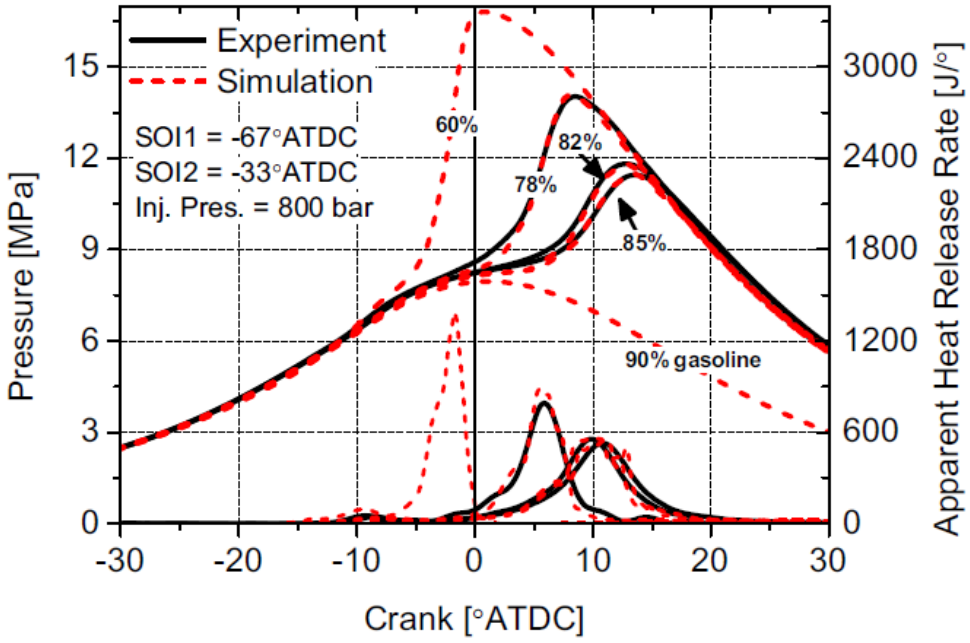

Figure 2.6: Simulated and experimental cylinder pressure and heat release rate for a gasoline percentage sweep at 11bar indicated mean effective pressure (IMEP), 1300rpm, 45.5% EGR, T_{in} = 32°C, and φ_c = 0.77. Reproduced from Kokjohn et al. [36]

Work by researchers including Splitter et al. [37-40], Hanson et al. [41-43], and Curran et al. [44-47] among many others have demonstrated a wide operable load range for RCCI combustion in both light and heavy-duty engine platforms with low NO_x and PM emissions utilizing a variety of high and low reactivity fuel sources. RCCI combustion has also demonstrated significant control over combustion phasing and heat release rate with moderate peak pressure rise rates relative to HCCI combustion [38, 39]. This controllability is a direct result of the equivalence ratio and reactivity stratification induced by direct injection of the high reactivity fuel. Optical engine work by Kokjohn et al. [48] demonstrated the effects of fuel distribution due to injection timing in RCCI combustion with iso-octane as the premixed fuel and n-heptane as the direct injected fuel. Figure 2.7 shows in-cylinder images of RCCI demonstrating the effect of injection timing on the

combustion process as the combustion event propagates throughout the cylinder due to equivalence ratio and reactivity stratification. The under-stratified (over-mixed) condition with use of early injection timing leads to a high heat release rate similar, to an HCCI type combustion event, while use of late injection timing resulted in an over-stratified (under-mixed) charge, also leading to high heat release rates. The -50°ATDC injection timing is representative of typical RCCI injection timings, and showed a long heat release duration due to the stratified nature of the charge.

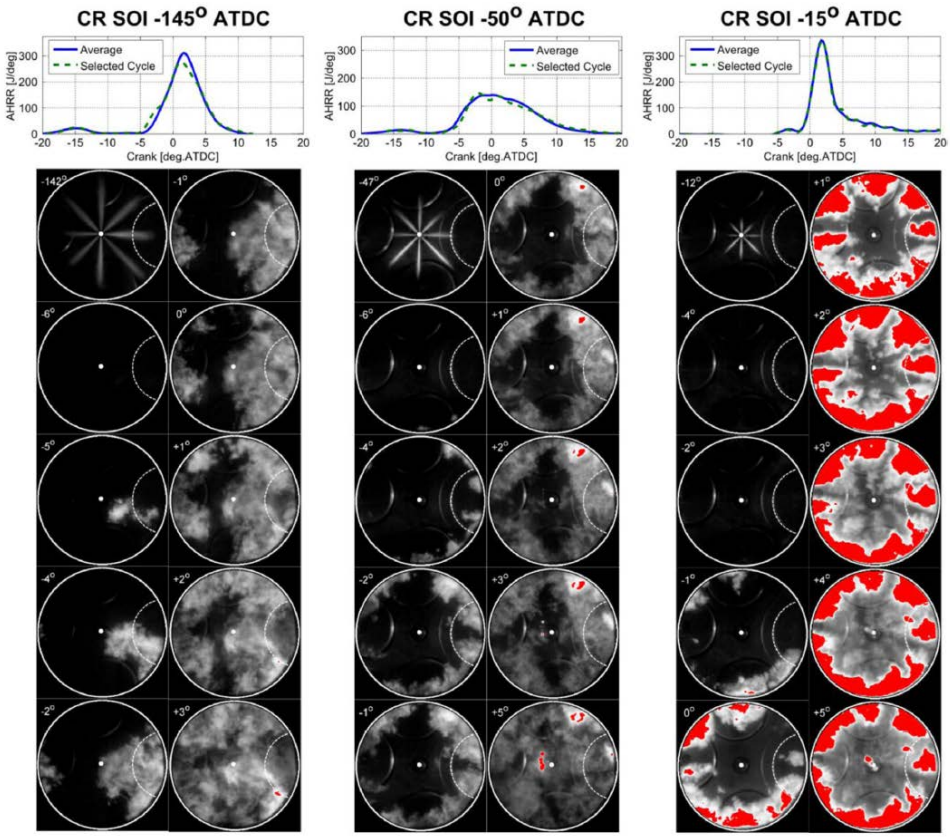

Figure 2.7: High speed movie sequence showing liquid fuel sprays and natural luminosity for the specified start of injection (SOI) timing at the crank angle specified in the upper left of each image, and the associated apparent heat release rate. Reproduced from [48]

Figure 2.8 shows the PRF, equivalence ratio, and ignition delay distributions near the cylinder wall from the optical results from Kokjohn et al. [48]. The authors concluded that the high equivalence ratio regions (φ>0.6) present in the -15° SOI case were responsible for the high heat release rate due to the near constant ignition delay of those regions, i.e., the sensitivity of ignition delay to φ

decreases as φ is increased beyond about φ = 0.6. The lack of ignition delay sensitivity then resulted in a mixture that ignited over a very small crank angle window. Similarly, the gradients in ignition delay, which define combustion timing and duration, i.e., short ignition delays, result in advanced phasing, while long ignition delays result in retarded phasing. Small gradients result in short durations, large gradients result in long durations. For the -145° SOI case, the ignition delay gradient is very small, resulting in a short combustion duration. The large gradient of ignition delay induced by both the reactivity and equivalence ratio distribution in Figure 2.8 was shown to be responsible for the broad heat release rate for the -50° SOI case shown in Figure 2.7.

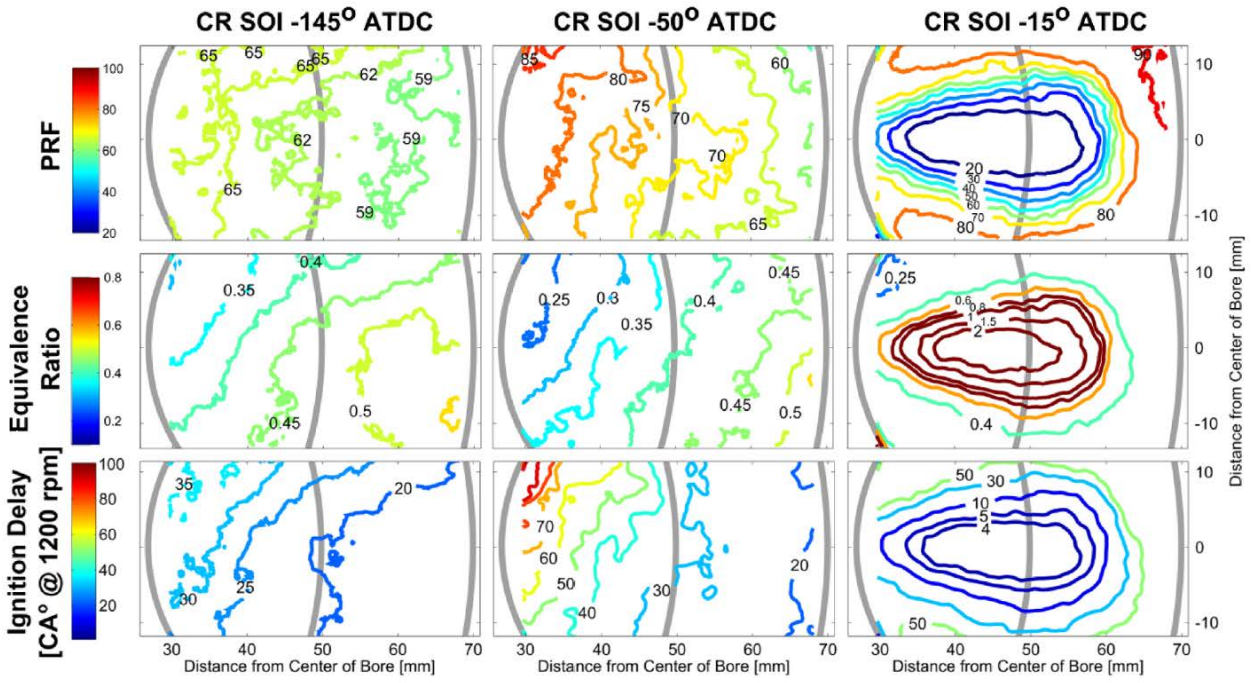

Figure 2.8: Ensemble-averaged PRF (top), equivalence ratio distributions (middle), and corresponding ignition delay (from constant volume adiabatic simulations) at -5°CA ATDC for SOI timings of -145°CA (left), -50° (middle) and -15° (right). Adapted from Kokjohn et al. [48]

The work of Kokjohn et al. [48] demonstrated the large degree of control over the shape and phasing of the combustion event that the RCCI strategy yields. Splitter [39] showed the effect of mixture stratification due to injection timing and number of injections on performance and losses

in RCCI combustion. Figure 2.9 shows the effect of the charge preparation strategy on the performance and losses of the LTC injection strategy.

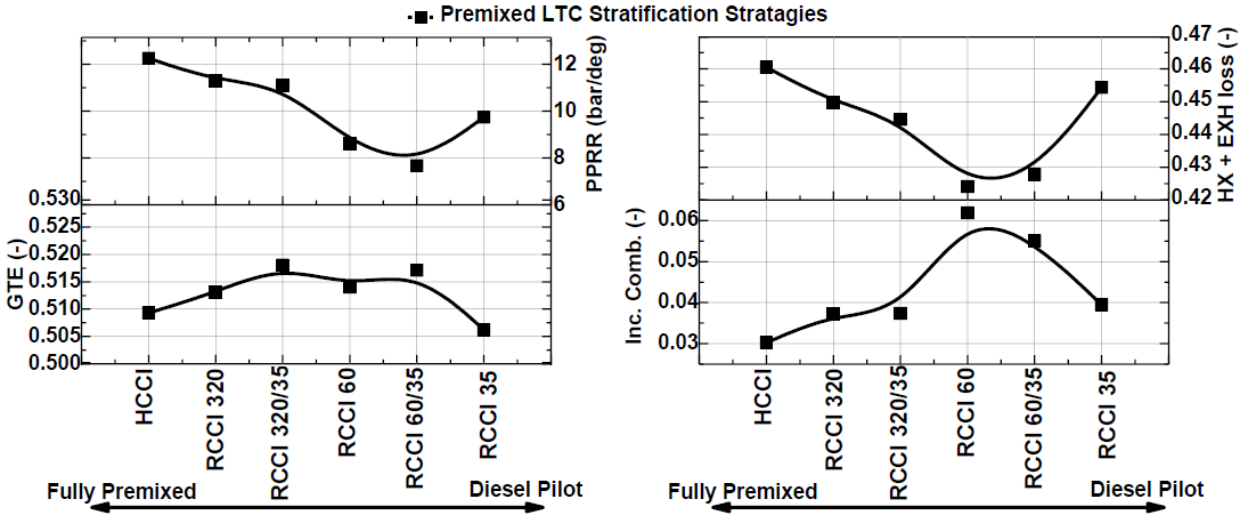

Figure 2.9: Peak pressure rise rate (PPRR), gross thermal efficiency (GTE, or η_g), and sources of losses such as heat transfer (HX), exhaust (EXH), and incomplete combustion in HCCI (gasoline only) and RCCI (gasoline/diesel) for different injection strategies (numbers denote SOI). Adapted from [39]

The increase in thermal efficiency of the RCCI strategies compared to the HCCI case was attributed to the decrease in heat transfer and exhaust losses due to the decreased pressure rise rate induced by the reactivity and equivalence ratio gradients in the cylinder despite the associated increase in combustion losses [39]. Similar to Kokjohn et al. [48], Splitter showed that the optimal dual fuel strategy occurred somewhere between the fully premixed cases and overly stratified late injection timings.

2.2.4 Fuel Effects in LTC Strategies

Christensen et al. [49] demonstrated that nearly any liquid fuel with ignition properties between that of gasoline and diesel could be used in an HCCI engine with variable compression ratio; however, the optimal compression ratio was a function of the fuel's reactivity (e.g., about 11:1 for n-heptane, and 21.5:1 for isooctane). Figure 2.10 shows the maximum and minimum operable load

limits for a variety of fuels with different derived cetane numbers from Bessonette et al. [23]. The work showed that low cetane number fuels (high octane) extended the upper load limit in HCCI combustion, but shifted the low load limit higher. The opposite was true for high cetane number fuels, which performed well at low loads, but could not reach high loads without excessive peak pressure rise rates due to overly advanced combustion phasing.

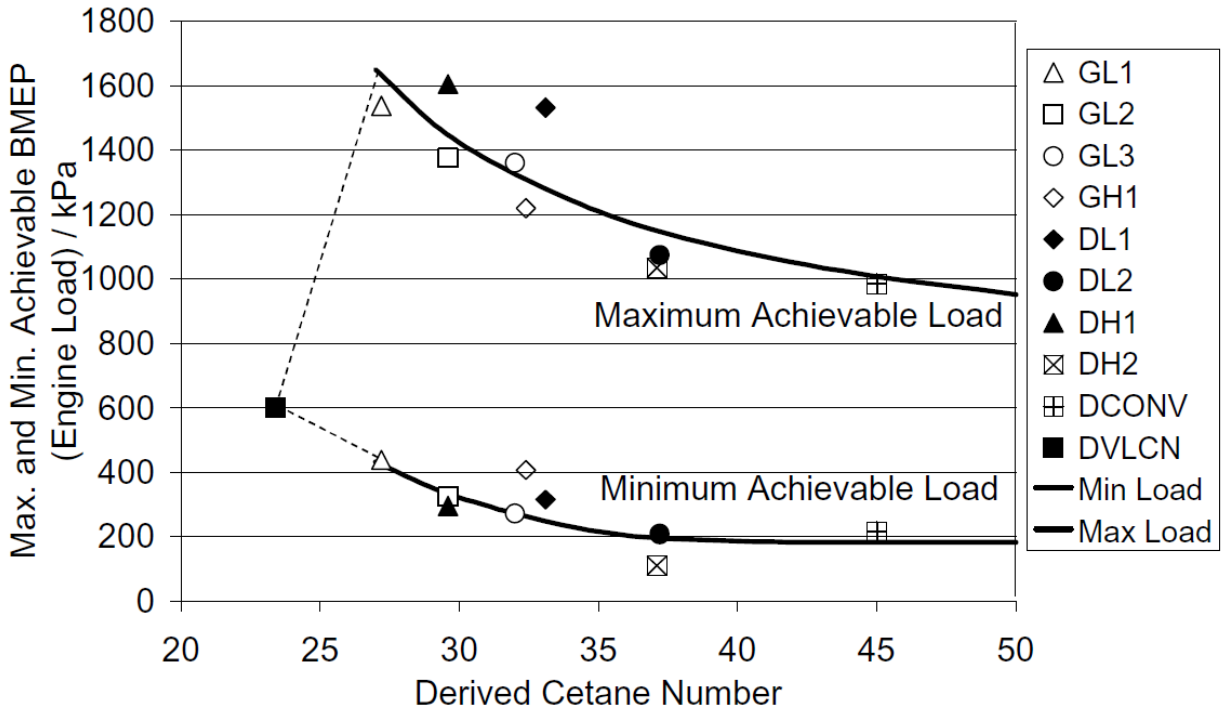

Figure 2.10: Engine operating load range vs. derived cetane number for a variety of fuels at 1200rpm in a single-cylinder heavy-duty engine. Reproduced from Bessonette et al. [23]

Researchers including Sjoberg et al. [27], Yang et al. [28], and Dec et al. [32] have investigated the effects of fuel properties and composition on PFS combustion, and researchers including Lewander et al. [33], Bakker et al. [30], Shen et al. [50], and Chang et al. [51] have studied the effects of fuel properties on PPC. Research has shown the benefit of using high octane fuels for extension of the high load limit [33], low octane fuels for the extension of the low load limit [30], and fuels with a high heat of vaporization to induce thermal stratification in the charge, thereby

decreasing pressure rise rates [27]. In addition, oxygenated fuels such as ethanol have been shown to offer reduced PM emissions at comparable operating points in stoichiometric PPC combustion [50]. Figure 2.11 shows the increase in combustion duration as a result of vaporization induced charge cooling in an ethanol fueled HCCI engine operating under a PFS strategy. Decreasing the peak pressure rise rate by means of fuel stratification and further decreasing these rates via thermal stratification, induced by charge cooling, was able to expand the operable window of PPC and PFS combustion strategies.

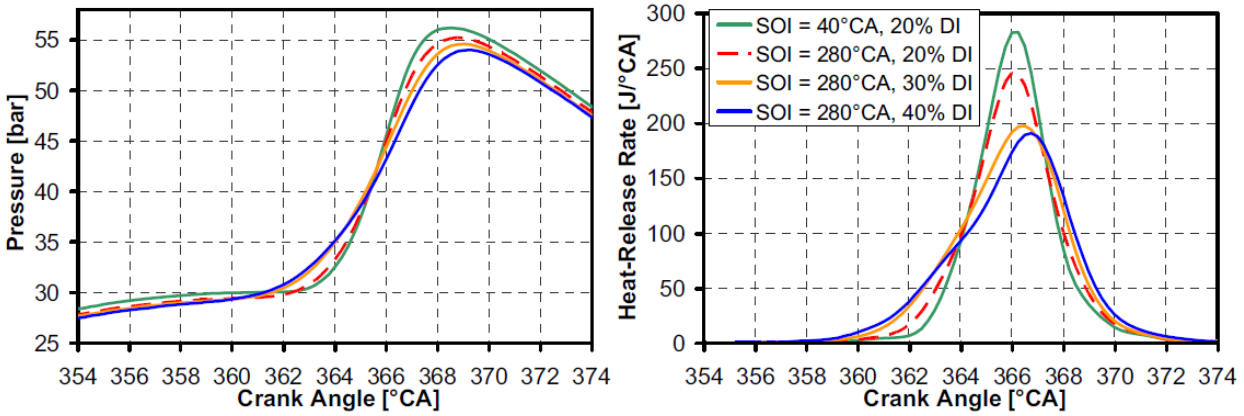

Figure 2.11: Pressure and heat release rate for well-mixed (SOI = 40°CA) and PFS (SOI = 280°CA) for various DI mass fractions at fixed CA50 with ethanol (T_{in} varied to match phasing). Adapted from Sjoberg et al. [27]

In order to better understand the effects of fuel composition and properties on RCCI combustion and to extend the operable limits of the strategy, significant research has been conducted utilizing many different high and low reactivity fuel sources. Nieman et al. [52] conducted simulation work using methane as the low reactivity fuel with diesel as the high reactivity fuel, and was able to achieve 23bar IMEP load while maintaining high efficiency and low emissions with the use of EGR. Hanson et al. [53] demonstrated RCCI combustion using natural gas and diesel over the entire operating range of a multi-cylinder heavy-duty engine, achieving 20bar brake mean effective pressure (BMEP) and a peak brake thermal efficiency (BTE) of 46.8% with EGR. Splitter et al. [37] demonstrated increased gross thermal efficiencies, load extension, and reduced EGR

requirements at high loads with the use of E85 (85% ethanol, 15% gasoline by volume) instead of pure gasoline as the low reactivity fuel. Figure 2.12 shows the effect of E85 on the pressure and heat release rate of the RCCI strategy employed by Splitter et al. [37]. The researchers found that the large distribution in reactivity with use of E85 led to the longer combustion duration seen in the experiment, which decreased pressure rise rates, reduced the EGR requirement, and decreased heat transfer to piston and cylinder wall surfaces. These effects in combination increased gross thermal efficiency relative to the gasoline/diesel baseline at the tested conditions [37].

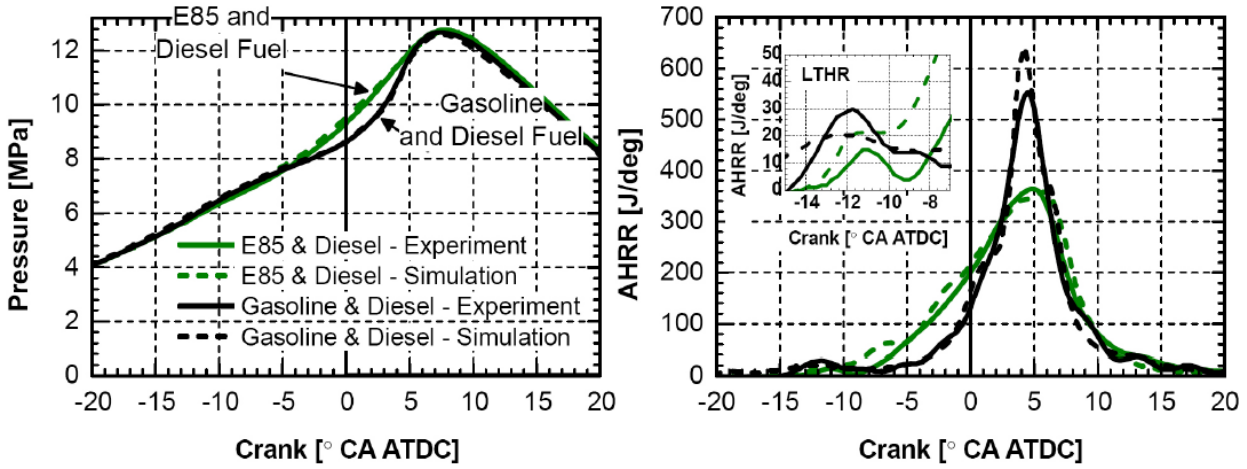

Figure 2.12: Measured and predicted pressure and heat release rates for gasoline/diesel and E85/diesel RCCI operation (9bar IMEP, 1300rpm). Adapted from Splitter et al. [37]

While researchers have shown that high octane fuels such as ethanol and methane are capable of extending the high load limit of RCCI [37, 52, 53], DelVescovo et al. [54] showed that at mid load in RCCI combustion, without adjusting the direct injection strategy for the specific fuel combination, matching combustion phasing resulted in decreased efficiency and increased emissions for high octane fuels (in this case isobutanol). The authors argued that the direct injection strategy should be tailored for the specific fuel combination to maximize performance and minimize emissions [54]. Figure 2.13 shows gross efficiency contours taken from this work for the three tested fuel combinations, EEE/diesel, isobutanol/diesel, and isobutanol/isobutanol doped

with 20% by volume of a cetane improver di-tert-butyl peroxide (DTBP) to increase the fuel's reactivity relative to neat isobutanol. The baseline injection strategy used in the work had shown good results in terms of efficiency and emissions for gasoline/diesel operation across a wide load range [36, 40, 55], however for the isobutanol cases the high octane rating of the fuel necessitated high DI fueling requirements to match the combustion phasing of the baseline EEE/diesel cases. Simulations showed that the high DI fueling requirements resulted in locally rich regions in the cylinder causing high local temperatures near the piston, which increased heat transfer as well as resulted in high NO_x emissions [54].

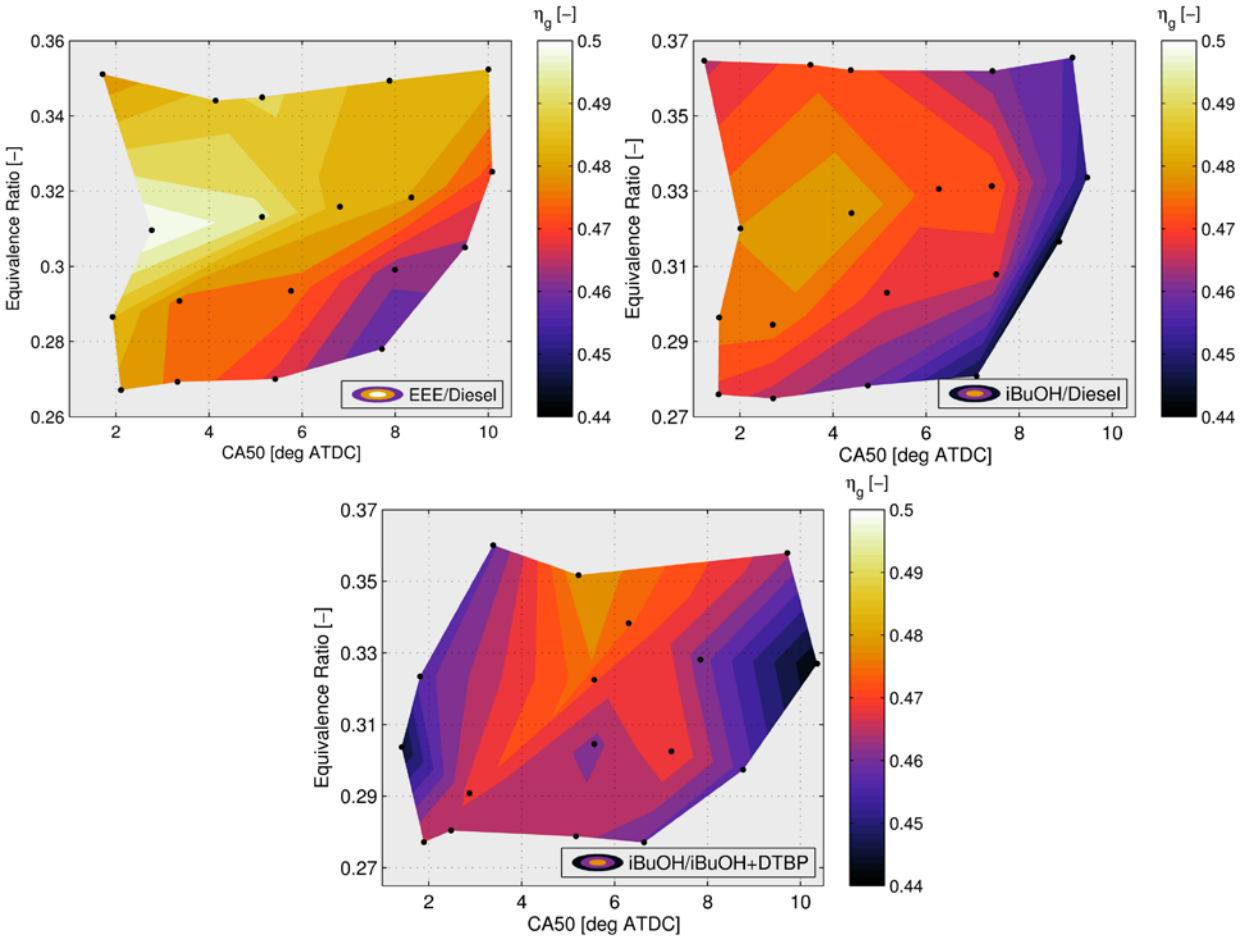

Figure 2.13: Gross efficiency contours as a function of global equivalence ratio and combustion phasing (CA50) for RCCI combustion for gasoline (EEE)/diesel (top left), isobutanol (iBuOH)/diesel (top right), and iBuOH/iBuOH doped with 20% DTBP (bottom) at 6bar $IMEP_n$. Adapted from DelVescovo et al. [54]

3 *EXPERIMENTAL DETAILS AND RESULTS*

3.1 Engine Setup and Geometry

All engine experiments presented in this work utilized a heavy-duty 2.44L displacement Caterpillar 3401 Single Cylinder Oil Test Engine (SCOTE). The 3401 SCOTE is a single cylinder variant of the commercially produced Caterpillar 3406E six-cylinder diesel engine, rated at 62kW (83hP) at 1800rev/min. The engine specifications and geometry are shown in Table 3.1.

Table 3.1: Stock 3401E SCOTE Engine Geometry

Displacement [L]	2.44
Bore x Stroke [cm]	13.72 x 16.51
Connecting Rod Length [cm]	21.16
Swirl Ratio [-]	0.7
Number of Valves	4
Intake Valve Opening (IVO) [^{o}ATDC]	335
Intake Valve Closing (IVC) [^{o}ATDC]	-143
Exhaust Valve Opening (EVO) [^{o}ATDC]	130
Exhaust Valve Closing (EVC) [^{o}ATDC]	-355
Piston Type	Articulated
Piston Profile	Stock
Compression Ratio [-]	16.1:1
Engine Cooling System	Engine Driven Pump with Wet Liner
Engine Oiling System	Externally Driven with Rotella T15W-40

The stock cooling system and water pump were used, however oil was supplied to the engine by an external electric oil pump, and the original fuel systems and fuel injector were replaced, as discussed in Section 3.3. The intake runner was also modified to accommodate two liquid port fuel injectors and two gaseous port fuel injectors, as discussed in in Section 3.2. A representation of

the piston geometry used in the experimental and simulation work presented in this document is shown in Figure 3.1, and a diagram of the experimental laboratory setup can be seen in Figure 3.2.

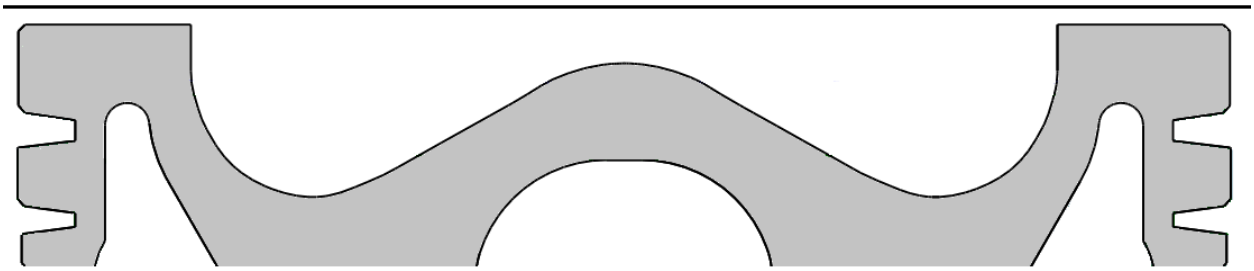

Figure 3.1: Stock piston profile (r_c=16.1:1). Horizontal black line indicates location of fire deck at TDC

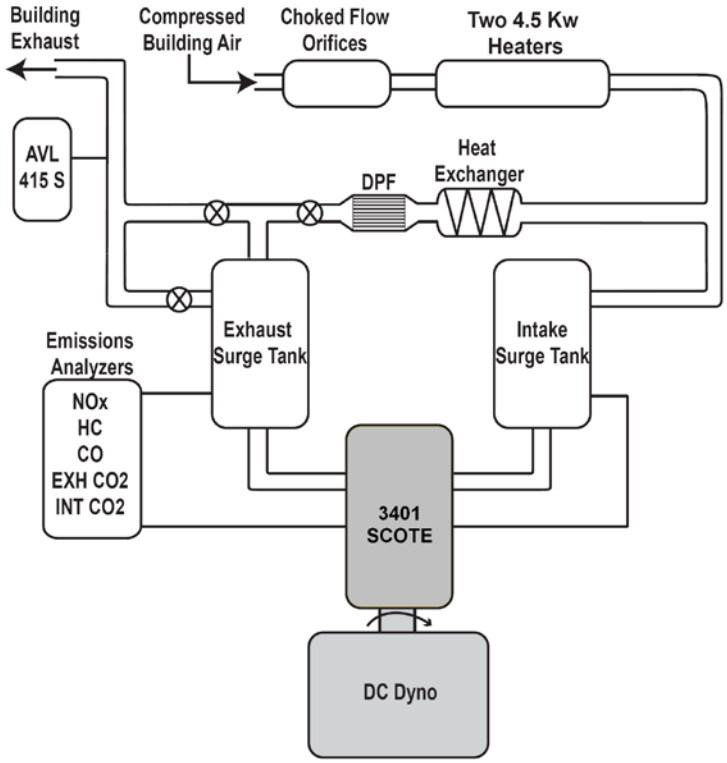

Figure 3.2: Diagram of the laboratory setup

Compressed building air was introduced into a choked flow orifice rack, which allowed for the metering of the air mass flowrate by controlling the upstream pressure. The air was then heated to the desired temperature using two 4.5kW immersion style air heaters and introduced into the intake surge tank. Intake and exhaust surge tanks were used to provide stable steady-state measurement

points for temperature, pressure, and emissions, and the relationship between the exhaust and intake pressure was used to simulate a turbocharger using the relationship for turbocharger efficiency outlined in Wissink et al. [56].

3.2 Intake Runner Design

The intake runner of the SCOTE engine was redesigned to accommodate multiple port fuel injectors to provide greater flexibility in the fuel delivery system. The final design utilizes two Bosch-style port fuel injectors, and two gaseous port fuel injectors made by Alternative Fuel Systems inc. (AFS). More information about the AFS injectors can be found in Appendix A.1.

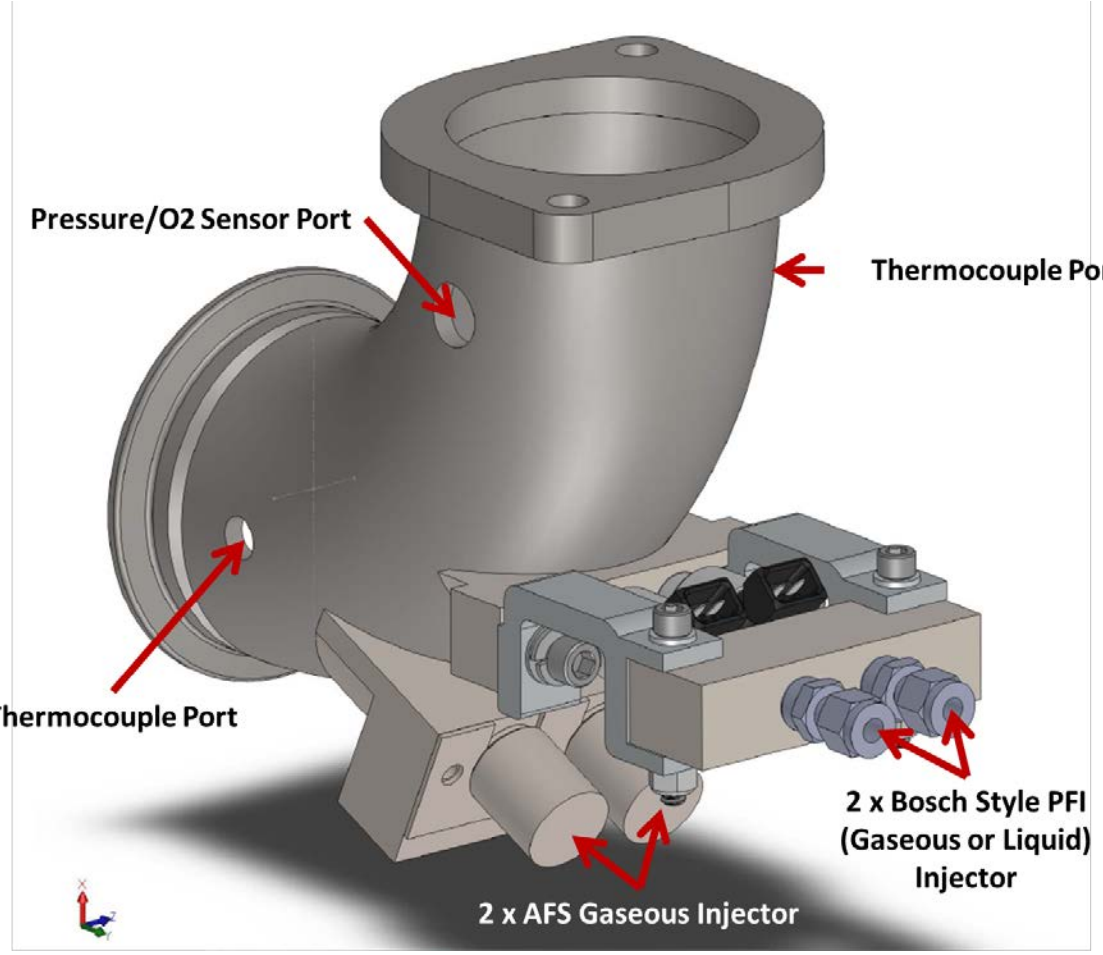

Figure 3.3: CAD model of the intake runner design showing the location of the PFI and AFS injectors

The injectors could be operated independently utilizing separate fuel streams, or simultaneously utilizing the same fuel stream branched to each injector independently, depending on the required fuel flowrate. A model of the intake design can be seen in Figure 3.3, however note that the pressure/O2 sensor port was unused and plugged in the experimental setup, and only the upper thermocouple port was utilized.

3.3 Fuel Delivery Systems and Injectors

The laboratory was equipped with two independent liquid fuel systems each capable of supplying low pressure fuel to a port fuel injector or high pressure fuel to a common rail injector, and a single gaseous fuel system capable of supplying low to intermediate pressures to a set of two gaseous port fuel injectors. A generic schematic of the liquid fuel systems can be found in Figure 3.4, and a detailed listing of the hardware comprising the liquid fuel systems can be found in Wissink [5]. The liquid fuel systems were designed with maximum fuel compatibility in mind. For this reason, all flexible hoses used in the systems were made of polytetrafluoroethylene (PTFE), more commonly known by its brand name Teflon, all rigid tubing was made from stainless steel, and the tube and pipe fittings were made of either stainless steel or anodized aluminum depending on the application.

A schematic of the gaseous fuel system can be found in Figure 3.5. The gaseous fuel system uses a custom brass manifold purchased from Airgas, Inc. in order to combine the volumes of up to four high pressure gas cylinders, also purchased from Airgas, Inc.

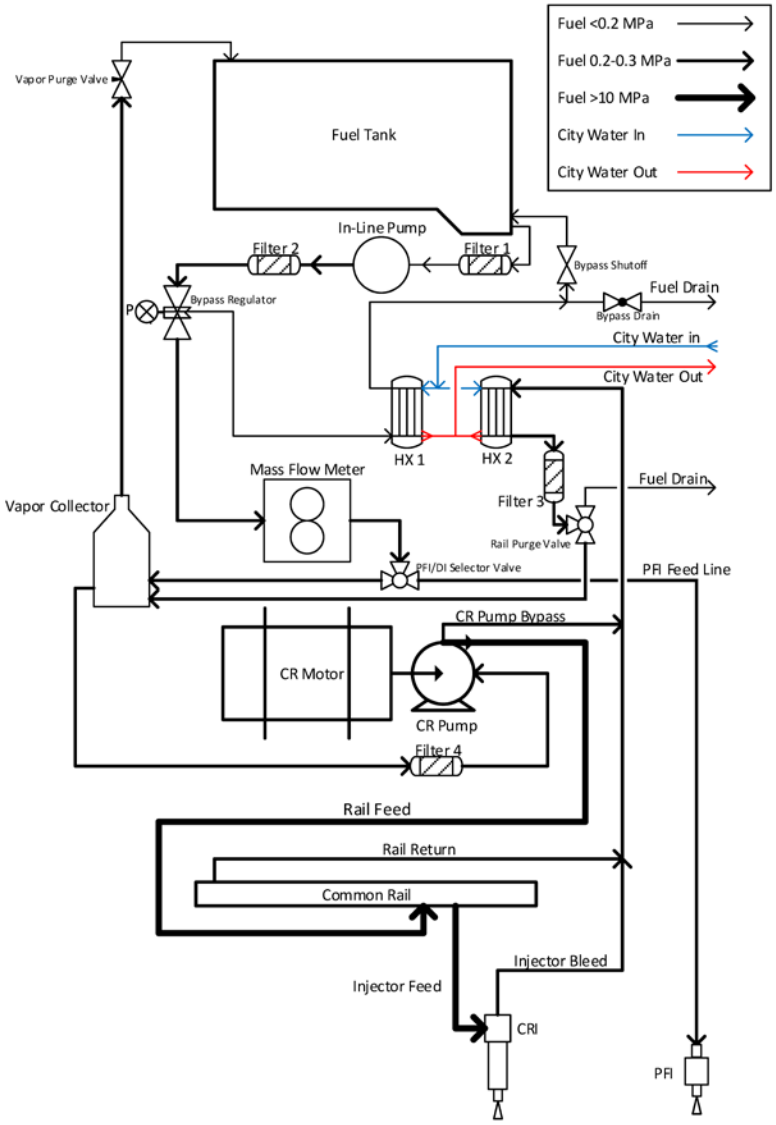

Figure 3.4: Liquid fuel system schematic. Reproduced from Wissink [5]

The high pressure gas was collected in the manifold and a pressure regulator maintained the pressure at the desired injection pressure, which varied between 275kPa and 825kPa depending on the desired mass flowrate. A normally-closed solenoid valve shuts off flow between the manifold and the fuel injectors when it loses power, and is combined with the laboratory emergency stop system for safety considerations. The fuel flowrate was measured by an Endress+Hauser Promass 80A02 Coriolis fuel flowmeter, and from the fuel flowmeter the fuel was routed directly to the

AFS gaseous fuel injectors. A 3-way valve allows the gas in the system to be purged to the building exhaust when no longer in operation. Table 3.2 lists the specifications of the liquid and gaseous port fuel injectors.

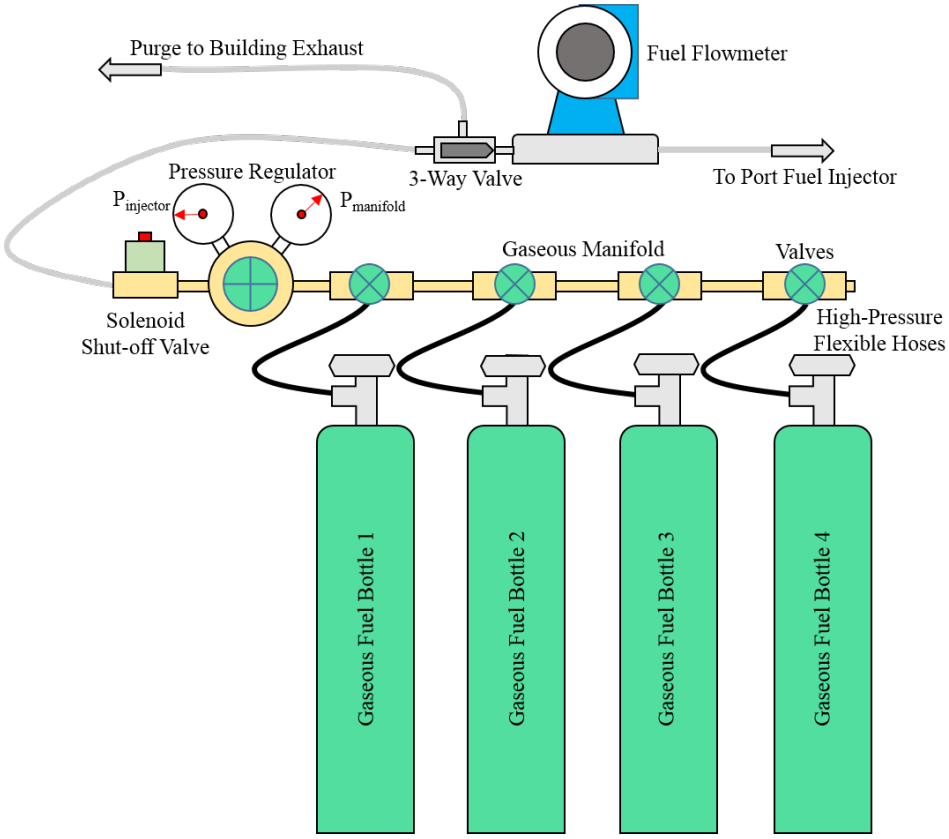

Figure 3.5: Gaseous fuel system schematic

Table 3.2: Port fuel injector specifications

Injector	PFI_1	PFI_2	PFI_3	PFI_4
Fuel Type	Gaseous	Gaseous	Liquid	Liquid
Manufacturer	Alternative Fuel Systems (AFS)	Alternative Fuel Systems (AFS)	Trick Flow	Trick Flow
Part Number	Gs60-05-5-H	Gs60-05-5-H	TFS-89024	TFS-89055
Current Profile [A]	8/2 peak and hold	8/2 peak and hold	4/1 peak and hold	4/1 peak and hold
Steady Flow Rate [cm^3/min]	Varies with operating pressure	Varies with operating pressure	255.0 @ 3bar	578.0 @ 3bar
Spray Angle [°]	N/A	N/A	15	15
Operating Pressure [bar]	2.75-8.25	2.75-8.25	2.75	2.75

Table 3.3: Common rail injector specifications

Manufacturer	Bosch
Body Style	CRI2 Series
Body Part Number	0986435088
Nozzle Part #	DLLA148P1347
Number of Holes	7
Included Angle [°]	148
Hole diameter [μm]	141

The experiments conducted in this work utilized a stock 3401E SCOTE cylinder head that was modified to accept a Bosch common rail injector in place of the 315B HEUI injector. A detailed discussion of the design of the insert can be found in Splitter [39]. Figure 3.6 shows the common-rail injector and clamp utilized in this work, as well as its position relative to the stock piston at TDC of the compression stroke, and Table 3.3 lists the common rail injector specifications.

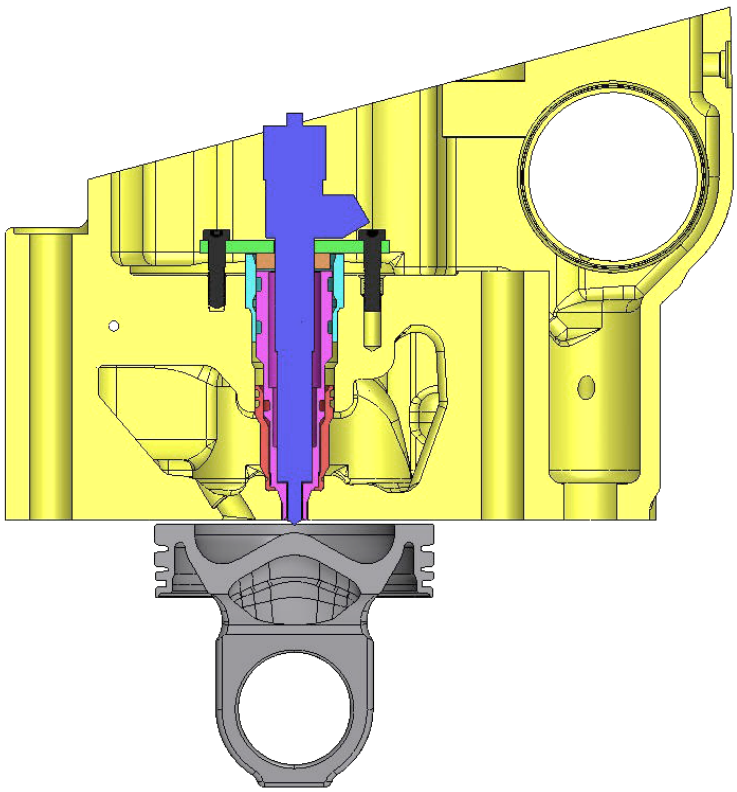

Figure 3.6: CAD model of Bosch common rail injector (blue) installed into stock injector location in Caterpillar SCOTE cylinder head with custom insert (pink) and clamps (orange and green). Reproduced from Splitter [39]

3.4 Instrumentation and Control

The experimental engine test cell was equipped with various measurement and control devices to adequately define the boundary conditions, operating conditions, performance, and emissions of the experiments. The instruments can be broken down into categories based on their relative sampling rate. Low-speed devices are sensors and control devices that do not require time-critical measurement or control. These include measurements with long residence times such as temperature and emissions, and measurements such as mass flowrates and surge tank pressure, which do not require crank angle resolution. The second category includes high-speed instrumentation devices such as the in-cylinder pressure and injector current probes which do require crank-angle-resolved measurement. Table 3.4 summarizes the low-speed and high-speed instrumentation used throughout the engine test cell in this work.

Table 3.4: Low-speed and high-speed instrumentation

Sampling Rate	Measurement	Model	Operating Range
Low-Speed	Upstream orifice pressure	Omega PX209-100A5V	0 to 100psia
	Intake surge tank pressure	Omega PX319-050AI	0 to 50psia
	Exhaust surge tank pressure	Omega PX215-200AI	0 to 200psia
	Thermocouples	Omega type-K	-200 to 1250^{o}C
	Liquid fuel flow rate	Endress+Hauser Promass 80A01	0 to 20kg/hr
	Gaseous fuel flowrate	Endress+Hauser Promass80A02	0 to 100kg/hr
High-Speed	In-cylinder pressure	Kistler 6125C21U20	0 to 300bar
	Charge amplifier	Kistler 5010	±10 to 999000pC
	Injector current probes	Tektronix A622	0 to 100A
	Optical encoder	BEI x H25D-SS-3600-ABZC-28V/V-SM18	3600pulses/rev

Table 3.5 lists the exhaust measurement instruments for each emissions species analyzed in this work. Gaseous engine-out emissions were sampled from the center of the intake and exhaust surge tanks and analyzed with a five gas Horiba tailpipe “bag” bench that was converted to a continuous

sampling engine bench with EGR measurement capabilities. Exhaust hydrocarbons were measured on a wet basis using a heated sampling system composed of a long heated line and heated filter. The other gaseous exhaust emissions were measured on a dry basis by condensing and separating the water vapor in the exhaust emissions before entering the instruments. PM emissions were measured with an AVL 415S smoke meter, which provides measurements of filter smoke number (FSN) which are then converted to mass density units (mg/m^3) using a correlation developed by AVL for CDC operation. 5 samples of 2L volume were taken at each steady state operating condition.

Table 3.5: Exhaust emissions measurement devices

Emissions Species	Manufacturer	Model Number	Measurement Principle
Exhaust NO_x	Horiba	CLA-220	Heated chemiluminescence detector
Exhaust CO	Horiba	AIA-220	Non-dispersive infrared light absorption
Exhaust HC	Horiba	FIA-236	Heated flame ionization detector
Exhaust CO_2	Horiba	AIA-220	Non-dispersive infrared light absorption
Intake CO_2	Horiba	AIA-220	Non-dispersive infrared light absorption
Particulate Matter	AVL	415S Smoke Meter	Filter paper reflectivity

Data acquisition and hardware control were performed on a PC using the National Instruments LabVIEW 2011 software package. The LabVIEW program which was originally developed for the laboratory by Sung [57], modified extensively by Wissink [58], and further adapted for the present work consisted of three separate virtual instruments (VIs), which individually controlled the low-speed data acquisition and visualization, high-speed data acquisition and visualization, and real-time control and acquisition, respectively. A breakdown of the National Instruments hardware for the specified sample rates which enabled the data acquisition and control is shown in Table 3.6. Low-speed data was acquired at a sampling rate of 2 Hz over 2 minutes of runtime. High speed data from the in-cylinder pressure transducer was recorded at a resolution of 0.1^oCA,

and 250 individual cycles of raw data were recorded at each steady state operating point. Further discussion of the laboratory instrumentation can be found in Wissink [5].

Table 3.6: Low-speed, real-time, and high-speed data acquisition and control hardware

Sampling Rate	Part Number	Description	Function
Low Speed	NI SCXI-1000	4-slot AC powered SCXI chassis	Houses SCXI modules
	NI SCXI-1300	General purpose voltage module	Receives all low-speed voltage inputs (pressure, fuel flow, etc.)
	NI SCXI-1303	Thermocouple module	Receives all thermocouple inputs
Real-time	NI cRIO-9074	Integrated 400 MHz real-time controller and 2M gate FPGA	Houses all cRIO I/O modules and contains the FPGA used for real-time control
	NI 9411	Differential digital input	Receives digital timing from shaft encoder
	NI 9215	Simultaneous analog input	Receives analog input from common rail pressure transducer
	NI 9758	Port fuel injector driver	Drives current to port fuel injectors, inlet meter valve on CR pump, and high-pressure valve on common rail
	NI 9751	Direct injector driver module	Drives current to common rail injector
High Speed	NI PCI-6143	Simultaneous sampling multifunction DAQ	Samples high-speed digital and analog inputs
	NI SHC68-68-EPM	68-pin X series and M series cable	Connects PCI-6143 to BNC-2090A
	NI BNC-2090A	Shielded rack-mount BNC connector block	Receives high-speed analog inputs and digital timing from encoder

3.5 Engine Operation

The location of TDC was set at before each experiment by setting the peak motored cylinder pressure to -0.4^{o}CA after top dead center (ATDC) of the compression stroke. This loss angle was based on hardware specifications from Caterpillar for the engine platform. Data was acquired at steady-state conditions determined by monitoring intake and exhaust surge tank pressures and temperatures, and by monitoring fluctuations in exhaust emissions over several minutes. Selected fuel properties used in the analysis of the data collected in this work can be seen in Table 3.7. The experiments shown in Sections 3.7.1-3.10 included the addition of a lubricity improver (Infineum

R655) to the direct injected n-heptane due to the fuel's low lubricity relative to the diesel fuel that the high pressure common rail injection system was designed for. The additive was splash blended to 100ppm by volume in the fuel tank, and the specification sheet for the additive can be seen in Appendix A.2.

Table 3.7: Selected fuel properties

Fuel	iso-Octane	n-Heptane	Methane	Syngas (50/50)
Chemical Formula	iC_8H_{18}	nC_7H_{16}	CH_4	$0.5H_2 + 0.5CO$
Molecular Weight [g/mol]	114.23	100.21	16.04	15.013
H/C Ratio [mol/mol]	2.25	2.286	4	2
O/C Ratio [mol/mol]	0	0	0	0.5
Density [kg/m^3]	692	684	~0.7	~1.0
RON [-]	100	0	~120	N/A
MON [-]	100	0	~120	N/A
Lower Heating Value [MJ/kg]	44.33	44.66	50.009	17.48
Stoichiometric AFR [-]	15.09	15.14	17.19	4.593

3.6 Data Analysis

Data analysis, post-processing of experimental data, and data visualization were all performed using custom MATLAB scripts. A detailed description of the data analysis procedures utilized in this work for steady-state calculations, such as emissions indices, efficiency metrics, and fuel mixture properties can be found in Wissink [5].

3.6.1 Propagation of Uncertainty and Ensemble Averaging

In order to robustly determine uncertainty in all measured and calculated quantities, a LabVIEW script was developed by Wissink [58] that reads in raw voltages from the data acquisition system, which enables the determination of a calibration curve for the given measurement device. 30 data points were taken at each calibration point to derive statistical quantities from the data including

confidence intervals and standard deviations. Calibration curves were determined for the emissions analyzers, fuel flowmeters, the exhaust and intake surge tank pressure tranducers, and the cylinder pressure transducer. The calibration data and curve fits for each measurement device can be found in Appendix B.

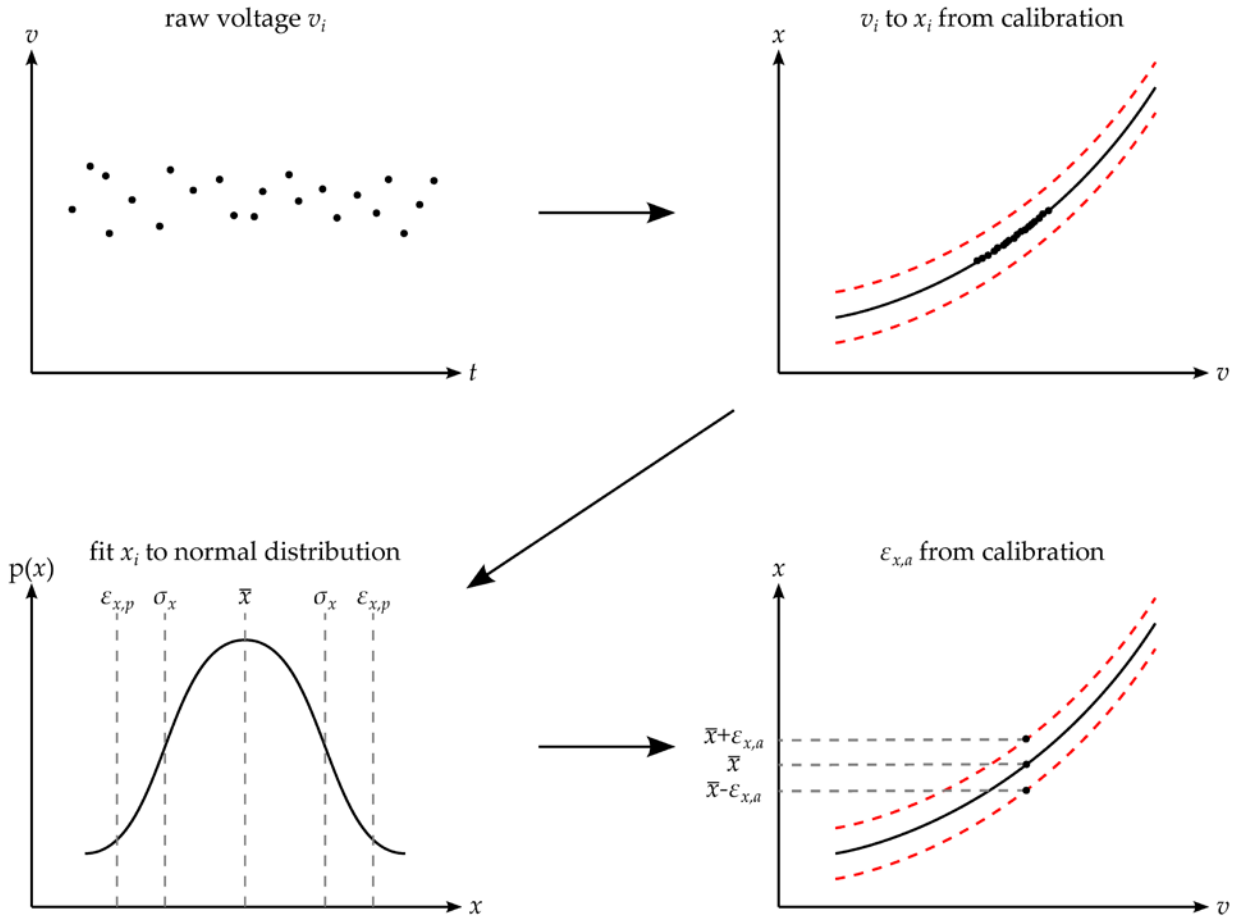

Figure 3.7: Process for converting raw measured voltage data (υ_i) into a measurement value (χ_i) with confidence intervals (ε_i). Reproduced from Wissink [5]

Low speed data voltages were saved and then converted into measured values through the calibration curves found in Appendix B. The low-speed data arrays were then fit to a normal distribution to determine statistical quantities such as the mean, standard deviation (σ), and the "precision" 95% confidence interval (ϵ_p). The mean value was then fed back to the calibration curve to determine the "accuracy" 95% confidence interval (ϵ_a) of the measurement. This process

is graphically depicted in Figure 3.7. The “precision” and “accuracy” error measures were then used to determine the total uncertainty of the measurement according to the relationship in Equation (3.1).

$$\epsilon = \sqrt{\epsilon_a^2 + \epsilon_p^2} \tag{3.1}$$

For each low-speed measured value this analysis resulted in scalar values of the mean ($\overline{x}$) and 95% confidence interval (ϵ_x). Calculated quantities involving multiple measured values such as combustion efficiency, emissions indices, or trapped mass of the functional form f = f(x,y,z,…) were calculated according to the variance formula [59] according to Equation (3.2).

$$\epsilon_f = \sqrt{\left(\frac{\partial f}{\partial x}\right)^2 \epsilon_x^2 + \left(\frac{\partial F}{\partial y}\right)^2 \epsilon_y^2 + \left(\frac{\partial F}{\partial z}\right)^2 \epsilon_z^2 + \cdots} \tag{3.2}$$

This relationship requires the calculation of the partial derivative of the calculated function with respect to each variable comprising the calculation. Partial derivatives were calculated with MATLAB’s Symbolic Math Toolbox™. This was accomplished by first representing each equation symbolically, then calculating the necessary partial derivatives for each independent variable at the specific mean value, next evaluating the symbolic expressions, and finally carrying out the uncertainty propagation as expressed in Equation (3.2). Thus, each calculated quantity has an associated uncertainty value which is defined as the 95% confidence interval through this work, unless otherwise indicated. This calculated confidence interval is represented on relevant plots by error bars above and below the mean value of the calculated or measured quantity.

High speed data measurements such as in-cylinder pressure (P), and heat release rate (HRR) which were functions of crank angle and were collected over many cycles were fit to normal distributions,

as shown in Figure 3.8 at each crank angle index from the crankshaft encoder, resulting in the calculation of an ensembled mean, standard deviation, and 95% confidence interval as a function crank angle.

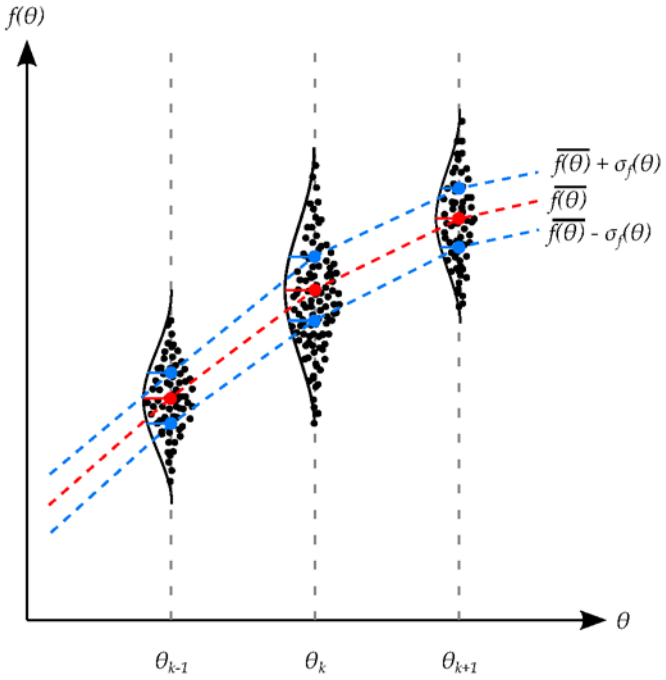

Figure 3.8: Fitting cycle array data to normal distributions at each crank angle index to create ensemble statistics. Reproduced from Wissink [5]

3.6.2 Pressure Measurement and Filtering

The in-cylinder pressure was measured with an un-cooled piezoelectric pressure transducer from Kistler, and the charge induced in the transducer was converted to a voltage output by a Kistler 5010 charge amplifier. The raw pressure data was then filtered with a zero-phase, low-pass, 5th-order Butterworth filter with a cutoff frequency at 2200 Hz which corresponds to the second resonance mode of the engine as described by Eng [60]. To account for drift in the pressure transducer measurement, each cycle was "pegged" by averaging the pressure data between -185 and -175^{o}CA and adding the difference between the intake surge tank pressure and the averaged

pressure in this window to the pressure array for each cycle. The numerical derivative of pressure was calculated via the central difference method shown in Equation (3.3), where k is the current array element, and h is the step size corresponding to the crankshaft encoder resolution, 0.1°CA in this work.

$$F_k' = \frac{F_{k+1} - F_{k-1}}{2h} \tag{3.3}$$

With arrays of P and dP/dθ calculated for each individual cycle, scalar quantities such as peak pressure (PP), location of peak pressure (LPP), peak pressure rise rate (PPRR), and location of peak pressure rise rate (LPPRR) were then be calculated.

3.6.3 Heat Release Rate Analysis

The adiabatic apparent heat release rate (AHRR or HRR) was calculated using a single-zone first law analysis with a constant mass assumption. For this reason, the calculation is only performed during the closed cycle portion of the cycle between IVC and EVO. The cumulative adiabatic heat release (HR) was calculated by trapezoidal integration of the HRR. Equation (3.4) shows the method by which the HRR was calculated.

$$HRR = \frac{dQ_{ad}}{d\theta} = \frac{\gamma}{\gamma - 1} P \frac{dV}{d\theta} + \frac{1}{\gamma - 1} V \frac{dP}{d\theta} \tag{3.4}$$

With the HRR and HR calculated, scalar quantities such as peak heat release rate (PHRR), location of peak heat release rate (LPHRR), and locations of 10%, 50%, 90%, etc., of HR (CA10, CA50, CA90, etc.) could then be calculated.

3.6.4 Ratio of Specific Heats (γ) Correlation for Heat Release Analysis

The calculation of Equation (3.4) requires an estimate of the ratio of specific heats, γ of the mixture. This parameter is a strong function of temperature and mixture composition (fuel/air/EGR), and a weak function of pressure. The effect of pressure on the ratio of specific heats is typically ignored in the calculation of γ. Many different methods for calculating the ratio of specific heats for use in HRR calculations exist in the literature, as described in Refs. [1, 61-65]. Heywood [1] recommends a constant value of γ for diesel combustion of 1.35, Gatowski et al. [61] proposed a first order polynomial that decreases in magnitude with increasing temperature for SI combustion. Klein et al. [62] developed separate first order polynomials for the unburned and burned gases in SI combustion. Krieger and Borman [64] developed a third order polynomial for the determination of the internal energy of the combustion products of iso-octane for lean and stoichiometric mixtures. The correlation includes correction terms which model dissociation of the unburned gas at T > 1450K. Chang et al. [63] determined a third-order polynomial fit for γ as a function of temperature for an HCCI engine with high internal residual.

In previous work of DelVescovo et al. [66], a new correlation for the ratio of specific heats was developed. Equilibrium properties were determined using the Cantera package in MATLAB for various mixtures of n-heptane (PRF0) and iso-octane (PRF100) in air at equivalence ratios of 0.3 to 1.5, EGR percentages from 0 to 40%, temperatures from 300 to 2000K, and pressures from 10 to 100bar. The effects of pressure and EGR ratio were determined to be largely insignificant to the formulation of the correlation. The functional form of the correlation was a third order polynomial of temperature and φ and can be seen in Equation (3.5).

$$\gamma = 1.46 - 2.247x10^{-4} * T + 1.106x10^{-7} * T^2 - 2.124x10^{-11} * T^3 + \varphi(-3.806x10^{-2} - 3.396x10^{-5} * T + 1.336x10^{-8} * T^2) \quad (3.5)$$

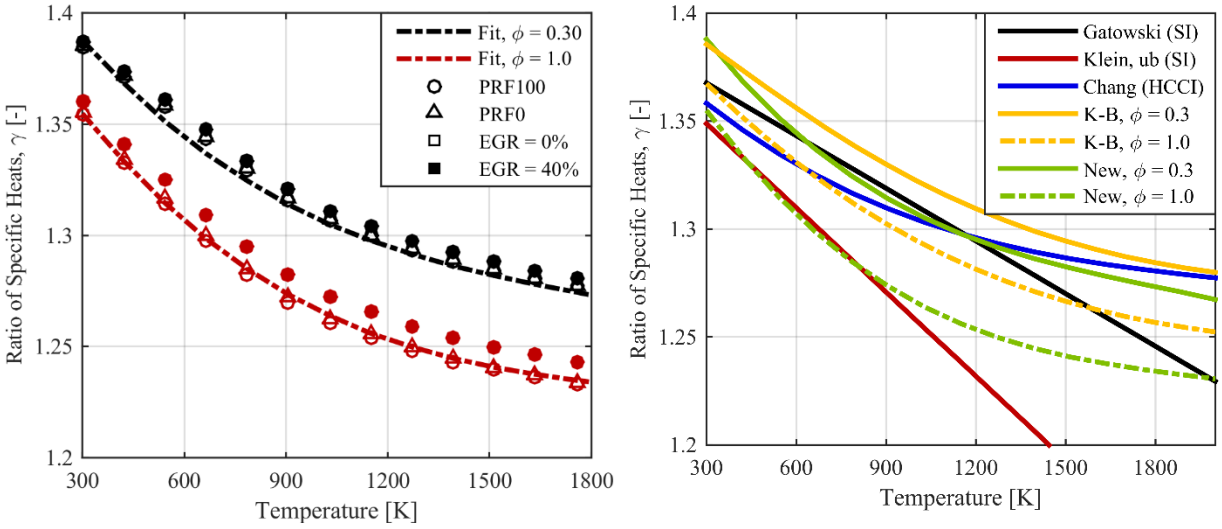

Figure 3.9: γ as a function of temperature for various mixture compositions including two φ's, and two EGR percentages for two fuels (PRF0 and PRF100) from Cantera equilibrium solver (left), and γ as a function of temperature for various correlations (right). Reproduced from DelVescovo et al. [66]

A plot of the data used to fit the correlation in the above equation is shown in Figure 3.9 on the left, and a comparison of the new correlation to correlations from literature discussed previously as a function of temperature and φ where appropriate can be seen on the right.

Figure 3.10 shows the effect of the various γ correlations on the heat release rate calculation. The Gatowski et al. [61] correlation, the Krieger and Borman (K-B) [64] correlation, and the new correlation defined by DelVescovo et al. [66] all show good agreement in terms of the shape and magnitude of the HRR. The Chang et al. [63] correlation was omitted from the plot for clarity as it was very similar to both the Gatowski correlation and the new correlation. The Klein et al. [62] correlation considering only the unburned gas relationship shows a much higher PHRR, and the constant gamma approach recommended by Heywood [1] shows a much lower PHRR than the other correlations.

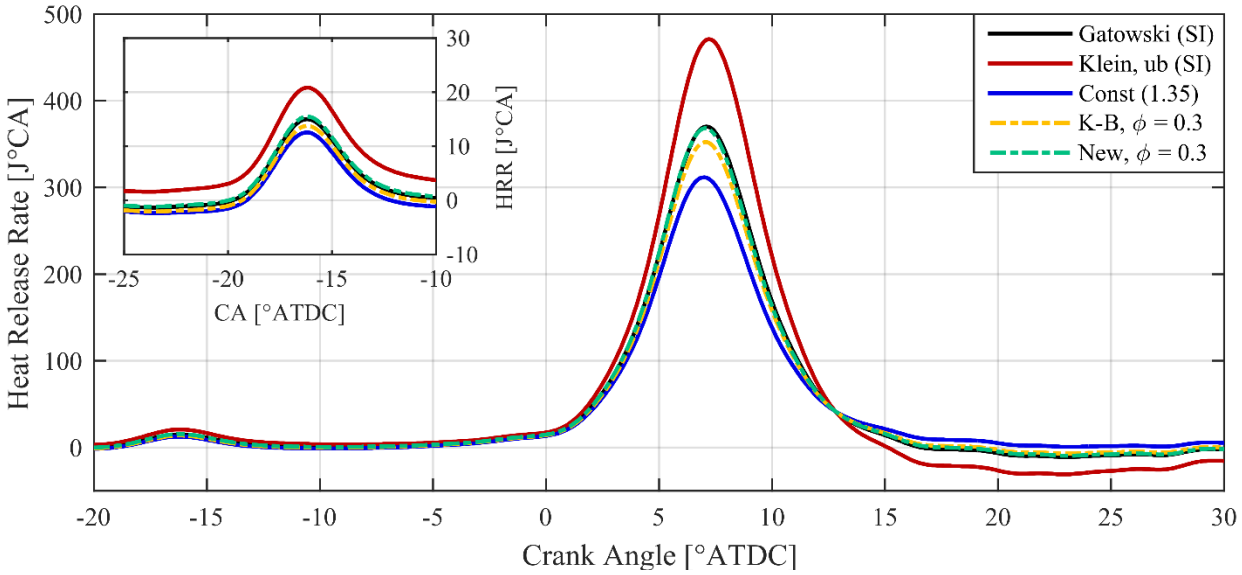

Figure 3.10: Heat release rate vs. crank angle for selected gamma correlation methods for HCCI combustion case with PRF90 at T_{in} = 40°C, φ = 0.30. Adapted from DelVescovo et al. [66]

Table 3.8 lists combustion timing and combustion phasing metrics for the tested correlations including CA10, CA50, CA90, and combustion duration (CA10-90). The table shows that the selection of the gamma correlation method can have a significant impact on the combustion phasing metrics, particularly early in the combustion process (CA10), and late in the combustion process (CA90).

Table 3.8: Combustion timing metrics for various γ correlations for an HCCI combustion case

γ Correlation	CA10 [°ATDC]	CA50 [°ATDC]	CA90 [°ATDC]	CA10-90 [°ATDC]
Gatowski et al. [61]	3.34	7.12	10.68	7.34
Klein et al. [62]	1.65	6.99	10.32	8.67
Constant [1], (1.35)	3.61	7.26	12.00	8.39
Chang et al. [63]	2.73	6.99	10.67	6.87
Krieger and Borman [64], (φ = 0.30)	3.75	7.18	10.86	7.11
DelVescovo et al. [66] (φ = 0.30)	3.37	7.09	10.71	7.34

In the present work the new correlation by DelVescovo et al. [66] was used. Ideally the correlation for γ would include the complete mixture effects, including equivalence ratio, EGR rate, and fuel

H/C and O/C ratios, however these global quantities would still not account for changes in the local values of γ due to non-uniformities in the mixture temperature caused by heat transfer and non-uniformities in mixture composition due to poor residual gas mixing, turbulence, and direct injection.

3.7 HCCI Engine Experiments

In order to assess the ignition characteristics of the fuels of interest in this work, and study the effects of intake parameters on the fuels, HCCI engine experiments were conducted in the heavy-duty single cylinder engine test cell described in Section 3.1 using port fuel injections of the tested fuels. A plug with the same dimensions as the common-rail injector described in Section 3.3 was installed in place of the direct injector to avoid needing to pressurize the common-rail system and to prevent damage to the fuel injector for all the HCCI experiments presented in this work.

3.7.1 Primary Reference Fuel (PRF) HCCI Experiments

The engine was operated in HCCI combustion using separate port fuel injections of isooctane and n-heptane. These fuels are referred to as primary reference fuels (PRFs) because of their use in the ASTM octane rating standards. The fuels provide the reference values for the research octane number (RON) [67], and the motor octane number (MON) [68], viz., 0 for n-heptane and 100 for isooctane. The relevant summarized engine operating conditions can found in Table 3.9. Included in the table is the approximate error of the measurement in parenthesis. The engine speed and total fuel energy (Q_{fuel}) was held constant while the PRF blend (a number from 0 to 100 denoting the volume percentage of isooctane to isooctane plus n-heptane) was varied at two intake temperatures and three equivalence ratios (set by adjusting intake pressure and therefore intake air flowrate) parametrically to provide a range of combustion phasings. The phasing was limited by high PPRR

in the more advanced cases, and low combustion efficiency (η_c) and high coefficient of variability of indicated mean effective pressure (COV_{IMEP}) in the more retarded combustion phasing cases.

Table 3.9: Operating conditions of PRF HCCI experiments

Engine speed [rev/min]	1300
Fuel Energy, (Q_{fuel}) [J/cyc]	2580 (±20)
Nominal Load ($IMEP_n$) [bar]	4.25-4.75
Intake Temperature [^oC]	40, 60 (±2.2)
Intake Pressure [kPa]	138.6, 122.7, 113.8 (±0.7)
Exhaust Pressure [kPa]	172.4, 144.1, 131.0 (±2.8)
Equivalence Ratio, φ [-]	0.25, 0.28, 0.30 (±0.01)
EGR [%]	0
PFI Timing [^oCA ATDC]	-320
PFI Pressure [bar]	2.5

Figure 3.11 shows the effect of intake conditions and PRF mixture on the combustion phasing, as indicated by CA50. It can be seen from the plot that PRF does not linearly adjust CA50, and the rate at which the PRF mixture affected CA50, indicated by the slope of the lines, was a stronger function of φ than of intake temperature at a fixed fuel energy condition. Because of the nature of the experiment, the pressure is coupled to the equivalence ratio as lower equivalence ratios are achieved by increasing the intake pressure. A sweep of equivalence ratio at a constant intake pressure by adjusting fuel energy would need to be performed to isolate the pressure and equivalence ratio effects.

An alternative way to view this data set is to switch the independent and dependent variables of Figure 3.11 such that the plot represents the PRF mixture required to achieve some desired CA50 for various intake conditions. This is shown in Figure 3.12.

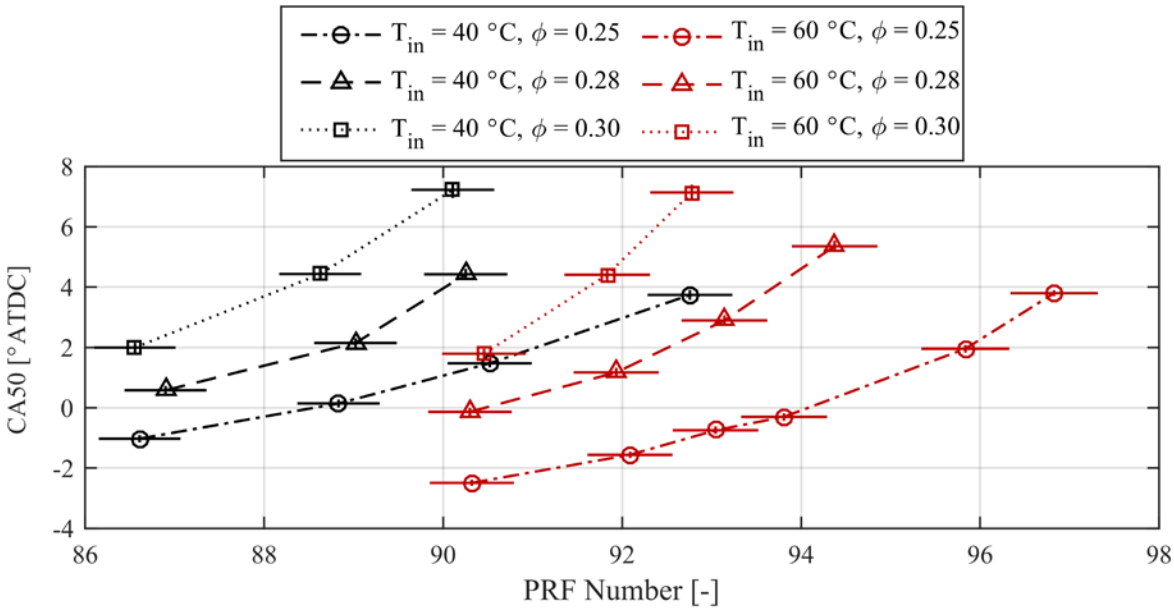

Figure 3.11: CA50 vs. PRF number for various intake conditions including sweeps of three φ's (indicated by symbols) at two different intake temperatures (indicated by color). Adapted from DelVescovo et al. [66]

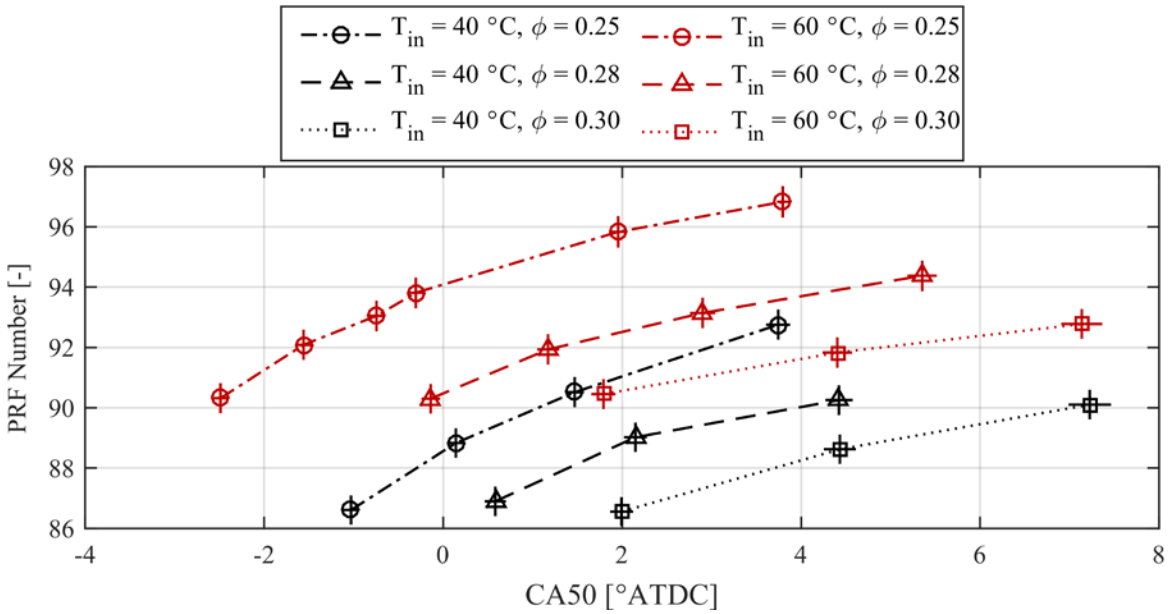

Figure 3.12: PRF number vs. CA50 for various intake conditions including sweeps of three φ's (indicated by symbols) at two different intake temperatures (indicated by color)

Here it can be seen that for a particular combustion phasing, there exists many PRF blends able to achieve this phasing depending on the intake pressure and temperature. Figure 3.13 shows the P and HRR profiles of a selection of the HCCI cases from the data set.

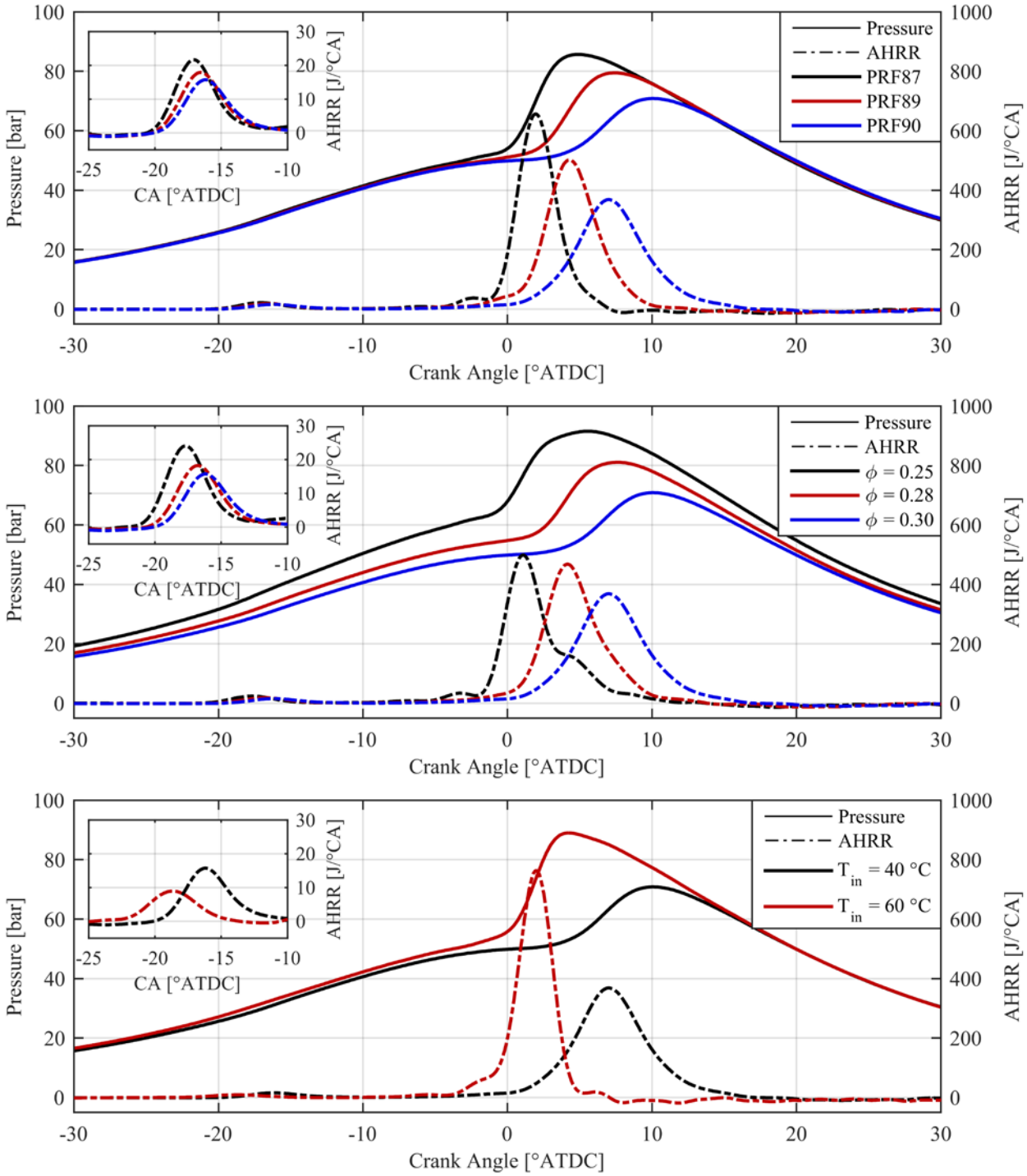

Figure 3.13: Pressure and HRR vs. crank angle showing the effects of the various intake parameters on combustion phasing at a fixed fuel energy of 2580 J/cyc. (Top: three PRF mixtures at T_{in} = 40ºC, and φ = 0.30.) (Middle: three φ's at T_{in} = 40ºC for PRF90). (Bottom: two intake temperatures for PRF90 at φ = 0.30). Adapted from DelVescovo et al. [66]

The effects of the various intake parameters on combustion phasing and the heat release profile can be clearly seen. Combustion phasing advanced with decreasing PRF, as expected due to the shorter ignition delay of n-heptane relative to iso-octane, as seen in the top plot. Counterintuitively, decreasing φ advanced combustion phasing for a fixed intake temperature and PRF mixture, as shown in the middle plot, though as discussed previously this is due to the increased pressure needed to drive the required airflow. The resulting higher cylinder pressures were responsible for the advanced combustion phasing of the leaner cases. Combustion phasing is strongly influenced by intake temperature as discussed by Chang et al. [69], and thus it is not surprising that for a fixed PRF mixture and φ, increasing intake temperature advanced combustion phasing significantly, which can be seen in the bottom plot.

The effects of the intake parameters on the LTHR are also shown in the inset axes of Figure 3.13. For a fixed intake temperature and equivalence ratio, decreasing PRF advanced the LTHR event slightly and increased its magnitude. For fixed PRF blend and intake temperature, increasing pressure (and decreasing φ) advanced and magnified the LTHR event. For a fixed equivalence ratio and PRF blend, increasing intake temperature advanced the LTHR.

As discussed previously, for a given combustion phasing there exists many combinations of fuel blend and intake conditions that can achieve this combustion phasing. Figure 3.14 demonstrates this fact for a fixed combustion phasing of $1.75^{o}\pm0.25$. The top plot shows that for a change in intake temperature of 20^{o}C, a decrease in PRF number of 3 was required to match combustion phasing at $\varphi = 0.30$. For a fixed PRF of 90, a change in intake temperature of 20^{o}C required an increase in equivalence ratio from 0.25 to 0.30 (and a corresponding decrease in intake pressure of 17.9kPa). The matched combustion phasing belies however the drastic change in heat release

behavior in the form of a decreased combustion duration and increased PHRR induced by this increase in equivalence ratio.

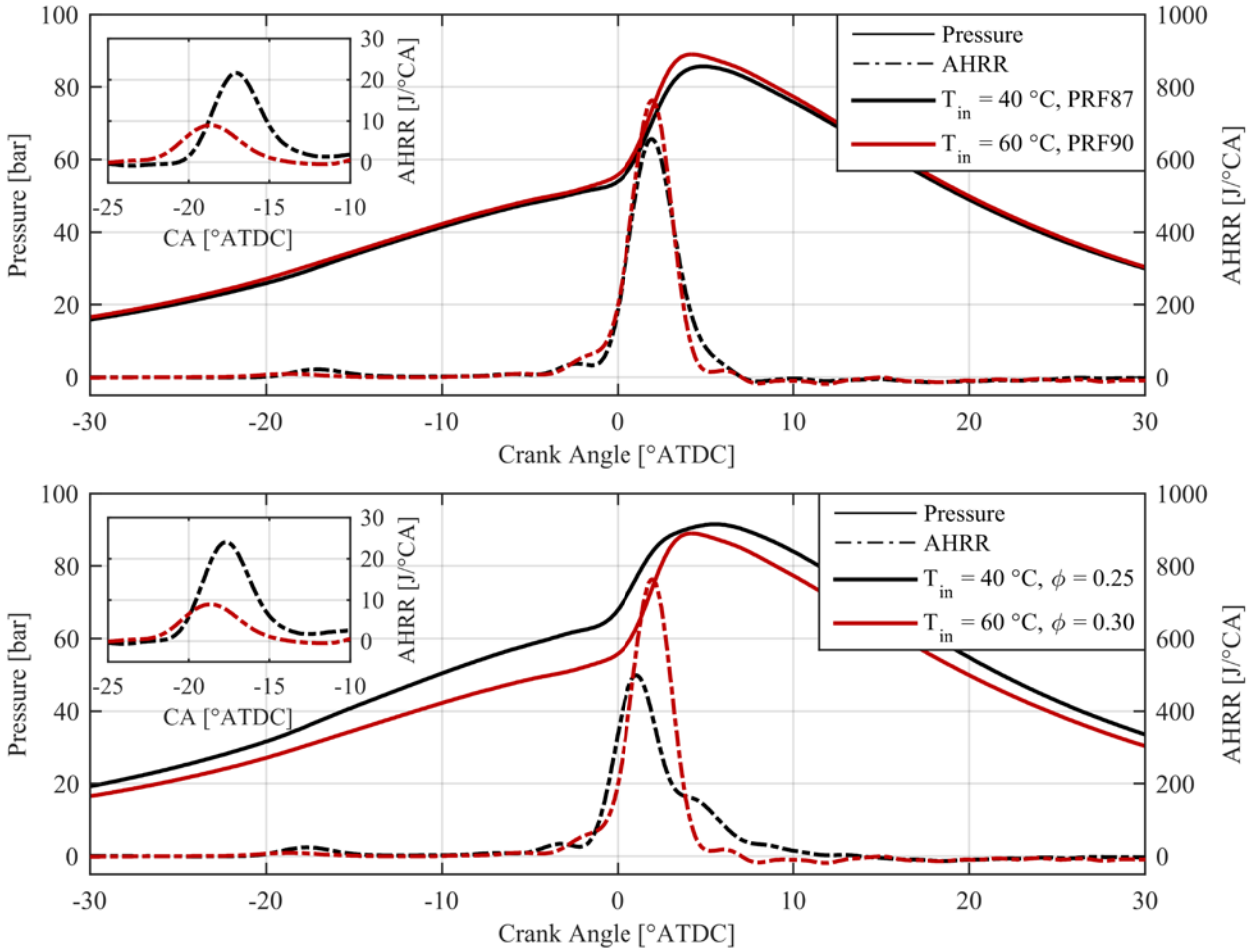

Figure 3.14: Pressure and HRR vs. crank angle with CA50 of 1.75±0.25 for the conditions listed in the legends. (Top: φ = 0.30, bottom: PRF90)

3.7.2 PRF + Syngas HCCI Experiments

HCCI experiments were performed to assess the ignition characteristics and provide experimental data for kinetic model validation of a reformed fuel surrogate comprised of 50% by mole hydrogen gas (H_2), and 50% by mole carbon monoxide (CO) referred to as syngas. The operating conditions of the HCCI experiments are summarized in Table 3.10, and the two independent intake conditions tested in the experiment are summarized in Table 3.11.

Table 3.10: Operating conditions of PRF + Syngas HCCI Experiments

Engine speed [rev/min]	1300
Fuel Energy, (Q_{fuel}) [J/cyc]	2580 (±20)
Nominal Load ($IMEP_n$) [bar]	4.0-4.25
EGR [%]	0
CA50 [^{o}ATDC]	3.75±0.25
Liquid PFI Timings [^{o}CA ATDC]	-320
Liquid PFI Pressure [bar]	2.5
Gaseous PFI Timing [^{o}CA ATDC]	-320
Gaseous PFI Pressure [bar]	4.0-5.5

Table 3.11: Intake conditions tested in PRF + Syngas HCCI Experiments

Intake Condition	1	2
Intake Temperature [^{o}C]	40 (±2.2)	60 (±2.2)
Intake Pressure [kPa]	137.9 (±0.7)	120.0 (±0.7)
Exhaust Pressure [kPa]	173.1 (±2.8)	142.0 (±2.8)
Equivalence Ratio, φ [-]	0.25 (±0.01) (PRF)	0.30 (±0.01) (PRF)

The approach utilized in the experiments was: first, stable HCCI operation was achieved at the listed intake conditions using a blend of 91% by mass of port injected isooctane and 9% by mass of port injected n-heptane (PRF91). This PRF was the blend required to achieve combustion phasing defined by CA50 of 4^o ATDC at intake condition 1 listed in Table 3.11 (which corresponded to an equivalence ratio of 0.25 for the PRF blend). After post-processing, the measured CA50s were in the range of 3.75^o±0.25. Next, syngas was added and the PRF blend was adjusted to match combustion phasing while holding the total fuel energy constant. This process was continued until the PRF blend necessary to match combustion phasing was PRF0. Figure 3.15 shows the PRF blend required to match combustion phasing as a function of premixed syngas energy percent and mass percent for reference for the tested intake conditions. Due to the low

energy density of syngas (17.48MJ/kg) relative to PRF fuels (>44MJ/kg), the mass percentage of syngas is significantly higher than the energy percentage for each case.

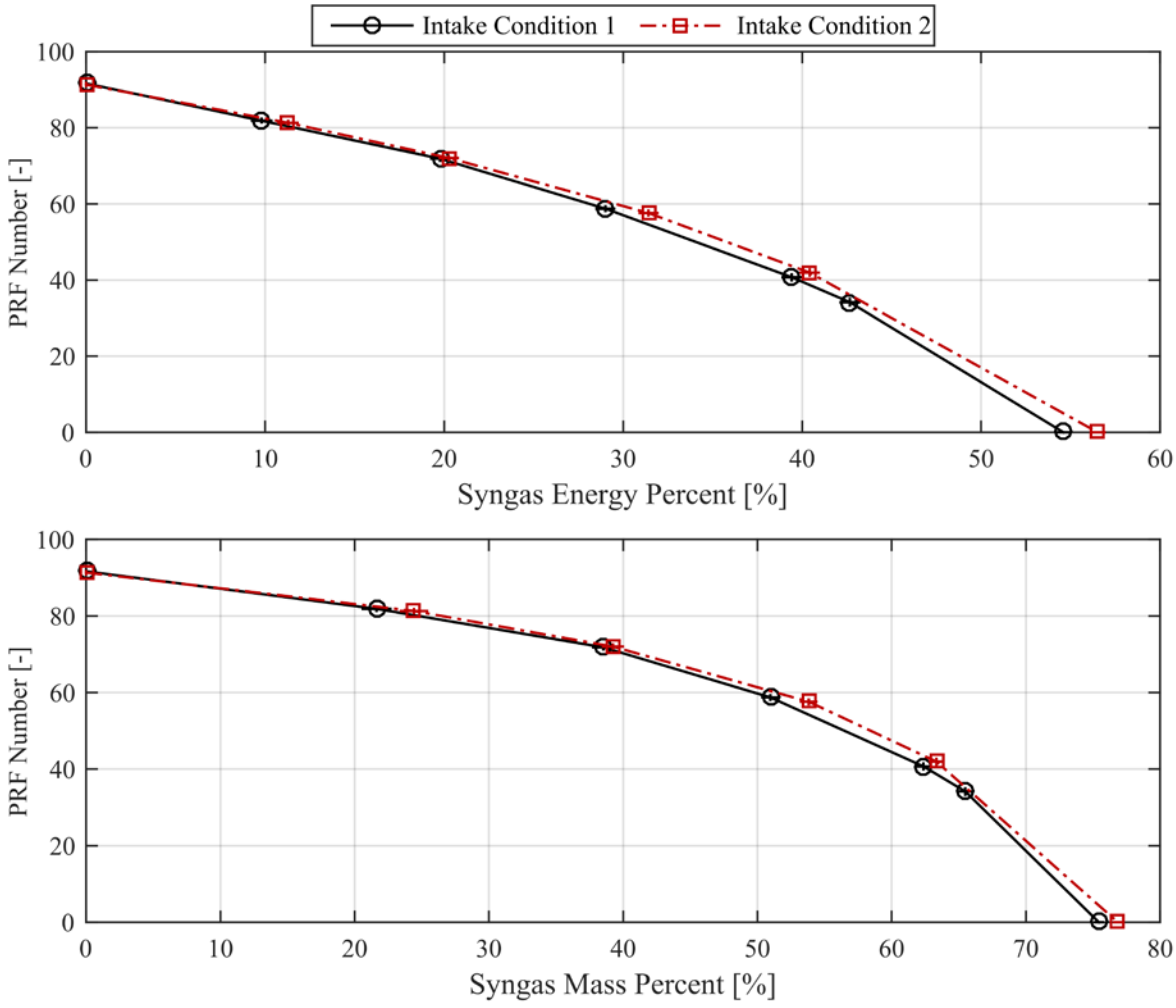

Figure 3.15: Required PRF number to achieve a CA50 of 3.75°±0.25 vs. syngas energy percent (top) and syngas mass percent (bottom) for the two intake conditions listed in the legend

The effective reactivity of the three-component mixtures was held constant by matching combustion phasing, and while the exact RON and MON of the 50/50 syngas blend is unknown, it is clear that syngas is less reactive than isooctane (RON=MON≡100) under these conditions due to the high n-heptane (RON=MON≡0) requirement to match combustion phasing (~25%$_m$, ~55%$_\varepsilon$ the subscripts m and ε denoting by mass and by energy respectively) compared to the case with no syngas which required only ~9%$_{m,\varepsilon}$ n-heptane. The two intake conditions follow nearly identical

paths with respect to required PRF number, especially for low (<30%ε) syngas percentages, i.e., for a given syngas percentage, the required PRF number is very similar for the two intake conditions within the margin of error of the measurement. At moderate syngas percentages (>30%ε) the two trends begin to deviate slightly, potentially indicating differences in either the pressure or equivalence ratio sensitivity between syngas and the PRF fuels.

Figure 3.16 shows the pressure and heat release rates for three syngas energy fractions each at the two intake conditions listed previously.

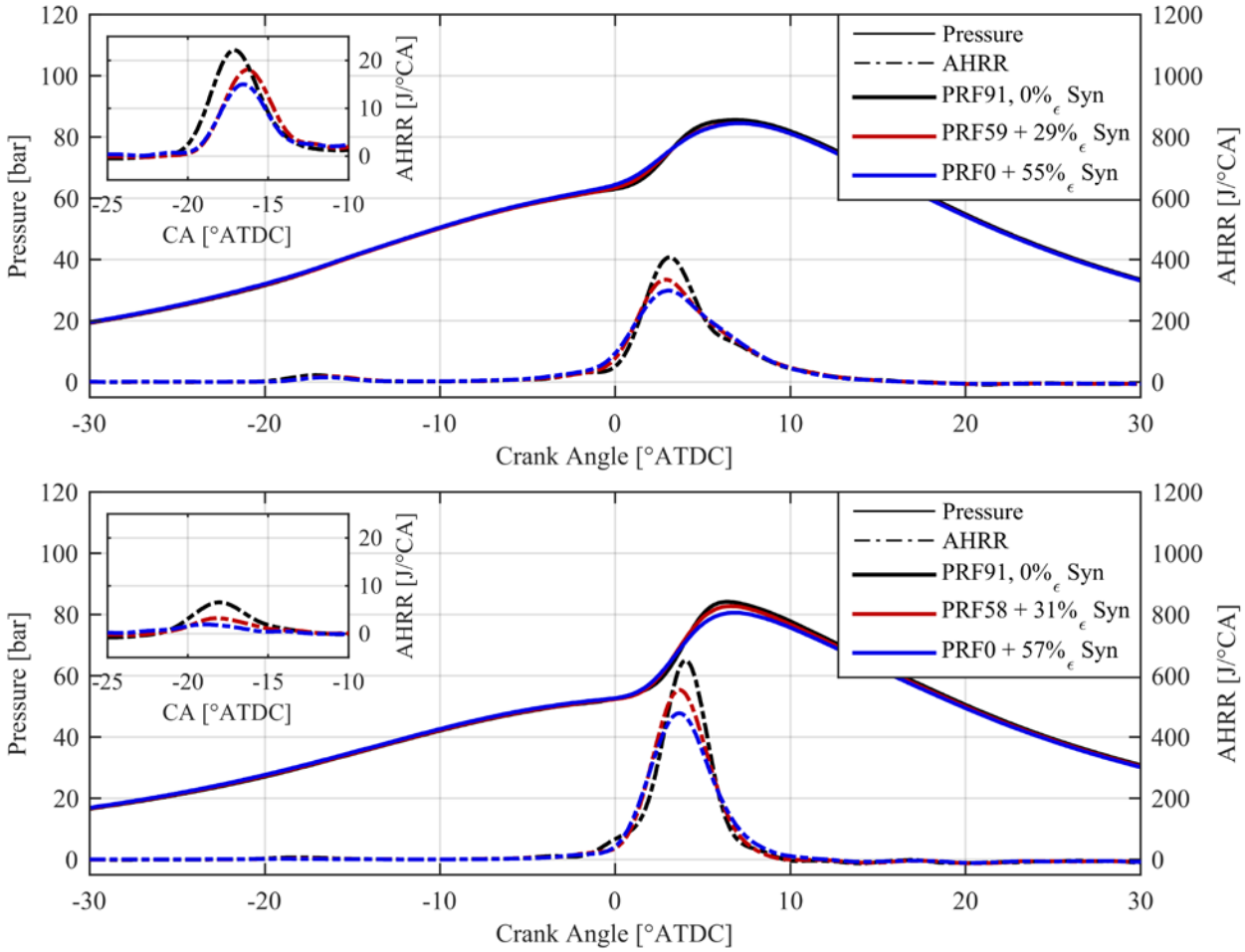

Figure 3.16: Pressure and HRR vs. crank angle for various PRF + Syngas blends at CA50 of 3.75°±0.25 for intake condition 1 (P_{in}=137.9kPa and T_{in} = 40°C at top) and intake condition 2 (P_{in} = 120.0kPa and T_{in} = 60°C at bottom)

Suppression of the low temperature heat release is seen for both sets of intake conditions as PRF fuels, which exhibit significant negative temperature coefficient (NTC) [70, 71] behavior, were substituted for syngas. The syngas cases demonstrate slightly reduced peak heat release rates relative to the cases with no syngas, however these differences are minor compared to the cycle-to-cycle variation in the pressure and heat release for these cases, which is depicted in Figure 3.17 by the standard deviation of the measured pressure and heat release data at each crank index. The syngas cases tended to have significantly higher cycle-to-cycle fluctuations in the measured pressure data, potentially due to higher variability in the shot-to-shot mass of fuel injected by the gaseous port fuel injector.

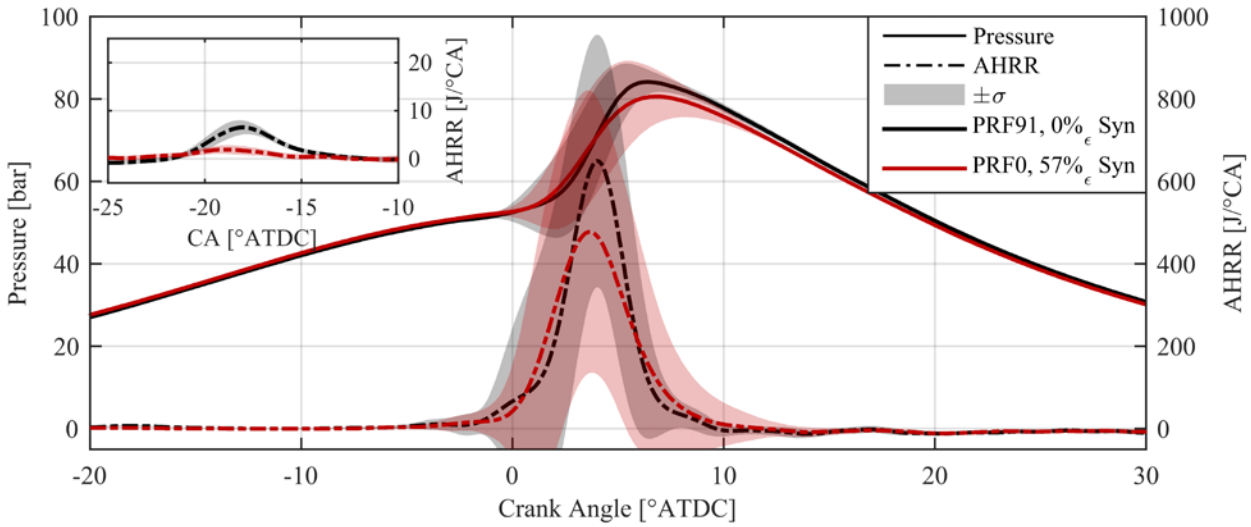

Figure 3.17: Pressure and heat release with standard deviation range (filled regions) for the case with no syngas and PRF91 (black), and 57%$_\varepsilon$ syngas with PRF0 (red)

3.8 Iso-Octane/n-Heptane RCCI Engine Data

In order to assess the performance and emissions of RCCI combustion with PRF fuels, the first set of experiments presented here examined the effect of injection timing and global equivalence ratio for a fixed premixed mass fraction. The relevant operating conditions of the first set of experiments are summarized in Table 3.12. These conditions utilized the same total fuel energy, and intake

temperature and equivalence ratio ranges as the HCCI conditions presented previously in order to provide direct comparisons between HCCI and RCCI combustion strategies.

Table 3.12: Nominal Operating Conditions for constant PRF SOI sweeps

Engine speed [rev/min]	1300
Fuel Energy, (Q_{fuel}) [J/cyc]	2590 (±20)
Nominal Load ($IMEP_n$) [bar]	4.5-4.75
EGR [%]	0
Intake Temperature [^oC]	40 (±2.2)
PFI Fuel	iso-octane (PRF100)
PFI Timing [^oCA ATDC]	-320
PFI Pressure [bar]	2.5
DI Fuel	n-heptane (PRF0)
DI Timing, (SOI) [^oCA ATDC]	Swept
Rail Pressure [bar]	500
Global PRF [-]	88.1 (±0.2)

The three intake conditions tested in the first set of RCCI experiments are summarized in Table 3.13. The fixed fuel energy condition required the adjustment of intake pressure to adjust the global equivalence ratio, the implications of which were discussed in Section 3.7.1. Higher intake pressures were required to achieve leaner global equivalence ratios.

Table 3.13: Intake conditions for constant PRF SOI sweeps

Intake Condition	1	2	3
Intake Pressure [kPa]	100.0 (±0.7)	114.5 (±0.7)	122.0 (±0.7)
Exhaust Pressure [kPa]	118.6 (±2.8)	135.8 (±2.8)	144.8 (±2.8)
Equivalence Ratio, φ [-]	0.35 (±0.01)	0.30 (±0.01)	0.28 (±0.01)

Figure 3.18 shows selected performance metrics including combustion phasing, gross efficiency and combustion efficiency, and NO_x emissions for the constant PRF SOI sweeps for the three intake conditions.

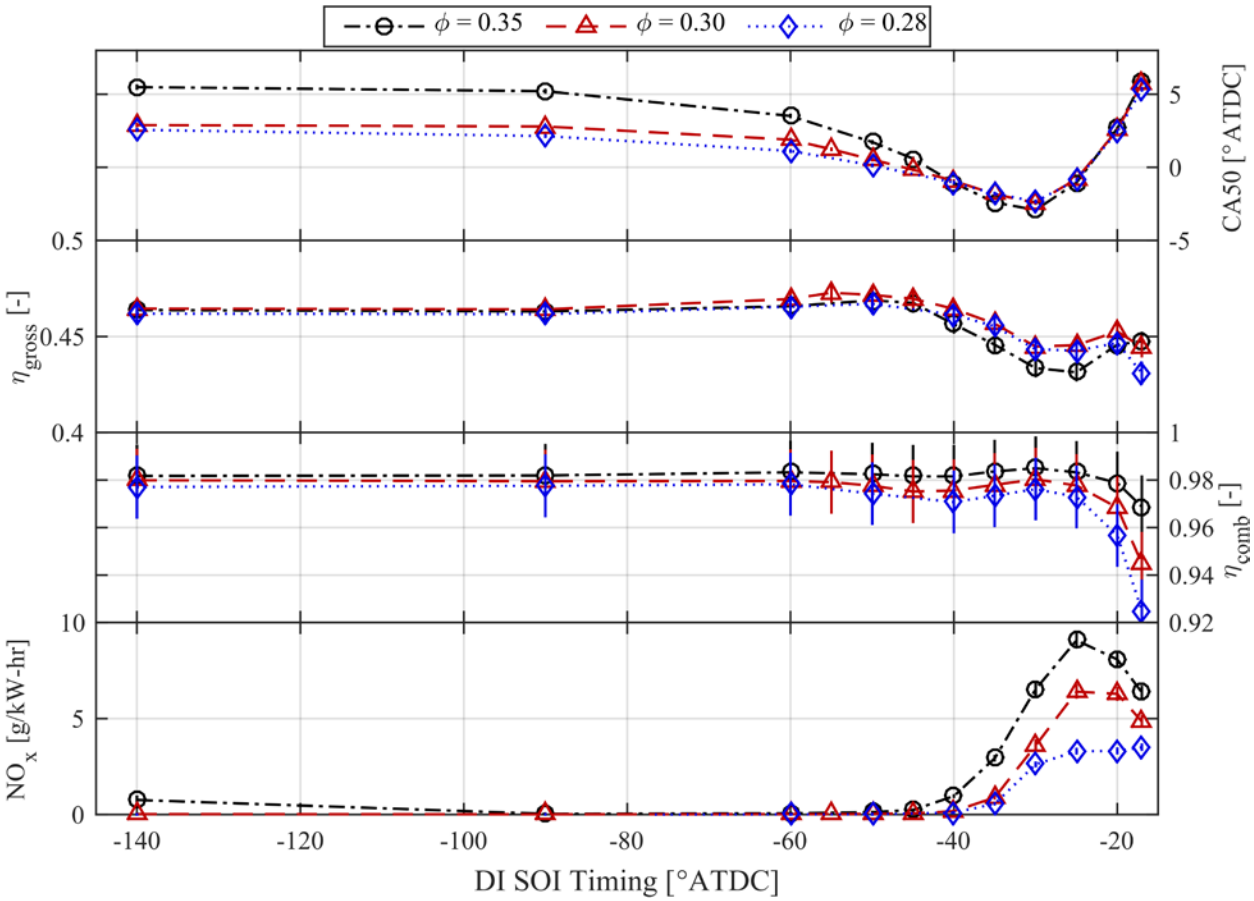

Figure 3.18: Selected performance and emissions metrics for PRF RCCI combustion as a function of SOI for three global equivalence ratios at T_{in} = 40°C, and PRF88 including CA50 (top), gross efficiency (second), combustion efficiency (third), and NO_x emissions (bottom)

Combustion phasing advanced as SOI was retarded between about -140° and -35° SOI, however as SOI timing was further retarded, combustion phasing also retarded, potentially indicating the transition from a kinetically controlled regime to a mixing controlled combustion regime. Another possible explanation is that as equivalence ratio is increased, the relative sensitivity of ignition delay to equivalence ratio is decreased, as discussed by Kokjohn et al. [48]. This decrease in ignition delay sensitivity implies that despite more fuel existing in locally very rich regions as the SOI is retarded, the time between the injection and ignition events does not decrease significantly due to the relatively unchanged ignition delay. In effect, the time between injection and ignition is then fixed, thus implying retarding injection will retard combustion phasing. The combustion

phasing advancement seen for decreased equivalence ratio was a function of the increased cylinder pressure required to increase air flowrate and decrease φ, as discussed previously. The combustion phasing of the three global φ lines converged around an SOI of about -30º and follow the same path, indicating a decrease in the sensitivity of combustion phasing to the intake pressure and supporting the idea of a change in combustion regime.

Peak gross efficiency was achieved in the range of -60º and -45º SOI for all three global equivalence ratios, however it is difficult to decouple the link between combustion phasing and gross efficiency from this test. The combustion efficiency was relatively constant around ~98% until combustion phasing retarded at late SOI timings, decreasing sharply, particularly for the leanest global case, φ = 0.28. NO_x emissions increased drastically as SOI was retarded beyond about -40º SOI likely due to regions of high local equivalence ratios resulting from decreased mixing time; and peaking around -25º SOI only to decrease again as combustion phasing retarded and peak cylinder temperatures decreased.

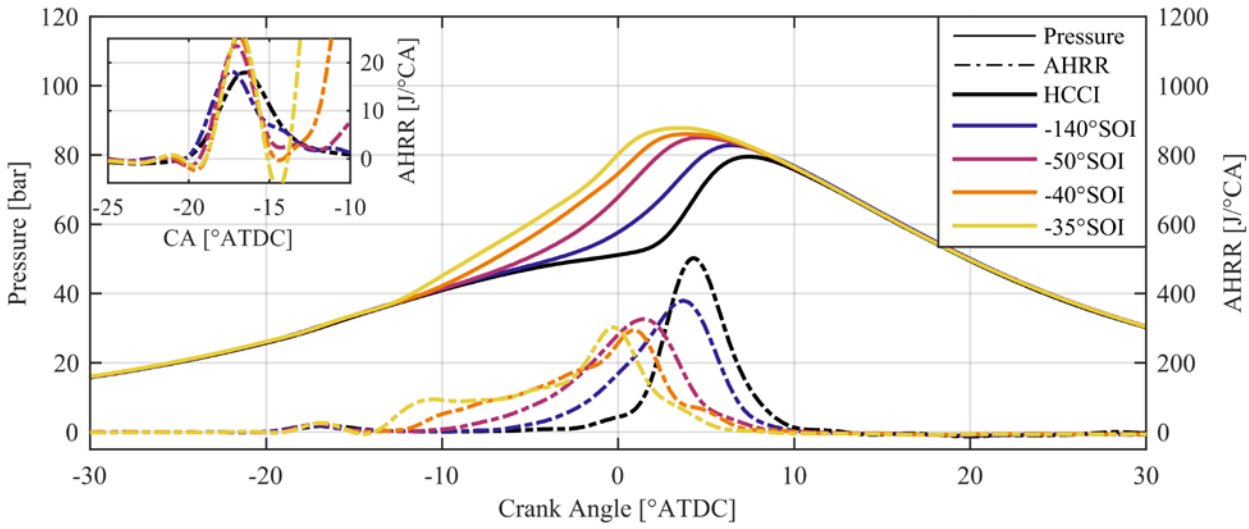

Figure 3.19: Pressure and HRR for RCCI SOI sweep at φ = 0.30, Tin = 40ºC for a fixed global PRF of 88.1±0.2 for early injection timings including port fueled HCCI

Figure 3.19 shows the pressure and heat release rate profiles for the early SOI cases, including a fully premixed port injected HCCI case at the same intake conditions for reference. It can be seen from the figure that, as the start of injection was retarded, thus inducing greater reactivity and equivalence ratio stratification in the cylinder, combustion phasing advanced and the duration of combustion increased. Due to the fixed fuel energy constraint, this increase in combustion duration also resulted in a decrease in the peak heat release rate as the area under the heat release rate corresponds to the total energy released, which is equal for all the cases assuming the same combustion efficiency.

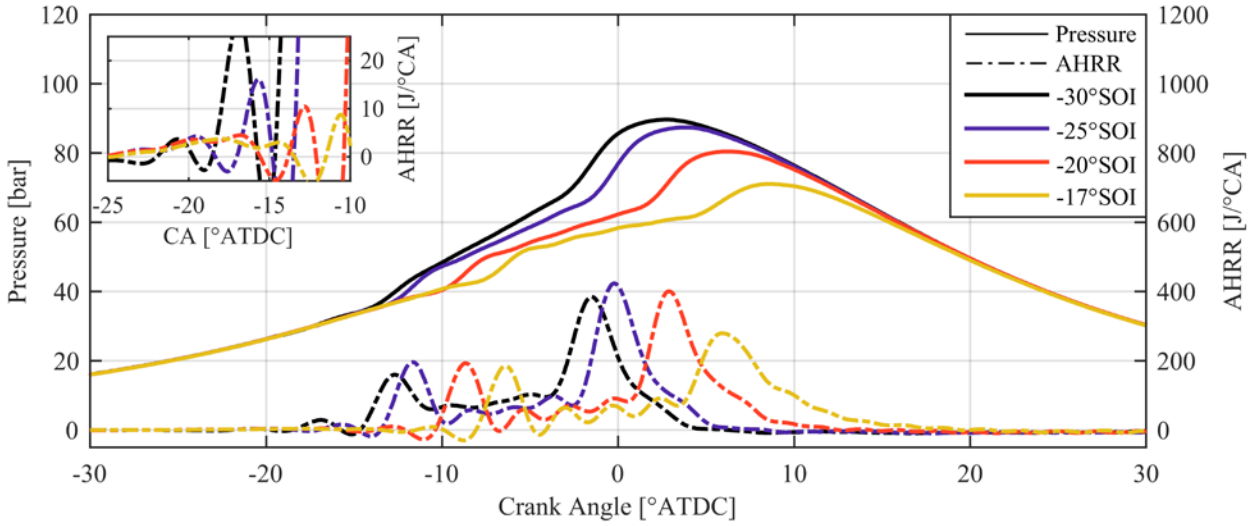

Figure 3.20: Pressure and HRR for RCCI SOI sweep at φ = 0.30, T_{in} = 40ºC for a fixed global PRF of 88.1±0.2 for late SOI timings

Figure 3.20 shows the pressure and heat release rate profiles for the late SOI cases. Here the opposite trend is seen in combustion phasing in relation to the injection timing as retarding the combustion phasing retarded the combustion phasing. The combustion duration is largely unchanged by the injection timing, except in the case of the most retarded phasing, which is likely due to the expansion of the charge cause by the piston motion after TDC.

In order to eliminate the influence of combustion phasing on the performance and emissions of the experimental results, a separate test was conducted where the combustion phasing was held constant at the peak efficiency location from the previous data set (CA50 ~ 1^{o}CA) corresponding to the -50^{o} SOI case. The injection timing was swept and the ratio of premixed to direct injected fuel (global PRF) was adjusted to match the combustion phasing. The operating conditions of this test are summarized in Table 3.14, and the intake conditions are listed in Table 3.15.

Table 3.14: Nominal operating conditions for constant CA50 SOI sweeps

Engine speed [rev/min]	1300
Fuel Energy, (Q_{fuel}) [J/cyc]	2590 (±20)
Nominal Load ($IMEP_n$) [bar]	4.3-4.75
EGR [%]	0
Intake Temperature [^{o}C]	40 (±2.2)
PFI Fuel	iso-octane (PRF100)
PFI Timing [^{o}CA ATDC]	-320
PFI Pressure [bar]	2.5
DI Fuel	n-heptane (PRF0)
DI Timing, (SOI) [^{o}CA ATDC]	Swept
Rail Pressure [bar]	500
CA50 [^{o}CA ATDC]	0.75 (±0.25)

Table 3.15: Intake conditions for constant CA50 SOI sweeps

Intake Condition	1	2
Intake Pressure [kPa]	114.5 (±0.7)	122.0 (±0.7)
Exhaust Pressure [kPa]	135.8 (±2.8)	144.8 (±2.8)
Equivalence Ratio, φ [-]	0.30 (±0.01)	0.28 (±0.01)

Figure 3.21 shows the performance and emissions metrics for the fixed CA50 sweeps as a function of SOI. Initially, as injection timing was retarded, the required PRF to achieve the desired combustion phasing was increased to counter the increased reactivity and equivalence ratio stratification. After -25^{o} SOI however, the required PRF decreased significantly as the combustion

process became dominated by the vaporization and mixing processes. In order to match combustion phasing with a late injection, the reactivity of the global mixture had to increase significantly. The design of the experiment meant that this increase in reactivity could only be achieved by direct injecting more n-heptane, making the late phasing cases more reliant on the mixing process. Gross efficiency again peaked between -60° and -45° SOI, and the two equivalence ratios performed similarly across the entire SOI range for the metrics shown, though the differences in the intake conditions were minor. The NO_x emissions again increased as SOI retarded beyond -35° due to high local φ's.

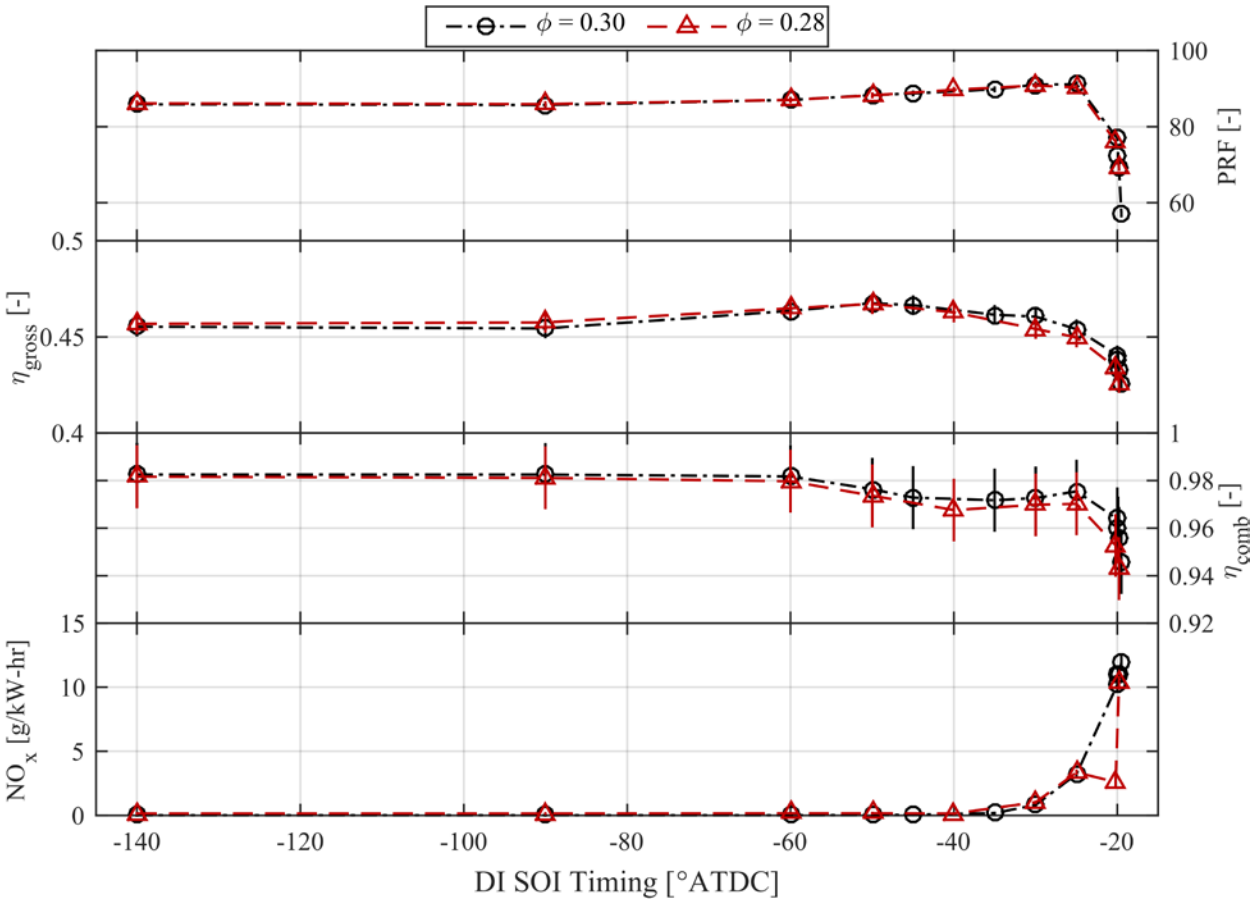

Figure 3.21: Selected performance and emissions metrics for PRF RCCI combustion as a function of SOI for two global equivalence ratios at T_{in} = 40°C, and PRF88 including CA50 (top), gross efficiency (second), combustion efficiency (third), and NO_x emissions (bottom)

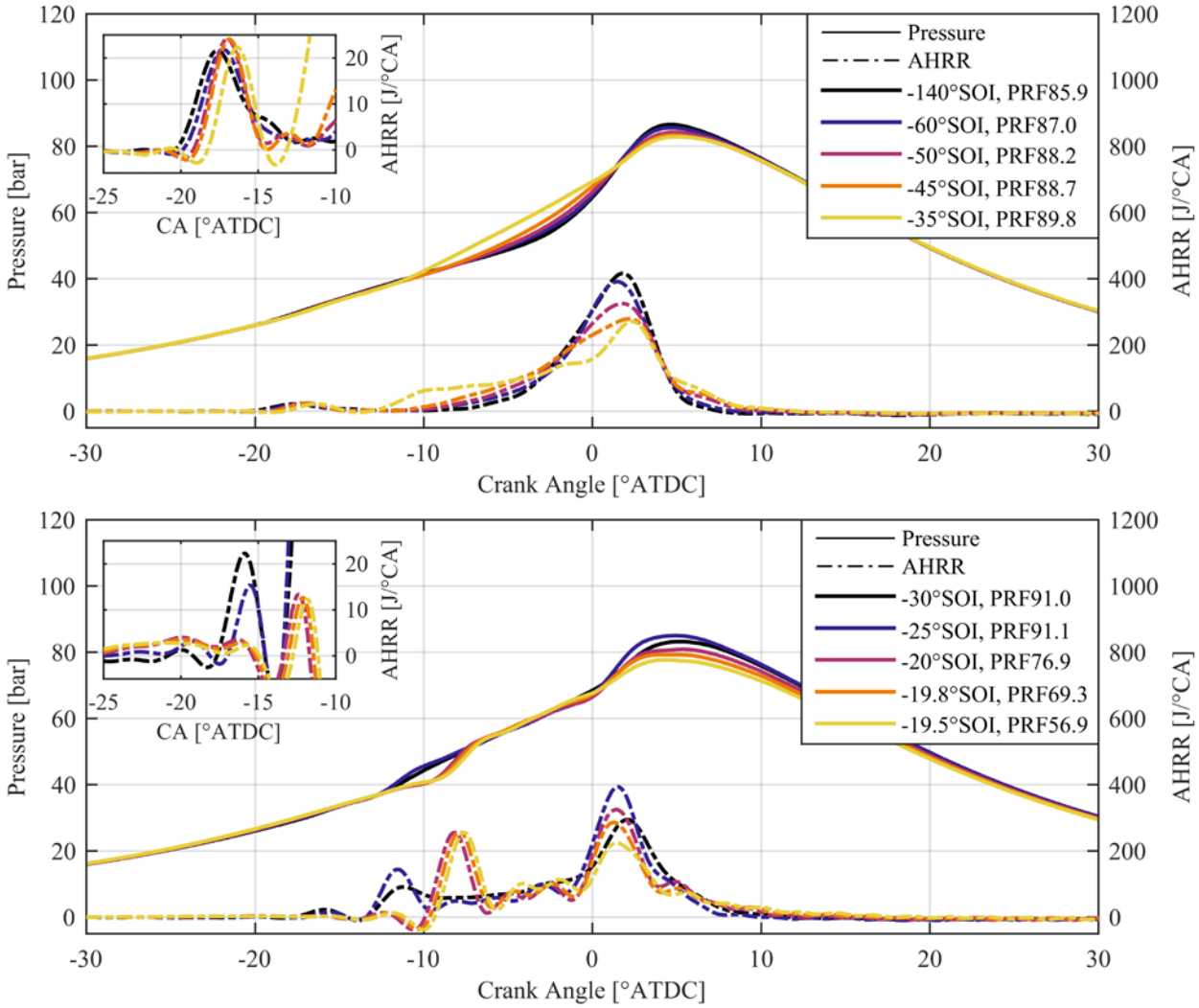

Figure 3.22: Pressure and HRR for RCCI SOI sweep at φ = 0.30, Tin = 40ºC for a fixed CA50 of 0.75±0.25 for the early injection timings (top), and the late injection timings (bottom)

Figure 3.22 shows the early SOI and late SOI pressure and HRR profiles for the fixed CA50 cases. As can be seen from the plot, as SOI is retarded in the early injection timing cases, the PRF required to match combustion phasing increases, and the combustion duration increases due to the greater induced stratification. The peak heat release rate thereby decreases for the reasons discussed previously. For the late SOI cases with fixed CA50, delaying the SOI beyond -25º delayed the onset of the first stage combustion, indicated by the first peak in HRR, by an approximately equal amount. The second stage combustion, indicated by the second large peak in HRR, occurred at

nearly identical timing regardless of SOI. This differs from the fixed global PRF test presented previously, which indicates that the increase in global reactivity was able to effectively overcome the decreased time between injection and ignition. Due to the higher n-heptane mass fraction, the first stage combustion was more pronounced, thereby overcoming the earlier heat release in the more advanced cases, and providing a similar pressure history (and temperature assuming equal trapped mass), thus ensuring the ignition of the premixed isooctane would occur at very close to the same timing in crank angle space.

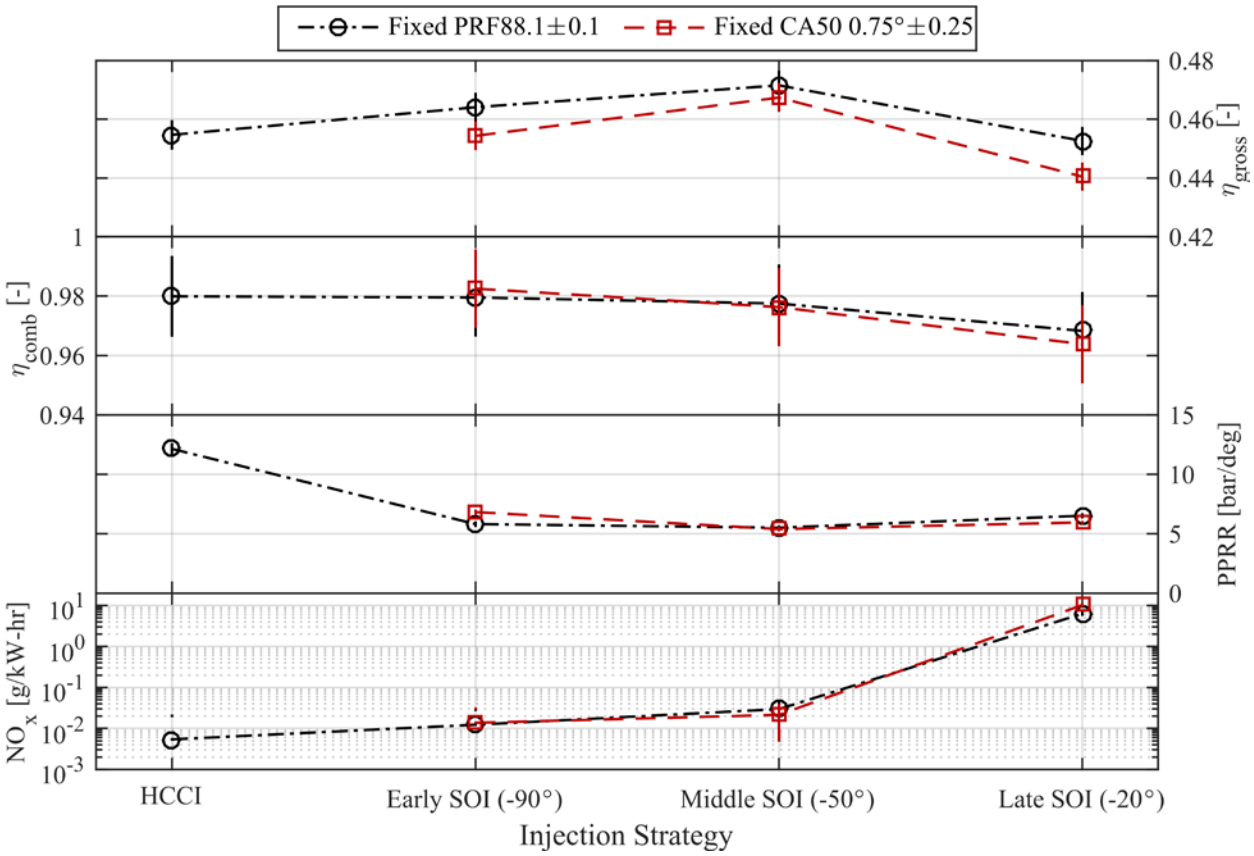

Figure 3.23: Selected performance and emissions metrics vs. of injection strategy at T_{in} = 40ºC and φ = 0.30. Note that the NO_x emissions are plotted on a log scale to see the relative differences

Figure 3.23 summarizes selected performance and emissions metrics as a function of injection strategy. HCCI combustion was not achievable at a CA50 of 0.75º at the intake conditions presented due to excessive pressure rise rates (>15 bar/deg), and is therefore omitted from the

analysis. It is clear that the optimal cases in terms of both gross efficiency and PPRR were in the mid-range SOI timings centered around -50° SOI, whether fixing either CA50 or global reactivity. Late injection timings resulted in decreased gross efficiency, decreased combustion efficiency, and high NO_x emissions due to the overly stratified mixture. Very early SOI timings, including HCCI, suffered from increased PPRR, resulting in increased combustion noise, and decreased η_{gross}.

3.9 Syngas/n-Heptane RCCI Engine Data

In order to assess the performance of the reformed syngas fuel (50% H_2, 50% CO) in RCCI combustion, isooctane was replaced as the low-reactivity fuel. The best case from the PRF data set presented in Section 3.8, which corresponded to an SOI of -50° at T_{in} = 40°C and φ = 0.30 was used as a reference condition for comparison and is referred to as the baseline condition in the following section. The relevant engine operating conditions are reproduced in Table 3.16.

Table 3.16: Nominal operating conditions of Syngas/PRF0 RCCI cases

Engine speed [rev/min]	1300
Fuel Energy, (Q_{fuel}) [J/cyc]	2590 (±20)
Nominal Load ($IMEP_n$) [bar]	4.25-4.75
EGR [%]	0
Intake Temperature [°C]	40 (±2.2)
PFI Fuel	Syngas (50% H_2 + 50% CO)
PFI Timing [°CA ATDC]	-320
PFI Pressure [bar]	4.0 – 5.5
DI Fuel	n-heptane (PRF0)
DI Timing, (SOI) [°CA ATDC]	-50
Rail Pressure [bar]	500

Because of differences in the stoichiometric air-fuel ratio (AFR_s) and the large volume displacement of intake air due to the low density of gaseous fuels, in addition to the low energy

density of syngas, which requires much greater fuel mass flowrates than PRF fuels, it is not possible to simultaneously match intake pressure, air mass flowrate and equivalence ratio for a baseline PRF condition. Matching intake pressure results in reduced air flowrate due to the displacement of intake air, while matching air flowrate requires higher intake pressures and results in a much leaner charge due to the low AFR_s of syngas, and matching φ requires significantly reduced intake pressure and air flowrate. For this reason, each parameter was matched independently to compare to the baseline PRF condition. A summary of the intake parameters tested is shown in Table 3.17; the red text indicating the parameters that were held constant.

Table 3.17: Intake conditions for relevant matched intake parameters for Syngas/PRF0 RCCI

Matched Intake Parameter	P_{in}	$\dot{m}_{air}$	φ
Intake Pressure [kPa]	114.5 (±0.7)	120.7 – 123.4	105.5 (±0.7)
Exhaust Pressure [kPa]	135.8 (±2.8)	142.7 – 144.8	126.9 (±0.7)
Air Flowrate [kg/min]	1.76 – 1.80	1.92 (±0.005)	1.57 – 1.66
Equivalence Ratio, φ [-]	0.27 – 0.28	0.25 – 0.27	0.30 (±0.01)

The two main parameters which control RCCI combustion, the DI timing and the ratio of premixed to direct injected mass, were adjusted independently to assess the relative performance of the two strategies to account for reactivity differences in the premixed fuel. Typically, researchers have compared different premixed fuels by matching combustion phasing and comparing the relative performance and emissions [37, 39, 54], however, as discussed in DelVescovo et al. [54], the direct injection strategy should be tailored to the specific fuel blend in order to maximize the performance and minimize the emissions. In order to more accurately compare the performance of two different premixed fuels, the bulk characteristics of the heat release should therefore be matched.

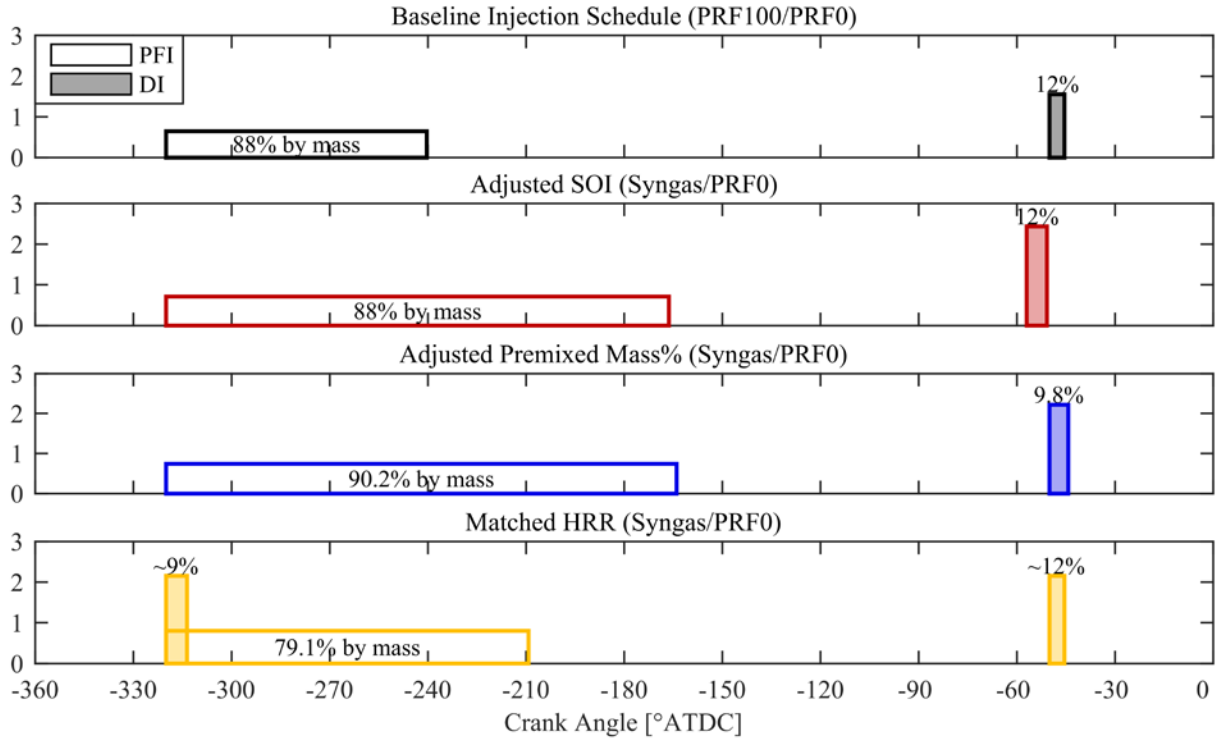

Figure 3.24: Injection schedule used for baseline PRF100/PRF0 case at -50° SOI (top in black), matched CA50 with SOI only (second in red), matched CA50 with premixed % only (third in blue), and matched HRR (bottom in yellow) for a fixed intake pressure of P_{in} = 114.5kPa. Area of rectangles is equal to the injected mass

Figure 3.24 shows the injection schedules used to realize the three comparison methods presented; matching CA50 with injection timing only, matching CA50 by adjusting the ratio of premixed mass to direct injected mass, and matching the HRR phasing and shape. Matching the CA50 with injection timing necessitated a significant increase in total fuel mass due to the low energy density of syngas. This can be clearly seen by the areas of the regions in the plot which correspond to the fuel mass injected. Because the ratio of premixed to DI fuel was fixed by the baseline condition at 88%, the increase in fuel mass meant that the n-heptane mass injected also increased, which can be seen by the significantly larger area of the adjusted SOI direct injection compared to the baseline case. This increase in DI mass meant that in order to match combustion phasing with the DI case, the injection timing needed to advance. A similar effect is seen in the matched premixed % case where, in order to match phasing, the premixed % increases for the syngas case. Without the

context regarding energy density, these trends would seem to indicate that syngas is more reactive than isooctane; however, as described in Section 3.7.2, the opposite is the case.

The HRR matching was achieved by matching the baseline direct injection of high reactivity fuel timing and duration, and adding a direct injection of high reactivity fuel during valve overlap to increase the background reactivity of the premixed fuel to something that approximated the baseline PRF100 condition. This strategy insured that the gradients in equivalence ratio and reactivity, which defined the shape and phasing of the heat release in the baseline condition, were approximately maintained and matched. Rail dynamics due to the early injection event were not accounted for, so some discrepancies may have been present in the DI quantity, though the injections were over 250 crank angle degrees apart and significant deviations were not expected.

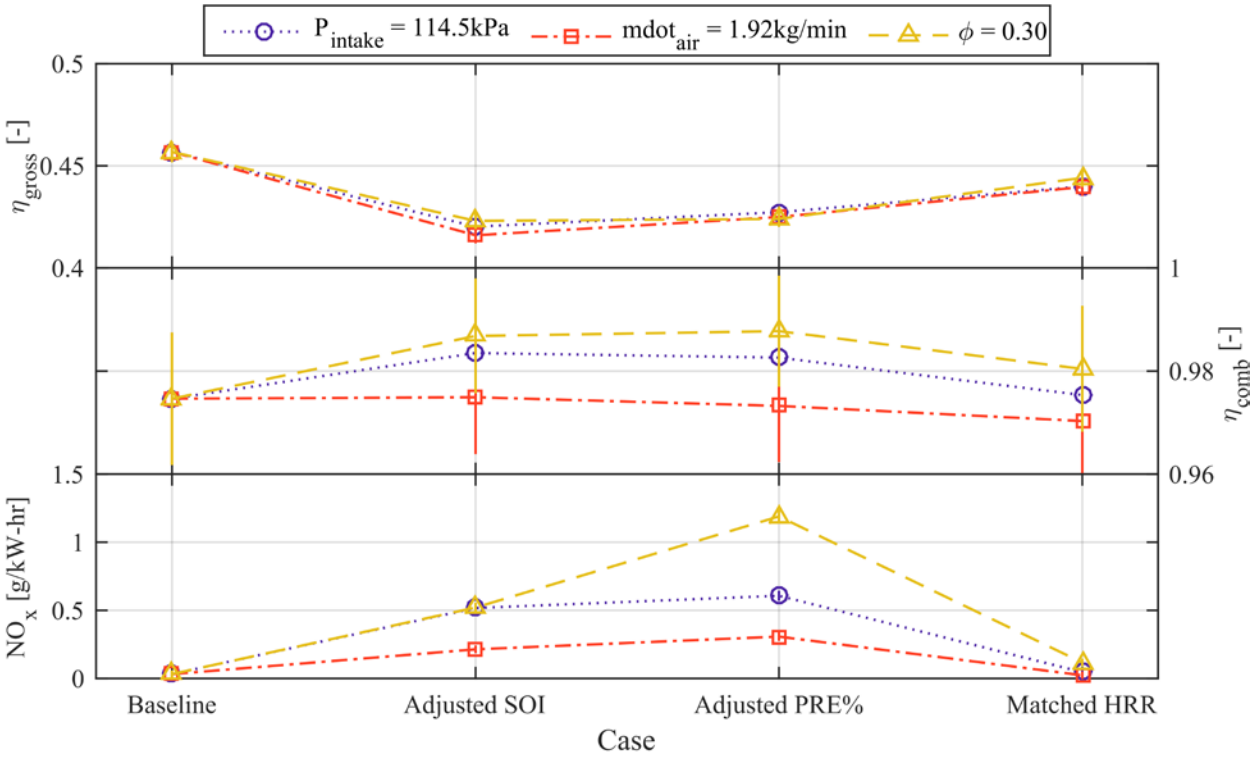

Figure 3.25: Gross efficiency (top), combustion efficiency (middle), and NO_x (bottom) for the baseline case -50° SOI with PRF100/PRF0, and the matched CA50 cases and the matched HRR case with Syngas/PRF0 for each of the three fixed intake parameters (P_{in} in purple, $\dot{m}_{air}$ in orange, φ in yellow)

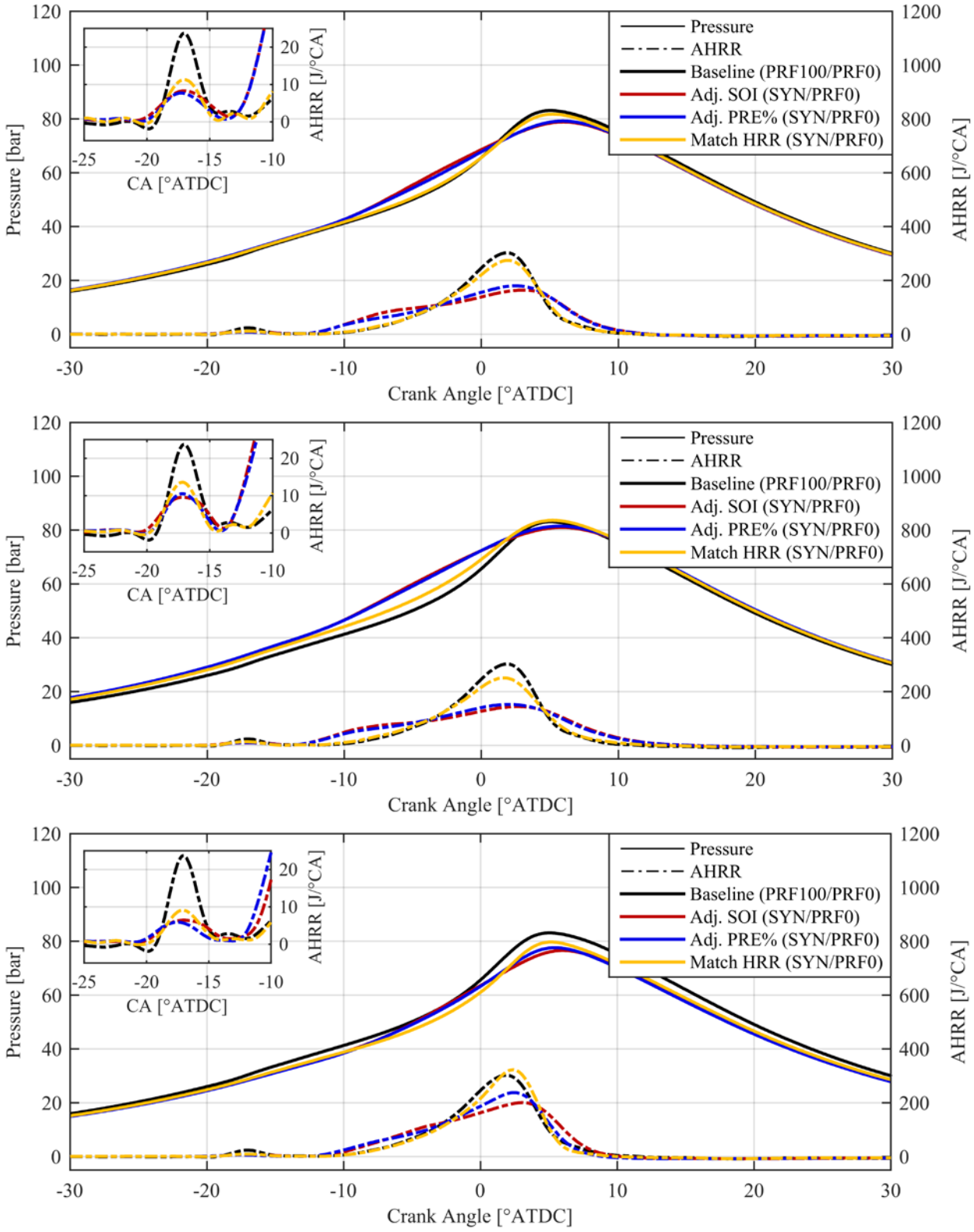

Figure 3.26: Pressure and HRR for Syngas/PRF0 RCCI cases (adjusted SOI in red, adjusted premixed mass percent in blue, and matched HRR in yellow) compared to the baseline PRF100/PRF0 case at -50º SOI (black) for the three fixed intake conditions. P_{in} = 114.5kPa (top), $\dot{m}_{air}$ = 1.92kg/min (middle), and φ = 0.30 (bottom)

Figure 3.25 shows the performance and NO_x emissions for the syngas cases compared to the baseline PRF100 case, and Figure 3.26 shows the pressure and HRR profiles for the cases for each matched intake parameter. Both matched CA50 strategies resulted in reduced η_g and drastically increased NO_x emissions due to the high DI requirements, which is consistent with the results shown by DelVescovo et al. [54]. The matched HRR case was able to regain most of the lost efficiency while decreasing NO_x emissions close to the baseline level for all of the matched intake parameters. This result shows the importance of matching the bulk heat release characteristics, instead of merely the combustion phasing in order to optimize the RCCI strategy for the given fuel combination.

3.10 Methane/n-Heptane RCCI Engine Data

Additional RCCI combustion tests were performed utilizing methane (CH_4) as the low-reactivity fuel. Methane was chosen as it is the predominant component of natural gas (>90%) and has a very high octane number. Researchers including Hanson et al. [53], Nieman et al. [52] and Walker et al. [72] have shown significant potential for natural gas and methane in RCCI for extension of the high-load limit, however the high octane number of natural gas presents a challenge at low and mid load conditions in RCCI combustion due to high DI fuel requirements. A comparison of CH_4 compared to the baseline PRF100 condition discussed in the previous section was performed, the relevant operating conditions of which can be seen in Table 3.18.

Similarly to the syngas experiments, the volumetric displacement of air caused by the injection of a gaseous fuel made simultaneously matching all the intake conditions (intake pressure, air flowrate, and equivalence ratio) impossible. However, due to the relatively similar energy density and stoichiometric air-fuel ratio of methane to isooctane, the air flowrate and equivalence ratio

could be simultaneously matched at least within the margin of error of the respective measurements. Two independent intake conditions were then run for all the tests presented here with methane, those being a matched intake pressure condition and a second condition which matched both air flowrate and φ. These conditions are summarized in Table 3.19.

Table 3.18: Nominal operating conditions of CH_4/PRF0 RCCI cases

Engine speed [rev/min]	1300
Fuel Energy, (Q_{fuel}) [J/cyc]	2590 (±20)
Nominal Load ($IMEP_n$) [bar]	4.25-4.75
EGR [%]	0
Intake Temperature [°C]	40 (±2.2)
PFI Fuel	Methane (CH_4)
PFI Timing [°CA ATDC]	-320
PFI Pressure [bar]	4.0 – 5.5
DI Fuel	n-heptane (PRF0)
DI Timing, (SOI) [°CA ATDC]	-50
Rail Pressure [bar]	500

Table 3.19: Intake conditions for relevant matched intake parameters for CH_4/PRF0 RCCI

Matched Intake Parameter	P_{in}	$\dot{m}_{air}$ and φ
Intake Pressure [kPa]	114.5 (±0.7)	116.5 – 117.2
Exhaust Pressure [kPa]	135.8 (±2.8)	137.9 – 138.6
Air Flowrate [kg/min]	1.86 – 1.89	1.92 (±0.005)
Equivalence Ratio, φ [-]	0.31-0.32	0.30 (±0.01)

With methane as the low-reactivity fuel, injection timing alone was not enough to control combustion phasing due to its very high octane number and high energy density (~50MJ/kg), however, adjusting the premixed mass percent at a constant SOI was able to match combustion phasing with the baseline case. The injection schedules used to match CA50 and HRR with the baseline condition can be seen in Figure 3.27, and the resulting gross efficiency, combustion efficiency, and NO_x emissions for the two intake conditions can be seen in Figure 3.28.

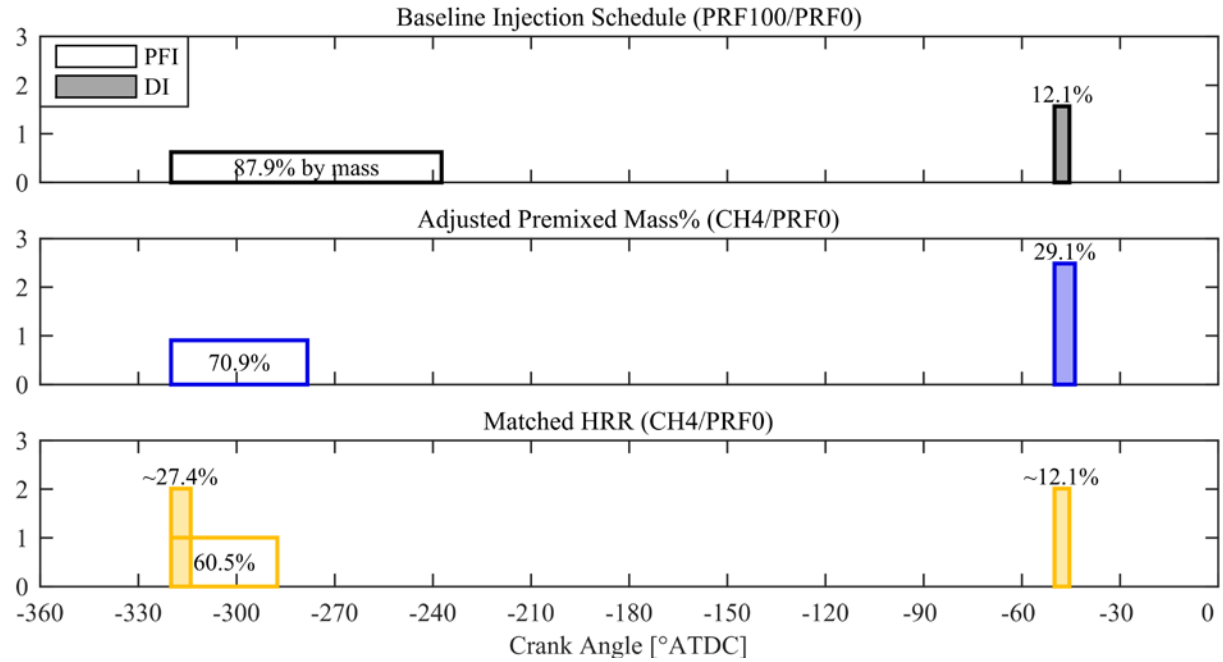

Figure 3.27: Injection schedule used for baseline PRF100/PRF0 case at -50° SOI (top in black), matched CA50 with premixed % only (middle in blue), and matched HRR (bottom in yellow) for a fixed intake pressure of P_{in} = 114.5kPa. Area of rectangles is equal to the injected mass

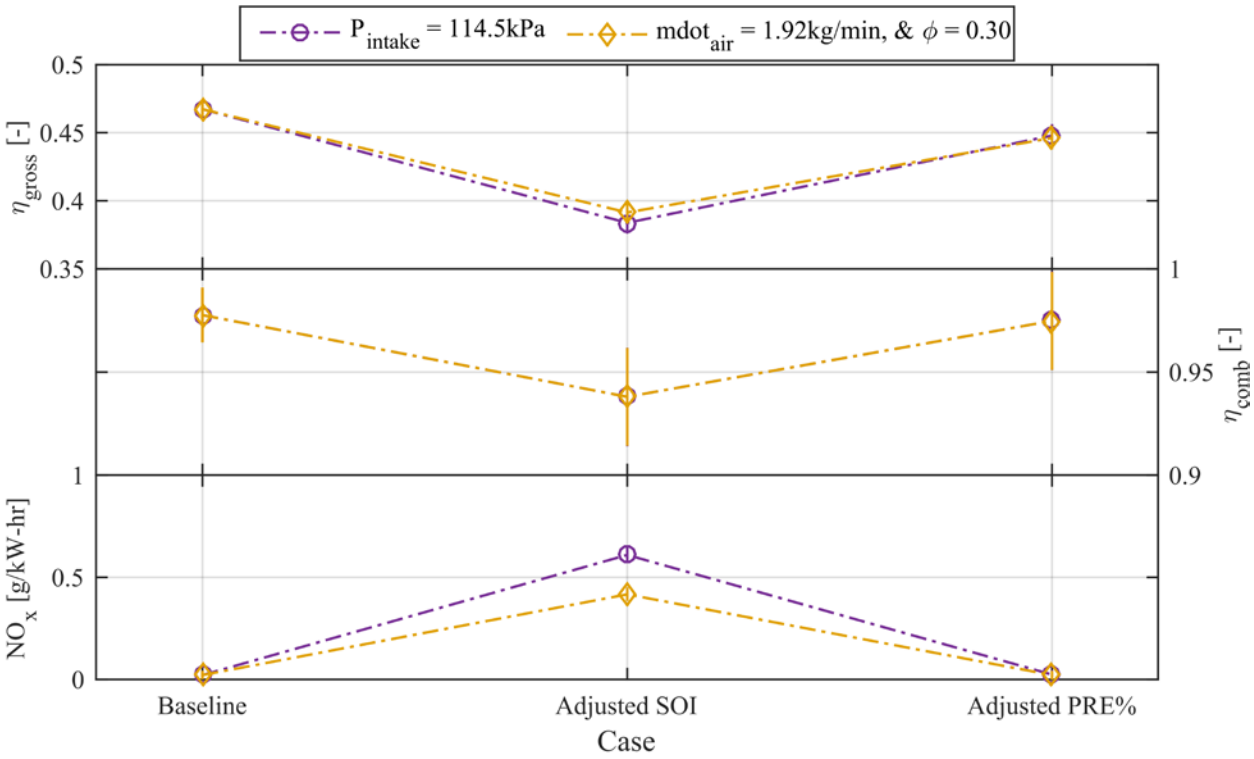

Figure 3.28: Gross efficiency (top), combustion efficiency (middle), and NOx (bottom) for the baseline case at -50° SOI with PRF100/PRF0, and the matched CA50 case and the matched HRR case with CH_4/PRF0 for each of the two fixed intake parameters (P_{in} in purple, $\dot{m}_{air}$ and φ in yellow)

Similar to the syngas results, matching combustion phasing by adjusting the premixed percentage resulted in a large decrease in gross efficiency and greater than an order of magnitude increase in NO_x emissions. The matched HRR case was again able to regain most of the lost gross thermal efficiency and improving combustion efficiency while simultaneously reducing NO_x emissions to the baseline level.

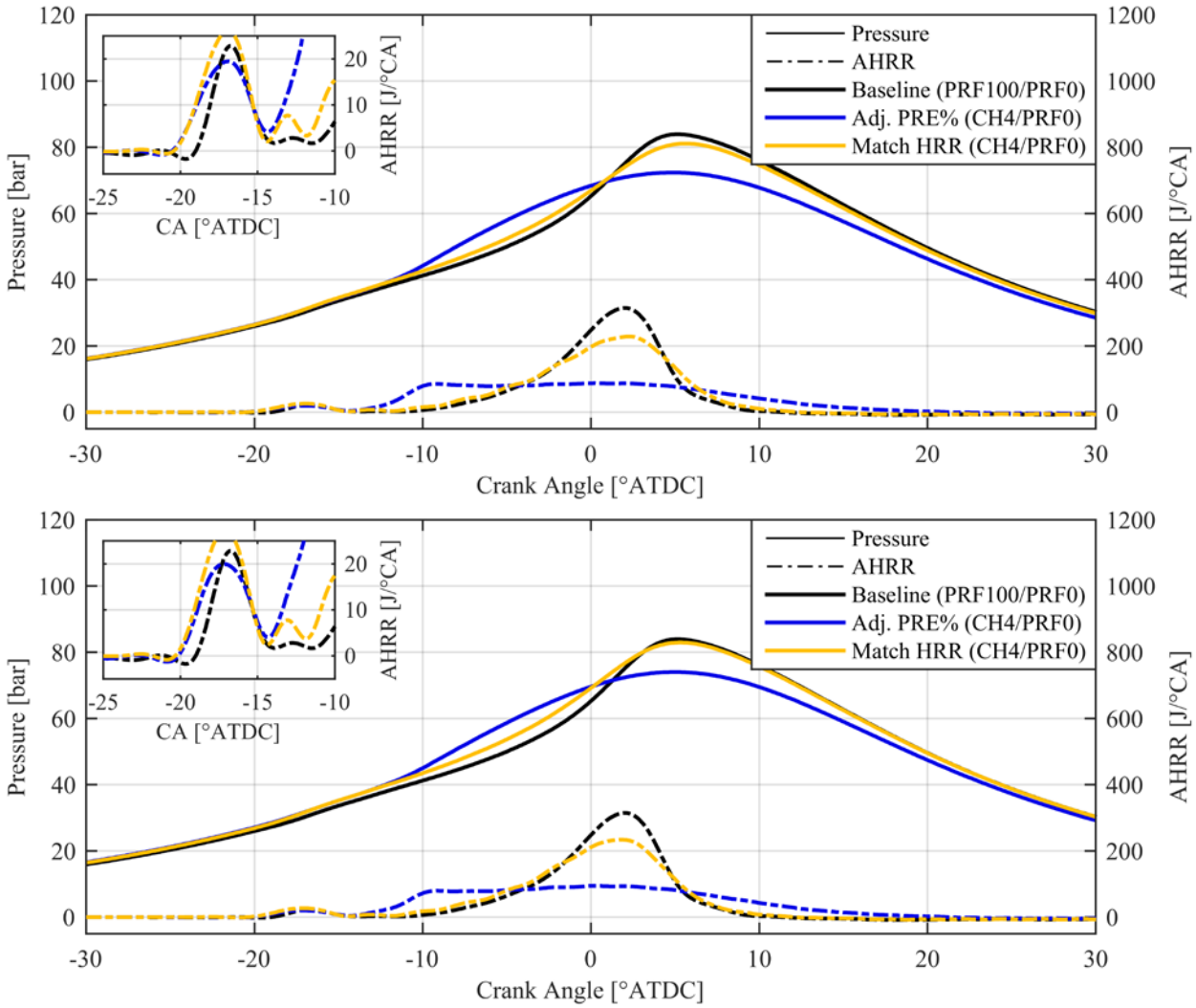

Figure 3.29: Pressure and HRR for CH_4/PRF0 RCCI cases (adjusted premixed mass percent in blue, and matched HRR in yellow) compared to the baseline PRF100/PRF0 case at -50° SOI (black) for the two fixed intake conditions. P_{in} = 114.5kPa (top), $\dot{m}_{air}$ = 1.92kg/min and φ = 0.30 (bottom)

Figure 3.29 shows the pressure and HRR for the baseline, matched CA50, and matched HRR cases for the two intake conditions. The matched CA50 case shows an extremely long combustion

duration due to the high DI fuel percentage while the matched HRR case with CH_4 demonstrated slightly reduced PHRR compared to the baseline case, potentially due to methane's slow reaction rates compared to PRFs. Despite this difference in PHRR, it is clear that in order to maximize the performance and emissions, the entire heat release event should be optimized for the given fuel combination. Additional results for different injection timings, including SOIs of -40^o and -30^o, can be found in Appendix C.1. The alternate injection timings exhibited the same trends in combustion performance and emissions behavior as the -50^o SOI case presented in this section, further verifying that matching the bulk heat release rate, instead of merely combustion phasing, is able to maintain the performance and emissions profile of some baseline case.

4 *IGNITION DELAY PREDICTIONS*

Premixed fueling strategies such as HCCI, PPC, PFS, and RCCI require a detailed description of fuel kinetics over an incredibly wide operating space in terms of temperature, pressure, and mixture composition in order to accurately predict parameters such as start of combustion (SOC), crank angle of 50% of mass fraction burned (CA50), and combustion duration (CA10-90), which are parameters helpful for control of a combustion system utilizing such a strategy. Dual fuel strategies such as RCCI require not only well defined chemistry for one fuel, but for two separate fuels and all potential mixtures of the two. To assist in the design and development of such advanced strategies, it is beneficial to turn to simplified computational models of the combustion process for predicting combustion behavior and trends in order to provide better control methods and algorithms necessary for advanced combustion implementation [15, 20, 73, 74].

4.1 Cantera Constant Volume Simulations

All ignition delays used in this work where simulated using a constant volume (CV) reactor in Cantera with MATLAB. The CV reactor inputs (temperature, pressure, EGR rate, equivalence ratio, and a parameter defining the mass ratio of two fuels) were varied parametrically to develop large 5-D matrices of ignition delay values. These matrices could then be used directly, or used to develop a correlation relating all the input parameters to the ignition delay algebraically.

4.1.1 Defining Ignition Delay

Ignition delay is defined as the time it takes a mixture of fuel and oxidizer at some initial temperature and pressure to ignite. Ignition delays can be determined experimentally with the use of shock tubes, rapid compression machines (RCM), and constant volume (CV) chambers [1, 70,

71]. The primary methods for defining the ignition time itself are by identifying either the peak or peak rate of change in concentration of some radical species (typically OH due to its importance in high temperature reaction pathways), or by identifying the peak rate of change of some thermodynamic quantity, such as pressure or temperature [75]. The choice of parameter depends on the application and available information, as well as the range of conditions. For the purposes of this work, the ignition delay was defined as the location of maximum temperature change with respect to time, backwards extrapolated to the initial temperature. A depiction of this process on an example ignition delay case can be seen in Figure 4.1.

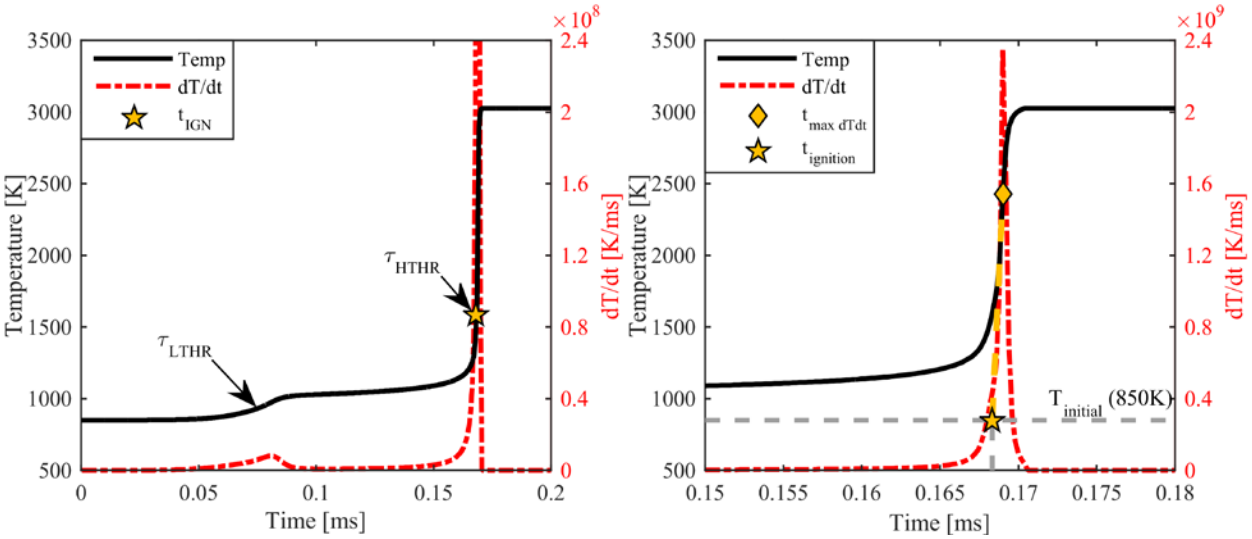

Figure 4.1: Constant volume temperature and derivative of temperature from Cantera depicting the location of ignition delay (left), and a zoomed window showing the backwards linear extrapolation from the location of maximum temperature change to the initial temperature (right)

This ignition delay criteria was coupled with the condition that the ignition temperature was at least equal to the initial temperature plus some critical temperature that defined the high temperature ignition event as shown in Equation (4.1).

$$T_{ignition} \geq T_{initial} + \Delta T_{crit} \tag{4.1}$$

The critical temperature (ΔT_{crit}), was defined as whichever was lower, the equilibrium temperature minus the initial temperature divided by four, or 400K. This condition, shown in Equation (4.2), was implemented to ignore any low temperature heat release behavior at the condition of interest, and to also account for conditions where the equilibrium temperature was not 400K greater than the initial temperature (e.g., very lean conditions). This ignition delay criterion was chosen as it provided a very robust prediction of high-temperature ignition delays for a large range of initial temperatures, pressure, equivalence ratios, and for various fuels.

$$\Delta T_{crit} = \frac{\left(T_{equilibrium} - T_{initial}\right)}{4}; \ \ or \ \ \Delta T_{crit} = 400K \tag{4.2}$$

4.1.2 Creating Ignition Delay Look-up Tables

As discussed previously, in order to predict autoignition using ignition delays in a premixed strategy such as HCCI, a very complete description of the ignition delay as a function of temperature and pressure is required. Direct injection strategies, like PFS and PPC, induce large gradients in equivalence ratio in the cylinder, and a dual-fuel strategy like RCCI has large in-cylinder gradients in fuel composition, in addition to equivalence ratio. These conditions create an incredibly wide operating space in terms of temperature, pressure, and mixture composition in which ignition delay must be defined. In addition to this, because it would be impossible and impractical to simulate every possible condition, the ignition delay data in a large multi-dimensional table must be interpolated at the conditions of interest. The more dimensions in the table, the more query points are required to perform this interpolation. Table 4.1 summarizes the number of data points needed in each dimension of a multi-dimensional matrix, as well as the total number of query points for a 5-D matrix for various interpolation methods. Higher order interpolation techniques require significantly more computational power at each condition of

interest, making them impractical for quick autoignition prediction. Linear interpolation requires the fewest data points, and is therefore the fastest method, however at the cost of decreased accuracy. Figure 4.2 compares a linear interpolation approach with a cubic interpolation approach for some arbitrary exponential function. An exponential function was chosen because this functional form is the most commonly chosen for ignition delay curves [73]. It is clear from the plot that the linear interpolation tends to over-predict the values between data points for a function with an exponential form, while cubic interpolation approach does not suffer from this drawback.

Table 4.1: Number of points required for each interpolation method for a 5-D dataset

Interpolation Method	N_p Required in Each Dimension	Total Number of Points Needed
Linear	2	32
Cubic	4	1024
Spline	4	1024

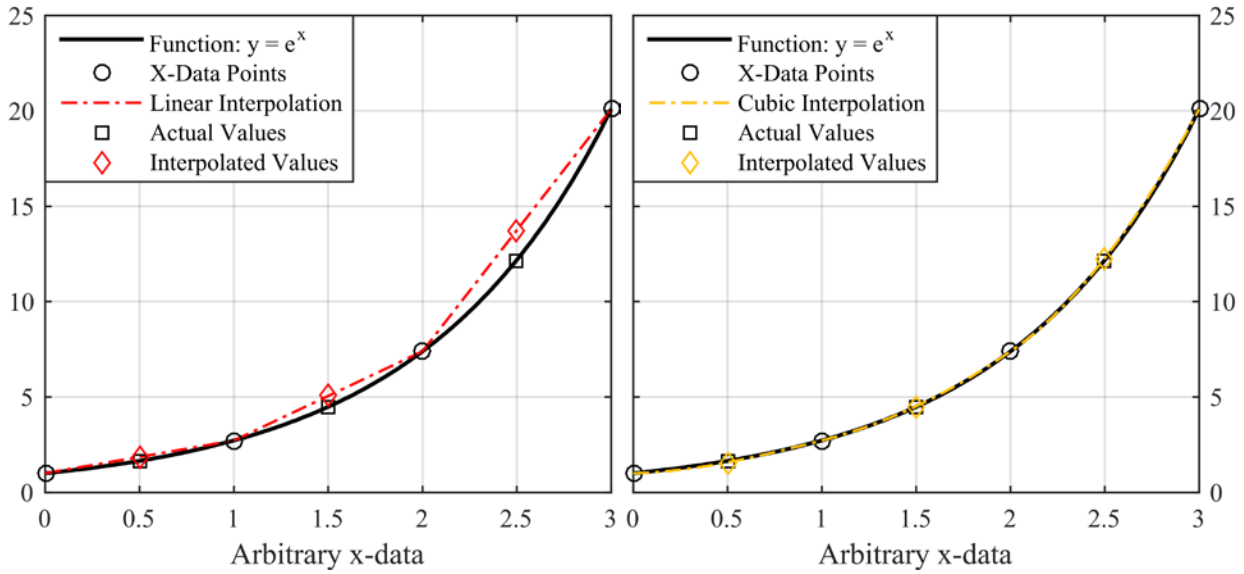

Figure 4.2: Comparison of interpolation techniques on an exponential function ($y=e^x$), with arbitrary x-data points (circles). Linear interpolation in red (left), and cubic in yellow (right). Diamonds show the interpolated points compared to the actual values in squares

Despite the inaccuracy induced by the linear interpolation method, this method was chosen for this work because of its speed relative to higher order methods. To reduce the effect of the inaccuracy,

many data points were needed in each dimension of the matrix, particularly in the dimensions where significant non-linear behavior was expected (temperature, pressure, fuel mixture). Instead of spacing the temperature and equivalence ratio data points evenly, logarithmic spacing was used for the data points in these dimensions to provide better fidelity at the low end of the ranges. Table 4.2 lists the parameters, ranges, number of cases, and scales used for the 5-dimensions in the ignition delay matrices. Mass fraction of F1 corresponds to the ratio of fuel 1 to total fuel. F1 was the premixed fuel for all the cases presented here.

Table 4.2: Range of initial conditions in 5-D ignition delay matrices

Parameter	Range	Number of Cases	Scale
Temperature [K]	550-1500	23	Logarithmic
Pressure [bar]	10-125	11	Linear
EGR [-]	0	1	Linear
Equivalence Ratio [-]	0.20-1.5	12	Logarithmic
Mass Fraction of F1 [-]	0-1	21	Linear
Total	-	63,756	-

In total, 63,756 independent ignition delay runs were simulated for each combination of premixed and direct injected fuel. The amount of time each matrix took to run depended on the number of reactions in the mechanism, but for a typical reduced mechanism with <100 species, the matrix would take between 10-20hrs. A maximum simulation time of 500ms was used, and the order of magnitude of the simulation time step was varied based on the order of magnitude of the ignition delay of the previous temperature index for a given pressure, equivalence ratio, and fuel mixture composition, i.e., the simulation time step was based on the expected order of magnitude of the ignition delay such that at least 100 time steps occurred before ignition. Figure 4.3 through Figure 4.5 show examples of the ignition delay curves generated with Cantera for various initial conditions with blends of PRFs.

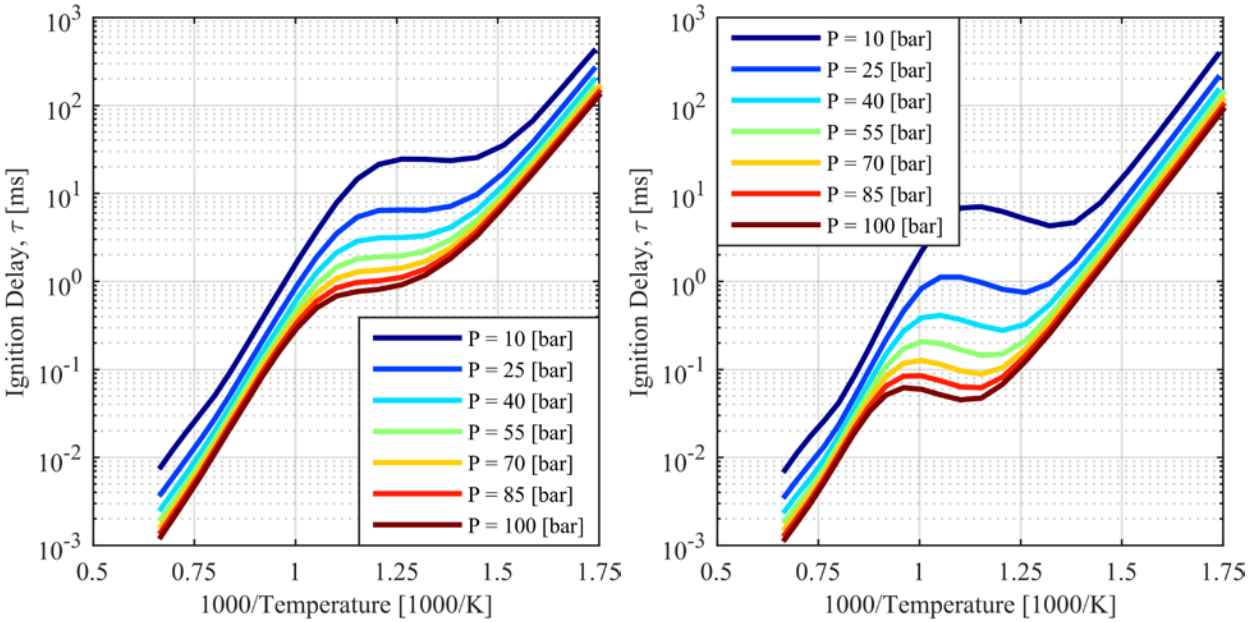

Figure 4.3: Ignition delay as a function of 1000/T for various initial pressures at φ = 1.0, and 0% EGR, for PRF100 (left) and PRF0 (right), respectively

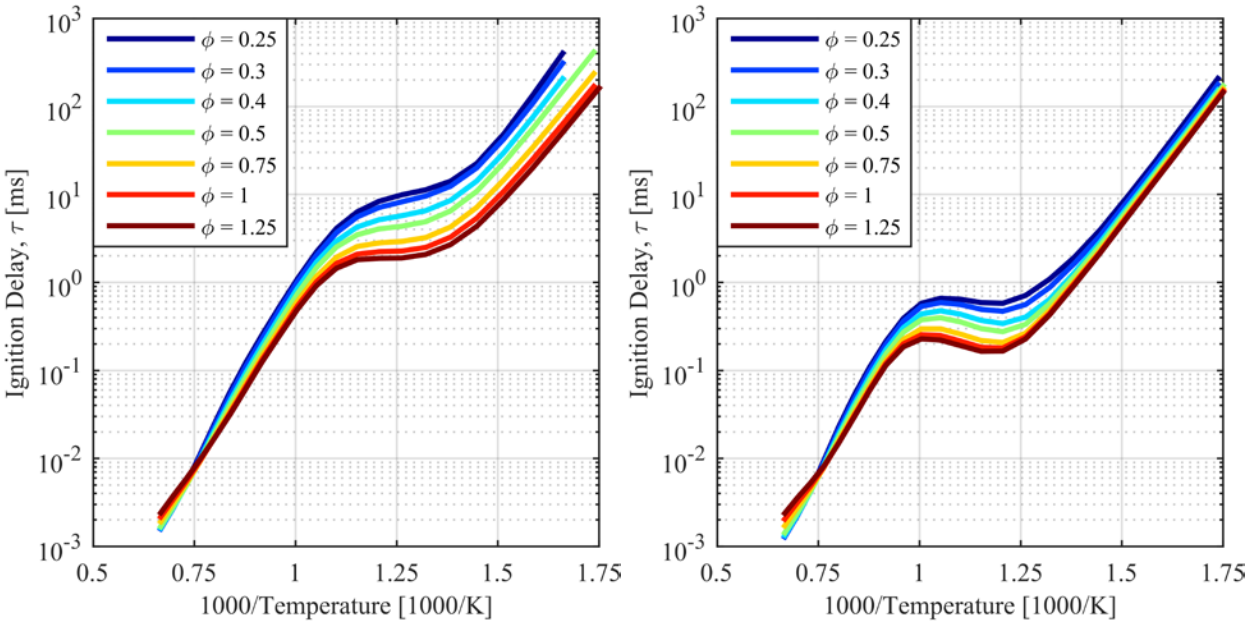

Figure 4.4: Ignition delay as a function of 1000/T for various equivalence ratios at P = 50bar, and 0% EGR, for PRF100 (left) and PRF0 (right), respectively

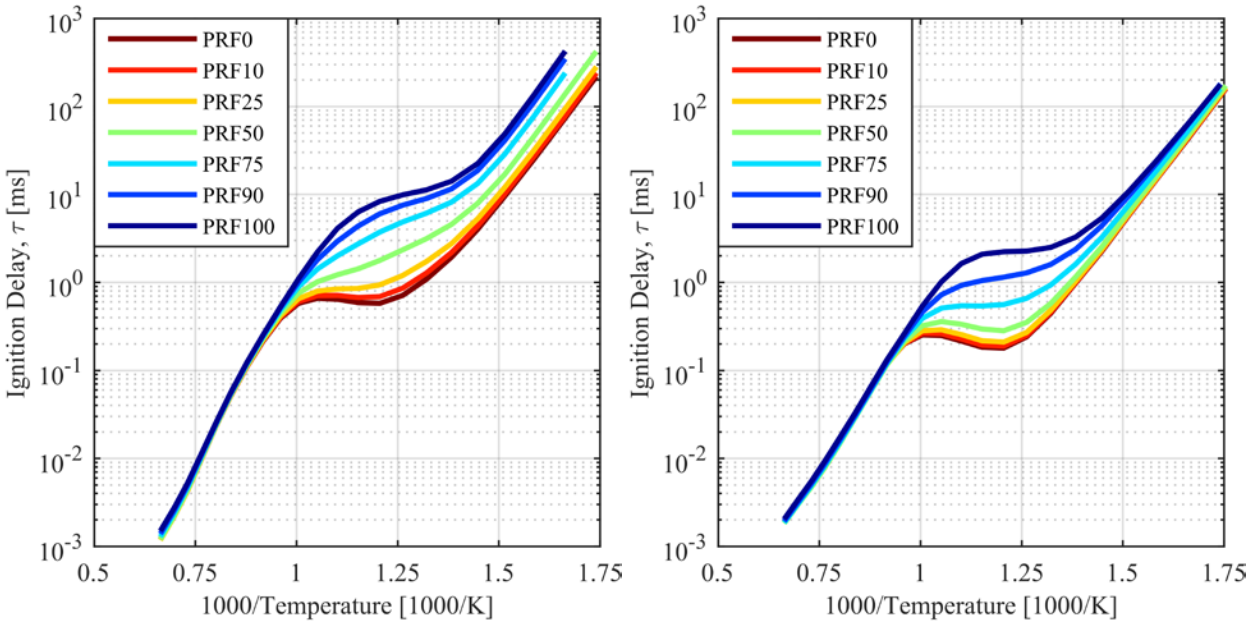

Figure 4.5: Ignition delay as a function of 1000/T for various PRF numbers at P = 50bar, and 0% EGR, for φ = 0.25 (left) and φ = 1.0 (right), respectively

4.2 Developing an Ignition Delay Correlation for a Fuel Blend

Primary reference fuel blends are often used as chemical surrogates for both gasoline and diesel fuels [36, 76], and the ignition delays of PRF fuels have been extensively studied. Algebraic expressions for ignition delay have been developed for various fuels including iso-octane (PRF100) [73, 77], and n-heptane (PRF0) [75, 78] as a means of correlating experimental data, and to examine the effect of various parameters such as pressure, temperature, equivalence ratios, etc., on the fuel chemistry [73, 75, 77]. However, for the reasons discussed previously, a dual-fuel strategy such as RCCI requires an ignition delay correlation for a blend of two fuels, possibly with very different ignition behavior, for a wide range of conditions, and for any possible mixture of the two fuel components.

Ignition delay correlations can avoid the use of large, computationally intensive, detailed chemical mechanisms to quickly predict ignition delay, and can be coupled with an auto-ignition predicting algorithm to model engine relevant parameters, such as knock in SI applications [79], and start of

combustion [80, 81] and thermal stratification [15, 20] in HCCI applications. As discussed by Goldsborough [73, 79], these applications require the ignition delay correlations to accurately and robustly match the actual fuel chemistry over a wide range of operating conditions, and these correlations can be a computationally efficient means of incorporating model-based control methods into an engine control system. Existing correlations, however, need to demonstrate good agreement, particularly in the low temperature and negative temperature coefficient (NTC) regimes to produce adequate results over the large operating space of conventional and advanced engine platforms, particularly in applications such as HCCI combustion where combustion stability and noise are highly sensitive to intake charge conditions and fuel chemistry [79].

The following section provides a method by which an ignition delay correlation for a blend of PRF100 and PRF0 was developed by DelVescovo et al [66]. The correlation used a reduced gasoline surrogate mechanism with 323 species from Lawrence Livermore National Laboratory [82]. The intention of this section is to illustrate a method by which an ignition delay correlation for any combination of two fuels may be established.

Ignition delay simulations were performed using a constant volume reactor in Cantera. The CV reactor input conditions (temperature, pressure, species mole fractions) were varied parametrically to provide a wide operating space to develop the correlation. Equivalence ratio (φ) is defined here as the fresh air equivalence ratio, and the oxygen mole percentage (x_{O_2}) is the percentage of oxygen in the diluent gas to eliminate the influence of φ on x_{O_2}. Because of this, x_{O_2} can be related to the exhaust gas recirculation (EGR) fraction by the relationship in Equation (4.3) (assuming that the inlet air is 21% by mole O_2).

$$x_{O_2} = 21\% * (1 - EGR) \tag{4.3}$$

In total, 6,480 ignition delay simulations were performed covering the ranges listed in Table 4.3. These initial conditions were selected as they are representative of the range of conditions seen in conventional combustion and advanced combustion modes.

Table 4.3: Cantera CV simulation initial conditions for correlation

Parameter	Range	Number of Cases
Temperature [K]	570-1860	18
Pressure [atm]	10-100	4
x_{O2} [%]	12.6-21	3
Equivalence Ratio [-]	0.30-1.5	6
PRF	0-100	5
Total	-	6,480

4.2.1 Formulating the Correlation

The functional form of the ignition delay chosen for this expression was the commonly used Arrhenius-based power law formulation. This formulation has been applied by numerous researchers [73, 75, 77, 78] for modeling the ignition delay of hydrocarbon fuels including n-heptane and isooctane. The general form of this expression is shown in Equation (4.4), where φ is the fresh air equivalence ratio, p is the pressure, x_{O2} is the oxygen mole percentage of the diluent gas, and the traditional activation energy term E_a/RT in the exponential is replaced by the term λ to remain consistent with the work of Goldsborough [73] in his ignition delay correlation for isooctane.

$$\tau = A\varphi^{\alpha} p^{\beta} x_{O_2}^{\gamma} \exp(\lambda) \tag{4.4}$$

Goldsborough's method for determining the values of the coefficients is employed throughout this work, and is expanded to consider all PRF mixtures. Solving Equation (4.4) for each parameter

value separately under the listed conditions yields Equations (4.5) to (4.7) for α, β, and γ, respectively.

$$\alpha_{param} = \frac{ln\left(\frac{\tau_2}{\tau_1}\right)}{ln\left(\frac{\varphi_2}{\varphi_1}\right)}; \quad \varphi_1 = 1.0$$
$$where: T_2 = T_1, P_2 = P_1, x_{O2_2} = x_{O2_1}, PRF_2 = PRF_1 \tag{4.5}$$

$$\beta_{param} = \frac{ln\left(\frac{\tau_2}{\tau_1}\right)}{ln\left(\frac{P_2}{P_1}\right)}; \quad P_1 = 50atm$$
$$where: T_2 = T_1, \varphi_2 = \varphi_1, x_{O2_2} = x_{O2_1}, PRF_2 = PRF_1 \tag{4.6}$$

$$\gamma_{param} = \frac{ln\left(\frac{\tau_2}{\tau_1}\right)}{ln\left(\frac{x_{O2_2}}{x_{O2_1}}\right)}; \quad x_{O2_1} = 21\%$$
$$where: T_2 = T_1, \varphi_2 = \varphi_1, P_2 = P_1, PRF_2 = PRF_1 \tag{4.7}$$

The correlation developed uses the same functional form for the α, β, and γ parameters as Goldsborough, with modifications to the exponential roll-off temperature and exponent that are linear functions of PRF. This modification can be made for any combination of fuels, substituting some predefined mass ratio for the PRF number. This modification adjusts the parameter values in the NTC region to account for the differences present in the mechanism in φ, p, and x_{o2} sensitivities for the PRF mixtures. The functional forms of the parameter values can be seen in Equations (4.8) to (4.10) where α, β, and γ correspond to the exponents in Equation (4.4), where T* is defined as 1000/T.

$$\alpha = \alpha' + \left(\sum_{i=0}^{3} a_i {T^*}^i\right) * \exp\left\{-\left[\frac{T^*}{(T_\alpha^* + dT_\alpha^* \times PRF)}\right]^{(n_\alpha + dn_\alpha \times PRF)}\right\} \tag{4.8}$$

$$\beta = \beta' + \left(\sum_{i=0}^{3} b_i T^{*^i}\right) * \exp\left\{-\left[\frac{T^*}{\left(T_\beta^* + dT_\beta^* \times PRF\right)}\right]^{\left(n_\beta + dn_\beta \times PRF\right)}\right\} \tag{4.9}$$

$$\gamma = \gamma' + \left(\sum_{i=0}^{3} c_i T^{*^i}\right) * \exp\left\{-\left[\frac{T^*}{\left(T_\gamma^* + dT_\gamma^* \times PRF\right)}\right]^{\left(n_\gamma + dn_\gamma \times PRF\right)}\right\} \tag{4.10}$$

The three parameters have identical functional forms, and the coefficients of the functions were determined using Matlab's built-in Curve Fitting Toolbox. A Levenberg-Marquardt algorithm and bisquare regression were selected in the Curve Fitting Toolbox, and care was taken in determining the initial values for the curve fitting to insure an appropriate solution. The resulting functions were then compared qualitatively to the parameter values calculated from Equations (4.5) to (4.7) to obtain adequate agreement between the curve fit and the data.

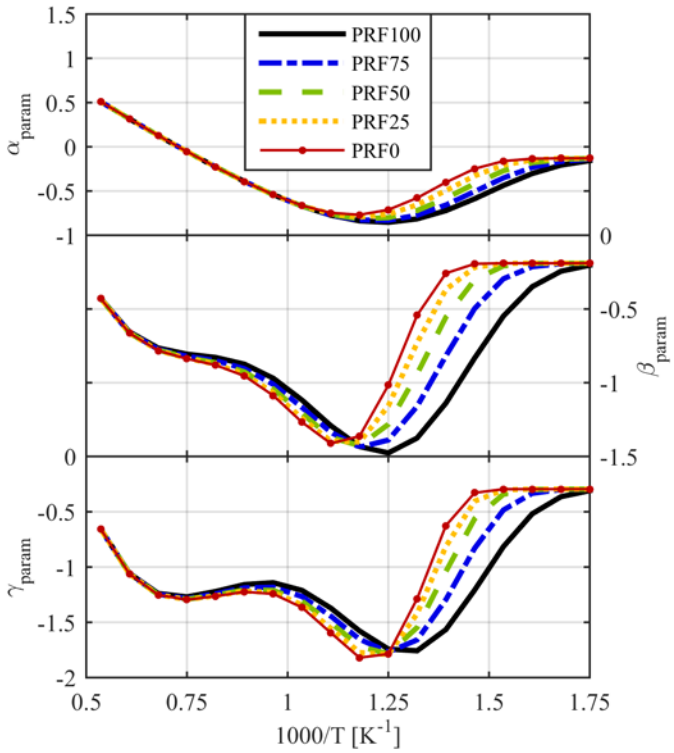

Figure 4.6: α_{param} (top), β_{param} (middle), and γ_{param} (bottom) vs. 1000/T for five PRF mixtures using the correlated parameter functions

The result of the parameter curve fitting can be seen in Figure 4.6. With the α, β, and γ terms fit, the activation energy term can be solved for using Equation (4.11). The value of the scaling coefficient, A, is set to 1.0 in this work.

$$\lambda_{param} = \ln\left(\frac{\tau}{A\varphi^{\alpha}p^{\beta}x_{O_2}^{\gamma}}\right) \tag{4.11}$$

A similar modification to the one made previously for the parameter values α, β, and γ is made to Goldsborough's formulation of the λ term to account for the differences in the activation energy term for PRF blends in the NTC region. For the activation energy term, the exponential roll-off function utilizes a second order function of PRF instead of the linear function of PRF used for the α, β, and γ terms. The second order functionality provides a better fit to the parameter values for the range of PRF. Equation (4.12) shows the functional form of the λ term.

$$\lambda = \sum_{i=0}^{2} d_i {T^*}^i - \left[\sum_{i=0}^{2} d_i {T^*}^i - \sum_{i=0}^{3} e_i {T^*}^i\right] * \exp\left\{-\left[\frac{T^*}{\left(T_{\lambda}^* + \sum_{i=1}^{2} dT_{\lambda i}^* \times PRF^i\right)}\right]^{\left(n_{\lambda}+\sum_{i=1}^{2} dn_{\lambda i}\times PRF^i\right)}\right\} \tag{4.12}$$

Figure 4.7 depicts the final curve fits for the various PRF mixtures as a function of inverse temperature. The curve fit captures the decreasing activation energy in the NTC region with decreasing PRF very well. The values of the 41 constants used in the correlation are shown in Table 4.4, and the results of the correlation compared to the ignition delays from the CV Cantera ignition delay simulations can be seen in Figure 4.8. A detailed description of the error associated with the correlation, as well as validation with autoignition predictions with HCCI engine data can be found in DelVescovo et al. [66].

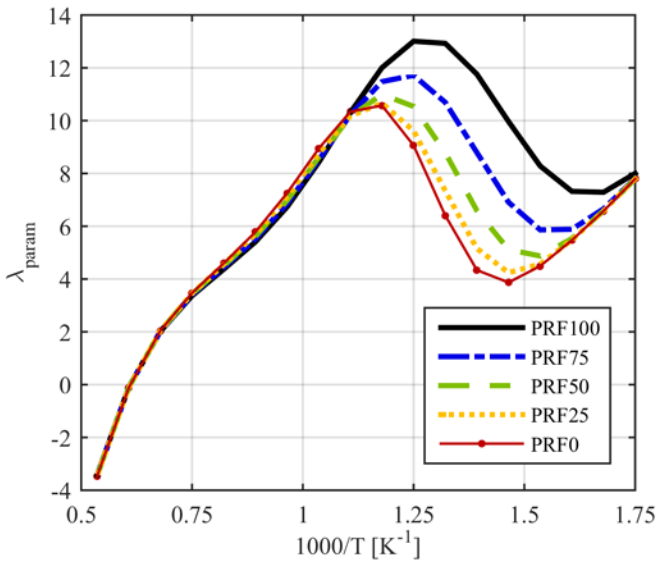

Figure 4.7: λ_{param} vs. 1000/T for five PRF mixtures

Table 4.4: Parameter values for the developed correlation

α Constants	Value	β Constants	Value	γ Constants	Value	λ Constants	Value
A	1.0	β'	-0.1896	γ'	-0.2956	d_0	9.314
α'	-0.1301	b_0	10.53	γ_0	16.78	d_1	-19.54
a_0	2.228	b_1	-42.87	γ_1	-65.79	d_2	10.67
a_1	-3.123	b_2	55.54	γ_2	80.55	e_0	132.2
a_2	0.1977	b_3	-24.35	γ_3	-32.57	e_1	-454.4
a_3	0.1887	T_β^*	1.199	T_γ^*	1.276	e_2	528.4
T_α^*	1.334	dT_β^*	0.0003184	dT_γ^*	0.0001591	e_3	-215.2
dT_α^*	0.001179	n_β	10.27	n_γ	12.53	T_λ^*	1.196
n_α	9.495	dn_β	-0.04541	dn_γ	-0.05869	$T_{\lambda1}^*$	9.683e-6
dn_α	-0.01916					$T_{\lambda2}^*$	4.592e-6
						n_λ	8.538
						$dn_{\lambda1}$	-0.02678
						$dn_{\lambda2}$	-2.063e-5

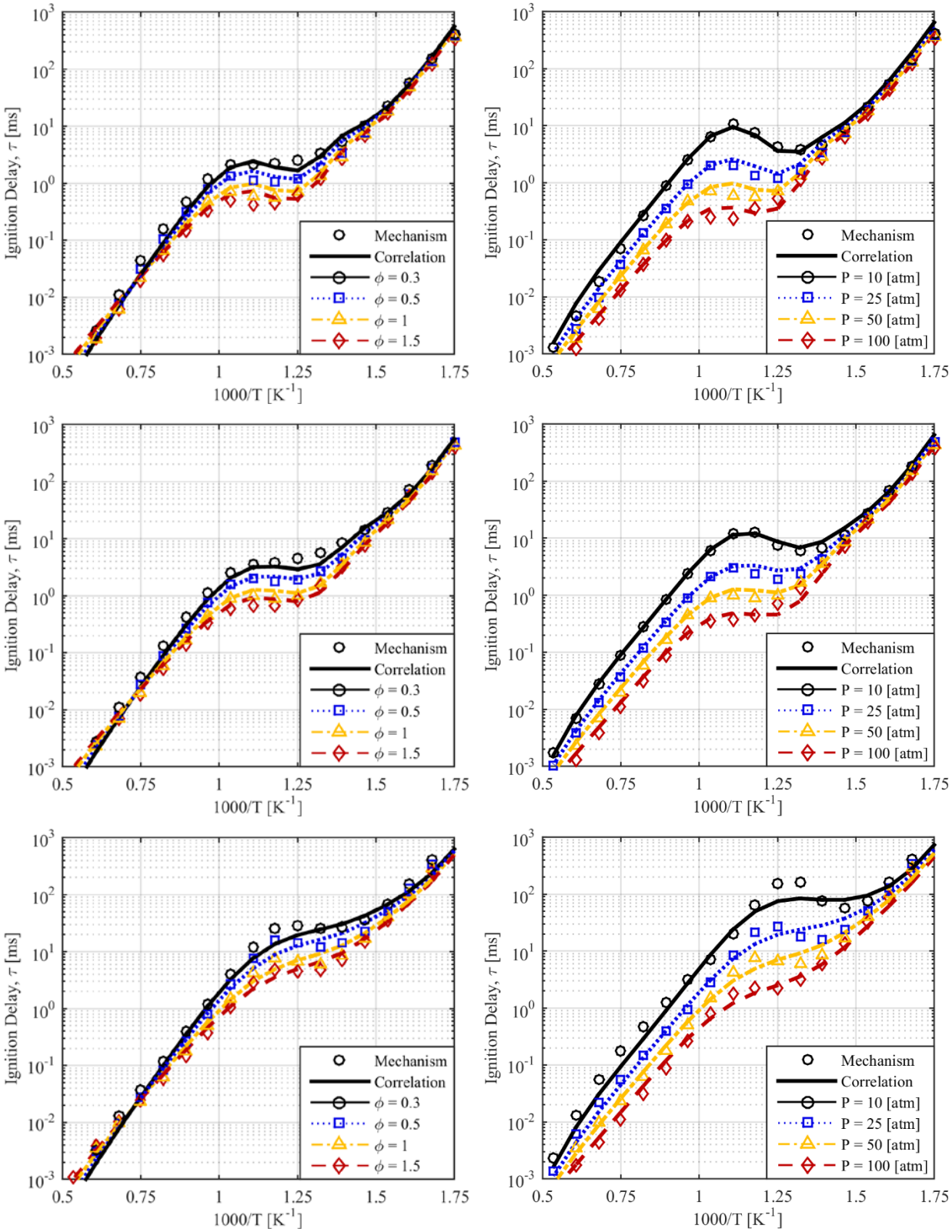

Figure 4.8: Ignition delay vs. inverse temperature for PRF0 (top), PRF50 (middle), and PRF100 (bottom) for various φ's at P = 50atm, and x_{O2} = 21% (left), for various initial pressures at φ = 1.0, and x_{O2} = 21% (right), comparing the mechanism predictions (symbols) to the correlation (lines)

5 *FUEL STRATIFICATION ANALYSIS (FSA)*

The experimental data presented in Chapter 3, and previous work comparing the performance and emissions characteristics of gasoline/diesel RCCI operation to RCCI experiments using isobutanol as the low and high reactivity fuel [54], has shown the importance of tailoring the direct injection strategy to the specific fuel combination to maximize performance and minimize emissions. Comparing cases using methane and syngas as the low reactivity fuel to baseline iso-octane/n-heptane cases showed the importance of matching the bulk heat release characteristics, including phasing, duration, and rates, and if this could be achieved, the performance and emissions could attain rates comparable to the baseline condition. The heat release shape is defined by the gradients of in-cylinder reactivity and equivalence ratio, which are directly related to the direct injection strategy through injection timing, injection pressure, and number of injections. Assuming some arbitrary optimal heat release profile, it would be beneficial to determine the required distribution of fuel necessary to achieve such a heat release. This notion serves as the motivation for the model referred to as Fuel Stratification Analysis (FSA) proposed in this section.

5.1 Background

The inspiration for this work came from an analysis methodology called Thermal Stratification Analysis (TSA) proposed by Lawler et al. [20], which used the Livengood and Wu autoignition integral [83], in combination with experimentally derived mass fraction burned curves, in order to determine the distribution of temperature in the combustion chamber due to natural thermal stratification in HCCI engines. The analysis breaks the cylinder into many thermal zones, each following a different self-similar temperature profile during the compression and expansion

process. The profile of the highest possible temperature region in the cylinder, referred to as the isentropic unburned temperature, and corresponding to the "adiabatic core" [22], can be thought of as the temperature that results from isentropically compressing an air-fuel mixture from the IVC temperature and pressure to the current cylinder pressure as a given crank angle. This isentropic relationship is expressed in Equation (5.1), where P_{cyl} is the instantaneous cylinder pressure, and γ is the ratio of specific heats of the mixture.

$$T_{isen,unburned} = T_{IVC}\left(\frac{P_{cyl}}{P_{IVC}}\right)^{\left(1-\frac{1}{\gamma}\right)} \tag{5.1}$$

After ignition, the unburned temperature will include the effects of compression heating from combustion elsewhere in the cylinder, though this effect is unimportant for the adiabatic core, as ignition starts in the hottest regions of the cylinder in HCCI combustion [22]. Figure 5.1 shows the bulk gas temperature from the ideal gas law and the isentropic unburned temperature.

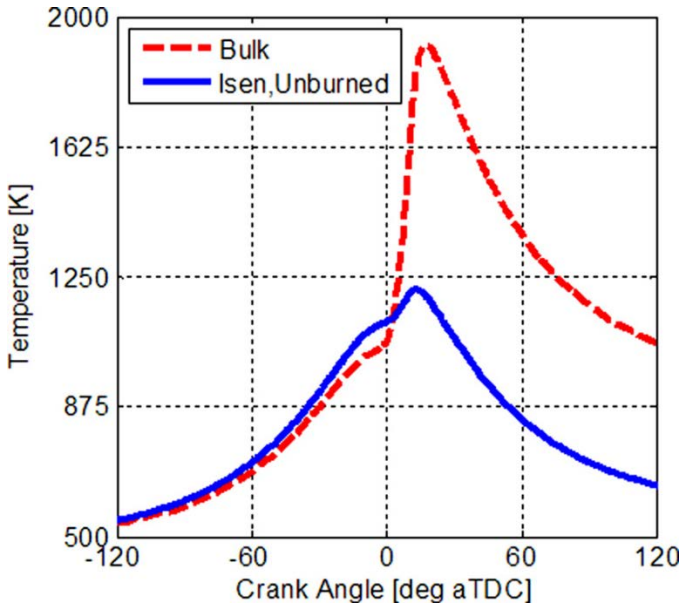

Figure 5.1: Mass-averaged bulk and isentropic unburned temperature vs. CA. Reproduced from Lawler et al. [20]

During compression, the isentropic unburned temperature is higher than the bulk gas temperature due to the lack of heat loss to the cylinder and piston surfaces. The bulk gas temperature after combustion corresponds to the burned gas temperature, while the unburned temperature includes the compression heating effect from the pressure increase due to combustion. While the upper bound of temperature in the cylinder is defined by the isentropic unburned temperature, the lower bound of possible temperatures in the cylinder is defined by the instantaneous wall temperature. With this in mind, a normalized scaling variable, referred to as the Normalized Zone Temperature (NZT), was developed in order to define the possible thermal profiles that exist in the cylinder. Equation (5.2) defines this normalized parameter, where T_{zone} when NZT = 1 corresponds to the isentropic unburned temperature, and T_{zone} when NZT = 0 corresponds to the wall temperature. $T_{isen,unburned}$ and T_{wall} are functions of crank angle, which implies that NZT corresponds to a particular temperature profile or contour in the cylinder.

$$NZT = \frac{T_{zone} - T_{wall}}{T_{isen,unburned} - T_{wall}} \tag{5.2}$$

The Livengood-Wu autoignition integral seen in Equation (5.3), coupled with an ignition delay correlation by He et al. [77] used to predict ignition delay, were used to predict the ignition timing in crank angle space of each thermal zone for the given fuel and intake conditions, including equivalence ratio and EGR rate. Ignition is defined when the cumulative integral, AI in Equation (5.3), is equal to 1.0. Figure 5.2 shows an example of the various possible thermal profiles present in the cylinder, along with the predicted crank angle at which each path would autoignite.

$$AI = \int_{t_0}^{t_{ign}} \frac{1}{\tau} dt \tag{5.3}$$

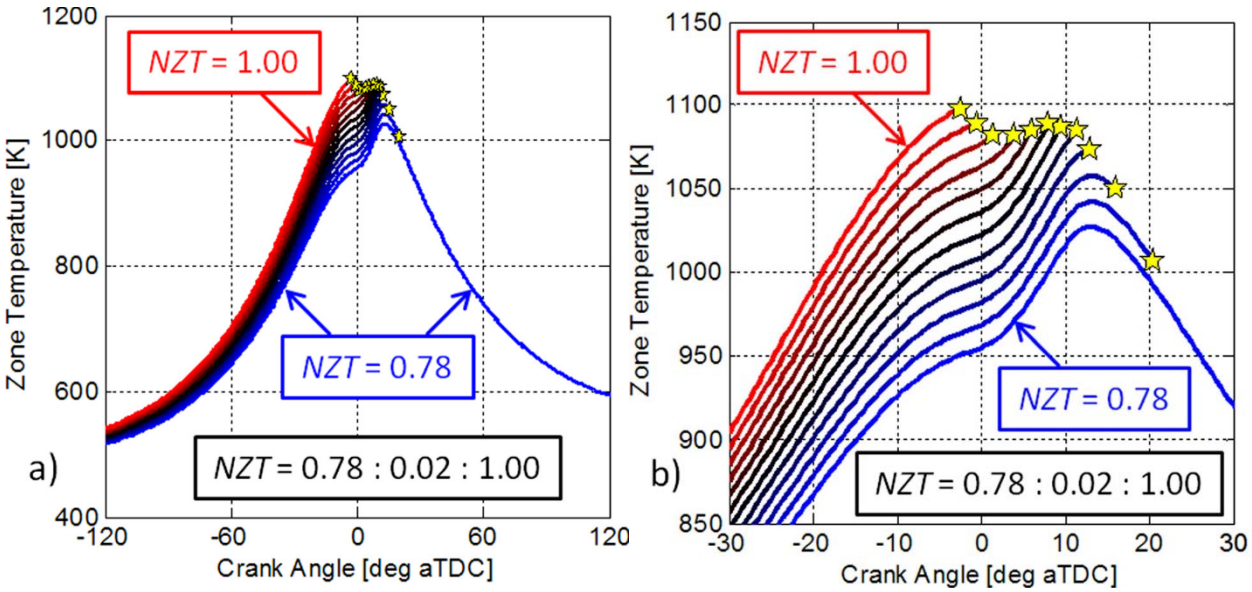

Figure 5.2: Temperature profiles for varying NZT used in TSA analysis. Adapted from Lawler et al. [20]

Once the ignition locations for the thermal zones have been calculated, these crank angle locations could be compared to the mass fraction burned (MFB) profile for the given experimental case. The MFB is a representation of the cumulative fraction of energy that has been released as a function of crank angle, and is defined as the calculated heat release profile normalized by the total fuel energy released. The process of equating the crank angle dimensions of the ignition locations with the engine crank angle from the MFB plot is shown in Figure 5.3.

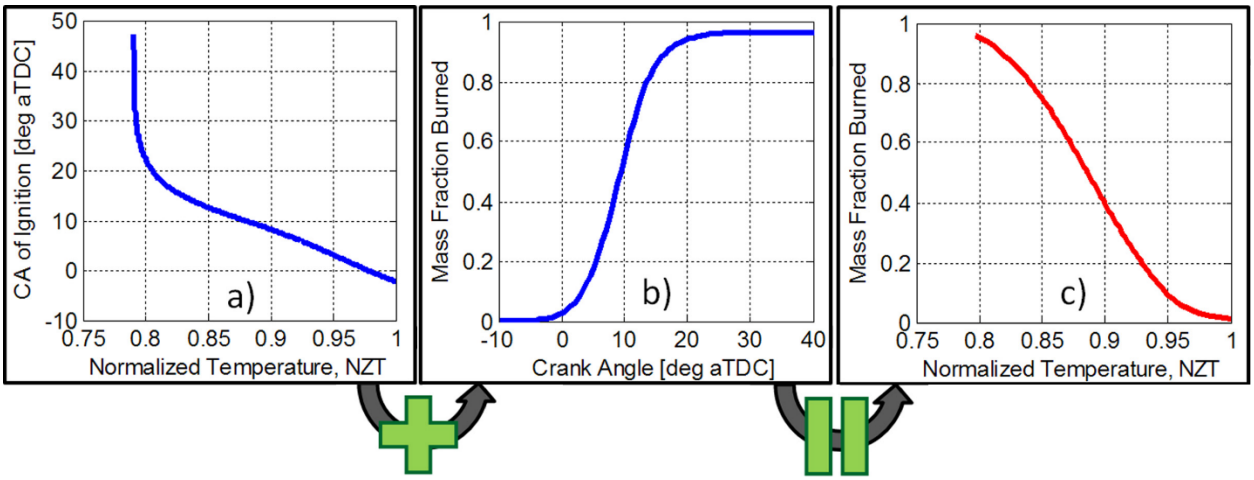

Figure 5.3: Ignition phasing vs. NZT (a), MFB vs. CA (b), and MFB vs.NZT (c). Adapted from Lawler et al. [20]

The mass fraction burned vs. NZT profile can then be converted into a cumulative density function (CDF) by subtracting the y-data in Figure 5.3c from 1.0. The probability density function was then calculated from the cumulative density function according to the relationship defined by probability theory shown in Equation (5.4), where the PDF is the derivative of the CDF with respect to the x-variable (NZT or temperature at some arbitrary crank angle in this case). Figure 5.4 shows the results of the TSA method in terms of CDF and PDF as a function of NZT and temperature at an arbitrary crank angle for a reference condition defined by Lawler et al. [20]. The expected value predicted by the TSA method was calculated from probability theory according to Equation (5.5), and compared to the bulk temperature at the arbitrary crank angle as an assessment of the relative error of the approach.

$$PDF = \frac{dCDF}{dx} \tag{5.4}$$

$$E[X] = \int_{-\infty}^{+\infty} x * PDF(x)dx \tag{5.5}$$

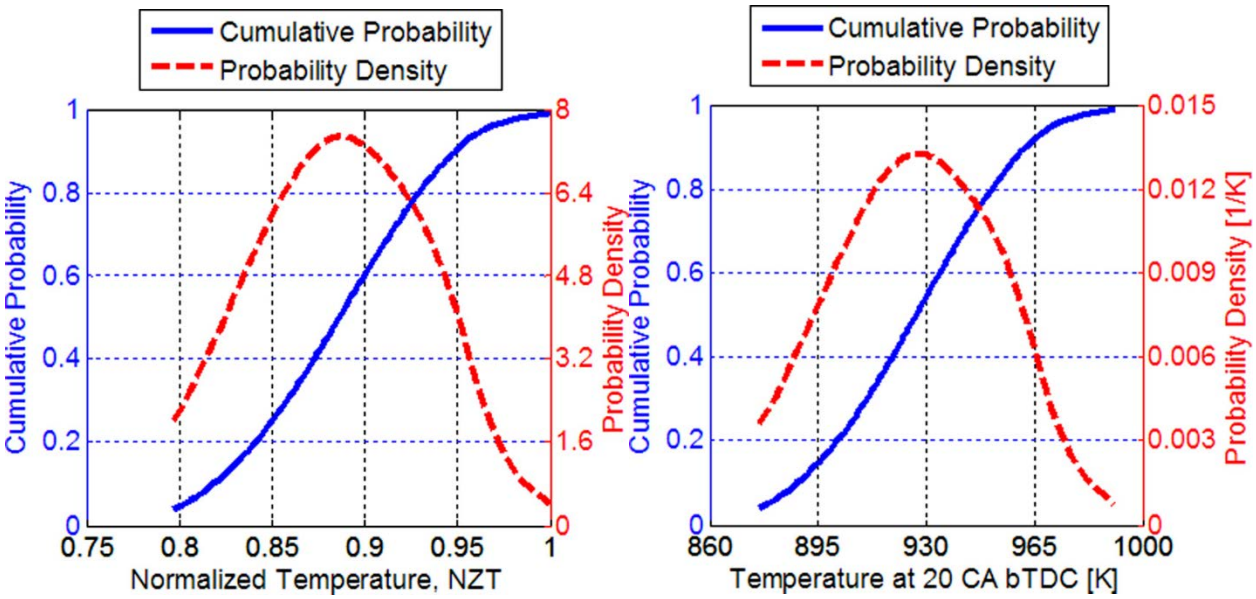

Figure 5.4: CDF and PDF vs. NZT (left), and vs. T at 20°BTDC (right). Reproduced from Lawler et al. [20]

The explicit and implicit assumptions of the TSA method are as follows:

- The pressure, equivalence ratio and mixture properties are completely uniform in the cylinder, and the only variable with spatial variations is temperature.
- Chemical reaction rates are very fast relative to engine time scales, and therefore when a zone autoignites it does so instantaneously.
- There is no heat or mass transfer between zones, implying that the hot burned gases do not mix with cold unburned gases, and in turn, accelerate the autoignition events.
- There is no flame propagation in the combustion chamber, which would cause zones to burn prior to the autoignition integral prediction.

Further improvements in the TSA methodology, particularly for handling the low temperature end of the distribution, as well as validation with CFD and optical engine data were published by Lawler et al. [15]. In general, the TSA predictions did a good job predicting the thermal stratification present in HCCI combustion. Unfortunately, due to the nature of HCCI combustion, these results do not have a great amount of practical significance as thermal stratification cannot be easily controlled, except by adjusting the coolant temperature (which is a parameter adjusted in the steady state experiments by Lawler et al. [15, 20]) or oil temperature, which have significant time lags associated with them, making next cycle control of HCCI combustion with these parameters impossible. As discussed previously, the biggest challenge facing HCCI combustion is the significant cycle-to-cycle variability associated with the strategy, as well as the lack of a direct combustion rate control mechanism. While thermal stratification is the main parameter for heat release rate control in HCCI combustion, this parameter is not as easily manipulated as the stratification of fuel induced by direct injection events, which has been shown to produce significantly improved heat release control and stability [25-29]. A similar methodology applied

to fuel stratification instead of thermal stratification would provide much more valuable information regarding the fuel distributions present in kinetically controlled combustion strategies such as PPC, PFS, GCI, and RCCI, as well as helping to specify fuel stratification requirements for these strategies.

5.2 Methodology

The major difference between the TSA and FSA methodologies is that the mixture composition is not assumed to be uniform throughout the combustion chamber. The combustion process in single-fuel stratified-charge strategies such as PFS, as well as dual-fuel stratified-charge strategies such as RCCI, have been shown to propagate by sequential autoignition from the most reactive regions, to the least reactive regions [13, 26, 36, 84-86]. Reactivity is effectively a measure of the relative ignition delay of the fuel mixture at its thermodynamic state. Dec et al. [13] showed that even with a perfectly homogeneous fuel distribution, thermal stratification in HCCI combustion resulted in sequential autoignition from hotter-to-cooler regions, thus implying that high temperature regions are more reactive than low temperature regions. This sequential autoignition from hot-to-cold mixtures is the basis for the TSA method, and sequential autoignition from high reactivity (induced by fuel chemistry and or high equivalence ratio) to low reactivity is the basis for the present proposed FSA method.

5.2.1 Initializing Zones

Similar to the TSA method, a non-dimensional, normalized parameter is defined in order to establish the possible fuel mixtures that may exist in the cylinder. This parameter, referred to as the premixed mass fraction (PRE), expresses the ratio of premixed fuel mass in a given “zone” or “region” to the total fuel mass in the zone, i.e., PRE = 1 means that the zone only contains premixed

(low reactivity) fuel, PRE = 0 means that a zone only contains direct-injected fuel, which, despite being impossible, assuming that the premixed fuel is thoroughly mixed, defines the lower bound of possible fuel mixtures. The premixed percentage, which is the premixed fraction multiplied by 100, is approximately equal to the PRF number if the premixed fuel is isooctane and the direct injected fuel is n-heptane. In these situations, the premixed percent and PRF number will be used interchangeably. This ignores the small difference in density between the two fuels, as PRF number is defined on a volumetric instead of mass basis. The maximum error of this assumption occurs at PRF50, and is equal to only 0.29% (i.e., PRF50 is 50.29% by mass isooctane).

Equation (5.6) shows the relationship for the premixed mass fraction, and the direct injected mass in the zone ($m_{DI,i}$) can be solved for by assuming some arbitrary value of PRE_i, where the 'i' subscript indicates the i^{th} zone. This relationship is shown in Equation (5.7).

$$PRE_i = \frac{m_{premixed}}{m_{premixed} + m_{DI,i}} \tag{5.6}$$

$$m_{DI,i} = m_{premixed}\left(\frac{1}{PRE_i} - 1\right) \tag{5.7}$$

The premixed mass ($m_{premixed}$) in the above equations does not necessarily correspond to the actual mass of premixed fuel in a zone, as the relative distribution of mass is yet unknown. For the purposes of this analysis, $m_{premixed}$ is the premixed fuel fraction, i.e., the analysis is performed on the basis of a unit of global fuel mass. This relative mass is used only to define the mixture properties of the zone, such as φ, the equation for which can be seen in Equation (5.8). The zone air-fuel ratio (AFR_i) can be calculated by dividing the mass of air in the zone by the total mass of fuel in the zone, as shown in Equation (5.9). Like $m_{premixed}$, m_{air} is a relative quantity that, for the purposes of the analysis, is equal to the global air-fuel ratio. This formulation implicitly assumes

that the premixed fuel and air is totally homogeneous, and that the direct injection event adds mass to a given zone linearly, i.e., the direct injection event entrains both premixed fuel and air equally.

$$\varphi_i = \frac{AFR_{stoich,i}}{AFR_i} \tag{5.8}$$

$$AFR_i = \frac{m_{air}}{m_{premixed} + m_{DI,i}} \tag{5.9}$$

The stoichiometric air-fuel ratio ($AFR_{stoich,i}$) of the zone is calculated according to Equation (5.10), where H/C_i and O/C_i are the ratio of hydrogens to carbons, and oxygens to carbons in the fuel mixture of the zone, respectively. In order to calculate these quantities, the mass fraction (y) of each fuel, denoted by the subscript 'j', is calculated from the zone premixed fraction according to Equation (5.11), and converted to mole fractions (x) according to Equation (5.12), where MW_j is the individual fuel's molecular weight, and n_f is the number of fuels considered. The zone H/C and O/C ratios can then be calculated from the relationships in Equation (5.13), and Equation (5.14) respectively, where $n_{H,j}$ is the number of hydrogen atoms in the j^{th} fuel, and $n_{O,j}$ is the number of oxygen atoms in the j^{th} fuel. The lower heating value of the zone (LHV_i), defined as the energy contained in a unit of fuel mass with the zone composition, is computed according to Equation (5.15), which becomes important if the fuel heating values differ significantly. The zone energy density (E_i), defined as the energy contained in a unit of total zone mass at the zone composition, is computed according to Equation (5.16).

$$AFR_{stoich,i} = \frac{28.97 * 4.76 * \left(1 + \frac{H/C_i}{4} - \frac{O/C_i}{2}\right)}{(12.011 + 1.008 * H/C_i + 15.999 * O/C_i)} \tag{5.10}$$

$$\begin{aligned} y_j &= PRE_i \quad &: if\ j\ is\ premixed\ fuel \\ y_j &= 1 - PRE_i \quad &: if\ j\ is\ DI\ fuel \end{aligned} \tag{5.11}$$

$$x_j = \frac{\frac{y_j}{MW_j}}{\sum_{k=1}^{n_f} \frac{y_k}{MW_k}} \tag{5.12}$$

$$H/C_i = \frac{\sum_{j=1}^{n_f} x_j * n_{H,j}}{\sum_{j=1}^{n_f} x_j * n_{C,j}} \tag{5.13}$$

$$O/C_i = \frac{\sum_{j=1}^{n_f} x_j * n_{O,j}}{\sum_{j=1}^{n_f} x_j * n_{C,j}} \tag{5.14}$$

$$LHV_i = \sum_{j=1}^{n_f} y_j * LHV_j \tag{5.15}$$

$$E_i = \frac{LHV_i}{1 + AFR_i(1 + EGR)} \tag{5.16}$$

A plot showing the trend of equivalence ratio as a function of premixed mass percentage for a condition with a global φ of 0.30, and 88% of the fuel mass being premixed isooctane with 12% direct injected n-heptane is shown in Figure 5.5.

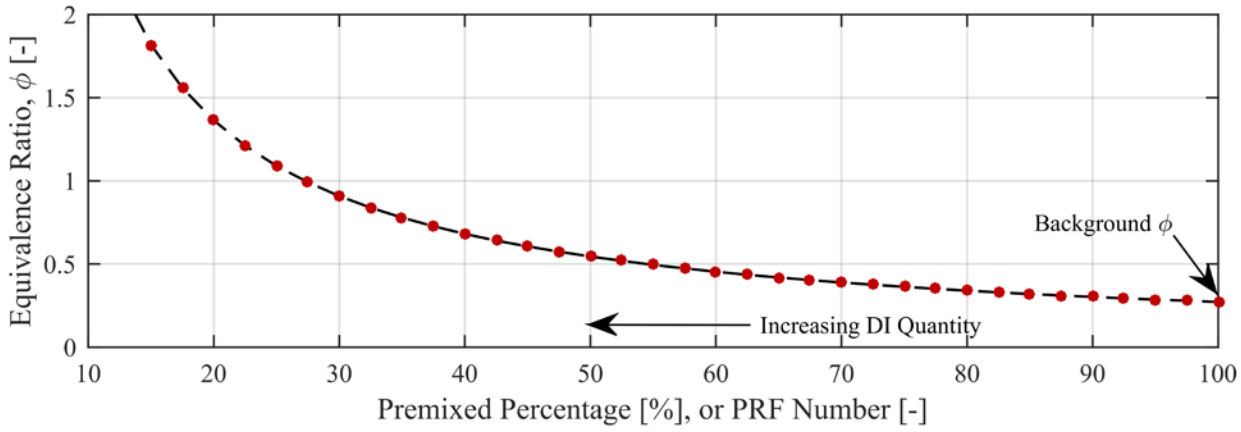

Figure 5.5: Local equivalence ratio as a function of local premixed mass percentage or PRF number assuming the premixed fuel is PRF100 and the DI fuel is PRF0 for a global φ of 0.30 and a global premixed percent of 88%

Using the methodology presented above, the calculated premixed equivalence ratio was about 0.27, and the local equivalence ratio increased non-linearly with decreasing premixed percentage,

corresponding to increased local DI quantity. The mass of premixed fuel and air defines the background equivalence ratio, while the premixed mass fraction of the zone defines the local equivalence ratio of the zone.

Like the TSA method, the temperature of the unburned gases must be approximated through the compression, combustion, and expansion processes in order to accurately predict the autoignition timing of a given zone. The average unburned temperature profile ($T_{avg,ub}$) can be defined following a polytropic relationship, as shown in Equation (5.17), where T_{IVC} and P_{IVC} are the IVC temperature and pressure, respectively, P_{cyl} is the instantaneous cylinder pressure, and γ is the compression polytropic coefficient which defines the slope of the compression process on a log-log plot, such as the example shown in Figure 5.6, within some arbitrary crank angle window (just after IVC at -140°CA to just before LTHR at -25°CA in this case).

$$T_{avg,ub} = T_{IVC}\left(\frac{P_{cyl}}{P_{IVC}}\right)^{\left(1-\frac{1}{\gamma}\right)} \tag{5.17}$$

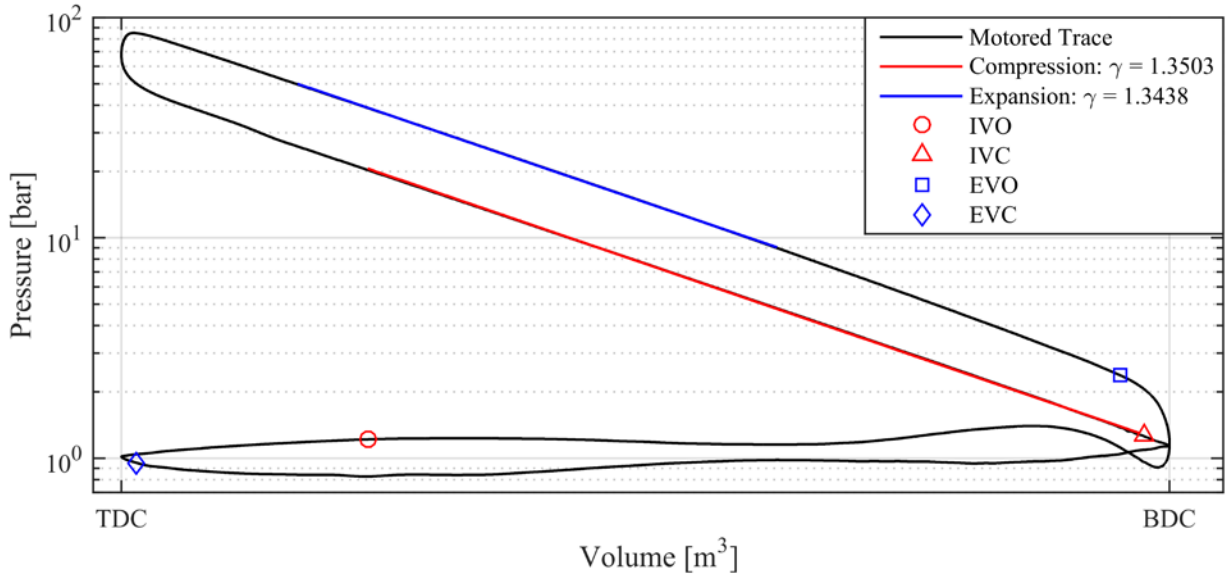

Figure 5.6: Example log P vs. log V plot with markers indicating the valve timing events, and linear polytropic fits for the compression (red) and expansion (blue) processes

In order to determine the effect on the zone temperature of the vaporizing DI fuel, a First-Law energy balance was performed on the zone, the result of which can be seen in Equation (5.18).

$$m_{DI}c_{p,l}(T_{bp} - T_{fuel}) + m_{DI}c_{p,v}(T_{z,f} - T_{bp}) + m_{DI}\Delta h^0_{vap} = (m_{air} + m_{pre})c_{p,air}(T_{z,i} - T_{z,f}) \quad (5.18)$$

$$T_{z,f} = \frac{(m_{air} + m_{pre})c_{p,air}T_{z,i} + m_{DI}(c_{p,v} - c_{p,l})T_{bp} + m_{DI}c_{p,l}T_{fuel} - m_{DI}\Delta h^0_{vap}}{(m_{air} + m_{pre})c_{p,air} + m_{DI}c_{p,v}} \quad (5.19)$$

Solving for the zone temperature after vaporization, ($T_{z,f}$), yields the relationship shown in Equation (5.19), where $T_{z,i}$ is the initial temperature of the zone, $c_{p,air}$ is the constant pressure specific heat of air, $c_{p,l}$ is the constant pressure specific heat of the liquid DI fuel, $c_{p,v}$ is the specific heat of the vapor fuel, T_{bp} is the boiling point of the DI fuel, T_{fuel} is the initial temperature of the fuel, Δh^o_{vap} is the enthalpy of vaporization of the fuel, and m_{air}, m_{pre}, and m_{DI} correspond to the mass of air, premixed fuel, and DI fuel in the zone respectively. The direct injected fuel is assumed to instantaneously vaporize at the end of injection (EOI) timing. The assumed vaporization and mixing process of the zones is illustrated in Figure 5.7.

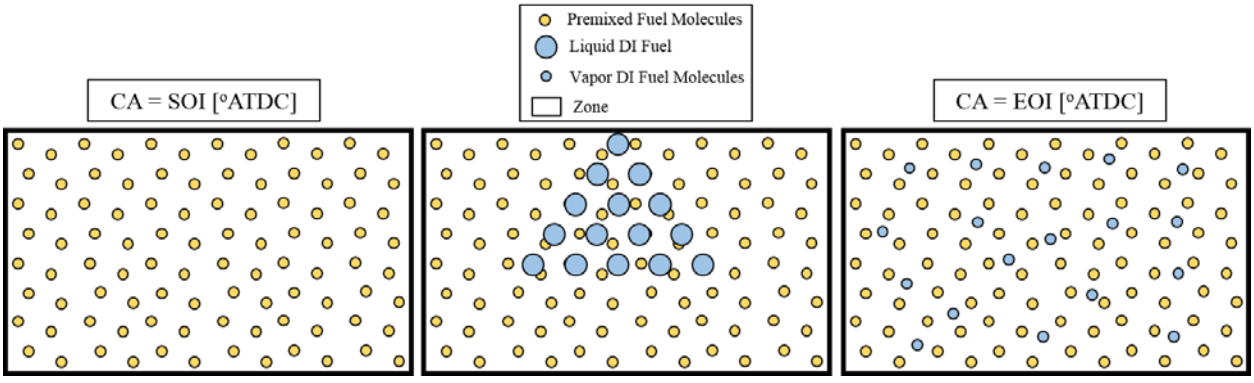

Figure 5.7: Illustration of the assumed vaporization and mixing process for a given zone with a specified premixed mass fraction

5.2.2 Accounting for Thermal Stratification

In order to account for the thermal stratification which exists in the cylinder due to wall heat transfer, various possible thermal paths can be established for the fuel in the cylinder. These paths are defined by the difference from the average unburned temperature path they are on at some arbitrary crank angle (CA_{arb}). This difference is equal to some multiple of the standard deviation of temperature (σ_T) at CA_{arb}, and therefore each thermal path follows a different polytropic compression and expansion process, starting at a uniform IVC condition (temperature and pressure), due to differences in heat transfer. Each thermal path 'j' then has a different effective polytropic coefficient (γ_j) in order to reach the required temperature at the arbitrary crank angle. The effective polytropic exponent can be calculated according to Equation (5.20), where n_j is the multiple of the standard deviation, $T_{ub,CAarb}$ is the temperature of the average unburned profile at CA_{arb}, V_{CAarb} is the cylinder volume at the arbitrary crank angle, and T_{IVC} and V_{IVC} are the temperature and volume at IVC, respectively. The unburned thermal profiles are then defined by the polytropic relationship seen in Equation (5.21) for the given value of γ_j.

$$\gamma_j = \frac{ln\left(\frac{T_{IVC}}{T_{ub,CAarb} + n_j\sigma_T}\right)}{ln\left(\frac{V_{CAarb}}{V_{IVC}}\right)} + 1 \tag{5.20}$$

$$T_{ub,j} = T_{IVC}\left(\frac{P_{cyl}}{P_{IVC}}\right)^{\left(1-\frac{1}{\gamma_j}\right)} \tag{5.21}$$

The predicted temperature distributions from the TSA method by Lawler et al. [15, 20, 21], and optical engine data showing thermal stratification from Dec et al. [13, 14], as well as CFD predictions from the present work tend to exhibit a skewed nature due primarily to the non-uniform piston bowl profile, squish regions, and crevice volumes. The distributions tend to show a negative

skew, i.e., more mass exists at lower than average temperatures than that of a normally distributed profile, as can be seen in the temperature distribution from a non-reacting CFD simulation for an HCCI combustion simulation with the Caterpillar SCOTE geometry shown in Figure 5.8. The large high temperature hump is representative of the large piston bowl volume, the second small hump likely corresponds to the squish volume, where more of the charge is exposed to the firedeck and piston boundaries, and the long tail of the distribution corresponds to the crevice fuel.

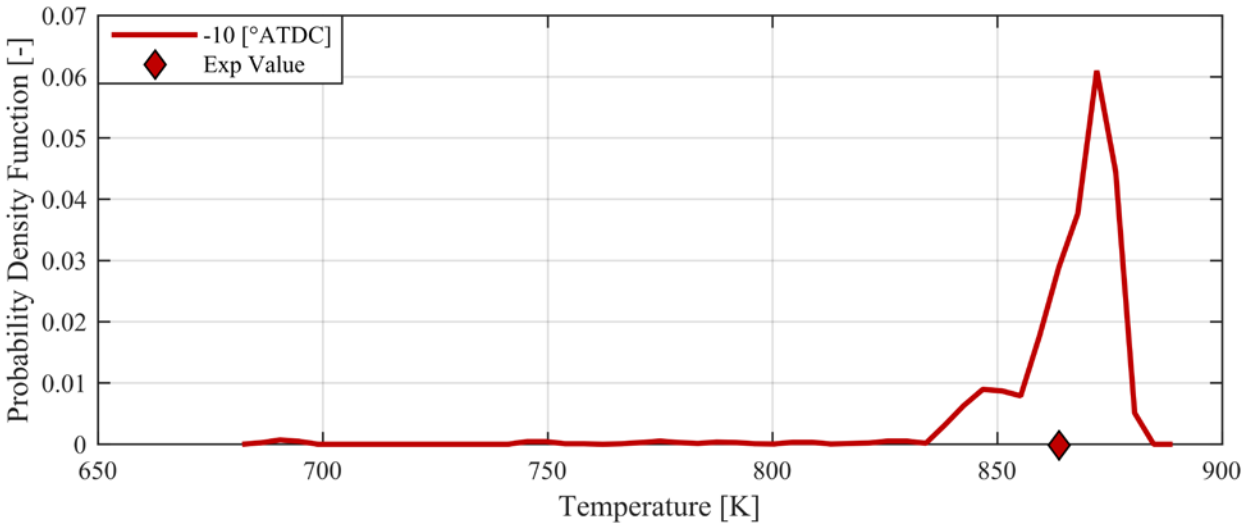

Figure 5.8: Example PDF of temperature from non-reacting HCCI simulation at -10°CA

To account for the skewed nature of the temperature distribution, more thermal paths less than the average unburned zone were considered. These various thermal paths, defined by the multiple of the standard deviation from the mean, are shown in Figure 5.9 for an example case, along with the bulk gas temperature calculated from the ideal gas law. The compression effect from combustion can clearly be seen after -10°CA, as the increase in pressure from combustion causes an increase in temperature due to compression heating. With these various thermal paths computed, the ignition location of each possible fuel mixture can be computed along each thermal path, i.e., the number of total zones is the number of fuel mixture zones considered multiplied by the number of thermal zones considered.

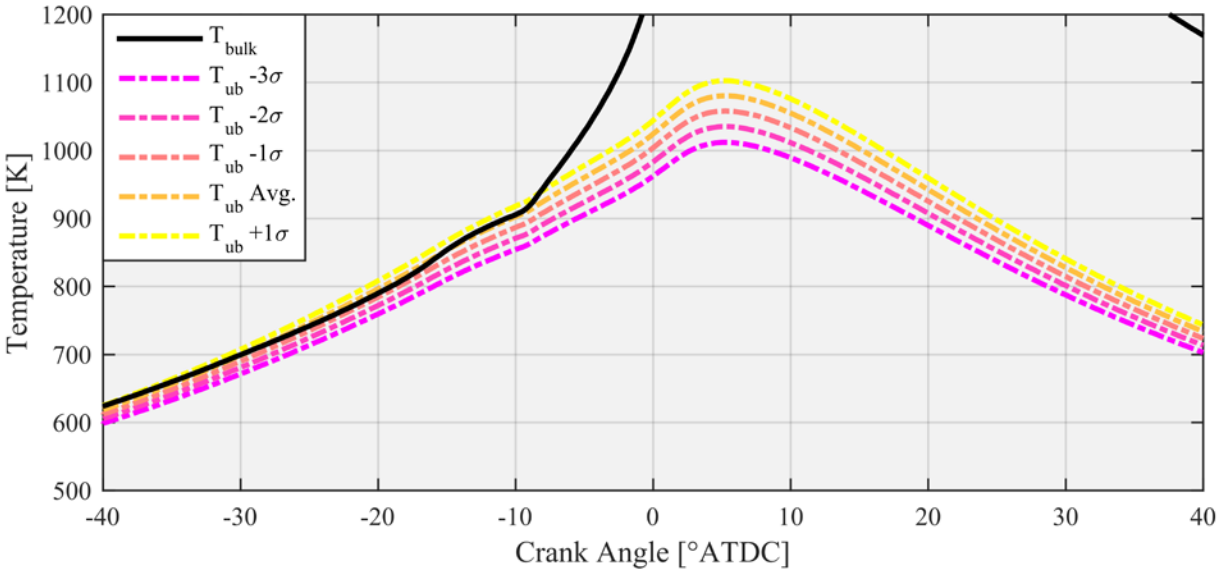

Figure 5.9: Unburned temperature profiles for various multiples of the standard deviation of temperature as a function of crank angle compared to the bulk gas temperature

5.2.3 Predicting Autoignition Locations

The Livengood-Wu autoignition integral, reproduced in Equation (5.24) was used to predict the ignition locations of the various possible fuel mixtures along each thermal path defined in the previous section. Like the TSA method, the pressure is considered to be uniform throughout the combustion chamber. The fuel mixture properties, such as the premixed mass fraction, equivalence ratio, and EGR rate, and thermodynamic information, such as temperature and pressure, are known as functions of crank angle. With this information, the ignition delays for the fuel mixtures for each fuel and thermal zone can be determined by linear interpolation of a large look-up table of ignition delay values, or by use of an ignition delay correlation, as discussed in Chapter 4. The ignition delays are determined at each crank step (dCA), which is converted into a time step (dt) by Equation (5.22). The crank angle domain is converted to the time domain by Equation (5.23). The calculation of ignition delays begins at the EOI timing. In reality however, the premixed fuel should be considered starting from the IVC timing. However, the cumulative integral between IVC

and EOI is very small $\ll 0.01$, due to the very long ignition delays associated with the low temperature and pressures of the early compression stroke, and is therefore ignored.

$$dt[s] = \frac{1000\frac{ms}{s} * 60\frac{s}{min}}{dCA * RPM * 360\frac{deg}{rev}} \tag{5.22}$$

$$t_{i+1} = t_i + dt \tag{5.23}$$

The autoignition integral can then be computed for each thermal and fuel mixture zone according to Equation (5.24), from the EOI timing which corresponds to t_0, until ignition when the cumulative integral equals 1.0. An example showing the ignition delay and cumulative autoignition integral is shown in Figure 5.10.

$$AI = \int_{t_0}^{t_{ign}} \frac{1}{\tau} dt \tag{5.24}$$

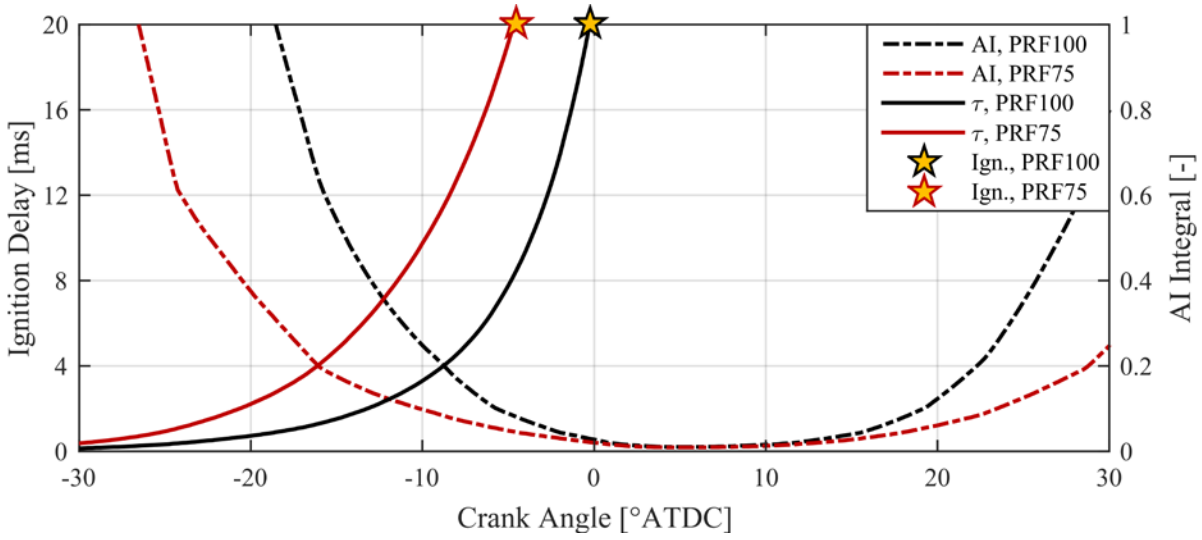

Figure 5.10: Ignition delay and cumulative AI integral as a function of crank angle for 2 PRF numbers (PRF100 in black, PRF75 in red) at the mean temperature path, showing the ignition locations (stars). EOI timing is 43°ATDC

As temperature and pressure increases due to compression, the ignition delay decreases and the cumulative AI integral increases in value until the defined ignition location where the value of the AI integral reaches 1.0.

Figure 5.11 shows the predicted autoignition crank angle locations for various thermal profiles as a function of PRF number for an example case. As expected, as PRF number decreases, the ignition zone advances due to the higher reactivity of n-heptane compared to isooctane and the associated increase in equivalence ratio. In addition, the colder zones autoignite later than the hotter zones. Figure 5.12 shows the same data but with the x and y axes switched. For a given crank angle, it is clear that multiple PRF blends may autoignite depending on the thermal path of the fuel. This is an important consideration when attempting to determine the relative energy released by a particular zone.

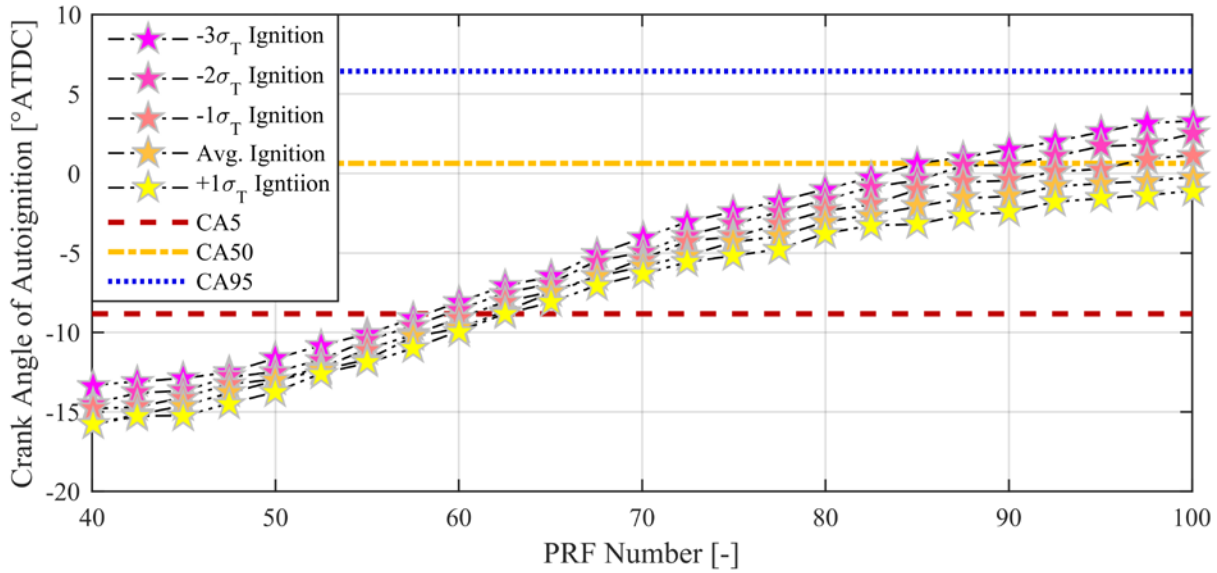

Figure 5.11: Predicted AI crank angle (indicated by stars) as a function of PRF number for various thermal profiles, with lines showing CA5 (red dashed), CA50 (yellow dash dotted), and CA95 (blue dotted)

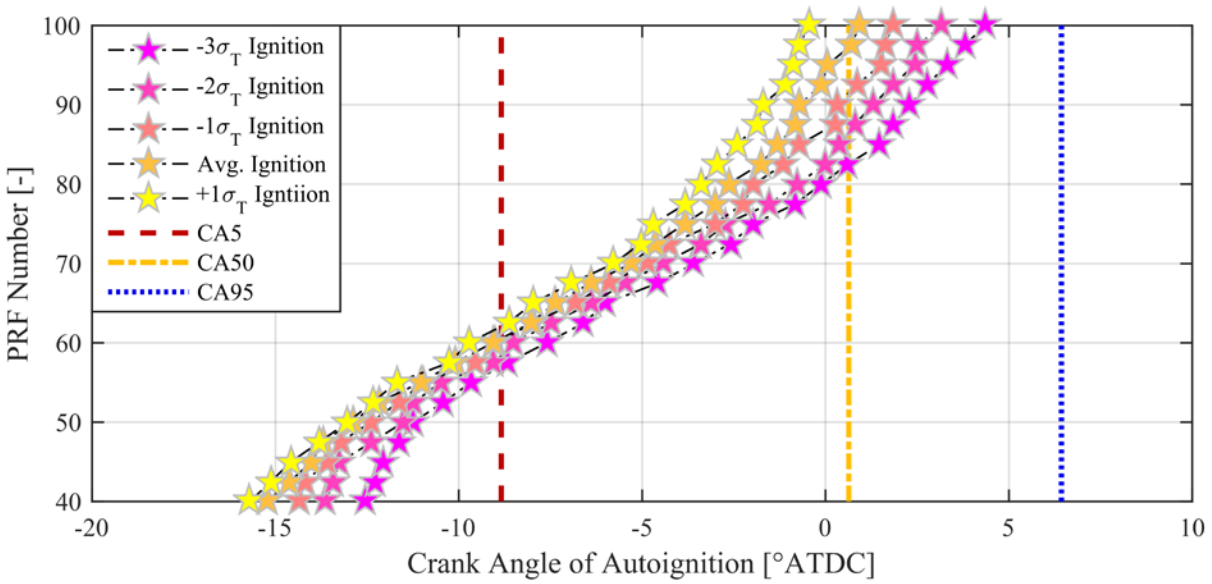

Figure 5.12: PRF number vs. predicted AI crank angle (indicated by stars) for various thermal profiles, with lines showing CA5 (red dashed), CA50 (yellow dash dotted), and CA95 (blue dotted)

5.2.4 Determining Probability Density Functions

With the autoignition locations of all the fuel mixture and thermal zones calculated, the next step in the analysis is to determine the distribution of mass responsible for the energy release. Like the TSA method, the FSA method uses the cumulative mass fraction burned profile to distribute energy amongst the various fuel and thermal zones. The MFB profile is calculated according to Equation (5.25) by dividing the calculated cumulative heat release by its maximum value. An example MFB profile versus crank angle is shown in Figure 5.13.

$$MFB = \frac{HR}{\max(HR)} \tag{5.25}$$

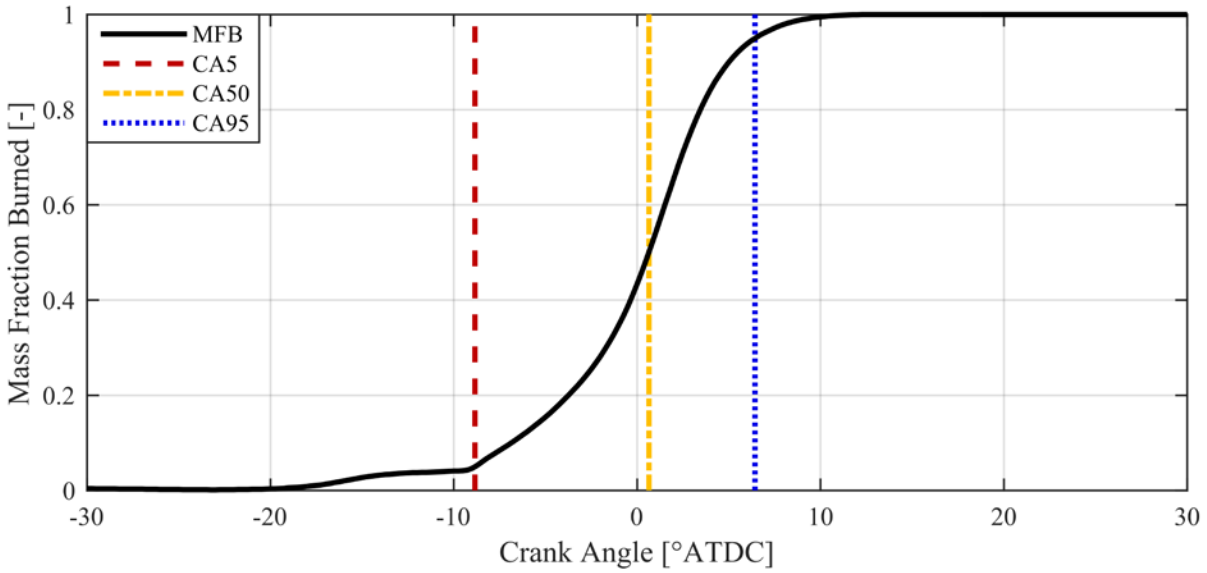

Figure 5.13: Example mass fraction burned profile from CFD RCCI simulation, with lines denoting CA5 (red dashed), CA50 (yellow dash dotted), and CA95 (blue dotted)

The autoignition crank angles belonging to the respective fuel and thermal zones were then grouped into crank angle windows, or "bins", between CA5 and CA95. The analysis considers only energy released between CA5 and CA95, in order to eliminate the effect of the LTHR, and late cycle oxidation, respectively. The crank angle bins used in the analysis were 1.0°CA wide. The bin width does not have a strong influence on the predicted fuel distribution as long as the bin width is greater than or equal to the resolution of the crank angle data. This resolution is typically either 0.25°CA or 0.1°CA. A bin width of 1.0°CA eliminates some amount of uncertainty in the autoignition prediction, as the typical accuracy of Livengood-Wu autoignition predictions compared to SI and HCCI ignition events is typically on the order of 1-2°CA [66, 80, 81, 87].

This binning process is represented in Figure 5.14, where the green region represents the bin of interest. The energy released within the window was determined by subtracting the value of the MFB at the right edge of the bin from the value of the MFB at the left edge of the bin. The minimum possible premixed fraction was defined by eliminating any premixed fuel zones on the +1σ path that autoignited before CA5. This is justified by the face that if this fuel existed, then there would

have been a corresponding heat release associated with the autoignition of this fuel. Since it was assumed that fuel is equally likely to be “hot” as to be “cold”, this implies that any fuel mixture that autoignites along the hottest possible path before CA5 is not possible.

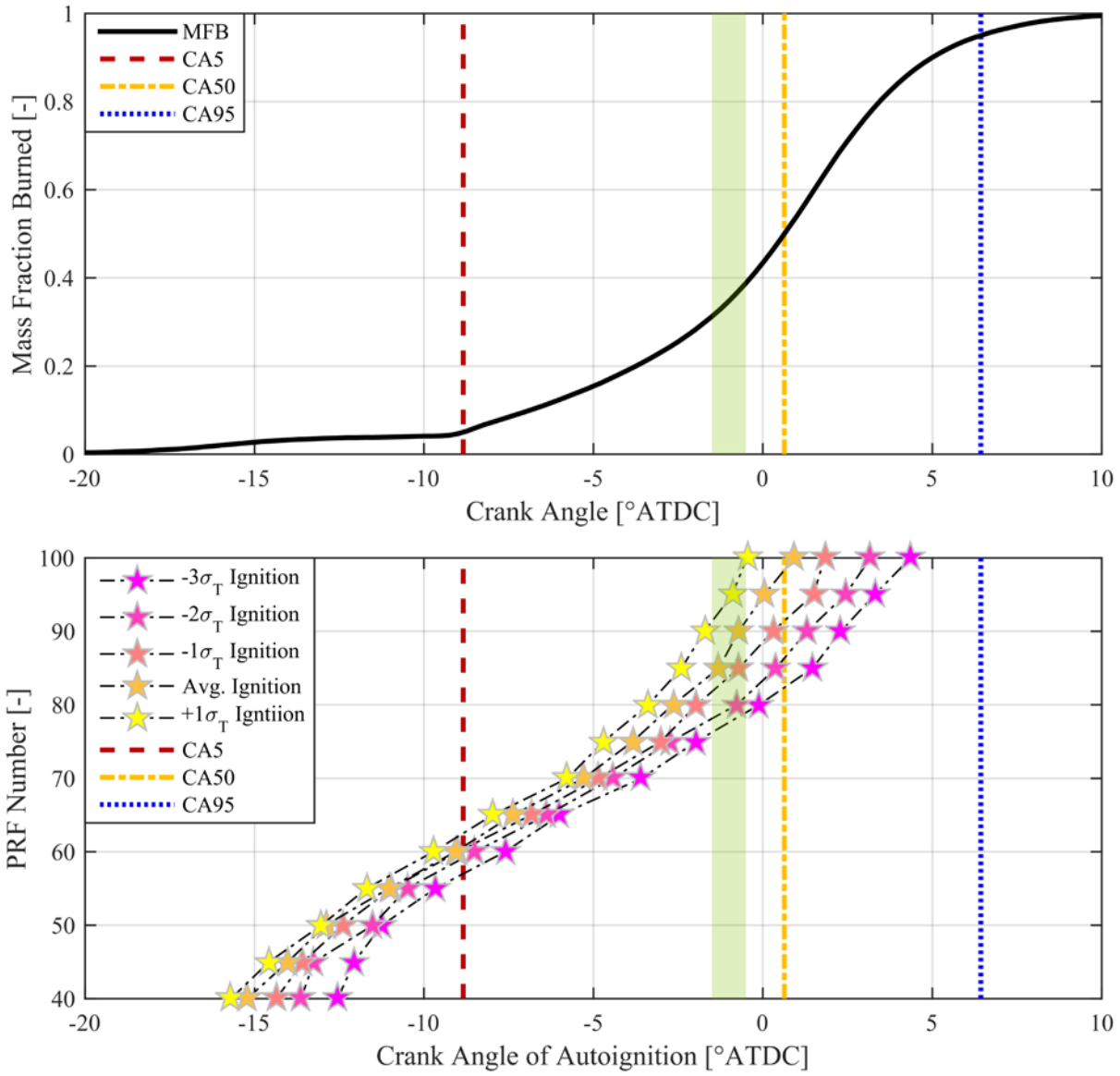

Figure 5.14: Graphical representation of the binning process by which autoignition zones for various PRF numbers and temperature paths were compared to the mass-fraction burned profile. The green region represents an example 1.0°CA wide bin

The maximum possible premixed fraction is defined in a similar manner, except that the coldest thermal path (-3σ) is considered, and if a premixed zone does not autoignite before CA95, then

this zone either does not exist or remains unburned throughout the cycle. Fuel that was outside the minimum and maximum possible premixed fraction was not considered in the analysis.

If there is overlap among thermal zones within a given crank angle window, then the energy within this window was distributed according to breakdown shown in Figure 5.15. The cumulative distribution shown is from a non-reacting CFD simulation of a representative HCCI combustion case. If all thermal zones are represented within a crank angle bin, then 80% of the energy is distributed into the fuel mixture zone at the mean thermal path, 5% is distributed to the +1σ thermal path fuel mixture, 12% to the -1σ thermal path, etc. If there is no overlap, and only one zone is accounted for in the crank angle bin, then all the energy is assumed to belong to the fuel mixture zone that ignites in the bin.

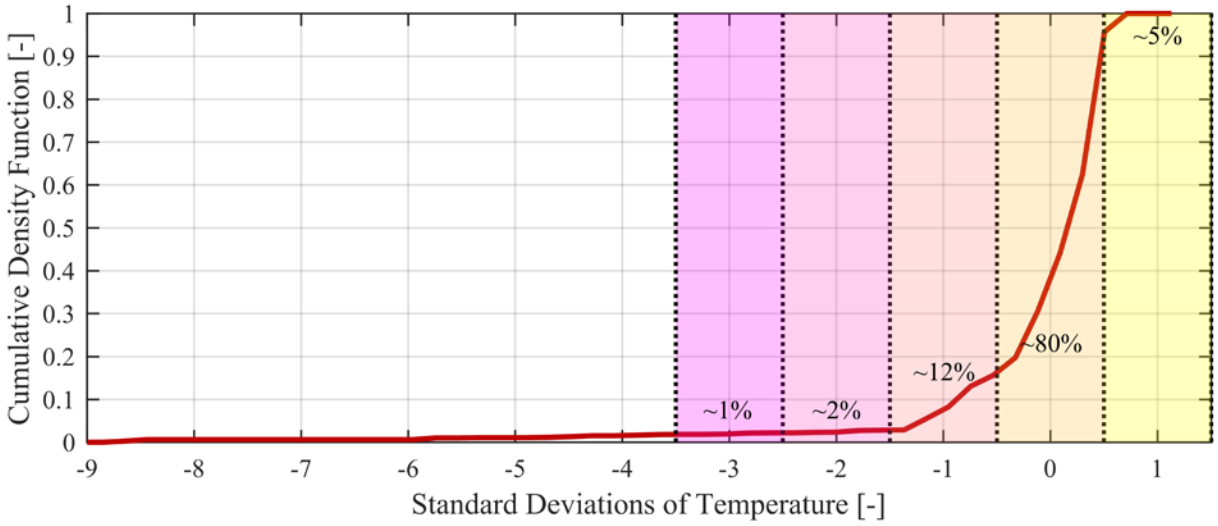

Figure 5.15: Cumulative density function of temperature normalized by standard deviation (red line), showing the relative distribution of temperature among “thermal zones” denoted by colors

This approach assumes that the natural thermal stratification present in a homogeneous charge simulation is representative of the thermal distribution in stratified fuel approach, not accounting for the effect of spray vaporization on the temperature distribution, which is handled separately. This approach served as a way in which to determine the relative weighting of a given thermal

pathway, in order to distribute the energy associated with a given crank angle bin into the appropriate fuel mixture zones. The energy for each fuel mixture zone could then be summed across all the thermal paths, establishing the cumulative density function of energy as a function of premixed fraction. One important consideration however is that this methodology only accounts for fuel that actually burns, so to approximate the fraction of the total fuel accounted for by the analysis, this cumulative density function was multiplied by the combustion efficiency (η_{comb}).

In order to convert from the cumulative density function of energy to fuel-mass density, the energy fraction of each premixed zone, (e_i) was multiplied by the average mixture LHV divided by the zone lower heating value (LHV_i). This is an important manipulation as, for a given fuel mass, a fuel mixture with a high lower heating value will release more energy than a fuel with a low lower heating value, yet would account for the same total fuel mass. This is not a consideration that has to be made in a single fuel strategy, or in a homogeneous charge strategy.

$$mf_i = e_i \frac{LHV_{avg}}{LHV_i} \tag{5.26}$$

A similar manipulation must be made to convert from the cumulative density of energy to cylinder-mass density. As shown in Equation (5.27), the energy fraction of each premixed zone was multiplied by the average energy density, which is equivalent to the fuel energy (Q_{fuel}) divided by the trapped mass (m_{trap}), and divided by the zone energy density (E_i). This is necessary because a unit of cylinder mass at a given local equivalence ratio has a very different quantity of energy depending on the equivalence ratio, i.e., a unit of total mass at φ of 0.25 contains much less fuel-energy than a unit of total mass at φ of 1.0. This is not a consideration that needs to be made for homogenous charge strategies, but is important for stratified approaches.

$$m_i = e_i \frac{\left(\frac{Q_{fuel}}{m_{trap}}\right)}{E_i} \tag{5.27}$$

The cumulative density functions for energy, fuel-mass, and total-mass are the cumulative sums of the respective fraction. Each respective PDF can be calculated according to Equation (5.28), where the x-variable is the variable of interest, e.g., PRE, PRF number, φ, temperature, etc. The premixed mass fraction and PRF number are fuel-mass weighted quantities, and temperature and equivalence ratio are total-mass weighted quantities. The expected value can then be calculated from the PDF according to Equation (5.29), and compared to the average value to determine the relative error of the methodology.

$$PDF = \frac{dCDF}{dx} \tag{5.28}$$

$$E[X] = \int_{-\infty}^{+\infty} x * PDF(x)dx \tag{5.29}$$

5.2.5 FSA Method Implicit and Explicit Assumptions

Like the TSA method, there are a number of implicit and explicit assumptions associated with the FSA method. These assumptions are as follows:

- The pressure is uniform in the cylinder.
- The premixed fuel, air, residuals, and EGR are completely mixed at IVC.
- Chemical reaction rates are very fast relative to engine time scales, and therefore when a zone autoignites it does so instantaneously.
- There is no heat or mass transfer between zones, implying that the hot burned gases do not mix with cold unburned gases, and in turn, accelerate the autoignition events.

- There is no flame propagation in the combustion chamber, which would cause zones to burn prior to the autoignition integral prediction.
- Fuel instantaneous vaporizes at the end of injection.

5.3 Validation

In order to validate the FSA model, reacting and non-reacting CFD simulations were performed with KIVA3V release 2 [88]. The reacting simulations were used to validate the CFD simulations against the experimental HCCI and RCCI data described in Chapter 3, and the non-reacting simulations were used to generate PDFs of fuel distributions, for various injection timings and initial conditions to compare to the FSA results. The two approaches were able to provide a direct comparison with the FSA method, as the non-reacting fuel distributions could be compared to the FSA results using the reacting pressure and heat release data, thus providing a known distribution of fuel and a known result to determine the validity of the FSA methodology, provided the chemical mechanism used in the CFD and CV ignition delay simulations was equivalent.

5.3.1 3-D CFD Simulation Details and Results

KIVA3V is a Reynolds Averaged Navier Stokes (RANS) modeling approach for the gas phase flow field, and uses the Lagrangian-Drop Eulerian-Fluid (LDEF) framework for the modeling of engine sprays. The liquid fuel is treated as a number of Lagrangian parcels, and the surrounding gas is discretized into Eulerian cells. The fuel parcels are coupled to the gas phase by the use of source terms in the conservation equations (i.e., mass, momentum and energy). Figure 5.16 shows a representation of the modeling approach used in the KIVA3V simulations presented in this work.

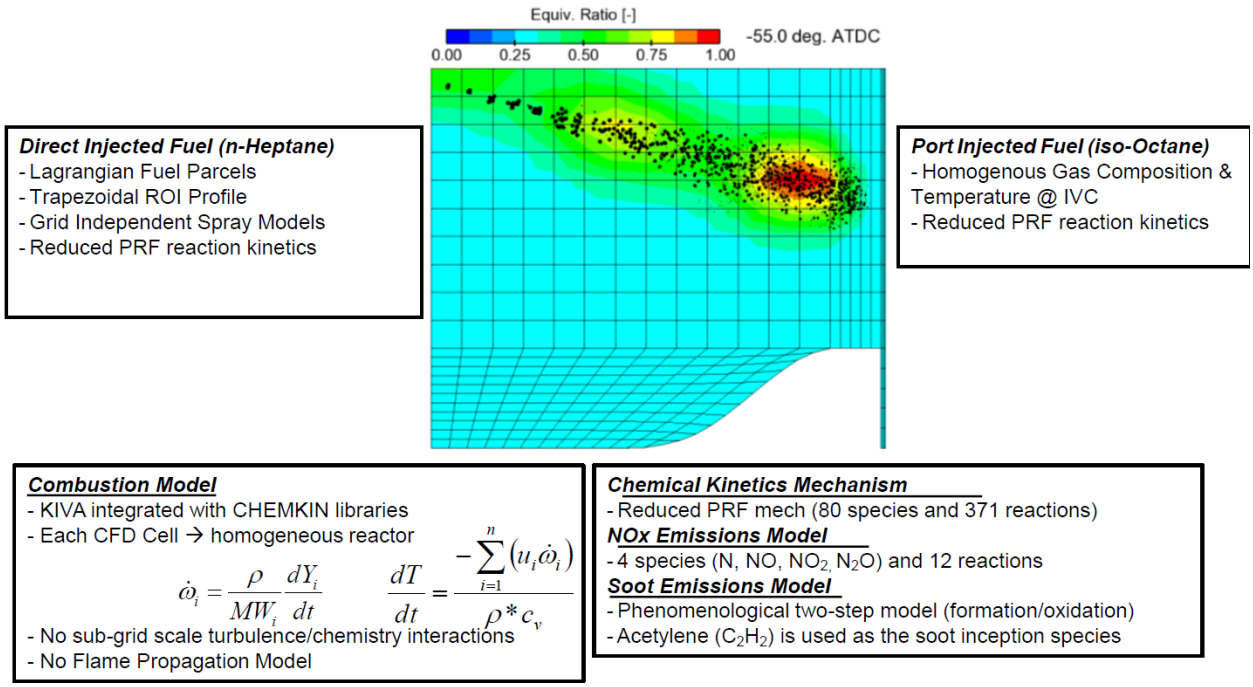

Figure 5.16: Illustration of multi-dimensional engine CFD modeling approach applied to RCCI combustion using KIVA. Adapted from Dempsey [89]

5.3.1.1 Modeling Setup and Submodels

A list of the improved ERC sub-models coupled to the KIVA3V code and utilized in this work are shown in Table 5.1. As it is not the focus of the present work, a detailed description of the simulation models is omitted, however a brief summary of each model is provided below. Significantly more detail regarding the computational models and methodology can be found in the appropriate reference in Table 5.1 and in Dempsey [89] and Kokjohn [85].

Table 5.1: Sub-models used in CFD simulations

Modeled Phenomenon	Model	Reference
Spray Breakup	KH-RT instability	Reitz [90], Patterson and Reitz [91]
Vaporization	Discrete multi-component fuel (DMC)	Ra and Reitz [92]
Turbulence	RNG k-ε	Han and Reitz [93]
Combustion	Sparse analytical Jacobian (SpeedChem)	Perini et al. [94]
Droplet collision	Radius of influence (ROI) model	Reitz and Munnannur [95]
Near nozzle flow	Gas-jet model	Abani et al. [96, 97]

The spray breakup model utilizes a hybrid Kelvin-Helmholtz/Rayleigh-Taylor (KH-RT) approach, which consists of two distinct steps. The Kelvin-Helmholtz (KH) instability model predicts the primary break-up of injected fuel parcels, while the secondary break-up model uses Rayleigh-Taylor (RT) instabilities to predict the aerodynamic break-up of the fuel droplets. The KH model predicts the primary break-up process by evaluating the break-up time, and calculating the radii of the child droplets. The transition from primary to secondary break-up is calculated using an empirical break-up length, and beyond this distance from the injector tip, the RT model is used to predict the secondary break-up stage. When the wavelength of the fastest growing wave on a droplet is smaller than its diameter, RT waves grow on the droplet surface, and when the wave growth time is equal to the break-up time, the droplet breaks up.

The vaporization model from Ra and Reitz [92] was used to model the evaporation process of multi-component fuels such as gasoline and diesel. The discretized approach of the model tracks individual fuel mixture components through the evaporation process, which allows coupling with the reaction kinetics of the individual components. An unsteady internal heat flux model, and a model for the droplet surface temperature, were used to calculate the evaporation process of the liquid fuel. An approximate solution to the quasi-steady energy equation was used to derive the expression for the heat flux from the surrounding gas to the droplet-gas interface [92].

The original RNG k-ε turbulence model was developed for incompressible flows, however flows in internal combustion engines are subject to large changes and gradients in density over space and time. Han and Reitz [93] modified the epsilon (dissipation route) transport equation through an isotropic rapid distortion analysis in order to include compressibility effects in the turbulence model. The authors noted that flow compressibility not only affects the compression and expansion

process, but also chemically reacting sprays, and should therefore be accounted for in the turbulence model.

The chemical kinetic solver for reactive gaseous mixtures developed by Perini et al. [94] and used in this work considers each computational cell as a time evolving adiabatic, constant volume, homogeneous chemical reactor, the solution of which is given through the integration of a system of ordinary differential equations. The chemical kinetic mechanism consists of n_s chemical species and n_r independent chemical reactions. The solver uses an analytical Jacobian formulation for solving sparse reaction kinetics, referred to as SpeedChem, which has been shown to significantly reduce computational times relative to the CHEMKIN-II chemistry solver from Kee et al. [98] for a wide range of reaction mechanism sizes (2x faster for a small mechanism and up to 2 orders of magnitude for a detailed mechanism) without significant changes to the combustion and emissions predictions [94].

The droplet collision model developed by Reitz and Munnannur [95] is used. This model uses a radius-of-influence collisional interaction approach whose outcomes include bounce, coalescence, and fragmenting and nonfragmenting separation processes. The approach includes discrete particle resolution improvements in order to reduce numerical dependencies. The improved collision and outcome predictions were coupled, and provided increased fidelity in the spray modeling predictions.

The GASJET model, developed by Abani et al. [96, 97] is used in the present work. This model accounts for interactions in the liquid droplet/gas phase momentum exchange near the injector tip. This model decreases the grid dependency of the spray model breakup and vaporization models, allowing for the use of significantly coarser and thus more efficient computational meshes. The

GASJET approach models the relative velocity between the liquid droplets and the gas phase in the near nozzle region, and allows use of coarse grids while maintaining accurate spray simulation.

Table 5.2: Spray model constants used in CFD simulations

Variable	Name	Value	Reference
KH breakup wavelength constant	B_0 (balpha)	0.6	Reitz [90]
KH child velocity	C_{vKH} (cnst1)	0.188	Reitz [90]
KH decay timescale after splash	$B_{1,s}$ (cnst21)	1.732	Reitz [90]
KH breakup decay timescale	B_1 (cnst22)	80	Dempsey [89]
KH child birth mass fraction	(f_{KHbcri})	0.03	Reitz [90]
RT breakup wavelength constant	$C_{\Delta RT}$ (cnst3rt)	0.1	Patterson et al. [91]
RT breakup time constant	C_{RT} (cnst2b)	1.0	Patterson et al. [91]
Initial breakup length	L_b (distant)	1.9	Patterson et al. [91]
GASJET distance (times of L_b)	L_{GJ}	2.0	
Max distance for GASJET model [cm]	Z_{GJ}	2.25	
GASJET entrainment constant	K_{entr}	0.85	

Table 5.2 lists the spray model constants used for the KH-RT spray breakup model and GASJET near nozzle flow model in this work. With the exception of the KH breakup decay timescale (cnst22), which was taken from Dempsey [89] for his work on the same engine platform, the values in the table are the values recommended by the authors.

A reduced chemical mechanism developed by Wang et al. [99] with 71 species and 360 reactions, developed to model the combustion and polyaromatic hydrocarbon formation for diesel and n-heptane/toluene mixtures, was used for the present work. The mechanism was validated with experimental shock tube data, premixed flame species concentration profiles, HCCI engine experiments, and direct injection constant volume spray experiments. The iso-octane portion of the reduced ERC PRF mechanism from Ra et al. [100] (9 additional species and 11 reactions) was present in the mechanism files from Wang et al. [99], and was enabled for the purposes of this

work. This mechanism was chosen as it performed very well for PRF fuels in HCCI and RCCI combustion CFD simulations, with very minimal modifications to the experimental operating conditions (typically well within the experimental uncertainty), as shown in following sections.

Figure 5.17 shows the computational sector mesh used to model the Caterpillar SCOTE stock piston bowl used in the HCCI and RCCI experiments presented in Chapter 3. The sector mesh was used in order to reduce simulation times and the total number of cells, and a periodic boundary condition was established on the sector faces. The squish height was increased slightly from the production piston profile in order to match the compression ratio, accounting for the lack of valve recesses and volume around the injector body in the mesh. The relatively coarse mesh was comprised of about 10,800 cells, and average reacting simulation times were on the order of 6-8hrs. Only the closed-cycle portion of the engine cycle could be simulated due to the lack of intake and exhaust runners and valves in the mesh setup.

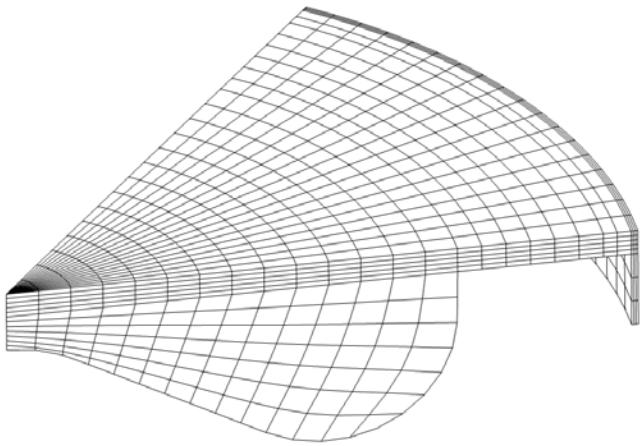

Figure 5.17: 51.4^{o} Sector mesh shown at TDC used in 3-D CFD simulations (~10,800 cells)

Table 5.3: Constant temperature boundary conditions

Cylinder Walls [K]	450
Cylinder Heat [K]	470
Piston [K]	500

Constant wall temperatures were applied as boundary conditions in the simulations. These temperatures varied depending on the nature of the boundary as seen in Table 5.3. The values in the table were optimized by matching simulated motored engine data to experimental "hot" motoring traces taken immediately after running when the engine was at operating temperature.

The injection rate was approximated by a trapezoidal shape with a closing rate that was twice as fast as the opening rate. This was approximated by qualitatively assessing the Bosch bench measured rate of injection (ROI) profiles in Dempsey [89], for the same model injector body and injector tip used in the experiments. The injection velocities, which serve as the input to KIVA, were computed by assuming a constant opening and closing rate that is a function of injection pressure, and calculating the duration of the injection required to provide the appropriate quantity of fuel based on the rate shape constraints. The initial slope of the injection rate was set by qualitatively matching the bulk heat release characteristics for a late injection RCCI case (-20^o SOI), where the influence of injection rate is the greatest as the mixing process controls the rate of heat release.

Table 5.4: Constant injector parameters used in CFD simulations

Parameter	Description	Value
Spray Angle [^{o}]	Angle of spray relative to cylinder axis	74
Nozzle Protrusion [cm]	Distance from nozzle to firedeck	0.21
cone [^{o}]	Mean cone angle of spray	10
n_{holes} [-]	Injector holes (defines sector angle)	7
d_{noz} [cm]	Diameter of nozzle	0.014
C_d [-]	Nozzle discharge coefficient	0.8
T_{fuel} [K]	Fuel temperature	333

The remaining injector parameters which model the Bosch 7 hole 141μm CRI2 injector used in the experiments are summarized in Table 5.4. A constant injector delay of 0.32ms, which is

equivalent to 2.5°CA at 1300rev/min engine speed, between the commanded SOI and the actual SOI was used for all simulations. This value comes from Bosch-Bench data from Dempsey [89] and was shown to be independent of injection duration and rail pressure.

5.3.1.2 Validation with PRF HCCI Engine Data

The CFD model was first validated against HCCI engine data presented in Section 3.7 taken on the heavy-duty Caterpillar SCOTE platform, the geometry and laboratory setup of which can be found in Section 3.1. The simulations were performed with the 3-D mesh shown in Figure 5.17, and the reactants were assumed to be completely premixed and uniform in composition. A constant residual fraction of 4% was assumed for all operating conditions, and the reactants were composed of fuel (iso-octane and n-heptane), air (O_2 and N_2), and residuals, which were assumed to be the products of complete combustion (CO_2, H_2O, O_2, and N_2). The reactant composition was calculated from the fuel mass, IVC conditions (assuming ideal gas law to determine number of moles of mixture at IVC), and the global fuel blend. The IVC temperature was adjusted up or down slightly from the experimentally calculated IVC temperature for these comparisons, effectively acting as a chemical kinetics tuning parameter.

The experimental IVC temperature was calculated by using the relationship outlined by Yun and Mirsky [101], which assumes an isentropic process during the gas exchange processes to determine the fraction of residual gases at IVC. The remaining initial conditions were taken directly from the time-averaged experimental values. A summary of the experimental operating conditions is reproduced from Section 3.7.1 and shown in Table 5.5, and the approximate uncertainties for the measurements used in the CFD analysis from this dataset are shown in Table 5.6 for reference. While each measured value has some amount of uncertainty, the magnitude of the uncertainties

are much less than the uncertainty in the IVC temperature and mixture homogeneity, therefore for the purposes of the CFD simulations these uncertainties were ignored.

Table 5.5: Operating conditions of PRF HCCI experiments

Engine speed [rev/min]	1300
Fuel Energy, (Q_{fuel}) [J/cyc]	2580 (±20)
Nominal Load ($IMEP_n$) [bar]	4.25-4.75
Intake Temperature [^oC]	40, 60 (±2.2)
Intake Pressure [kPa]	138.6, 122.7, 113.8 (±0.7)
Exhaust Pressure [kPa]	172.4, 144.1, 131.0 (±2.8)
Equivalence Ratio, φ [-]	0.25, 0.28, 0.30 (±0.01)
EGR [%]	0

Table 5.6: Approximate experimental uncertainties

Measurement	Experimental Uncertainty
Fuel Mass [mg/cyc]	±0.5mg
PRF [%]	±0.5%
P_{IVC} [kPa]	±1.5kPa
T_{IVC} [kPa]	±10-15K

The initial conditions provided to the CFD simulations for the T_{in} = 40^{o}C and φ = 0.25 cases are listed in Table 5.7. The calculated experimental IVC temperatures for the operating points listed in the table were within the range of 350-360K, while the CFD simulations required IVC temperatures between 356 and 368K to match combustion phasing. Variations between the simulated and experimental residual composition, charge stratification, heat transfer, and uncertainties in the experimental pressure measurement and temperature calculation could easily be responsible for the range of IVC temperature adjustment required in the simulations.

Table 5.7: Initial conditions of HCCI validation simulations (T_{in} = 40°C, φ = 0.25)

Condition	Fuel Mass [mg/cyc]	PRF [-]	P_{IVC} [kPa]	Exp. T_{IVC} [K]	Sim. T_{IVC} [K]
1	57.96	86.6	152.9	359	368
2	58.42	88.8	152.9	359	368
3	57.89	90.5	152.2	356	367
4	58.57	92.8	151.6	355	362

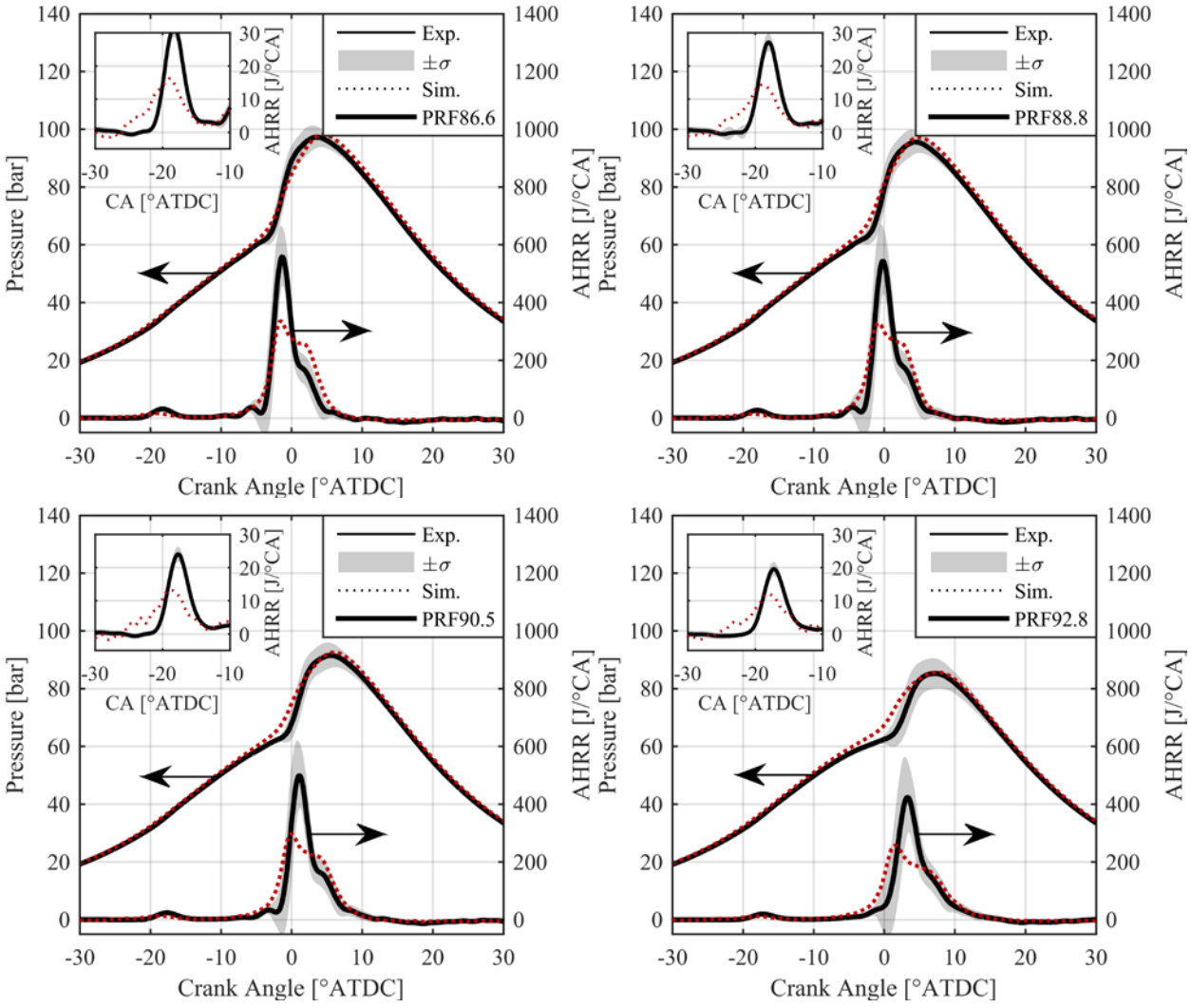

Figure 5.18: Comparison of experimental HCCI pressure and heat release rate data (black lines), including standard deviation (grey region) with simulated pressure and heat release rate (red dotted lines) at T_{in} = 40°C, φ = 0.25 and specified PRF mixture.

Figure 5.18 shows the ensemble-averaged pressure and heat release traces for the experimental data in black overlaid on the region of ±1σ in grey. The CFD predictions are plotted in red dotted

lines, and in general, show very good agreement with the experimental data for these very lean conditions. Some discrepancies are seen in the peak heat release rates, with the simulations tending to under-predict the peak values and slightly over-predicting the combustion duration. However the peak pressure and pressure histories are typically well within the experimental variability, as depicted by the standard deviation region.

The initial conditions for the experimental data and CFD simulations at $\varphi = 0.28$ and $\varphi = 0.30$ are summarized in Table 5.8 and Table 5.9, respectively, and the pressure and HRR results for the two cases are shown in Figure 5.19.

Table 5.8: Initial conditions of HCCI validation simulations ($T_{in} = 40^oC$, $\varphi = 0.28$)

Condition	Fuel Mass [mg/cyc]	PRF [-]	P_{IVC} [kPa]	Exp. T_{IVC} [K]	Sim. T_{IVC} [K]
1	58.03	86.9	135.5	354	364
2	58.19	89.0	135.3	355	364
3	57.92	90.3	134.3	352	360

Table 5.9: Initial conditions of HCCI validation simulations ($T_{in} = 40^oC$, $\varphi = 0.30$)

Condition	Fuel Mass [mg/cyc]	PRF [-]	P_{IVC} [kPa]	Exp. T_{IVC} [K]	Sim. T_{IVC} [K]
1	58.06	86.6	126.3	354	362
2	58.03	88.6	125.7	354	360
3	58.23	90.1	125.5	352	356

Both the $\varphi = 0.28$ and 0.30 cases show very good agreement between the experimental and CFD predicted pressure and heat release rates. At these slightly higher equivalence ratios, the simulations are able to match the peak heat release rates seen in the experiment better compared to the $\varphi = 0.25$ cases. For all cases shown here, the IVC temperature required an adjustment of between +7K and +11K from the IVC temperature calculated from the experimental results.

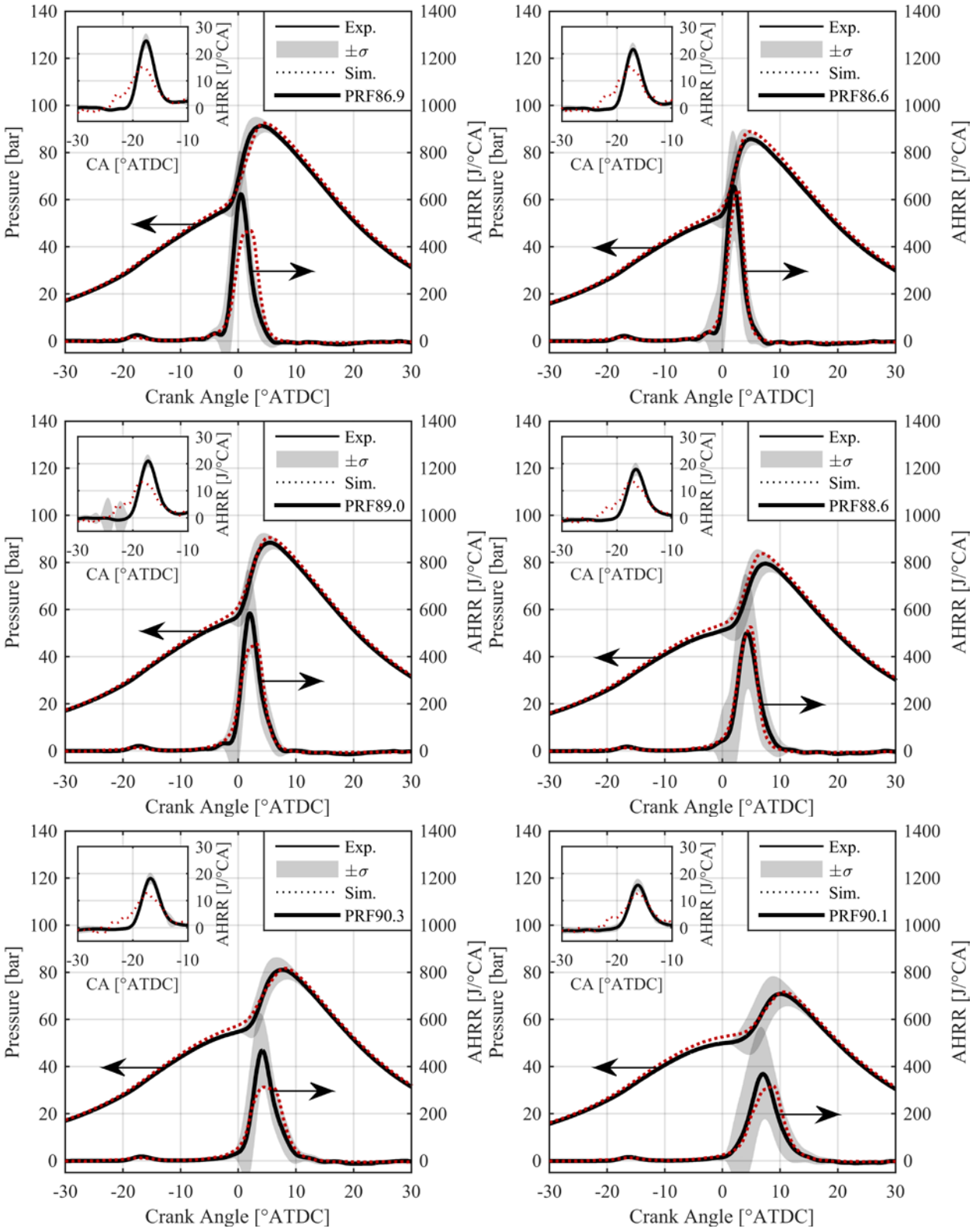

Figure 5.19: Comparison of experimental HCCI pressure and heat release rate data (black lines), including standard deviation (grey region) with simulated pressure and heat release rate (red dotted lines) at T_{in} = 40ºC, specified PRF mixture, and φ = 0.28 (left), and φ = 0.30 (right)

Similar behavior was seen for the comparisons at 60°C, the results of which are shown in Appendix E.1, however the IVC adjustments ranged from -2K to -11K from the experimentally calculated IVC temperature. This discrepancy was associated with an over-prediction of the cylinder pressure in the simulations compared to the experimental pressure measurement after the LTHR event. The discrepancy could be a result of an over-prediction in the energy released by the LTHR in the kinetic mechanism, differences in heat transfer between the 40°C and 60°C intake temperature cases, or error in the experimental pressure measurement. Despite this discrepancy, the experimental heat release phasing and magnitudes are well matched with the simulations.

5.3.1.3 Validation with RCCI Engine Data

With the CFD model showing good agreement with HCCI engine data with the chosen chemical mechanism (Wang et al. [99]), the CFD model was compared to the PRF RCCI engine cases described in Section 3.8, in order to assess its performance under RCCI conditions using premixed iso-octane and direct injected n-heptane for various direct injection timings and intake conditions. The reactant composition was calculated as described in the previous section for the HCCI simulations, with the exception that only the iso-octane was premixed. The IVC temperature was again used as a tuning parameter for the global chemical kinetics to match the combustion phasing of the simulations relative to the experiments.

A summary of the experimental operating conditions for the experimental RCCI data is reproduced from Section 3.8 and shown in Table 5.10, and the initial conditions of the CFD simulations for the T_{in} = 40°C, φ = 0.30 with PRF88 cases are listed in Table 5.11. In this case, the PRF number refers to the percentage of total fuel that is premixed (i.e., 88% premixed iso-octane, 12% direct injected n-heptane). Figure 5.20 and Figure 5.21 show the experimental and calculated pressure and heat release rates for the early SOI timing cases between -140° and -45°, and for the late

injection timing cases between -40° and -17°, respectively. Similar to the previous section, the ensemble-averaged pressure and heat release traces for the experimental data are shown in black overlaid on the region of ±1σ in grey, while the CFD predictions are plotted in red dotted lines.

Table 5.10: Operating conditions for constant PRF SOI sweep

Engine speed [rev/min]	1300
Fuel Energy, (Q_{fuel}) [J/cyc]	2590 (±20)
Nominal Load ($IMEP_n$) [bar]	4.5-4.75
EGR [%]	0
Intake Temperature [°C]	40 (±2.2)
PFI Fuel	iso-octane (PRF100)
DI Fuel	n-heptane (PRF0)
DI Timing, (SOI) [°CA ATDC]	Swept
Rail Pressure [bar]	500
Global PRF [-]	88.1 (±0.2)

Table 5.11: Initial conditions of RCCI validation simulations (T_{in} = 40°C, φ = 0.30, PRF88)

SOI [°ATDC]	Fuel Mass [mg/cyc]	PRF [-]	P_{IVC} [kPa]	Exp. T_{IVC} [K]	Sim. T_{IVC} [K]
-140	58.36	88.4	127.3	351	360
-90	58.55	88.0	127.0	350	358
-60	58.46	88.1	126.4	347	355
-55	58.27	88.4	126.1	346	358
-50	58.48	88.0	126.3	346	355
-45	58.27	88.2	126.3	347	358
-40	58.60	88.0	126.6	348	358
-35	58.46	88.1	127.3	351	358
-30	58.33	88.2	128.0	354	358
-25	58.32	88.1	127.9	353	355
-20	58.49	88.1	127.2	350	350
-17	58.33	88.2	126.7	347	346

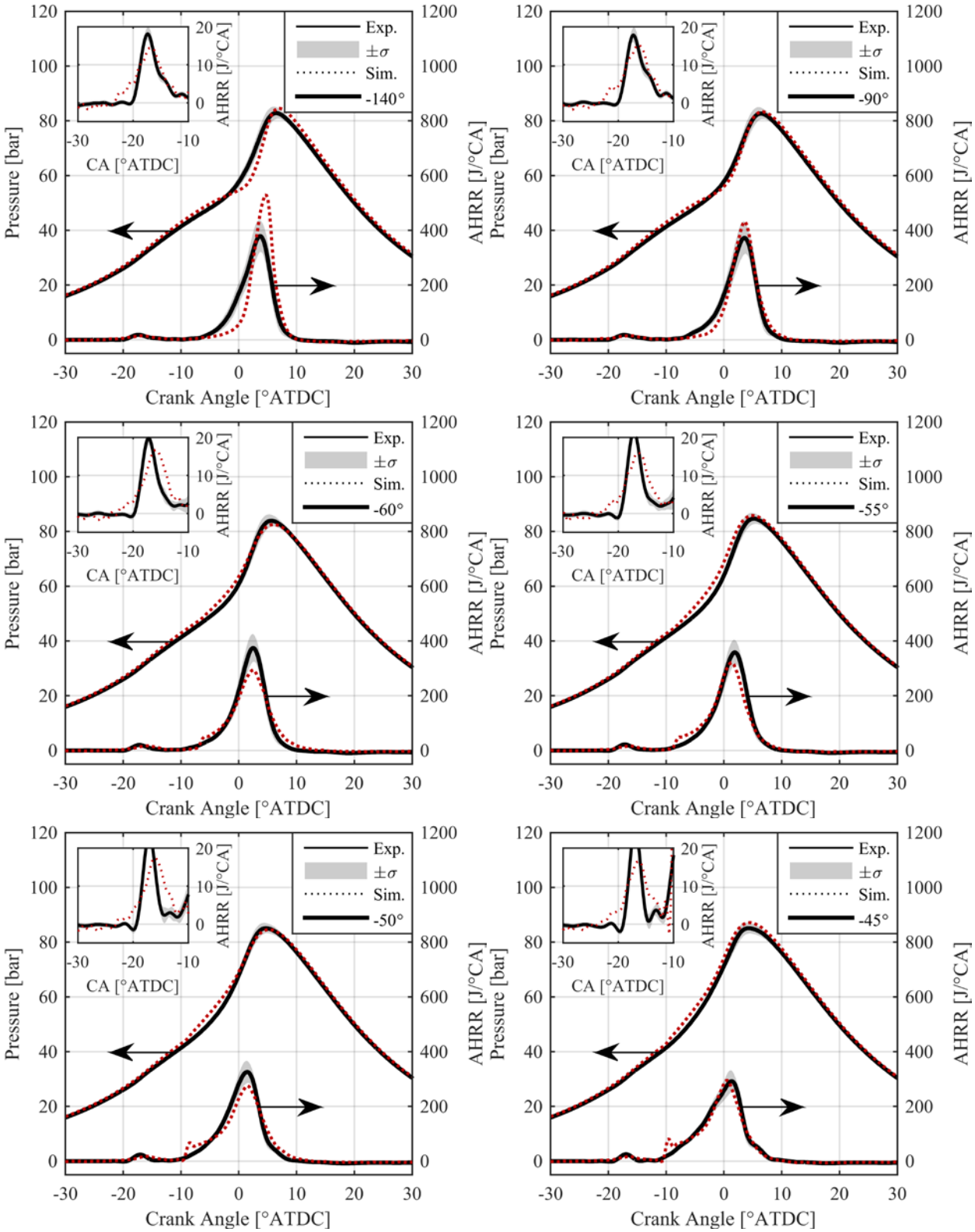

Figure 5.20: Comparison of experimental RCCI pressure and heat release rate data (black lines) including standard deviation (grey region) with simulated pressure and heat release rate (red dotted lines) at Tin = 40ºC, φ = 0.30, PRF = 88.1±0.2 and SOI timing specified in legend

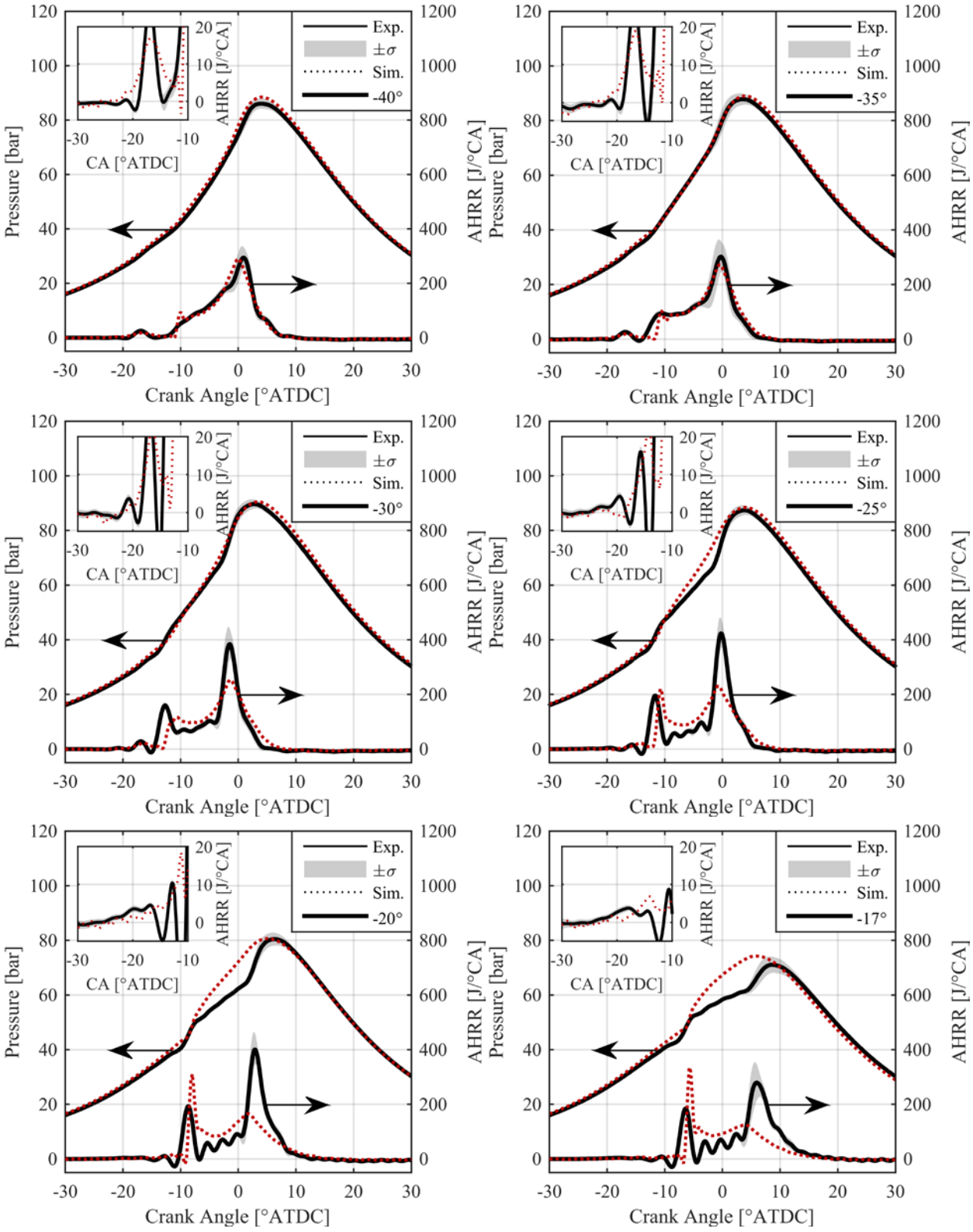

Figure 5.21: Comparison of experimental RCCI pressure and heat release rate data (black lines) including standard deviation (grey region) with simulated pressure and heat release rate (red dotted lines) at Tin = 40ºC, φ = 0.30, PRF = 88.1±0.2 and SOI timing specified in legend

Exceptionally good agreement is seen in the pressure and heat release comparisons between the experimental and simulated results between injection timings of -90^o and -30^o, which is the range of interest in typical RCCI combustion [85]. The earliest injection timing of -140^o SOI over-predicted the mixing of the direct injected fuel, and therefore resulted in a shorter combustion duration than the experiment. The late injection timing cases, particularly -20^o and -17^o SOI, did not capture the two stage combustion event seen in the experiment particularly well, and the general trends in combustion for these two cases were not as well captured.

A summary of the experimental operating conditions for the fixed combustion phasing RCCI data is reproduced from Section 3.8, and shown in Table 5.12. The initial conditions of the CFD simulations for the T_{in} = 40^{o}C, φ = 0.30, and CA50 = 0.75^o ATDC cases are listed in Table 5.13.

Table 5.12: Nominal operating conditions for constant CA50 SOI sweep

Engine speed [rev/min]	1300
Fuel Energy, (Q_{fuel}) [J/cyc]	2590 (±20)
Nominal Load ($IMEP_n$) [bar]	4.3-4.75
EGR [%]	0
Intake Temperature [^{o}C]	40 (±2.2)
PFI Fuel	iso-octane (PRF100)
DI Fuel	n-heptane (PRF0)
DI Timing, (SOI) [^{o}CA ATDC]	Swept
Rail Pressure [bar]	500
CA50 [^{o}CA ATDC]	0.75 (±0.25)

The two RCCI combustion cases required similar adjustments to the IVC temperatures between the simulation and the experimental results, as shown in Table 5.11 and Table 5.13. These adjustments were within the range of the HCCI simulations shown in the previous section. The results of the matched combustion phasing cases can be seen in Figure 5.22 and Figure 5.23 for early SOI timings, and late SOI timings, respectively.

Table 5.13: Initial conditions of RCCI validation simulations (T_{in} = 40ºC, φ = 0.30, CA50 = 0.75º ATDC)

SOI [ºATDC]	Fuel Mass [mg/cyc]	PRF [-]	P_{IVC} [kPa]	Exp. T_{IVC} [K]	Sim. T_{IVC} [K]
-140	58.16	85.9	127.8	349	363
-90	58.30	85.7	127.3	351	361
-60	58.24	87.0	126.3	354	357
-50	58.41	88.2	126.3	355	357
-45	58.22	88.7	126.1	349	355
-35	58.33	89.8	126.5	350	353
-30	58.08	91.0	126.8	351	353
-25	58.36	91.1	127.5	354	353
-20	58.09	76.9	127.2	351	345
-19.9	58.04	72.5	127.1	353	343
-19.8	58.00	69.3	126.9	352	343
-19.5	57.97	56.9	126.5	352	343

Similar to the matched global PRF case, the matched CA50 simulation predictions showed exceptionally good agreement in the range of interest for RCCI combustion (-90º to -30º SOI), but over-predicted the mixing of the DI fuel in the earliest SOI case, and did not match the bulk heat release characteristics of the late SOI cases (after -25º SOI) particularly as well. Additional simulation results can be seen in Appendix E.2 for various intake conditions, including intake temperature, equivalence ratio, and premixed fuel fraction, and for various injection pressures. Similar results are seen for all cases, i.e., very good agreement is seen within the SOI range of interest for RCCI combustion, but late injection cases were not as well captured by the present model formulation. These discrepancies could be a result of the spray model constants chosen for this work, the injector rate shape formulation, grid dependencies influencing the fuel distribution, or issues in the equivalence ratio and PRF sensitivity in the chemical mechanism. Significantly more work is needed to assess these potential sources of error.

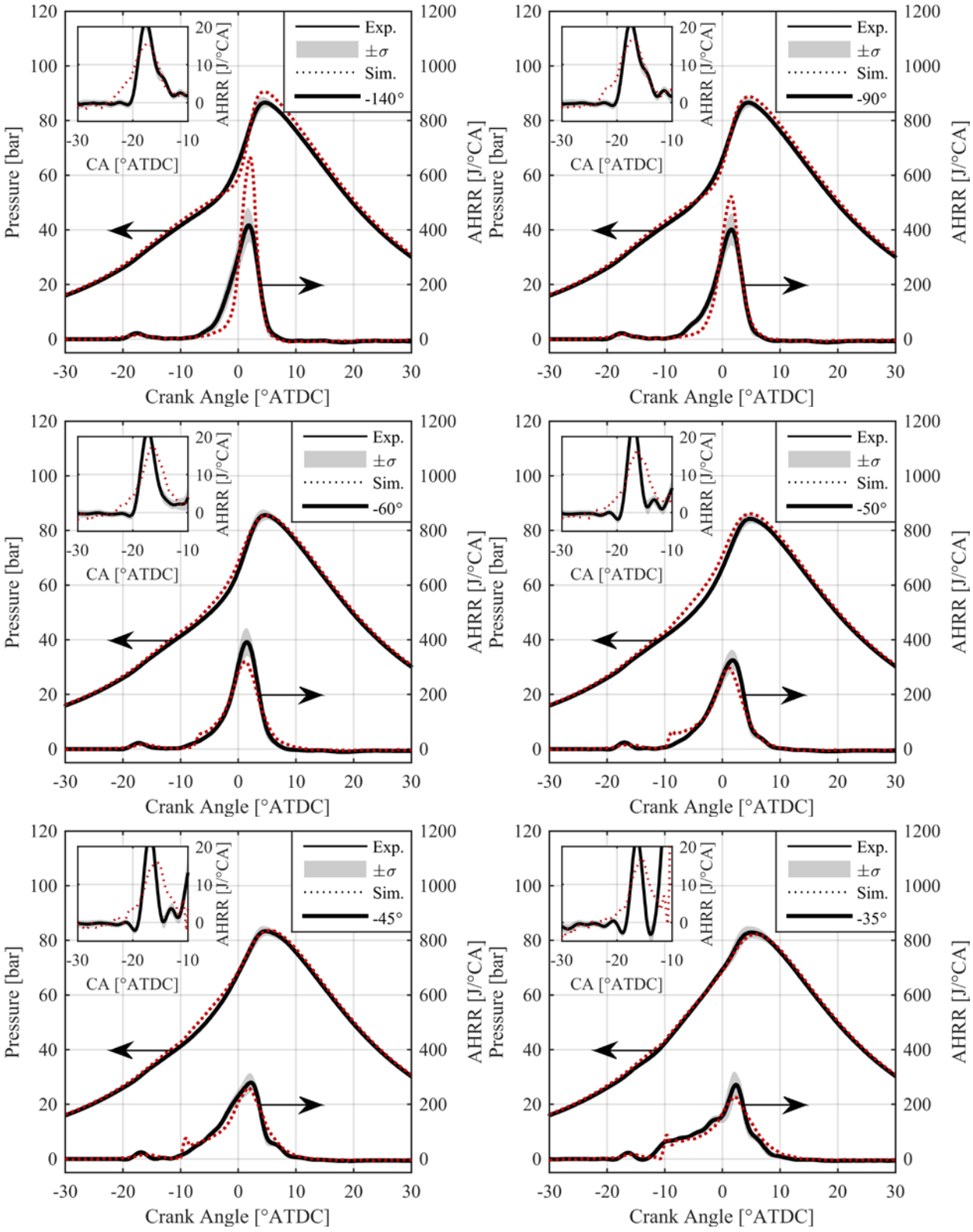

Figure 5.22: Comparison of experimental RCCI pressure and heat release rate data (black lines) including standard deviation (grey region) with simulated pressure and heat release rate (red dotted lines) at Tin = 40ºC, φ = 0.30, CA50 = 0.75º±0.25, varying PRF blends, and SOI timing specified in legend

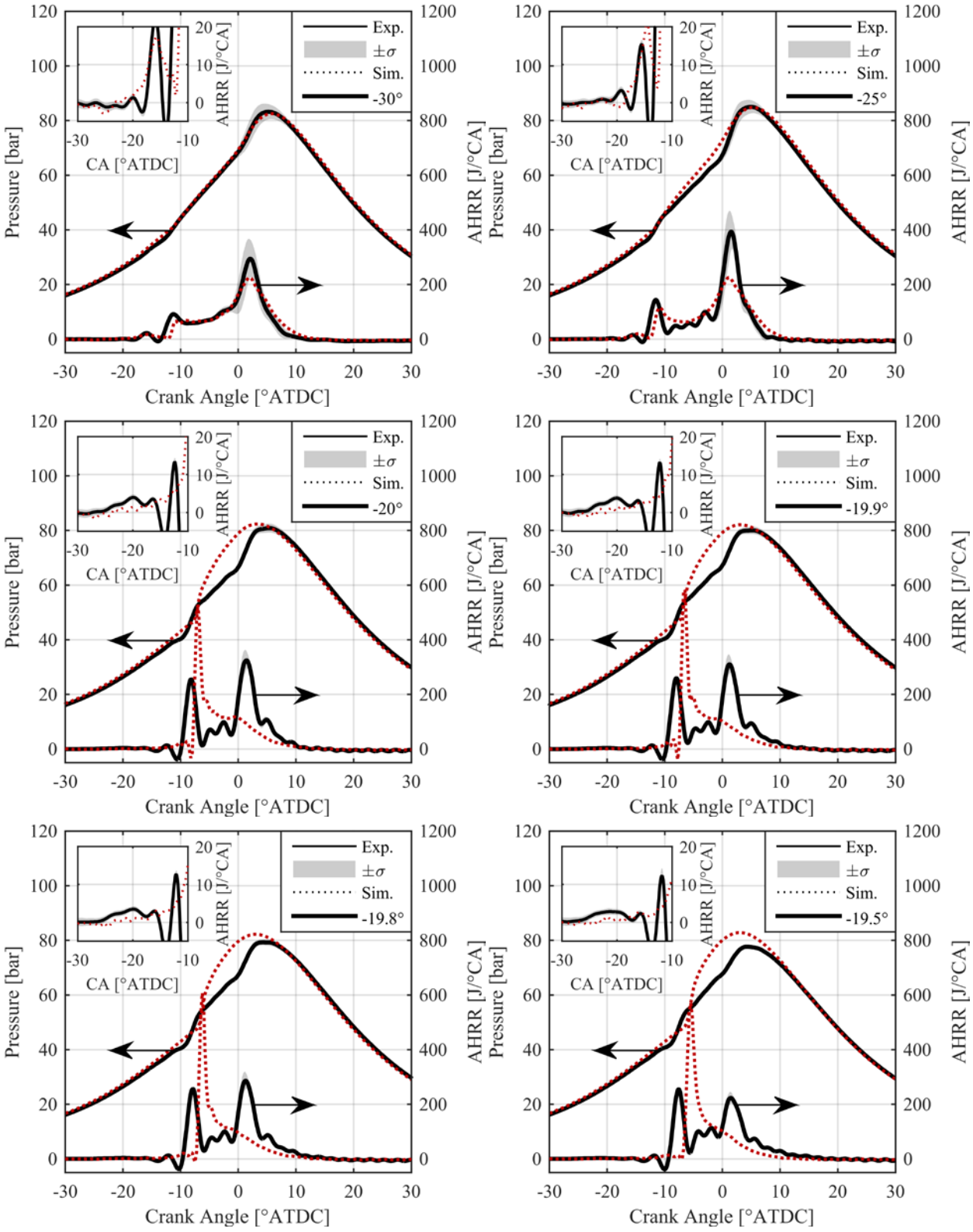

Figure 5.23: Comparison of experimental RCCI pressure and heat release rate data (black lines) including standard deviation (grey region) with simulated pressure and heat release rate (red dotted lines) at Tin = 40ºC, φ = 0.30, CA50 = 0.75º±0.25, varying PRF blends, and SOI timing specified in legend

5.3.2 Comparison of FSA with non-Reacting CFD Cases

Non-reacting CFD simulations of the validated cases presented in the previous section were used to validate the FSA method. The CFD simulations were used to determine the extent of the natural thermal stratification, and as a comparison between the FSA predicted fuel distribution and the known fuel distribution provided by the CFD result. The reacting CFD pressure, temperature, and mass fraction burned profiles were used as input conditions in the FSA analysis to predict ignition locations and the representative fuel distribution. The non-reacting CFD provided a direct comparison between the FSA and CFD results, as the fuel distribution in the CFD simulations yields the CFD pressure and HRR trace, and working backwards, the reacting pressure and HRR trace should return the fuel distribution using the FSA method. Assuming the FSA method could recover the global averaged PRE, φ, and fuel distribution shape, the methodology was assumed to be applicable.

One of the inputs of the FSA method is the standard deviation of temperature (σ_T) at some arbitrary crank angle (CA_{arb}). This parameter defines the various thermal profiles which may exist in the cylinder. This parameter was determined from non-reacting CFD results by analyzing the development of the cell temperatures as a function of crank angle. The standard deviation was calculated from the cell temperatures weighted by cell mass at each crank angle; as the mass-averaged cylinder temperature increased due to compression, so too did the standard deviation of temperature. Mass-weighted PDFs of temperature were also calculated at each crank angle, showing the evolution of the relative distribution of temperature over time. Figure 5.24 shows the evolution of the mass-averaged temperature profile as a function of crank angle for a representative HCCI case. The second peak that starts to define itself around -15^o CA is a result of heat transfer in the squish region. This bimodal distribution would likely not present itself with a flat-top piston

geometry. The long tail of the distribution extending to low temperatures is a result of the crevice region, where heat transfer to the piston and cylinder walls keeps the cell temperatures low.

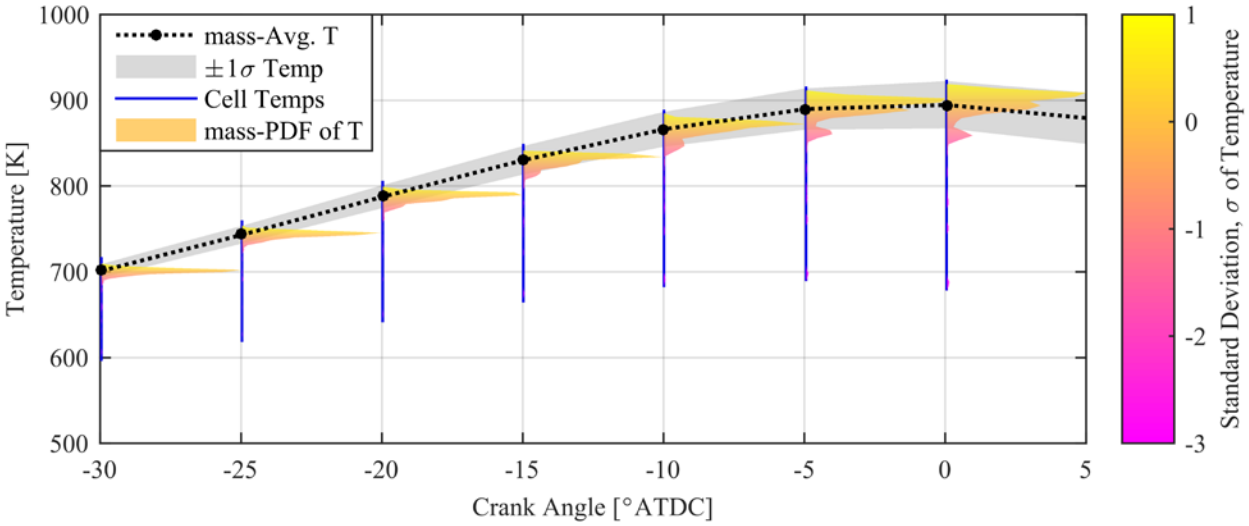

Figure 5.24: Temperature evolution as a function of crank angle for a representative HCCI case, showing the mass-averaged temperature (in black), the range of ±1σ at each index (grey region), and the mass-weighted PDF of temperature at each crank angle index colored by the multiple of σ, with the range of cell temperatures in blue

In order to assess the effect of the spray vaporization on the thermal stratification in the cylinder, non-reacting RCCI cases with various SOI timings were simulated, and the same analysis was performed. Figure 5.25 shows the development of the temperature distributions for two SOI cases, 50º SOI and -20º SOI. In general, the temperature distributions, standard deviation, and average bulk gas temperature are largely unaffected by the SOI timing, though in the -20º SOI case in Figure 5.25, the effect of the vaporization process can be clearly seen as the range of cell temperatures at -15º CA, which occurs during the injection event, extends downwards significantly due to the injection and subsequent vaporization of the cool fuel. Beyond this timing, after the end of injection, it is seen that this seems to have little effect on the temperature distributions, however. This result implies that the evaporative cooling induced by the direct-injected fuel has much less effect on the temperature distribution than the natural thermal stratification, even for a relatively large bore engine in this case.

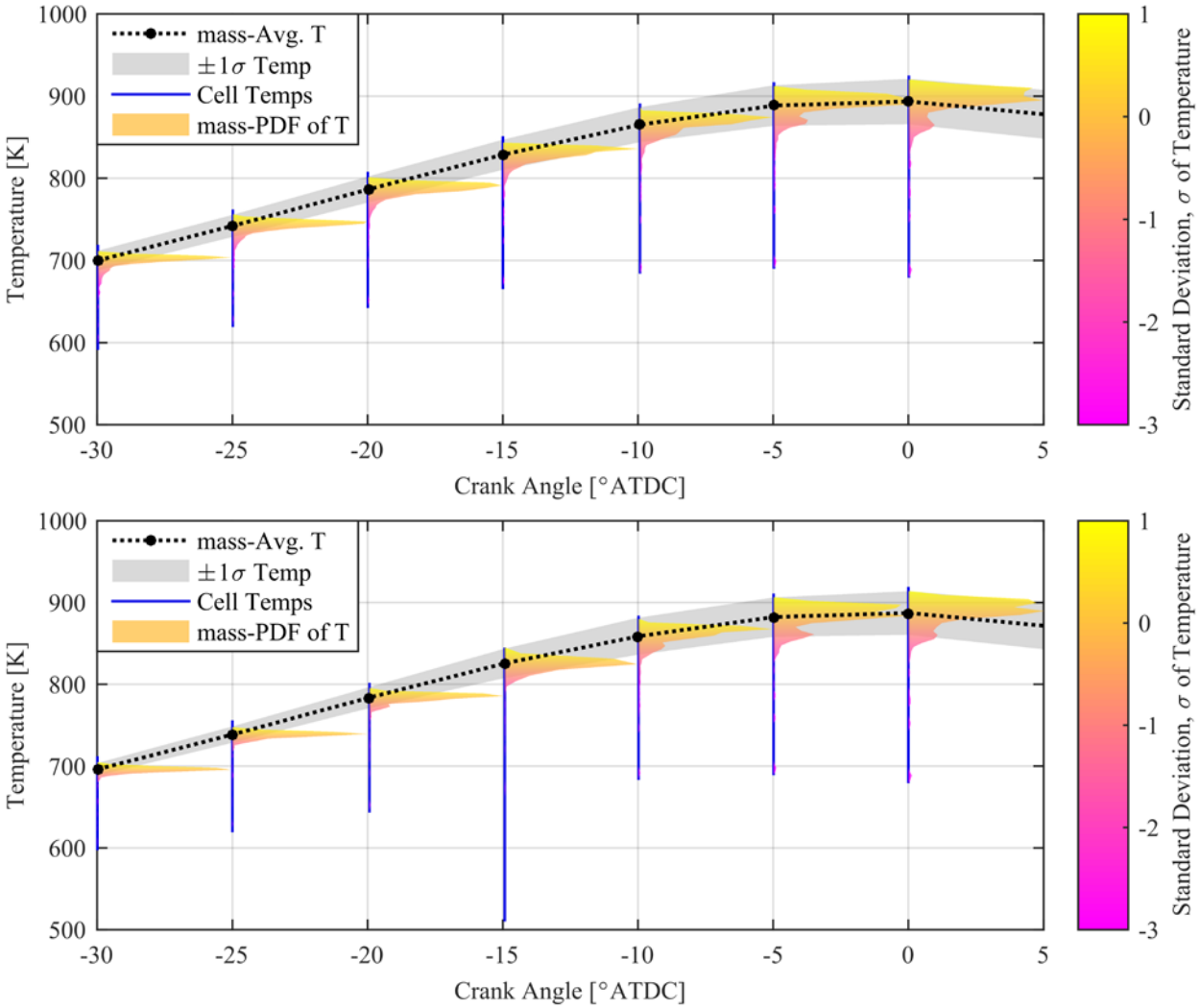

Figure 5.25: Temperature evolution as a function of crank angle for representative RCCI cases with SOI of -50° (top) and SOI of -20° (bottom), showing the mass-averaged temperature (in black), the range of ±1σ at each index (grey region), and the mass-weighted PDF of temperature at each crank angle index colored by the multiple of σ, with the range of cell temperatures in blue

The standard deviation of temperature parameter (σ_T), which is effectively a measure of the magnitude of thermal stratification, was plotted for various SOI timings as a function of crank angle for the non-reacting CFD simulations. Figure 5.26 shows the result of these simulations for the various timings shown in the legend. As can be seen in the plot, the SOI timing initially has an effect on the temperature distribution, but by around -10°CA and beyond, the effect of the SOI timing on the thermal stratification is largely absent.

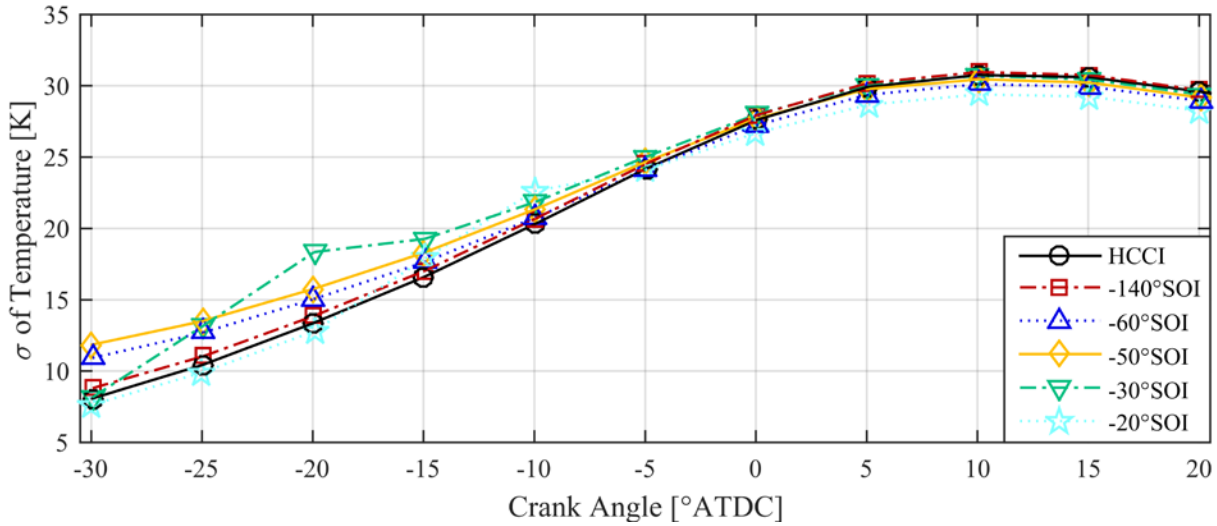

Figure 5.26: Standard deviation of temperature as a function of crank angle for various SOI timings with PRF fuels

This analysis led to -10°CA being chosen as the arbitrary crank angle at which to match the temperature profiles, with a σ_T of 21K. This crank angle was chosen because it was close to the start of combustion for the various cases tested in the validations shown here, and because as shown in Figure 5.26, the standard deviation at this crank angle was largely independent of SOI within the range of conditions tested in the experiments and CFD modeling for RCCI combustion.

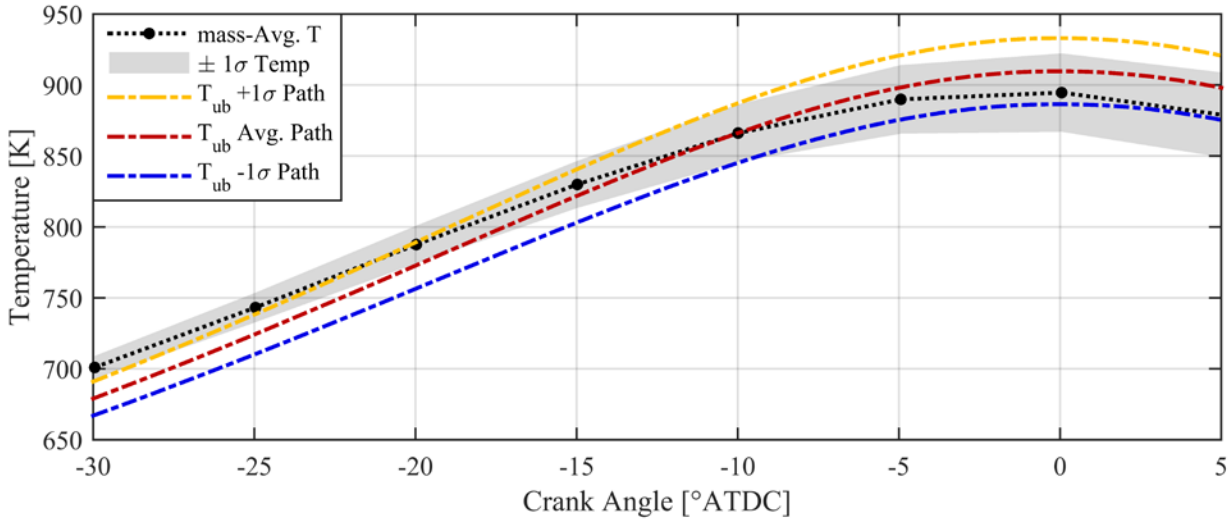

Figure 5.27: CFD predicted temperature (black) with ±1σ region (grey) as a function of crank angle. Also plotted are the polytropic average temperature path (red), +1σ path (yellow), and -1σ path (blue) as functions of crank angle

Using the effective polytropic coefficient method outlined in Section 5.2.2, the various thermal paths could be calculated for the non-reacting case to examine the agreement between the calculated thermal paths using just the polytropic coefficients, and the CFD predictions, which include a full heat transfer model. The result of this process is shown in Figure 5.27. Early in the compression stroke, heat is transferred from the relatively hot cylinder walls and piston surfaces into the combustion chamber. After the chamber gas exceeds the temperature of the walls and piston surfaces, heat is transferred in the opposite direction back into the walls and piston surfaces. This heat transfer process leads to the discrepancies seen between the polytropic processes defined by the effective γ values, and the CFD predicted temperature paths. The polytropic processes match the in-cylinder temperatures at the IVC condition, and at the arbitrary crank angle defined (in this case -10^{o}CA). As would be expected, it was found to be most important to match the temperature distribution near the start of combustion in order to accurately predict the autoigntion locations of the various fuel mixture zones. It is clear from Figure 5.27, however, that a better methodology for determining the various thermal paths in the cylinder is needed. A multizonal temperature approach, such as those employed by Fiveland et al. [22], or Komninos et al. [102], may provide an improved temperature prediction methodology, and could help the predictive ability of the FSA method.

The ignition locations were determined by linearly interpolating a large 5-D matrix of ignition delay values simulated with the Cantera package in MATLAB. The 5-dimensions of the matrix corresponded to temperature, pressure, EGR rate, equivalence ratio, and the mass ratio of fuel one to total fuel. For these validation cases, fuel 1 was isooctane, and fuel 2 was n-heptane. The same reduced chemical mechanism used in the 3-D CFD simulations shown in Section 5.3.1 (Wang et al. [99]) was used in this section to simulate the ignition delays of the fuels.

Another consideration that has to be made is that the FSA method predicts a static distribution that is essentially the fuel distribution at the start of combustion. In reality, the fuel distribution in the CFD simulations, and on a real engine, is constantly evolving due to the effects of turbulent mixing and swirl effects. The evolution of the fuel distribution as a function of crank angle for two different SOI timings in RCCI CFD simulations can be clearly seen in Figure 5.28.

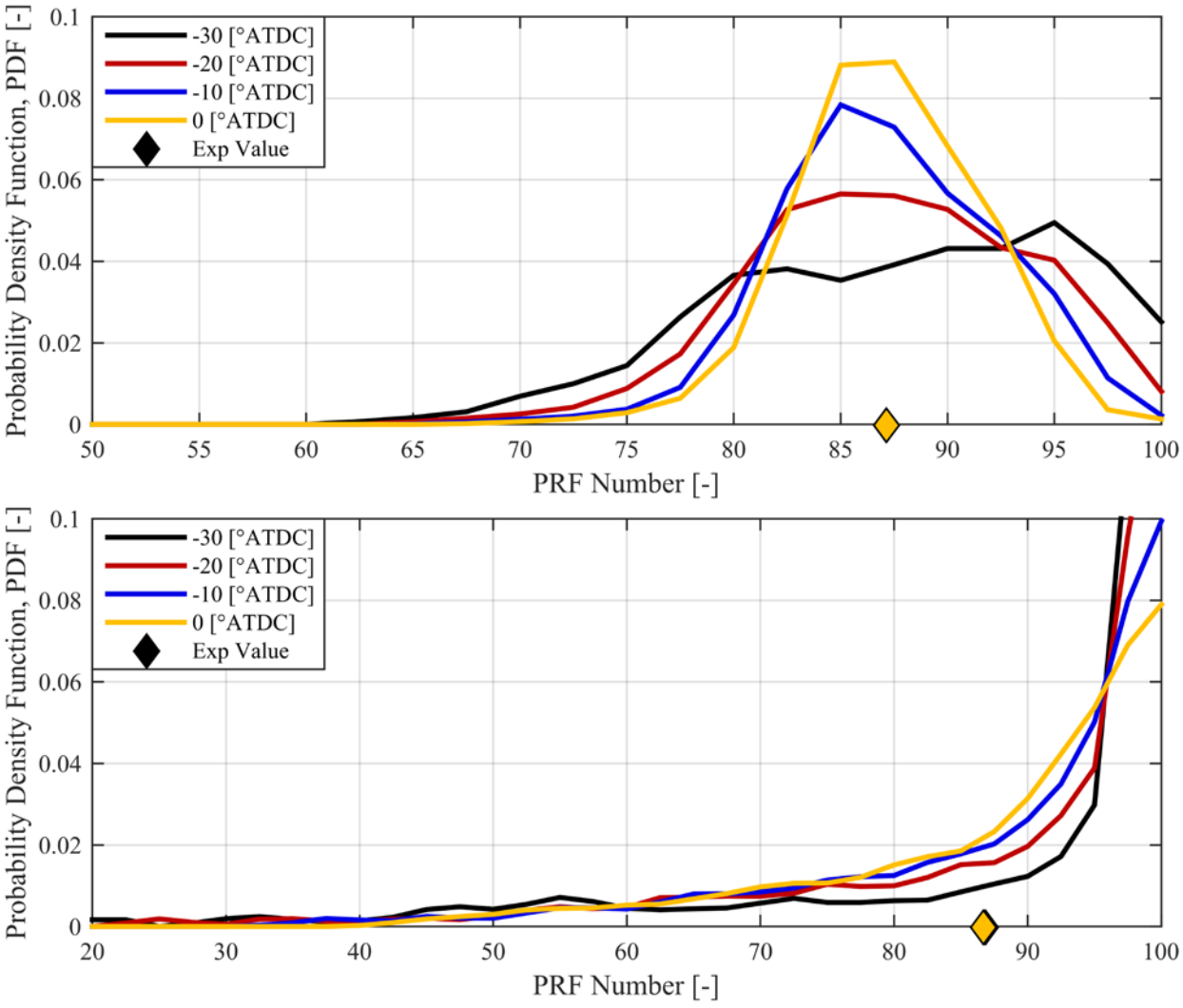

Figure 5.28: PDFs of PRF number for two SOI cases, -140° SOI (top), and -50° SOI (bottom), for various crank angles, showing the mixing of the fuel over time

To compare the FSA result and the CFD predictions, a crank angle needs to be defined at which to determine the CFD predicted fuel distribution. Since the FSA method predicts the fuel

distribution at the start of combustion, a crank angle near the beginning of the combustion process was chosen for each individual case. The crank angle chosen was the crank angle closest to the approximate start of combustion that had been outputted for post-processing.

Because the FSA method cannot account for unburned fuel, and because of differences between the actual fuel chemistry and the assumed sequential autoignition, i.e., energy released due to late cycle CO oxidation, the maximum value of the cumulative density function determined from the FSA method was always less than 1. The missing mass could be accounted for in a number of ways, including assuming that the mass belonged to the 100% premixed fuel zone, as this zone is the least likely to ignite, and most likely to be trapped in the crevice regions. The missing mass could also be assumed to be equally likely to belong to any possible zone. This involves the normalization of the CDF by its maximum value. Figure 5.29 shows the non-normalized result of the FSA method compared to a non-reacting CFD simulation for an RCCI case with a -140º SOI. The FSA method only accounts for ~96% of the total fuel mass. Because the CDF does not end at 1.0, the expected value cannot be compared directly to the actual value.

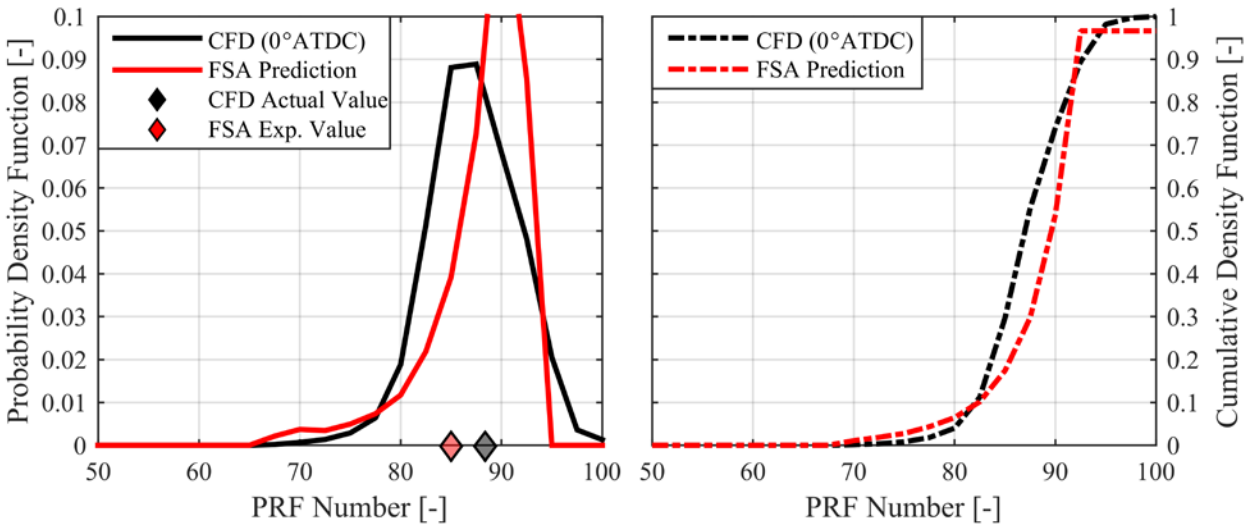

Figure 5.29: Non-reacting CFD at 0ºCA for -140º case (black lines) compared to non-normalized FSA method result (red lines), with actual global PRF number from the CFD (black diamond), and FSA predicted expected value (red diamond). PDF vs. PRF number on left (solid lines), CDF vs. PRF number on right (dashed lines)

Figure 5.30 shows the normalized FSA result compared to the CFD predicted fuel distribution. Here the expected value matches the actual value, and all the mass is accounted for by the analysis.

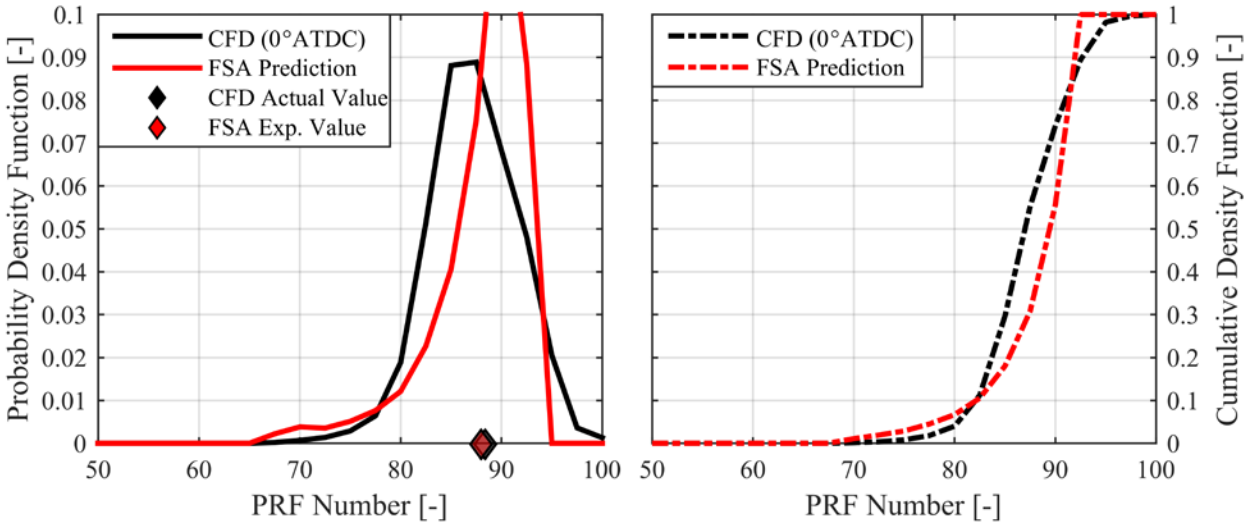

Figure 5.30: Non-reacting CFD at 0ºCA for -140º case (black lines) compared to normalized FSA method result (red lines), with actual global PRF number from the CFD (black diamond), and FSA predicted expected value (red diamond). PDF vs. PRF number on left (solid lines), CDF vs. PRF number on right (dashed lines)

Figure 5.31 shows the non-normalized FSA method result compared to the non-reacting CFD fuel distribution for an RCCI case with a -30ºSOI. Here the FSA method is only able to account for about ~65% of the total fuel mass, though the general shape of the distribution, except for the very large quantity of unmixed PRF100, is well captured. For this late injection timing case, the FSA method assumptions seem to break down. Normalizing the distribution, as seen in Figure 5.32, does not improve the FSA prediction, and the expected value is not able to recover the global averaged value of PRF.

In this work, all the CDFs shown were normalized by their maximum value. The approach taken for the validation cases was: normalize the FSA predicted distribution and adjust the IVC temperature up or down to recover the global averaged premixed mass fraction and equivalence ratio. Very late injection timing cases were never able to recover the global average values, and

therefore are assumed to have violated one or more of the inherent assumptions of the FSA method, namely, that there is no flame propagation, or the instantaneous vaporization at EOI stipulation.

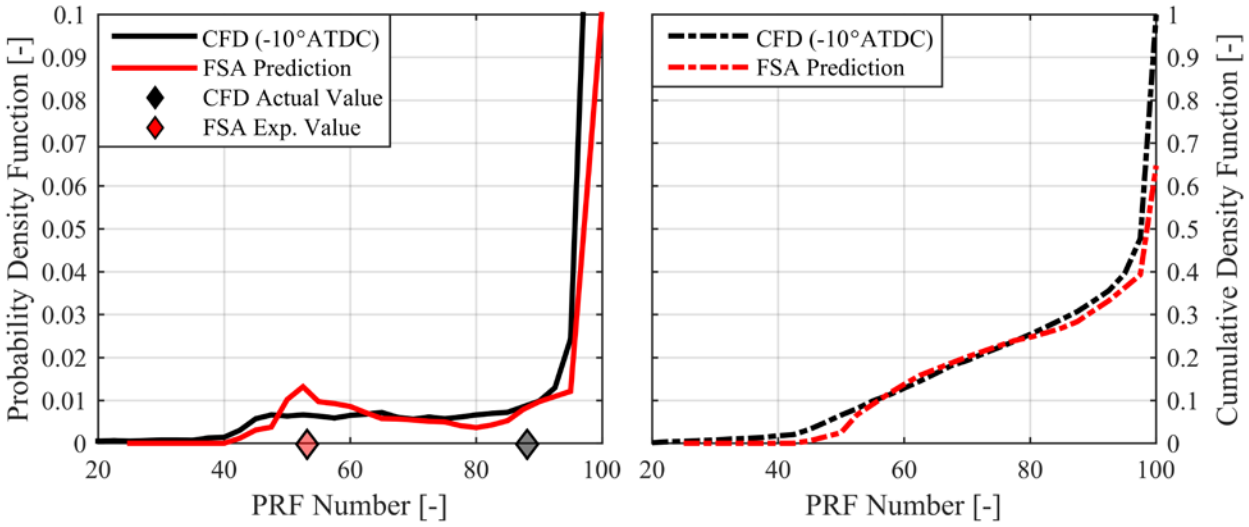

Figure 5.31: Non-reacting CFD at 0ºCA for -30º case (black lines) compared to non-normalized FSA method result (red lines), with actual global PRF number from the CFD (black diamond), and FSA predicted expected value (red diamond). PDF vs. PRF number on left (solid lines), CDF vs. PRF number on right (dashed lines)

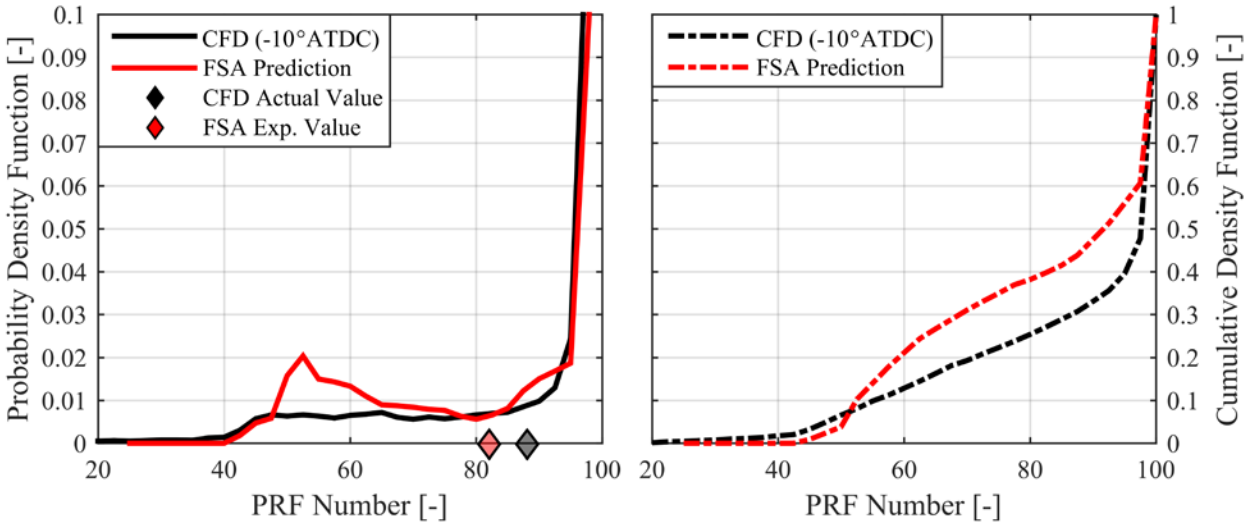

Figure 5.32: Non-reacting CFD at 0ºCA for -30º case (black lines) compared to normalized FSA method result (red lines), with actual global PRF number from the CFD (black diamond), and FSA predicted expected value (red diamond). PDF vs. PRF number on left (solid lines), CDF vs. PRF number on right (dashed lines)

5.3.2.1 Constant PRF Cases with Varying Injection Timing

The validated PRF RCCI cases with fixed global PRF shown in Section 5.3.1.3, as well as an HCCI case with a similar global PRF number from Section 5.3.1.2 were used as the preliminary validation cases for the FSA analysis. The initial conditions of the reacting and non-reacting CFD simulations are shown in Table 5.14, reproduced from the respective section.

Table 5.14: Initial conditions of constant PRF CFD simulations ($\varphi = 0.30$)

SOI [°ATDC]	Fuel Mass [mg/cyc]	Global PRF [-]	P_{IVC} [kPa]	T_{IVC} [K]
HCCI	58.03	88.6	125.7	360
-140	58.36	88.4	127.3	360
-90	58.55	88.0	127.0	358
-60	58.46	88.1	126.4	355
-55	58.27	88.4	126.1	358
-50	58.48	88.0	126.3	355
-45	58.27	88.2	126.3	358
-40	58.60	88.0	126.6	358
-35	58.46	88.1	127.3	358
-30	58.33	88.2	128.0	358
-25	58.32	88.1	127.9	355
-20	58.49	88.1	127.2	350

Figure 5.33 shows the reacting CFD pressure and heat release traces for the fixed global PRF cases shown in the table at the various injection timings shown in the legend. The CFD pressure and MFB traces served as an input for the FSA method to predict the fuel distribution. The non-reacting CFD simulations served as the validation of the predicted fuel distributions. Figure 5.34 to Figure 5.37 show the FSA method results compared to the CFD-predicted fuel distributions for the various SOI timings, and the one HCCI case presented here. In general, very good agreement is seen between the CFD and FSA method results between SOI timings of -140° and about -35°, at which point the predictions begin to deviate significantly, likely due to the violation of one or more of

the inherent assumptions of the methodology. The HCCI case with no fuel stratification shows reasonable agreement between the FSA method and CFD predictions, though despite the minor amount of fuel stratification predicted by the CFD result for the -140°SOI case, the reacting CFD pressure and heat release for the HCCI and -140°SOI case are nearly identical. The result of this validation shows that the FSA method is able to provide relatively good agreement between the predicted and actual fuel distributions from CFD simulations within the range of injection timings of interest in RCCI combustion (-140° to about -35°ATDC).

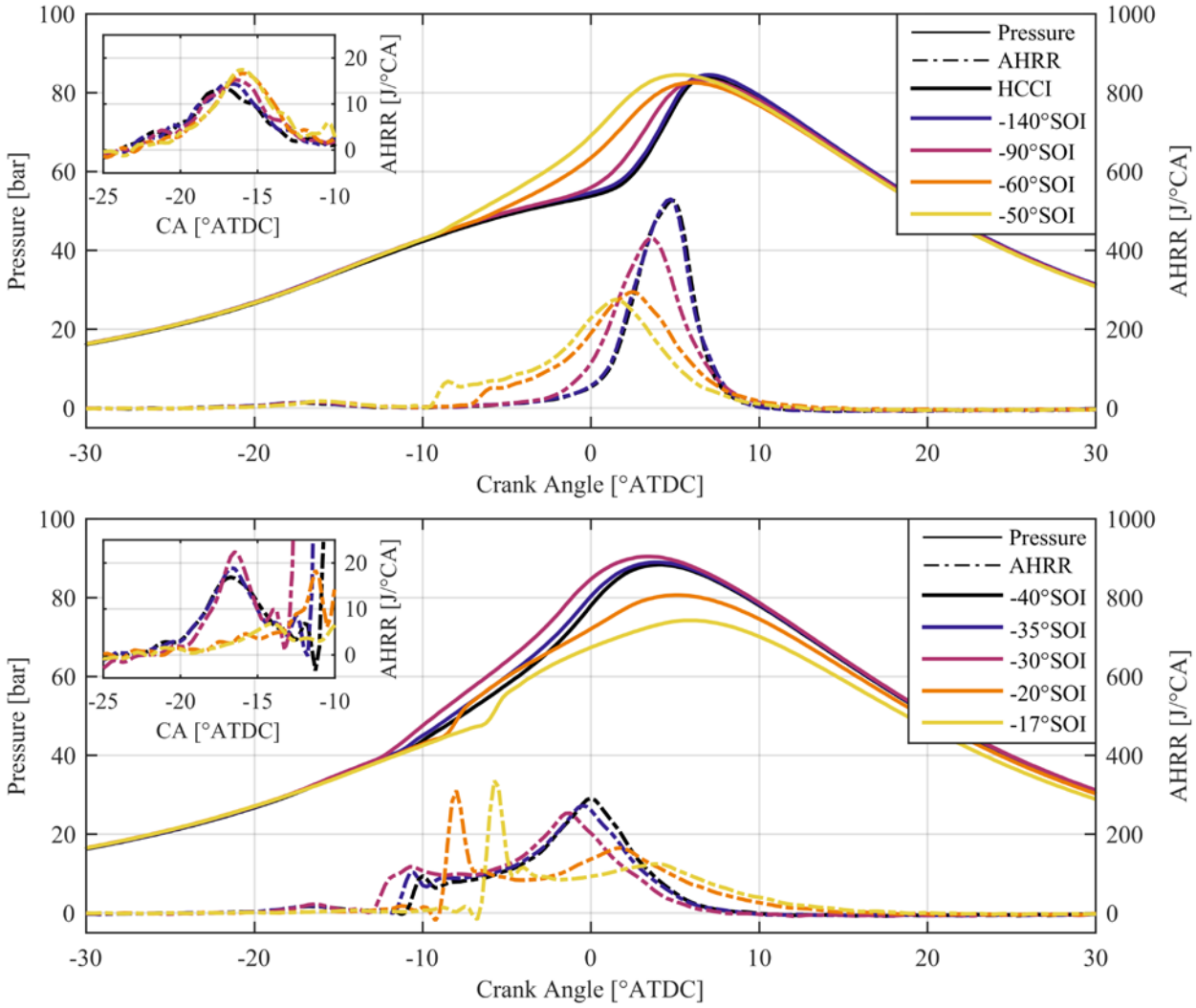

Figure 5.33: Reacting CFD pressure and HRR for fixed global PRF RCCI cases at various SOI timings (φ = 0.30, T_{IVC} = 350-360K)

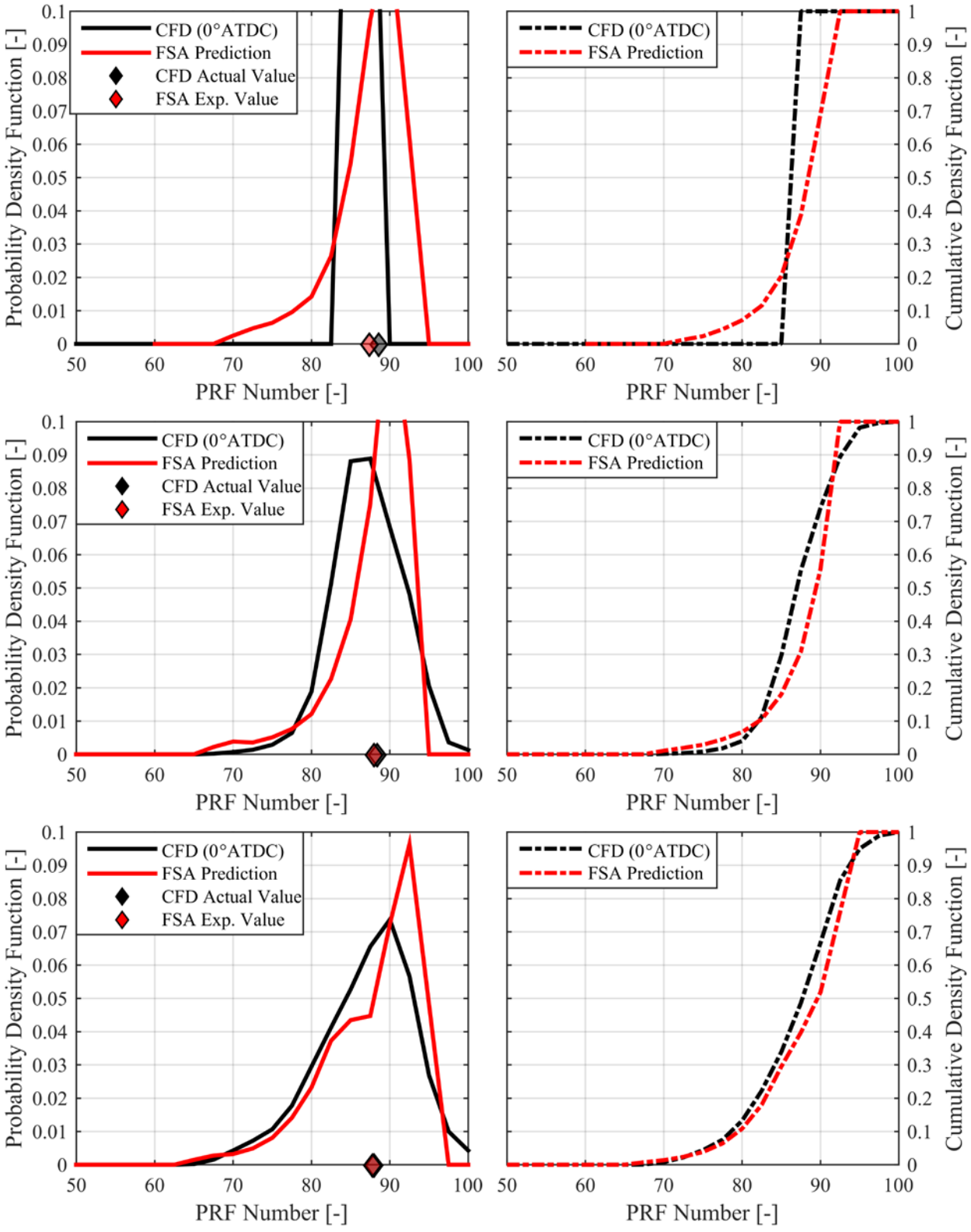

Figure 5.34: Non-reacting CFD at specified CA (black lines) compared to normalized FSA method result (red lines), with actual global PRF number from CFD (black diamond), and FSA predicted expected value (red diamond). PDF vs. PRF number on left (solid lines), CDF vs. PRF number on right (dashed lines), for HCCI case (top), -140°SOI (middle), and -90°SOI (bottom)

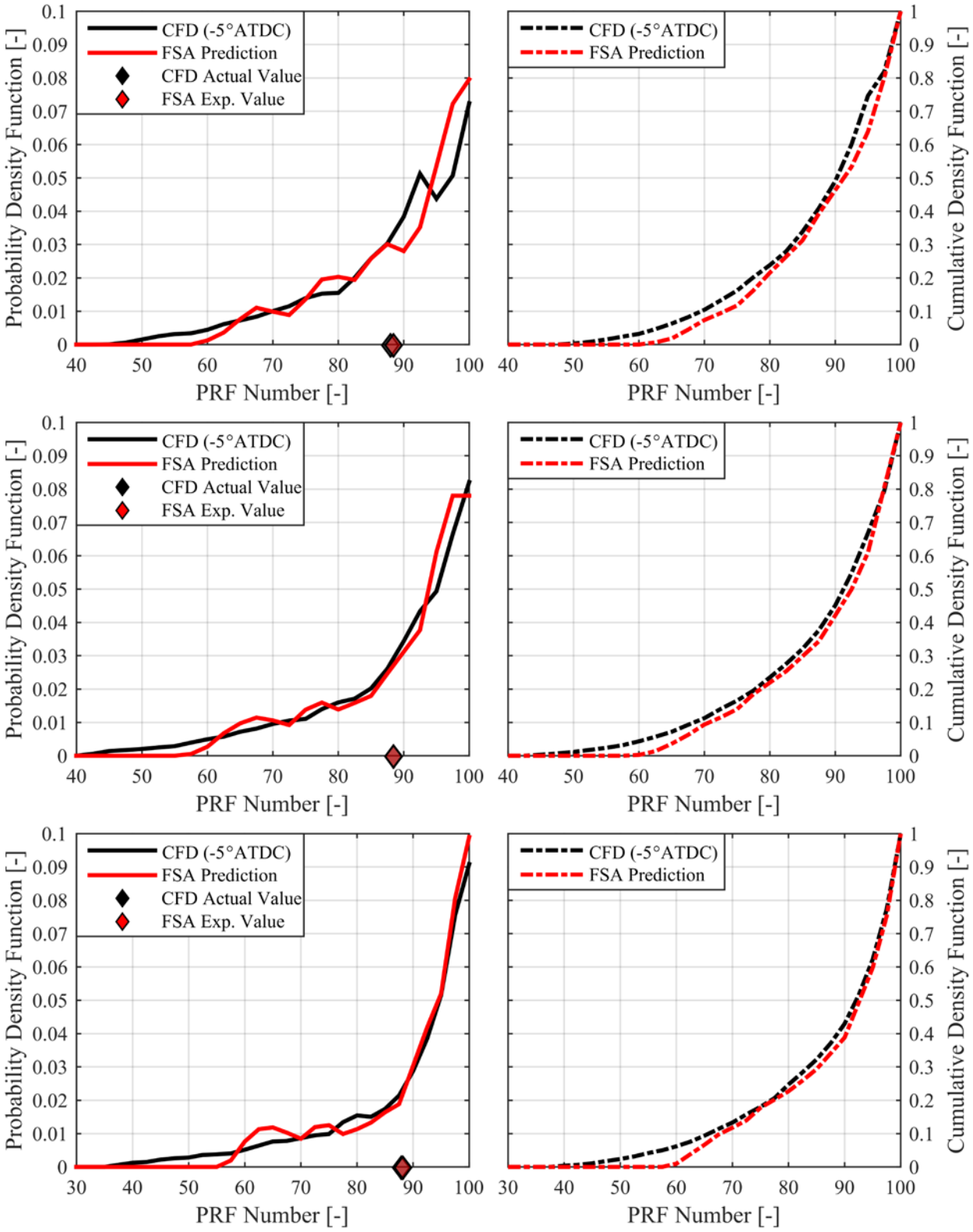

Figure 5.35: Non-reacting CFD at specified CA (black lines) compared to normalized FSA method result (red lines), with actual global PRF number from CFD (black diamond), and FSA predicted expected value (red diamond). PDF vs. PRF number on left (solid lines), CDF vs. PRF number on right (dashed lines), for -60°SOI case (top), -55°SOI (middle), and -50°SOI (bottom)

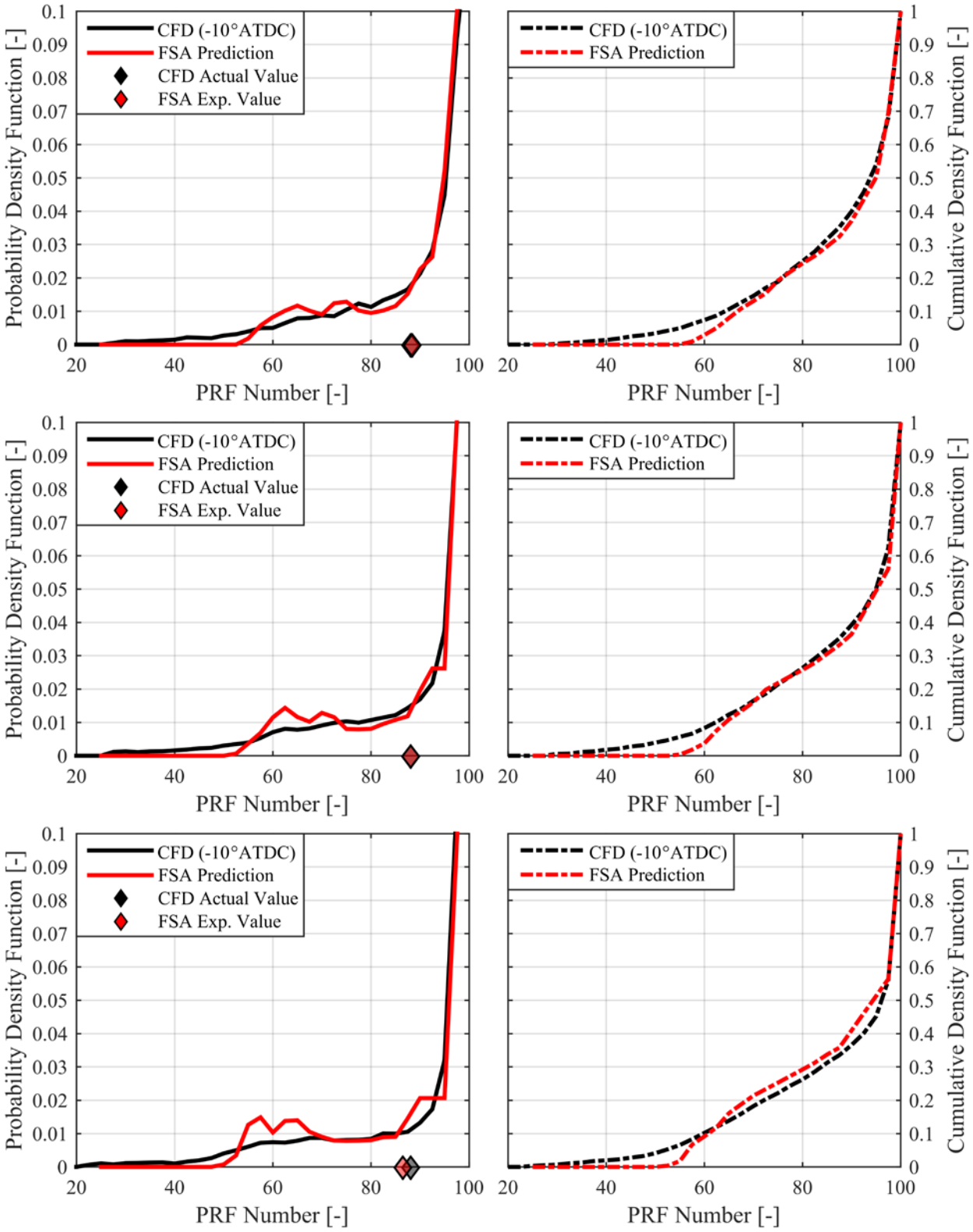

Figure 5.36: Non-reacting CFD at specified CA (black lines) compared to normalized FSA method result (red lines), with actual global PRF number from CFD (black diamond), and FSA predicted expected value (red diamond). PDF vs. PRF number on left (solid lines), CDF vs. PRF number on right (dashed lines), for -45°SOI case (top), -40°SOI (middle), and -35°SOI (bottom)

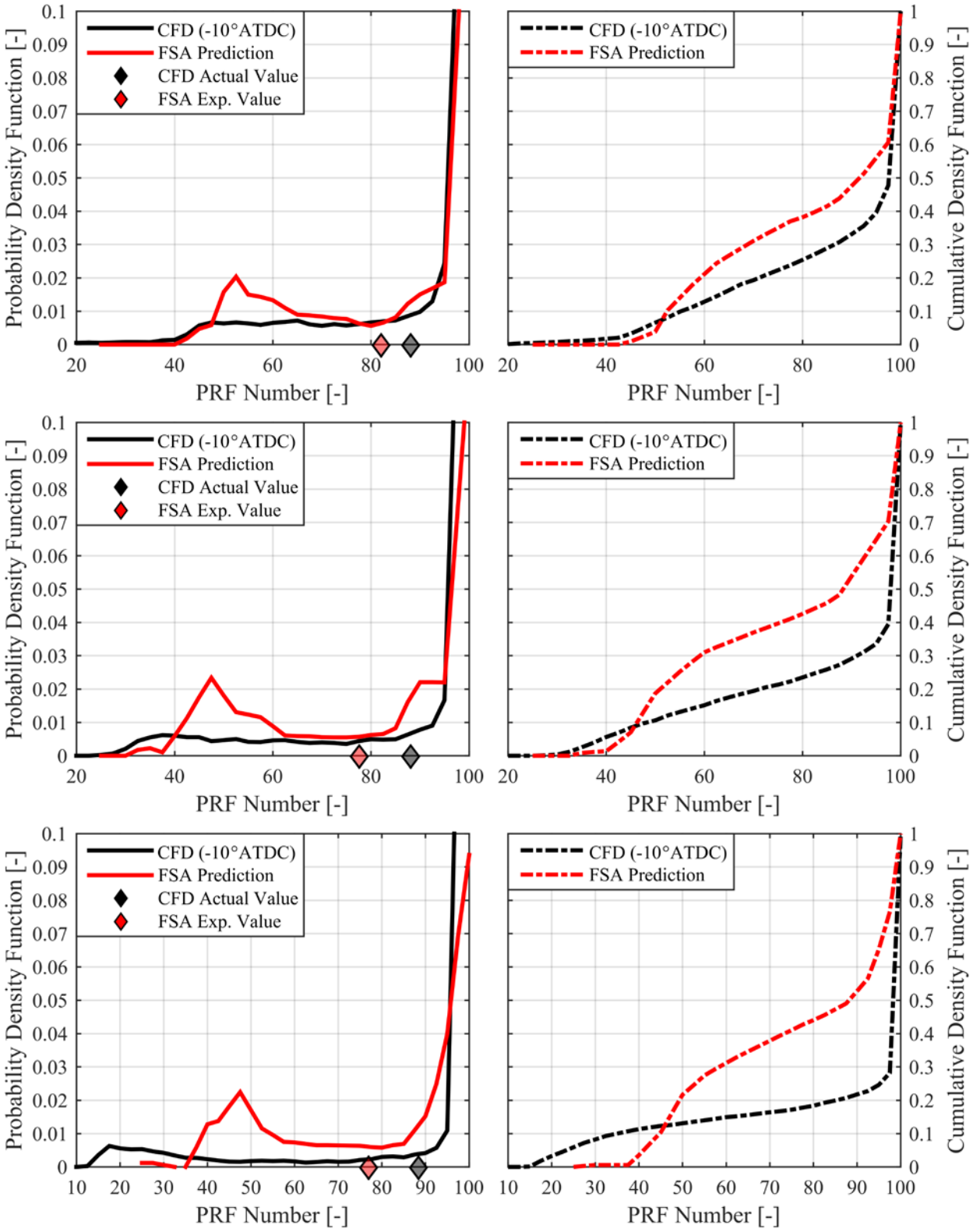

Figure 5.37: Non-reacting CFD at specified CA (black lines) compared to normalized FSA method result (red lines), with actual global PRF number from CFD (black diamond), and FSA predicted expected value (red diamond). PDF vs. PRF number on left (solid lines), CDF vs. PRF number on right (dashed lines), for -30°SOI case (top), -25°SOI (middle), and -20°SOI (bottom)

5.3.2.2 Constant Combustion Phasing Cases with Varying Injection Timing

To further validate the FSA method, the validated CFD cases with fixed combustion phasing, and varying global PRF number from Section 5.3.1.3 were compared to the FSA method predicted fuel distributions. The initial conditions of the reacting and non-reacting CFD simulations are shown in Table 5.15, reproduced from Section 5.3.1.3.

Table 5.15: Initial conditions of constant CA50 CFD simulations (φ = 0.30)

SOI [°ATDC]	Fuel Mass [mg/cyc]	Global PRF [-]	P_{IVC} [kPa]	T_{IVC} [K]
-140	58.16	85.9	127.8	363
-90	58.30	85.7	127.3	361
-60	58.24	87.0	126.3	357
-50	58.41	88.2	126.3	357
-45	58.22	88.7	126.1	355
-35	58.33	89.8	126.5	353
-30	58.08	91.0	126.8	353
-25	58.36	91.1	127.5	353
-20	58.09	76.9	127.2	345

Figure 5.38 shows the reacting CFD pressure and heat release traces for the fixed combustion phasing cases shown in the table at the injection timings shown in the legend. The CFD pressure and MFB traces again served as an input for the FSA method to predict the fuel distribution, while the non-reacting CFD simulations served as the validation of the predicted fuel distributions. Figure 5.39 to Figure 5.41 show the FSA method results compared to the CFD-predicted fuel distributions for the various SOI timings. Similar to the constant PRF cases shown previously, the constant combustion phasing cases presented here showed very good agreement between the FSA predicted fuel distribution, and the fuel distribution from the non-reacting CFD simulations between about -140°SOI and -35°SOI, or the range of interest in RCCI combustion. For injection timings later than -35°, the FSA predictions deviated significantly from the fuel distributions seen

in the CFD results. This transition between good predictions to poor predictions clearly indicates a transition region where the assumptions of the FSA method are no longer applicable. This transition corresponds to the transition in trend between injection timing and combustion phasing, i.e., retarding injection between -140^{o} and about -35^{o} results in an advanced combustion phasing for a fixed global PRF, while retarding injection beyond -35^{o} resulted in a retarded combustion phasing at these operating conditions, as discussed in Chapter 3. This transition could be a result of flame propagation, or a result of entering a mixing limited combustion regime.

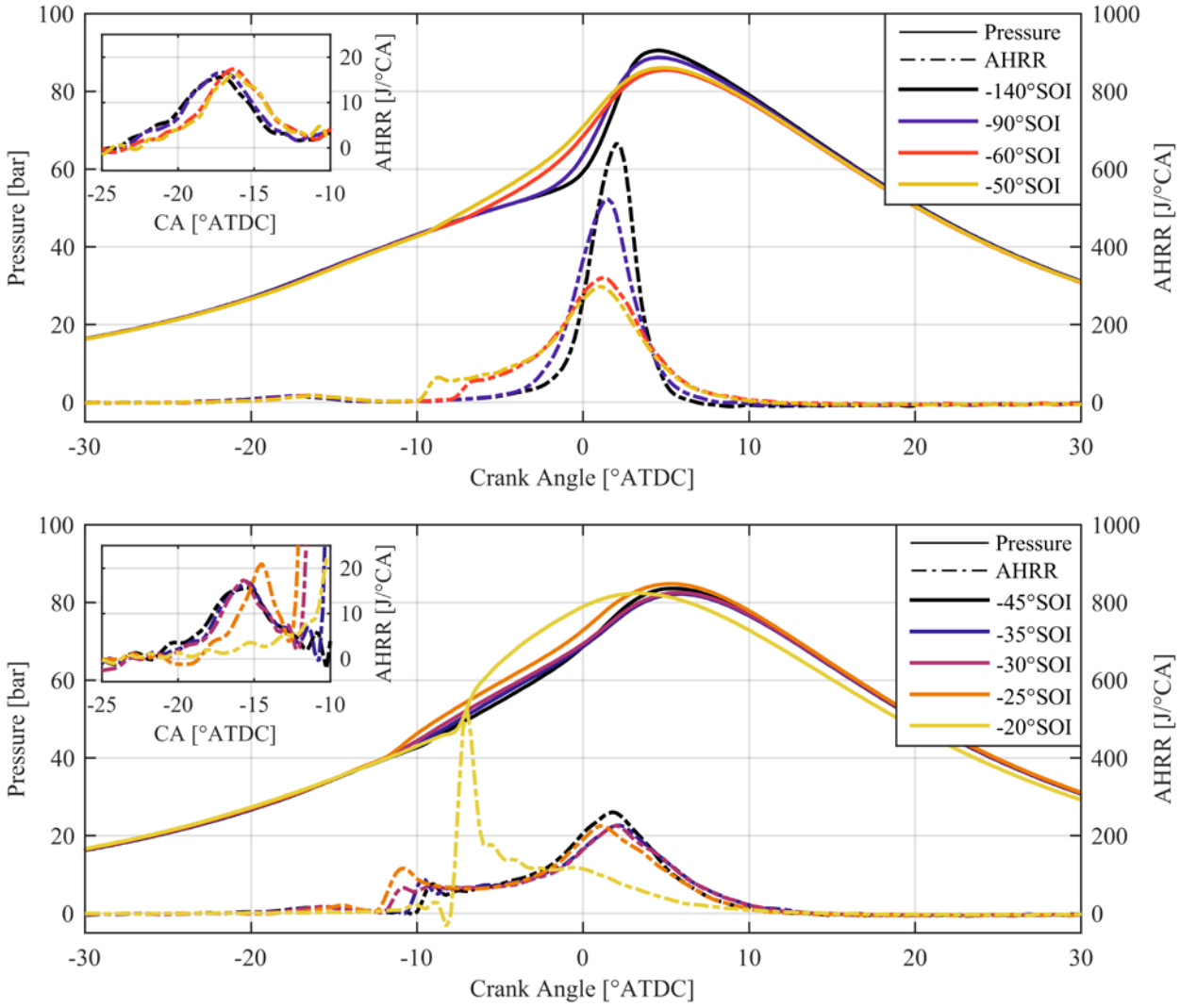

Figure 5.38: Reacting CFD pressure and HRR for fixed combustion phasing (CA50 = 0.75±0.25) RCCI cases at various SOI timings (φ = 0.30, T_{IVC} = 345-363K)

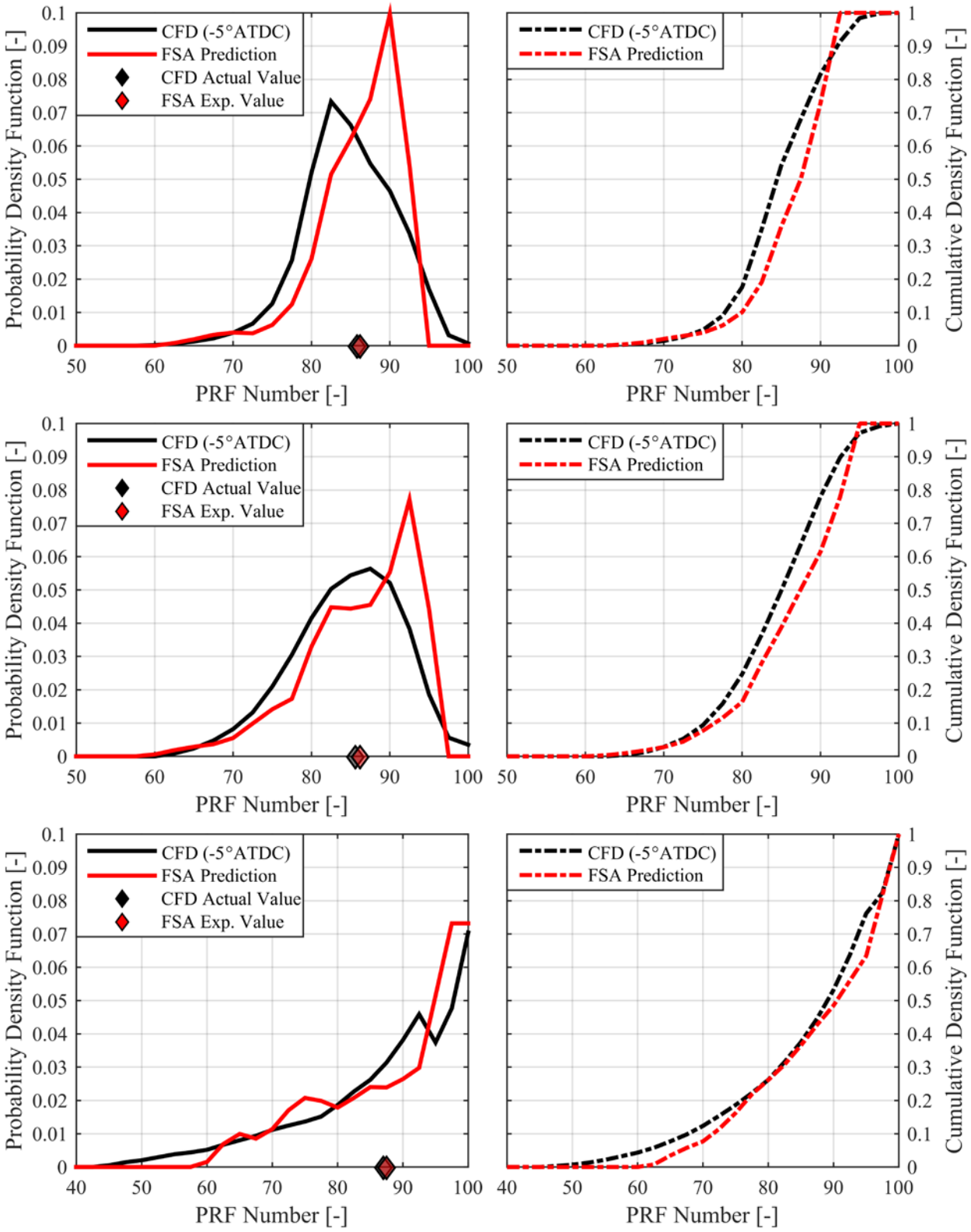

Figure 5.39: Non-reacting CFD at specified CA (black lines) compared to normalized FSA method result (red lines), with actual global PRF number from CFD (black diamond), and FSA predicted expected value (red diamond). PDF vs. PRF number on left (solid lines), CDF vs. PRF number on right (dashed lines), for -140°SOI case (top), -90°SOI (middle), and -60°SOI (bottom)

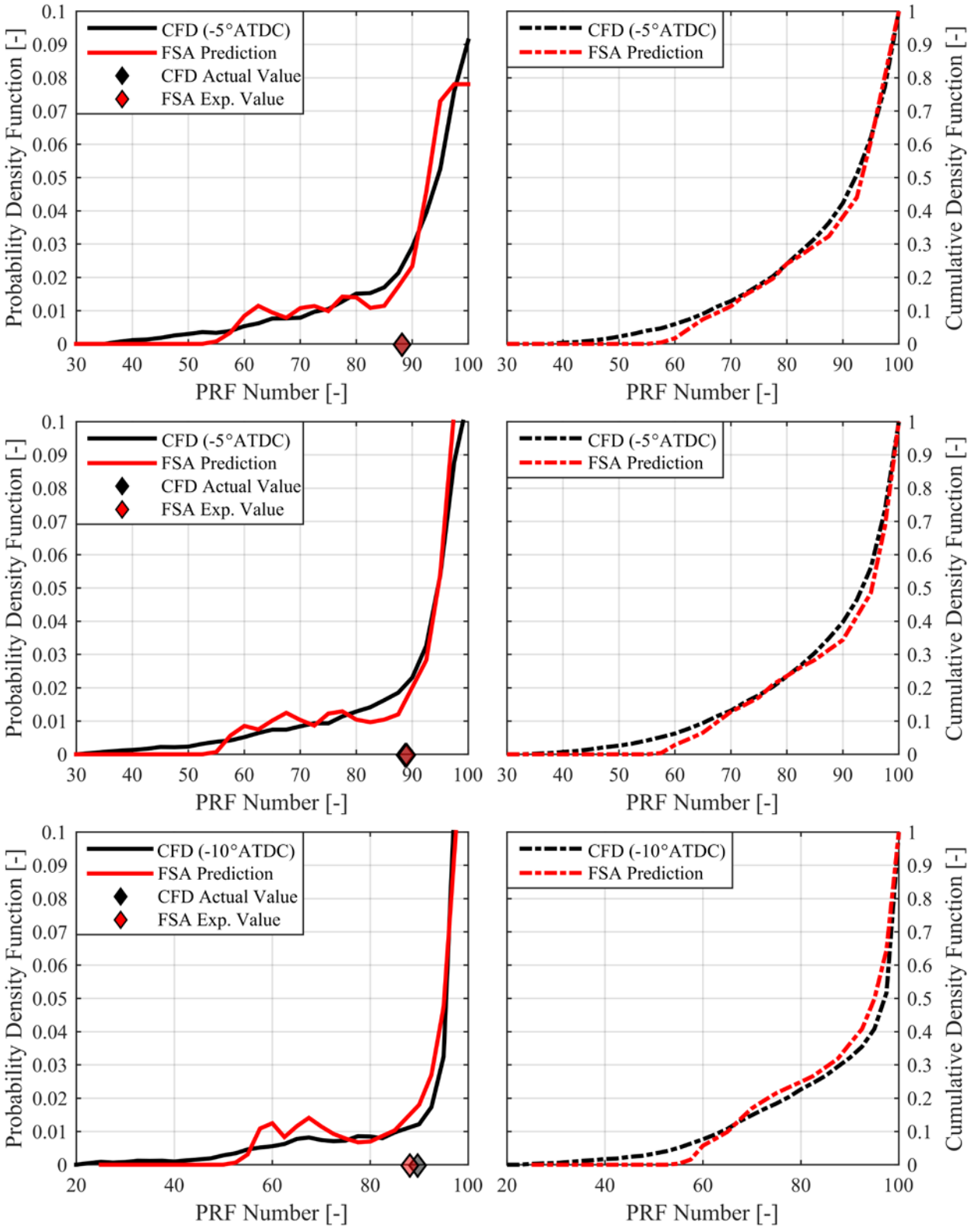

Figure 5.40: Non-reacting CFD at specified CA (black lines) compared to normalized FSA method result (red lines), with actual global PRF number from CFD (black diamond), and FSA predicted expected value (red diamond). PDF vs. PRF number on left (solid lines), CDF vs. PRF number on right (dashed lines), for -50°SOI case (top), -45°SOI (middle), and -35°SOI (bottom)

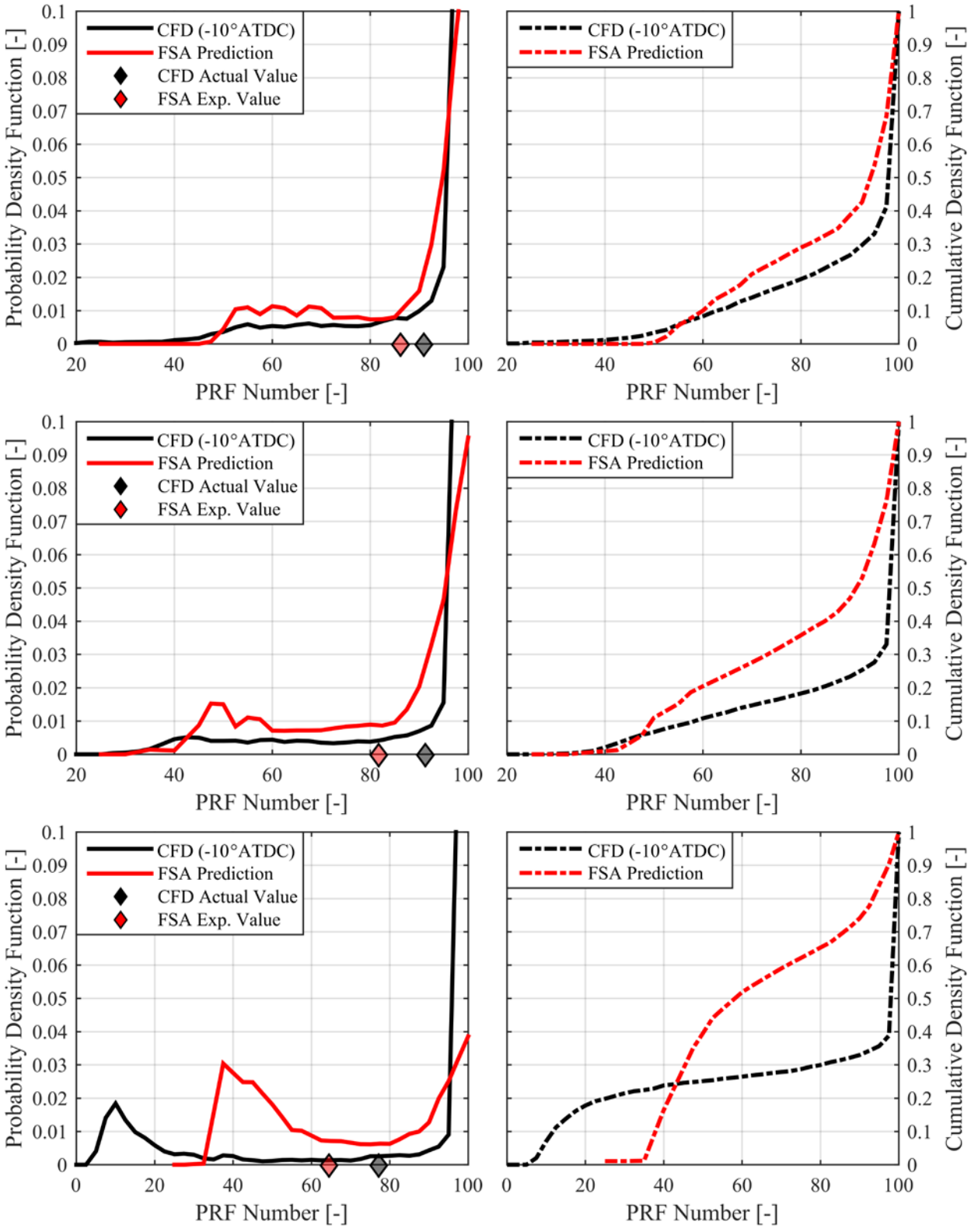

Figure 5.41: Non-reacting CFD at specified CA (black lines) compared to normalized FSA method result (red lines), with actual global PRF number from CFD (black diamond), and FSA predicted expected value (red diamond). PDF vs. PRF number on left (solid lines), CDF vs. PRF number on right (dashed lines), for -30°SOI case (top), -25°SOI (middle), and -20°SOI (bottom)

6 *APPLICATIONS OF THE FSA METHOD*

The validations presented in Chapter 5 showed good agreement between the FSA predicted fuel stratification and fuel distributions generated with non-reacting CFD simulations within the range of SOI timings of interest to RCCI combustion. With this agreement established, various applications of the FSA method could be tested. The following section explores a number of applications of the FSA method, including predicting fuel stratification requirements for favorable heat release rates, varying premixed and DI fuel chemistry, and alternative premixed fuels.

6.1 Fuel Stratification Requirements for Favorable HRRs

One application of the FSA method is to generate thermodynamically favorable heat release rates, and predict the required fuel stratification to achieve such a heat release. The heat release rate can be constrained by some operational limitations such as maximum PPRR, maximum peak pressure, or can simply be the optimized heat release for gross efficiency. The heat release could have some predefined shape defined by a mathematical function such as a Gaussian distribution, or Wiebe function, or some arbitrary profile. The FSA method would then predict the necessary fuel distribution, based on the initial conditions and chosen fuel chemistry.

6.1.1 Calculating the Pressure and HRR Trace from a MFB Profile

In order to study the effects of heat release shape on the stratification requirements of RCCI combustion, the pressure trace which would produce such a heat release shape must be determined based on some initial conditions. The HRR is a quantity that is calculated from the pressure trace via a simple 1st law energy balance, as described in Section 3.6.3, and the MFB profile is the heat release normalized by its maximum value (Q_{ad}). Given some arbitrary MFB profile, the adiabatic

heat release (HR_{ad}) can be calculated according to Equations (6.1) and (6.2), where η_{comb} is the combustion efficiency, Q_{fuel} is the total fuel energy, and Q_{HT} is the cumulative energy lost to heat transfer. The heat release rate can then be calculated by taking the derivative of the heat release with respect to crank angle as shown in Equation (6.3). HR, HRR, and MFB are functions of crank angle, while Q_{ad}, Q_{fuel}, Q_{HT}, and η_{comb} are scalar values.

$$Q_{ad} = \eta_{comb} * Q_{fuel} - Q_{HT} \tag{6.1}$$

$$HR_{ad} = Q_{ad} * MFB \tag{6.2}$$

$$HRR_{ad} = \frac{dHR_{ad}}{dCA} \tag{6.3}$$

The adiabatic heat release rate, as defined in Section 3.6.3, is reproduced in Equation (6.4), where γ is the ratio of specific heats of the mixture, P is the cylinder pressure, V is the cylinder volume, and θ is the crank angle.

$$HRR_{ad} = \frac{\gamma}{\gamma - 1} P \frac{dV}{d\theta} + \frac{1}{\gamma - 1} V \frac{dP}{d\theta} \tag{6.4}$$

Solving Equation (6.4) for the dP term numerically yields Equation (6.5), where 'i' denotes the current crank angle index. Assuming some initial IVC pressure (P_{IVC}), the rest of the pressure trace as a function of crank angle can be solved by using Equation (6.6).

$$dP_i = \frac{HRR_{ad_i}(\gamma_i - 1) - \gamma_i P_i \frac{dV}{d\theta_i}}{V_i} * d\theta_i \tag{6.5}$$

$$P_{i+1} = P_i + dP_i \tag{6.6}$$

Assuming some total fuel energy input, this process must be solved iteratively by solving for the heat transfer, which is a function of the cylinder temperature and pressure. In this work, the instantaneous γ value was also a function of temperature and global equivalence ratio, the expression for which is described in Section 3.6.4. The heat transfer model used for this analysis was developed by Chang et al. [63] for HCCI combustion. The correlation was based on the widely used Woschni [103] formulation, with several modifications in order to better approximate the measured heat transfer in HCCI operation. The main difference between Chang's correlation and Woschni's was a significant reduction in the combustion induced velocity term (C_2), as the steep increase in heat transfer due to combustion was not observed under HCCI conditions.

Due to the similar nature of the combustion processes in HCCI and RCCI combustion, Chang's correlation was chosen as a better representation of the bulk heat transfer characteristics than the original Woschni correlation. Equation (6.7) and (6.8) show the calculation of the heat transfer coefficient based on Chang's model, where L is the instantaneous combustion chamber height, P(t) is the instantaneous cylinder pressure, T(t) is the instantaneous bulk gas temperature, $\overline{S}_p$ is the mean piston speed, V_d is the displacement volume, T_r, P_r, and V_r are the reduced temperature, pressure, and volume respectively, and $P_{motored}$ is the instantaneous non-firing pressure.

$$h(t) = \alpha_{scaling} * L(t)^{-0.2} * P(t)^{0.8} * T(t)^{-0.73} * v_{tuned}(t)^{0.8} \tag{6.7}$$

$$v_{tuned}(t) = C_1 \bar{S}_p + \frac{C_2}{6}\frac{V_d T_r}{P_r V_r}(P - P_{motored}) \tag{6.8}$$

Equation (6.9) shows the calculation of the cumulative heat transfer, where A_s is the total instantaneous surface area of the combustion chamber, and T_{wall} is the instantaneous wall temperature (assumed constant and equal to 500K). Table 6.1 lists the coefficients used in the heat transfer calculations for this work.

$$Q_{HT} = \int_{t_{IVC}}^{t_{EVO}} h(t) * A_s * (T(t) - T_{wall}) dt \tag{6.9}$$

Table 6.1: Heat transfer model constants

Constant	Value	Notes
C_1	2.28	
C_2	0	During compression
	3.24e-3	During combustion
$\alpha_{scaling}$	7.0	Tuned to match experiments

The scaling parameter ($\alpha_{scaling}$) was adjusted empirically until the calculated pressure and heat release traces were approximately equal to the experimental pressure and heat release for the cases shown in Figure 6.1. The operating conditions for these experimental data points can be seen in Table 6.2, reproduced from Section 3.8. The individual experimental MFB profiles were calculated, and used to recreate the pressure and heat release traces.

Table 6.2: Operating conditions of heat transfer scaling cases

Engine speed [rev/min]	1300
Fuel Energy, (Q_{fuel}) [J/cyc]	2590 (±20)
Nominal Load ($IMEP_n$) [bar]	4.5-4.75
EGR [%]	0
Intake Temperature [^{o}C]	40 (±2.2)
PFI Fuel	iso-octane (PRF100)
PFI Timing [^{o}CA ATDC]	-320
DI Fuel	n-heptane (PRF0)
DI Timing, (SOI) [^{o}CA ATDC]	HCCI, -140^o, -50^o, -40^o
Rail Pressure [bar]	500
Global PRF [-]	88.1 (±0.2)

With the exception of the HCCI case, the experiments used a premixed injection of isooctane, and a direct injection of n-heptane. The HCCI case utilized premixed injections of both fuels. Very

good agreement is seen between the calculated and experimental pressure and HRR traces, indicating that for a wide range of SOI timings and heat release shapes, the pressure trace could be reproduced with this methodology at these conditions. Therefore, given some arbitrary MFB profile, engine geometry, IVC conditions, and fuel energy input, the resulting pressure trace and heat release rate can be calculated.

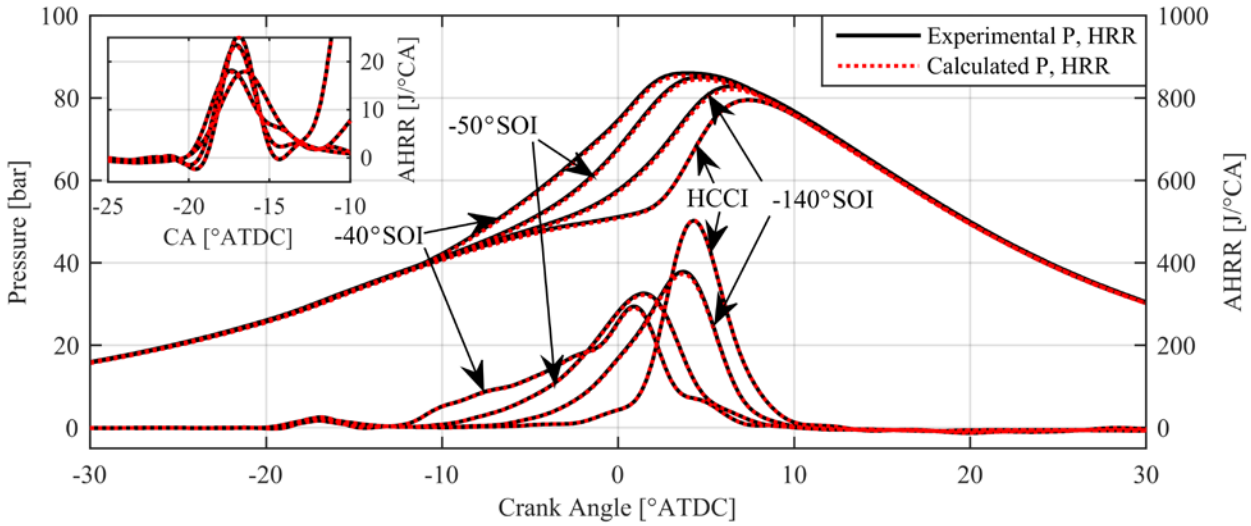

Figure 6.1: Experimental P and HRR for various injection timings (black lines), compared to the calculated P and HRR using the method described above

6.1.2 Heat Release Rate Shaping

With the method in the previous section established and validated, any heat release shape can be modeled and analyzed, given some initial conditions. In order to explore different heat release shapes, the operating conditions from the experiments and simulations from the previous section were chosen, and are shown in Table 6.3, along with the relevant engine geometry parameters of the Caterpillar SCOTE.

Table 6.3: Engine geometry (left), and operating conditions (right) of HRR shaping study

Displacement [L]	2.44	Fuel Energy, (Q_{fuel}) [J/cyc]	2590
Bore x Stroke [cm]	13.72 x 16.51	η_{comb} [-]	0.98
Connecting Rod Length [cm]	21.16	EGR [%]	0
IVO [°ATDC]	335	IVC Temperature [K]	355
IVC [°ATDC]	-143	IVC Pressure [bar]	1.27
EVO [°ATDC]	130	Fuel 1	n-heptane (PRF0)
EVC [°ATDC]	-355	Fuel 2	isooctane (PRF100)
Compression Ratio [-]	16.1:1	Percent Fuel 1 [%]	10
Displacement [L]	2.44	Percent Fuel 2 [%]	90

The first heat release shapes explored were the ideal thermodynamic heat release cycles discussed in Section 2.1. These cycles are the constant volume (CV) combustion cycle, which represents the ideal Otto cycle, and the constant pressure (CP) combustion cycle, which represents the ideal Diesel cycle. The mass fraction burned profiles for the two ideal cycles, and corresponding pressure and HRR traces for the initial conditions can be seen in Figure 6.2.

The inherent benefit of the constant volume combustion cycle is that the maximum gross work is extracted. The CV cycle therefore represents the maximum possible gross efficiency of an engine cycle. The inherent disadvantages of the CV cycle include high peak pressures, an effectively infinite peak pressure rise rate, and increased heat transfer due to the high cylinder temperature and pressure. The constant pressure combustion cycle offers low peak cylinder pressures for a given fuel energy input, reduced bulk-gas heat transfer compared to the CV cycle, and low pressure rise rates. The inherent disadvantage of the CP cycle is a reduction in the attainable gross efficiency of the cycle due to the long combustion duration. The maximum attainable efficiency of an engine cycle can be defined by the efficiency of the ideal closed Otto cycle, the relationship for which is shown in Equation (6.10), where r_c is the compression ratio, and γ is the ratio of specific heats, typically assumed to be constant throughout the cycle [104]. While it is convenient to model an

engine with these thermodynamic cycles to analyze trends in performance, it is important to consider than an IC engine is not a closed thermodynamic cycle, and therefore these conclusions are only trend-wise correct.

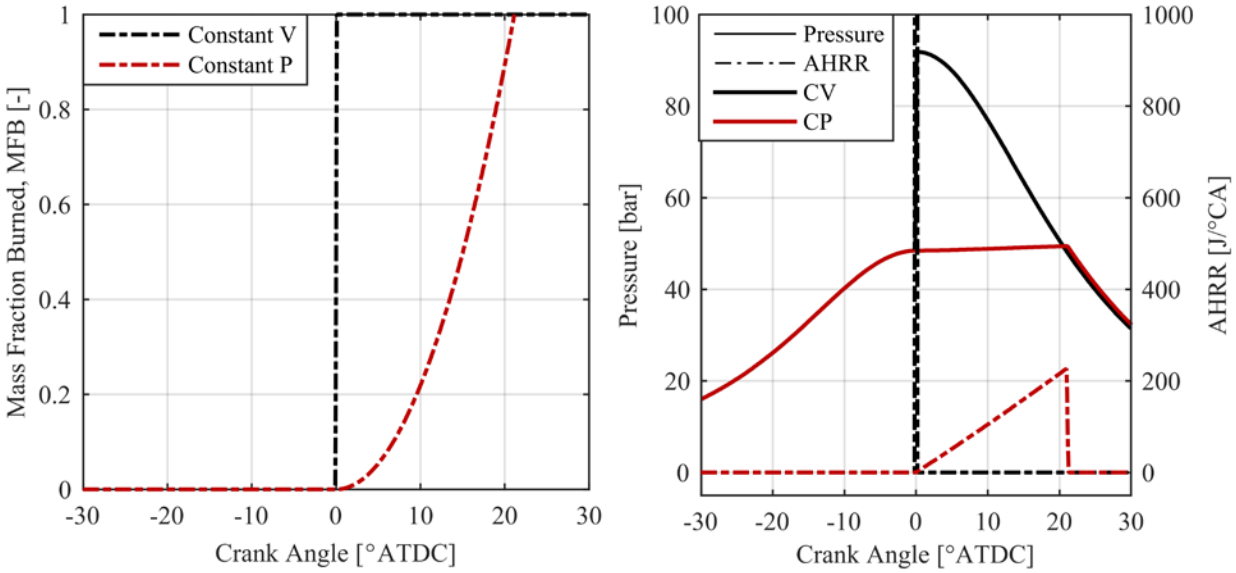

Figure 6.2: Constant volume (black), and constant pressure (red) cases showing the mass fraction burned profiles (left), and the associated pressure and HRR traces (right)

$$\eta_{ideal} = 1 - \frac{1}{r_c^{\gamma-1}} \tag{6.10}$$

The effective compression ratio (ECR), defined by Northrop et al. [104], for a given engine cycle can be calculated according to Equation (6.11), where end of combustion (EOC) is defined as CA95, SOC is defined as CA5, and $\dot{Q}_{HR}$ is the heat release at a given crank angle θ.

$$ECR = \frac{\sum_{SOC}^{EOC} \dot{Q}_{HR}(\theta) * \frac{V_{BDC}}{V(\theta)}}{\sum_{SOC}^{EOC} \dot{Q}_{HR}(\theta)} \tag{6.11}$$

The ECR is a measure of the maximum achievable efficiency based on the combustion phasing. The maximum ECR is the geometric compression ratio, if combustion is phased earlier or later than TDC, then the ECR will be less than the geometric compression ratio. Replacing the

geometric ratio in Equation (6.10) with the effective compression ratio implies that the maximum attainable efficiency is lower. Actual combustion events do not occur instantaneously, and therefore the ECR of these events is reduced from the maximum value due to the portion of the heat release occurring either before or after TDC. For the two ideal cycles shown, the CV combustion case has an ECR of 16.10 (i.e., the geometric compression ratio), and the CP combustion case has an ECR of 12.25. The maximum gross efficiency for these cases correspond to 62.2% and 58.4%, respectively, assuming a constant γ value of 1.35.

Any arbitrary heat release shape can be calculating using this methodology. Figure 6.3 shows the MFB profiles and pressure and heat release rate traces for various functional shapes defined in MATLAB. Each heat release has the same CA50 (0°CA) and combustion duration (8°CA).

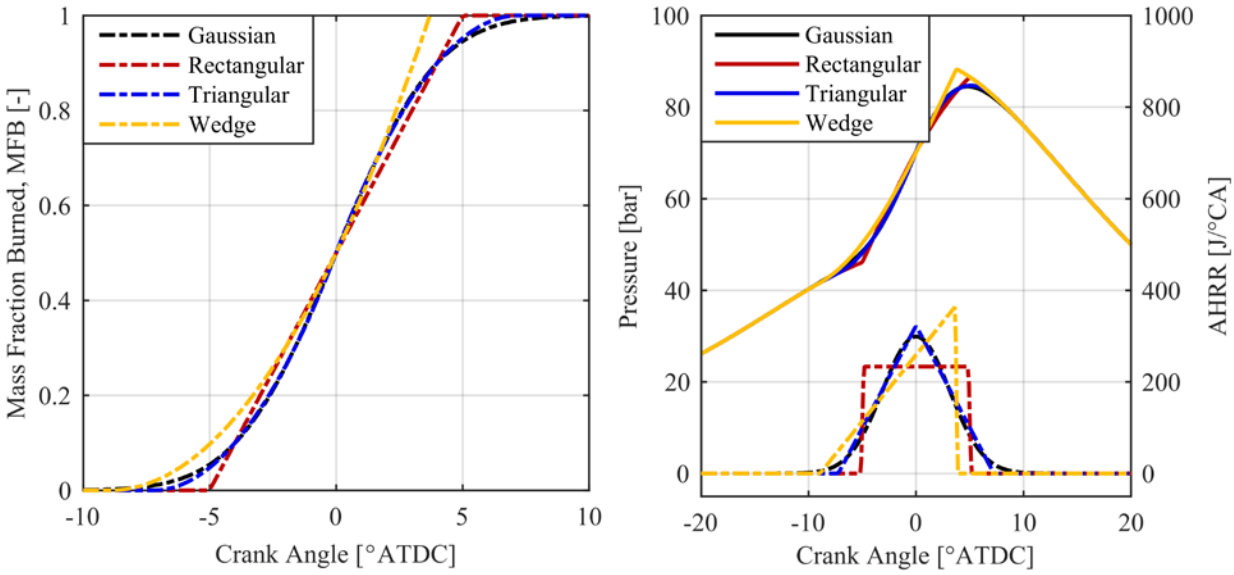

Figure 6.3: Various arbitrary heat release shapes with equal combustion phasing (0°CA) and duration (8°CA), showing the mass fraction burned profiles (left), and the associated pressure and HRR traces (right)

Focusing on the Gaussian shaped HRRs, as these most closely resemble the heat release rates seen in the experimental HCCI and RCCI experiments shown in Chapter 3, the combustion phasing and combustion duration can be adjusted independently, as shown in Figure 6.4, or simultaneously

assuming that some correlation between combustion phasing and combustion duration is known. In HCCI combustion, as phasing is advanced, CA10-90 tends to decrease. In RCCI cases, however, these effects can be decoupled by adjusting the SOI timing and ratio of premixed to DI fuel.

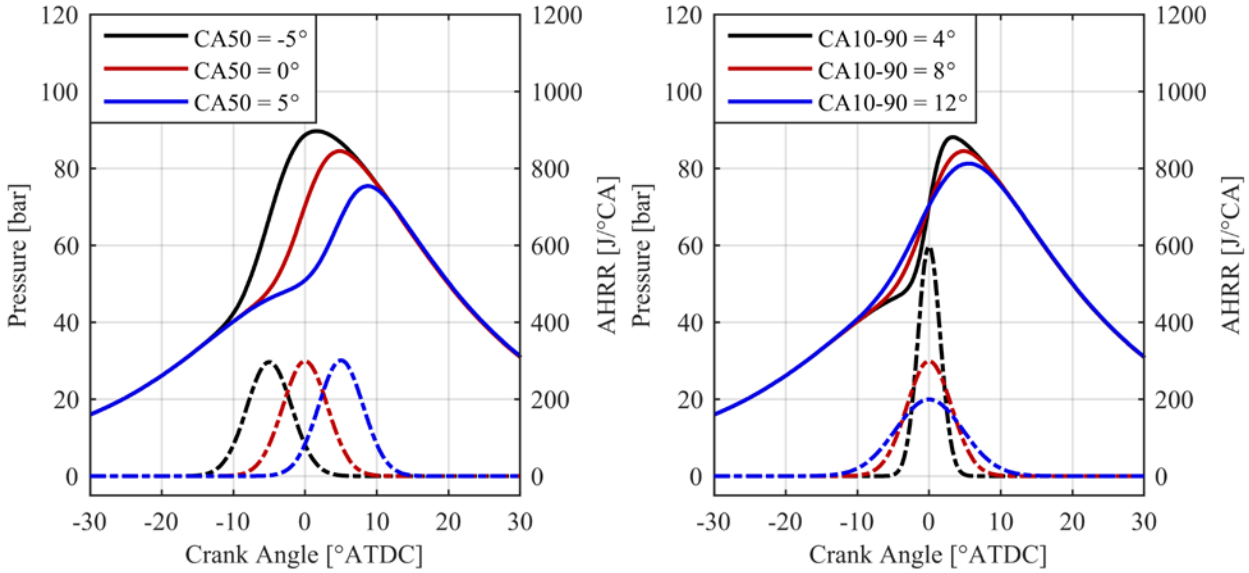

Figure 6.4: Pressure and HRR vs. crank angle for three Gaussian HRRs with CA10-90 = 8º, and various CA50s (left), and three Gaussian HRRs with CA50 = 0º, and various CA10-90 (right)

Instead of arbitrarily assigning a combustion phasing and duration, the heat release could be optimized for the maximum gross efficiency. The MATLAB fminsearch function was used to determine the optimum combustion phasing and duration for a Gaussian shaped heat release rate. Using this approach, the function converged on what essentially equates to a constant volume combustion process (CA50 = 0ºCA, CA10-90 ~ 0ºCA). Because the incredibly high peak pressure rise rate associated with such an approach is infeasible in practice, a PPRR constraint was implemented. If the PPRR was greater than the limit, then the efficiency was set to 0%. It is also important to note that the heat transfer model employed does not account for increases in heat transfer due to boundary layer scrubbing caused by high ringing intensity or knocking [39, 105-108]. The resulting mass fraction burned and pressure and heat release traces for three different PPRR constraints can be seen in Figure 6.5. The traces converged on the minimum combustion

duration which did not exceed the PPRR constraint. This is an intuitive result, as the fuel energy and mathematical profile were constrained, therefore the only way to decrease the PPRR would be to increase the combustion duration, therefore decreasing the maximum attainable efficiency.

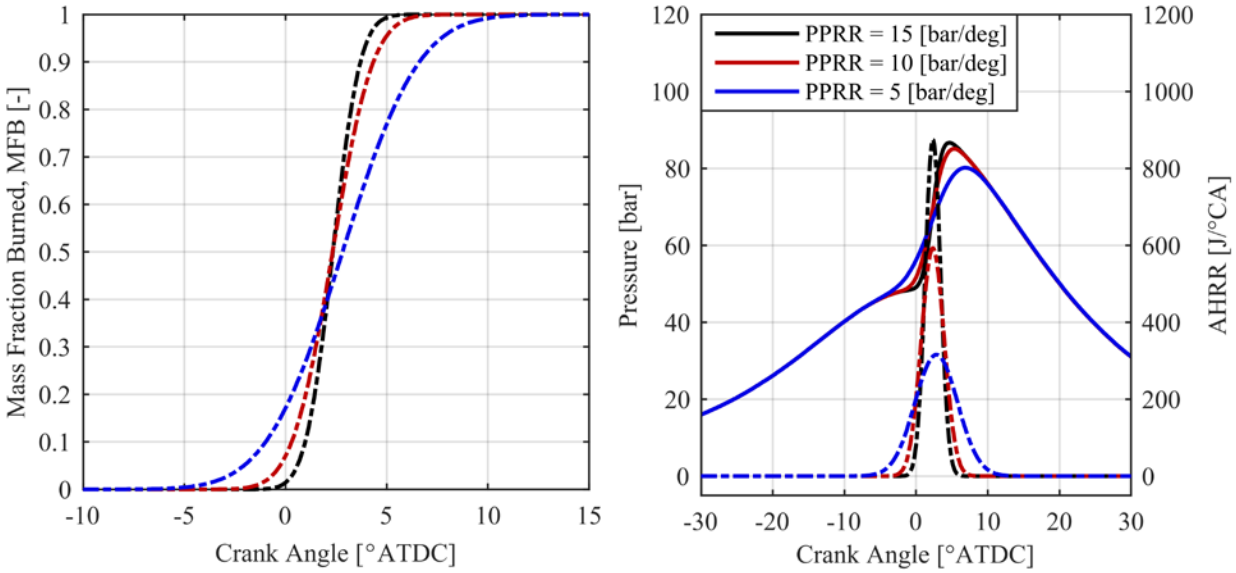

Figure 6.5: Maximum gross efficiency traces with a Gaussian shaped heat release rate and PPRR constraints showing the mass fraction burned profiles (left), and the associated pressure and HRR traces (right)

The optimal gross efficiencies for Gaussian heat release shapes converged on combustion phasing just after TDC, such that only a small portion (<15%) of the heat release occurred before TDC. These results can be explained by examining the tradeoff between the effective compression ratio as a function of combustion phasing and duration, and heat transfer losses.

Figure 6.6 shows the ECR, η_g, and heat transfer losses as a fraction of the fuel energy input, as a function of combustion phasing and duration. The ECR, which measures the maximum achievable efficiency, is maximized for TDC combustion phasing, and increases with decreasing combustion duration. Heat transfer losses increase with advanced combustion phasing, but are not strongly correlated to combustion duration, therefore, the optimal gross efficiency occurs where the two effects balance, and a local maxima is reached. This corresponds to a combustion phasing between

2-3ºCA for all combustion durations at these conditions. It is important to note that the combustion efficiency was held constant for all the cases tested, while in practice, combustion efficiency is likely to be a function of both combustion phasing and duration, generally increasing with advanced phasing and decreased duration for RCCI.

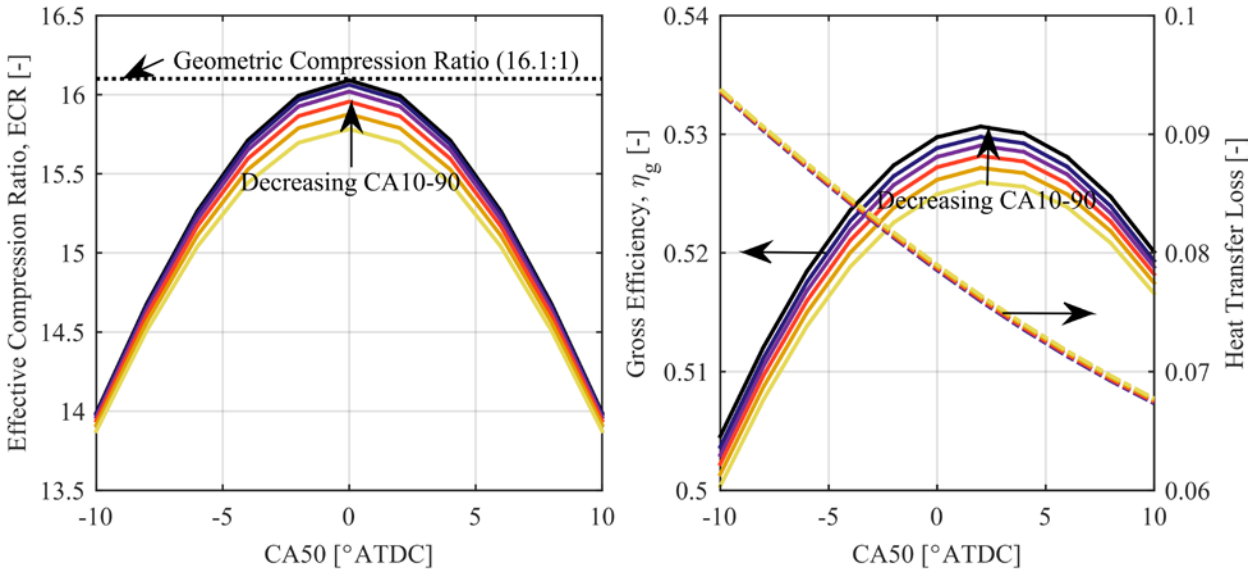

Figure 6.6: Effective compression ratio as a function of CA50 for various CA10-90s (left), and gross efficiency (solid lines) and heat transfer losses (dashed lines) as a function of CA50 for various CA10-90s (right)

Thus far, only high temperature heat release events have been considered, but as seen in the experiments and simulations in the previous sections, these operating conditions exhibit significant discernable LTHR behavior for PRF fuels. To explore the effects of the LTHR on the global efficiency, and stratification requirements, a Gaussian LTHR event was modeled, and combined with a Gaussian HTHR event, the result of which can be seen in Figure 6.7. The low temperature heat release location, duration, and magnitude (3.5% of fuel energy) was approximated from experimental data at similar global conditions to provide a realistic representation of the LTHR event. The effective compression ratio for the case without a LTHR is 15.96, with a η_g of 52.7%, compared to 15.93 with a η_g of 52.5% for the case with a 3.5% LTHR. Half of the difference in gross efficiency comes from the difference in heat transfer due to the increase in cylinder pressure

and temperature in the LTHR case (7.9% heat transfer loss for the no LTHR case, 8.0% heat transfer loss for the LTHR case). This difference is small, however if the maximum possible gross efficiency is desired, then a fuel that does not express NTC behavior, such as ethanol [39], should be utilized. This however ignores the fact that without the LTHR event, higher DI fuel fractions would be required because of the decreased cylinder pressure and temperature, thus potentially resulting in higher local temperatures and more heat transfer.

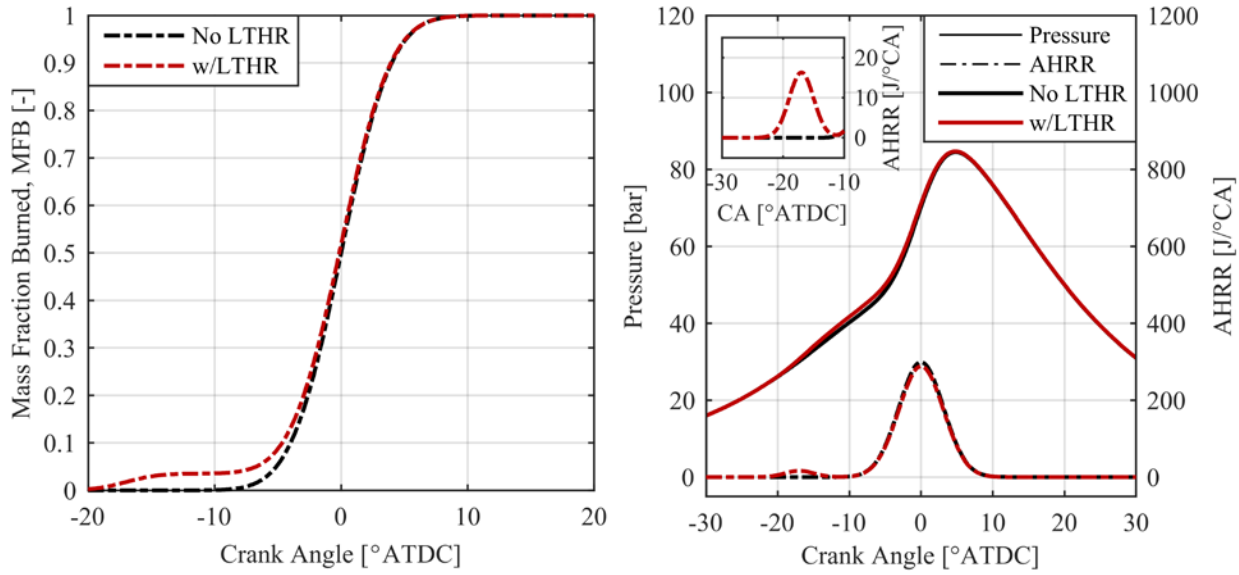

Figure 6.7: Mass fraction burned (left), and associated pressure and HRR traces (right), for a Gaussian heat release rate shape with CA50 = 0°CA, and CA10-90 = 8°CA without a LTHR (black), and with 3.5% of the fuel energy in the LTHR (red)

6.1.3 FSA Predicted Stratification with PRF100/PRF0

The FSA method proposed in Chapter 5, coupled with the heat release profiles generated in the previous section, could be used to predict the fuel stratification requirements to achieve such heat release profiles. The process of predicting the fuel stratification required an iterative approach. An initial guess value for the global premixed mass percentage was arbitrarily chosen as 90% premixed. This quantity is required to calculate the premixed equivalence ratio, and the equivalence ratio of all subsequent zones. This value influences the auto-ignition predictions, and

so it is imperative that the expected value from the fuel distribution and the global premixed percentage are equivalent. The method was initialized with the guess value, and the fuel distribution was predicted. If the calculated average value from the distribution was not within ±0.25% of the global premixed percentage, then the initial premixed fuel mass percentage was adjusted in the appropriate direction, and the method was run again. This process continued until the two values converged, which typically required between 3 and 5 iterations.

The first set of heat release rates tested were the Gaussian shaped distributions shown in Figure 6.4, to explore the effects of combustion phasing and duration on the fuel stratification requirements. PRF100 was used as the premixed fuel, and PRF0 was used as the DI fuel. The kinetics were approximated by linear interpolation of an ignition delay matrix, as described in Section 4.1.2, with a reduced chemical mechanism by Wang et al. [99]. Figure 6.8 shows the predicted fuel distributions for the Gaussian shaped HRRs with a fixed combustion duration of 8ºCA, and three combustion phasing values.

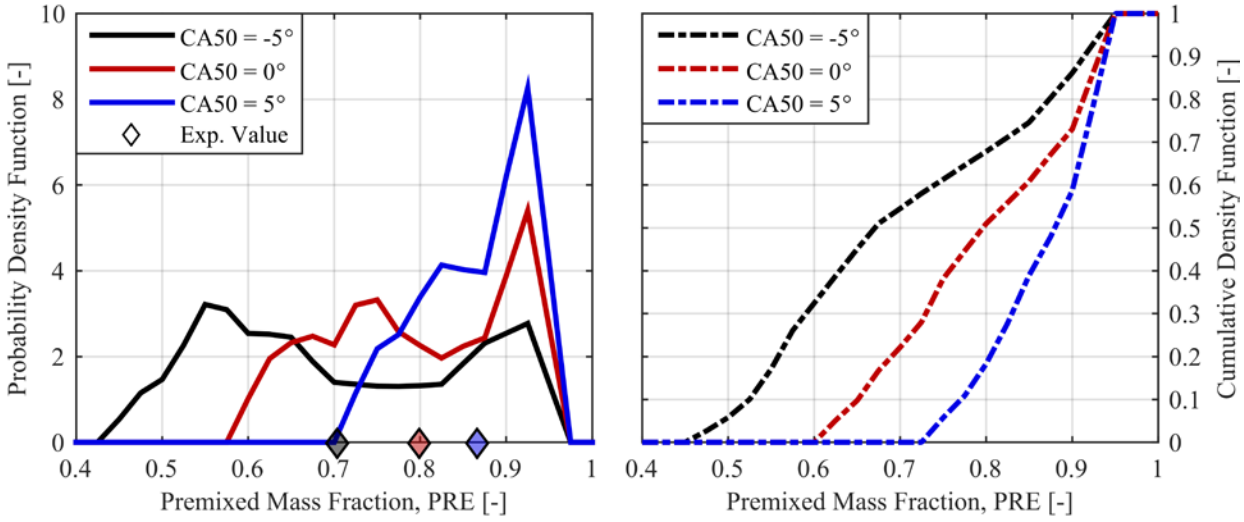

Figure 6.8: FSA predicted PDF (left), and CDF (right) of fuel distribution, for three Gaussian distribution shaped HRRs with different phasing, and CA10-90 of 8ºCA, with the global premixed percentage shown (diamonds)

Despite having a constant combustion duration, the fuel stratification requirements for the three combustion phasing cases show significant differences in both the global premixed percentage, and the magnitude of stratification required. To result in advanced combustion phasing with a fixed combustion duration, significantly more fuel stratification is required, and a globally more reactive mixture is necessary. Typically, as combustion phasing is advanced, combustion duration decreases. This trend can be clearly seen in the HCCI combustion cases shown in Figure 6.9, where, as combustion phasing is advanced by increasing the global reactivity of the mixture (decreasing PRF), the combustion duration shortens significantly. In other words, for a fixed fuel stratification (e.g., homogeneous), advancing phasing should result in decreased duration. This effect is primarily a result of the higher pressure and temperature induced by advanced phasing.

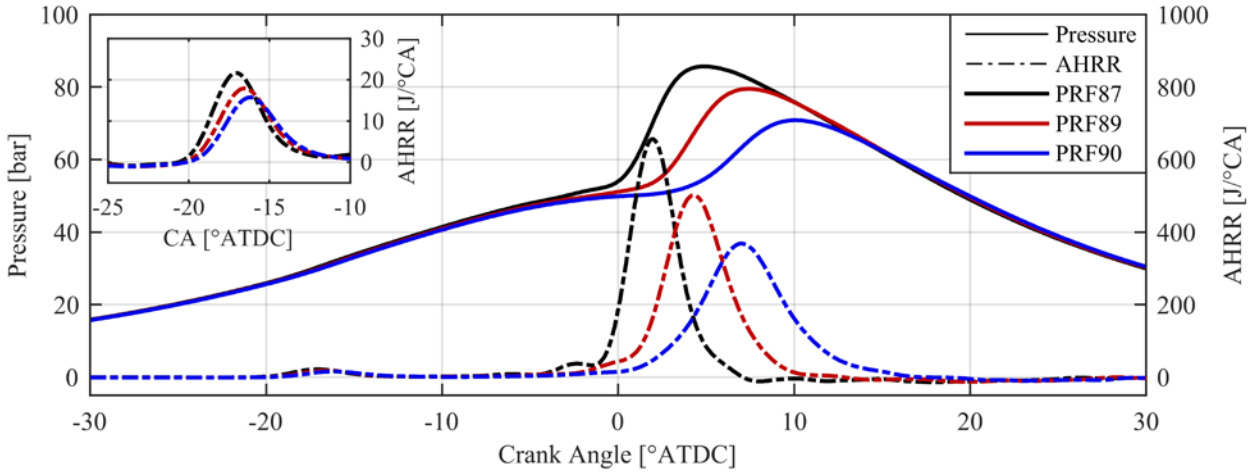

Figure 6.9: Pressure and HRR vs. crank angle for HCCI combustion of three PRF mixtures at T_{in} = 40°C, and φ = 0.30, reproduced from Section 3.7.1

Figure 6.10 shows the FSA predicted fuel distributions for the fixed combustion phasing, varied combustion duration cases shown in Figure 6.4. Unsurprisingly, the shorter the combustion duration, the less fuel stratification required. Because of the fixed phasing condition, increasing the combustion duration requires more high reactivity fuel to initiate the combustion event earlier, and more low reactivity fuel to sustain the combustion event later, thus increased stratification.

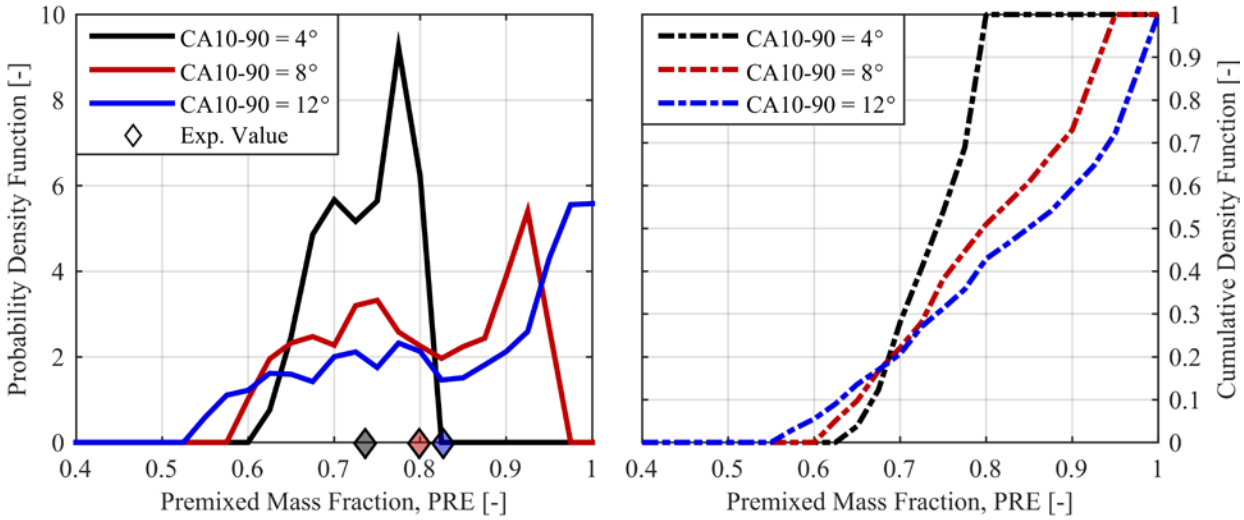

Figure 6.10: FSA predicted PDF (left), and CDF (right) of fuel distribution, for three Gaussian distribution shaped HRRs with different combustion durations, and CA50 of 0ºCA, with the global premixed percentage (diamonds)

Because of the early start of combustion, the temperature and pressure is increased earlier in the cycle than the short combustion duration cases, thereby requiring a globally less reactive mixture to maintain the same combustion phasing. In practice, the varying levels of stratification can be achieved most effectively by injection timing, although injection pressure and number of injections also influence fuel stratification. A case such as the 4ºCA combustion duration case would require mixing of the majority of the DI fuel, most resembling the -140º SOI timing case shown in Section 5.3.2.1, whereas the 12ºCA duration case most resembles the -60º to -50º SOI timing cases from Section 5.3.2.1, at least in terms of distribution shape and range.

Alternatively, instead of maintaining CA50 with varying combustion duration, a different combustion metric such as CA10 or CA90 could be held constant with varying combustion duration. Figure 6.11 shows the pressure and heat release traces for Gaussian-shaped HRRs with various combustion durations, and fixed CA10 or CA90, respectively, and Figure 6.13 and Figure 6.13 show the FSA predicted fuel distributions for these cases.

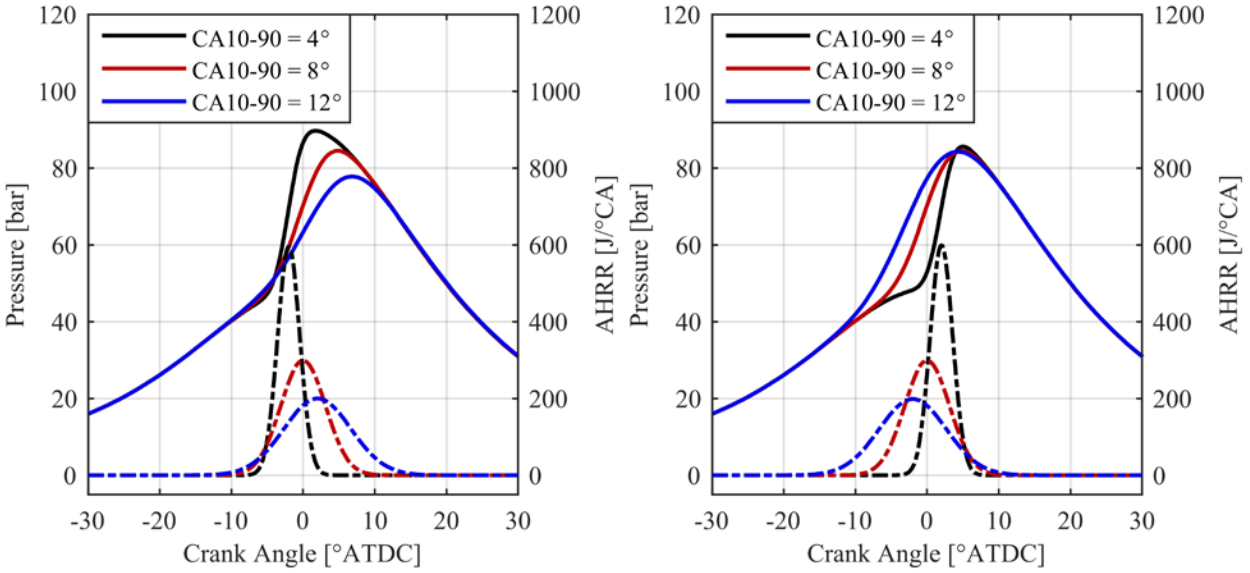

Figure 6.11: Pressure and HRR vs. crank angle for three Gaussian HRRs with CA10 =-4º, and various CA10-90 (left), and three Gaussian HRRs with CA90 = 4º and various CA10-90 (right)

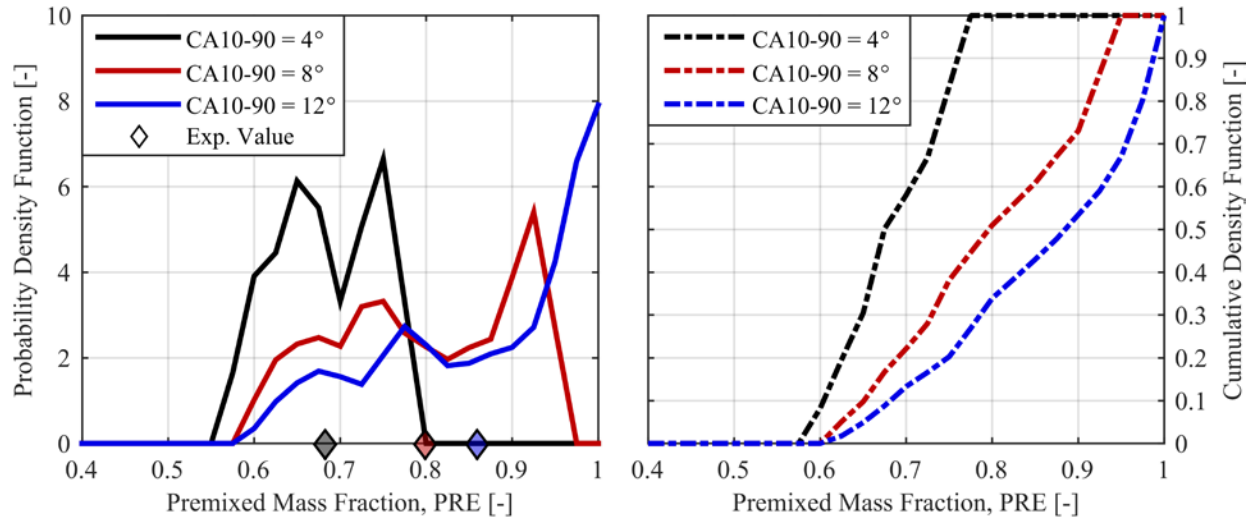

Figure 6.12: FSA predicted PDF (left), and CDF (right) of fuel distribution, for three Gaussian distribution shaped HRRs with various CA10-90s with CA10 of -4ºCA, including the global premixed percentage (diamonds)

For the fixed CA90 cases, the global premixed percentages are very similar. This seems to indicate that the end of combustion (or CA90) fixes the global percent of premixed fuel, while the duration determines the stratification of the DI fuel. Examining the CDF curves, for the fixed CA10 cases, there seems to be a translational shift towards a more reactive global mixture as the combustion duration decreases, along with a slight rotational shift towards less stratified mixtures. For the

fixed CA90 cases, there is a purely rotational shift about a common global premixed fuel percentage, representative of a decrease in fuel stratification for decreasing combustion duration, without a significant translational shift towards a more reactive global fuel blend.

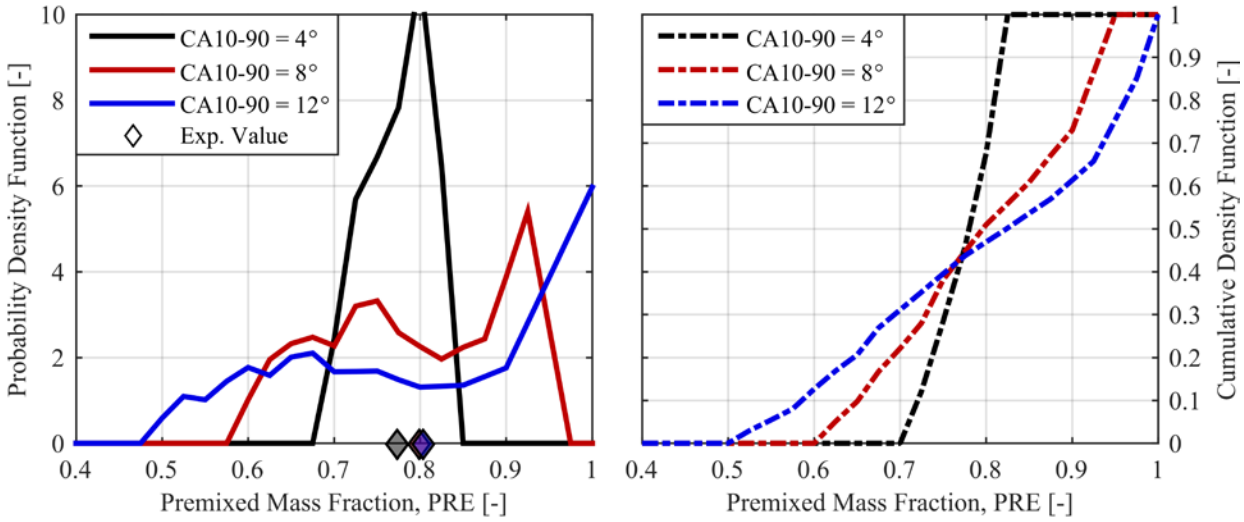

Figure 6.13: FSA predicted PDF (left), and CDF (right) of fuel distribution, for three Gaussian distribution shaped HRRs with various CA10-90s with CA90 = 4ºCA, including the global premixed percentage (diamonds)

Figure 6.14 shows the predicted fuel stratification from the FSA method for the cases shown in Figure 6.5, i.e., the maximum gross efficiency cases constrained by a Gaussian heat release shape with a maximum peak pressure rise rate limitation. Again it is seen that the more homogeneous the mixture is, the more globally reactive the mixture must be. In the limiting case of a completely homogeneous mixture, i.e., HCCI combustion, this would be the most reactive mixture capable of achieving a given combustion phasing, and any induced fuel stratification would require a less globally reactive mixture to match combustion phasing. Depending on the peak pressure rise rate constraint, the required fuel stratification varies significantly, trending towards more stratification for lower PPRR limits due to the implicit increase in combustion duration.

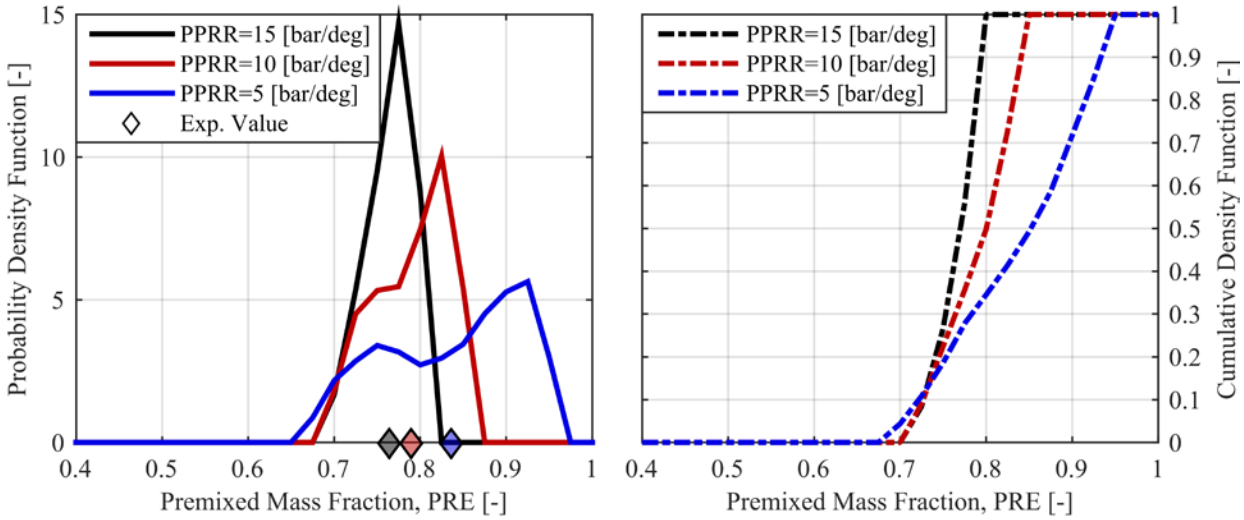

Figure 6.14: FSA predicted PDF (left), and CDF (right) of fuel distribution, for the maximum gross efficiency, Gaussian-shaped HRR for three different PPRR constraints, with the global premixed percentage shown (diamonds)

Figure 6.15 shows the effect of the LTHR on the fuel stratification requirements for a Gaussian shaped HTHR with TDC combustion phasing and a duration of 8ºCA. The LTHR event results in an increased temperature and pressure prior to combustion, which in turn decreases local ignition delays, thus accelerating autoignition events. The result of this in terms of the required fuel stratification is a globally less reactive mixture, as can be clearly seen.

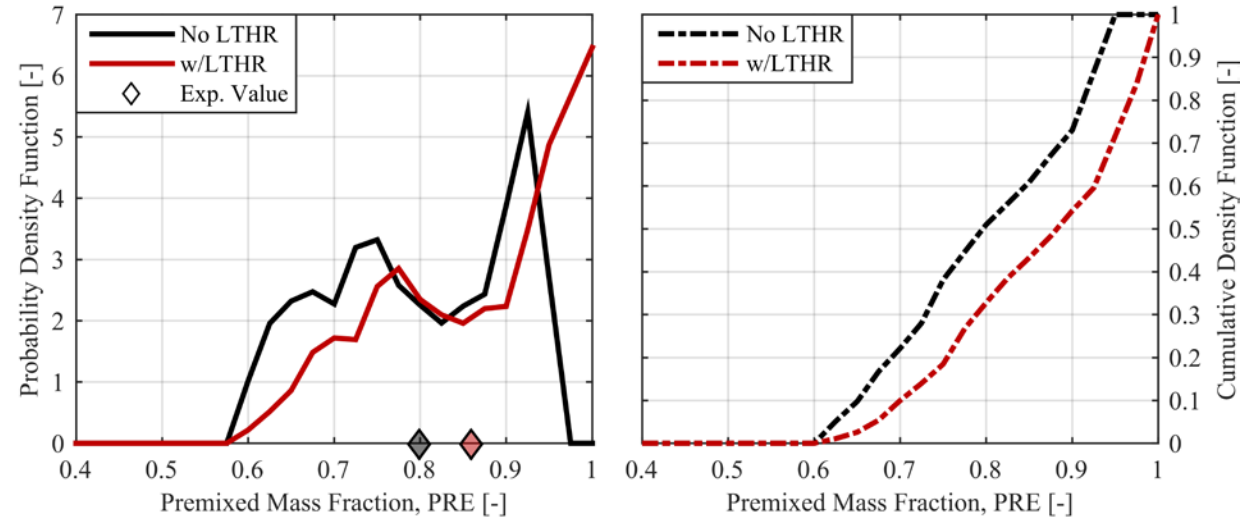

Figure 6.15: FSA predicted PDF (left), and CDF (right) of fuel distribution, for a Gaussian HRR shape with CA50 = 0ºCA, and CA10-90 = 8ºCA without a LTHR (black), and with 3.5% of the fuel energy in the LTHR (red)

The global PRF required to achieve the prescribed heat release increases from about 80 to 86, solely based on the introduction of a low temperature heat release event that accounted for only 3.5% of the total fuel energy. This result indicates that it is important to consider the potential for NTC behavior when considering the shape and nature of these theoretical heat release events.

6.2 Varying Premixed and DI Fuel Chemistry

Using the FSA method, the effect of the premixed and direct-injected fuel chemistry on the fuel stratification requirements can be explored. Assuming some optimal HRR at given initial conditions, the stratification requirements for any combination of premixed and direct-injected fuel could be predicted. Using this method the user is able to gain significant insight into the optimization of alternative fuels in a kinetically-controlled, stratified-charge strategy. The method does, however, require the fuel chemical kinetics to be well characterized.

6.2.1 Stratification Requirements of Various PRF Blends

In order to explore the effects of premixed and DI fuel chemistry on the fuel stratification requirements in RCCI combustion, various PRF blends were tested, bracketing the range of commercially available diesel and gasoline fuels in terms of octane and cetane number. Using the linear correlation shown in Equation (6.12), developed by Kalghatgi [109], the approximate cetane number of the PRF blends could be calculated, the results of which are shown in Table 6.4.

$$CN = 54.6 - 0.42 * RON \tag{6.12}$$

By definition, the RON and MON of a mixture of PRFs is the PRF number itself. Each fuel combination required the formation of its own ignition delay matrix, following the method described in Section 4.1.2, using the chemical mechanism by Wang et al. [99].

Table 6.4: Calculated cetane numbers of various PRF blends

Premixed PRF Numbers	Cetane Number[109]	DI Fuel PRF Numbers	Cetane Number[109]
100	12.6	65	27.3
90	16.8	32.5	41.0
80	21.0	0	54.6

The effect of the PRF number of the premixed fuel was analyzed by comparing three different premixed PRF mixtures with PRF0 as the direct injected fuel for a Gaussian shaped heat release, with CA50 = 0ºCA, and a fixed combustion duration of 8ºCA. This case corresponded to the Gaussian heat release rate with no LTHR event shown in Figure 6.7.

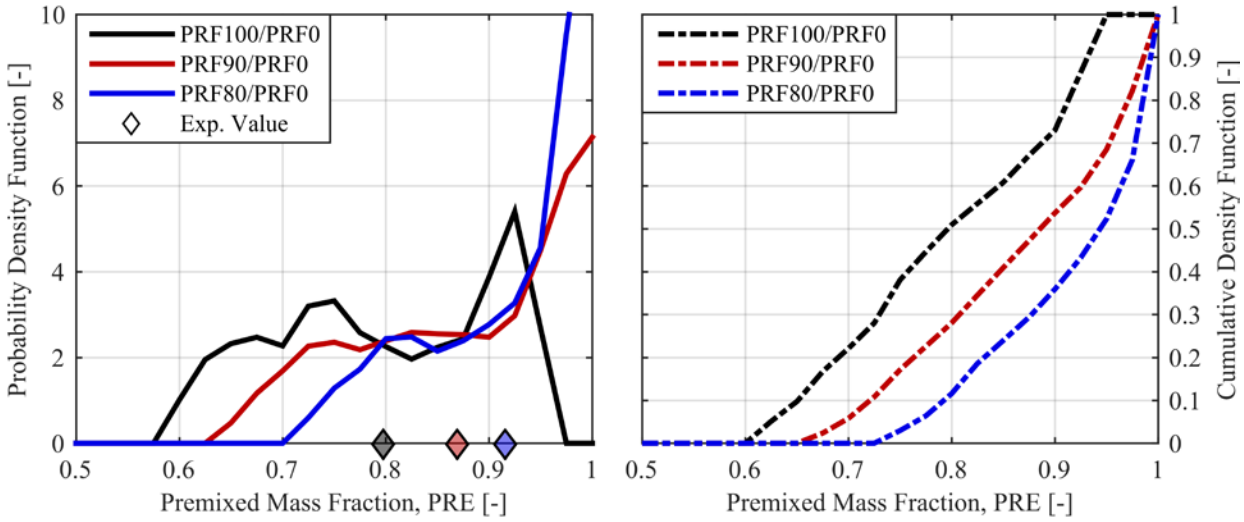

Figure 6.16: FSA predicted PDF (left), and CDF (right) of fuel distribution, for a Gaussian HRR shape with CA50 = 0ºCA, and CA10-90 = 8ºCA for three different premixed PRF mixtures (100, 90, 80), with DI n-heptane (PRF0)

The FSA predicted fuel distributions for premixed PRF100, PRF90, and PRF80, with DI n-heptane (PRF0) can be seen in Figure 6.16. As expected, the use of more reactive premixed fuels such as PRF90 and PRF80 required a less globally reactive mixture overall (i.e., less DI fuel, and higher premixed percent) to match the combustion behavior.

The fuel distributions shown for the three premixed fuels would require significantly different direct-injection strategies, as the trend is towards less required stratification for the more reactive

PRF fuels. Taken to its extreme, there must be some PRF fuel with a PRF number less than 80 that could not achieve the desired combustion phasing and duration with the addition of any DI fuel (i.e., HCCI). This effect may be more clearly seen in the predicted equivalence ratio distributions shown in Figure 6.17 for these cases. As the premixed fuel becomes more reactive, the spread in the equivalence ratio distribution necessary to achieve the combustion event decreases, while the global equivalence ratio remains constant because it is determined by the IVC conditions.

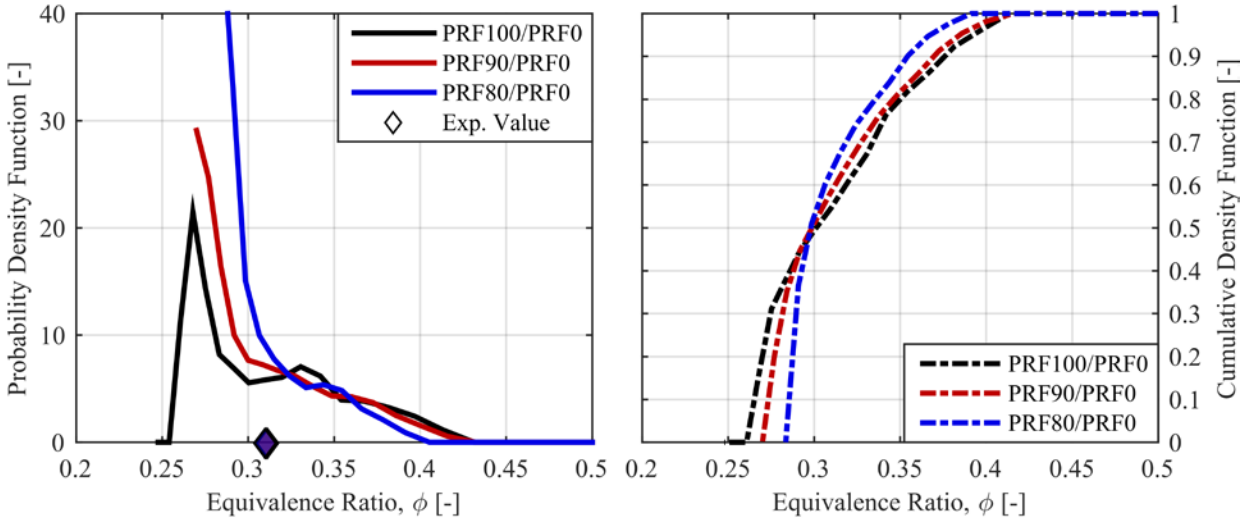

Figure 6.17: FSA predicted PDF (left), and CDF (right) of fuel distribution, for a Gaussian HRR shape with CA50 = 0°CA, and CA10-90 = 8°CA for three different premixed PRF mixtures (100, 90, 80), with DI n-heptane (PRF0)

The effect of the DI fuel reactivity was studied by comparing three different DI PRF mixtures with premixed PRF100 for the same Gaussian shaped heat release discussed previously. The FSA predicted fuel distributions for direct-injected PRF0, PRF32.5, and PRF65 with isooctane (PRF100) as the premixed fuel are shown in Figure 6.18. Again, as expected, decreasing the difference in reactivity between the DI and premixed fuels necessitates a shift towards greater DI fuel quantities to match the combustion phasing. The predicted fuel distributions are generally similar in shape, but shifted towards more total DI fuel for the less reactive PRF blends. There is a slight stretching in the distribution, as the PRF100/PRF0 case covers between about 0.58 to 0.98

premixed mass fraction, while the PRF100/PRF65 covers a range between 0.20 and about 0.68 premixed fraction. This slight stretching is amplified when the distribution is viewed in equivalence ratio space as shown in Figure 6.19.

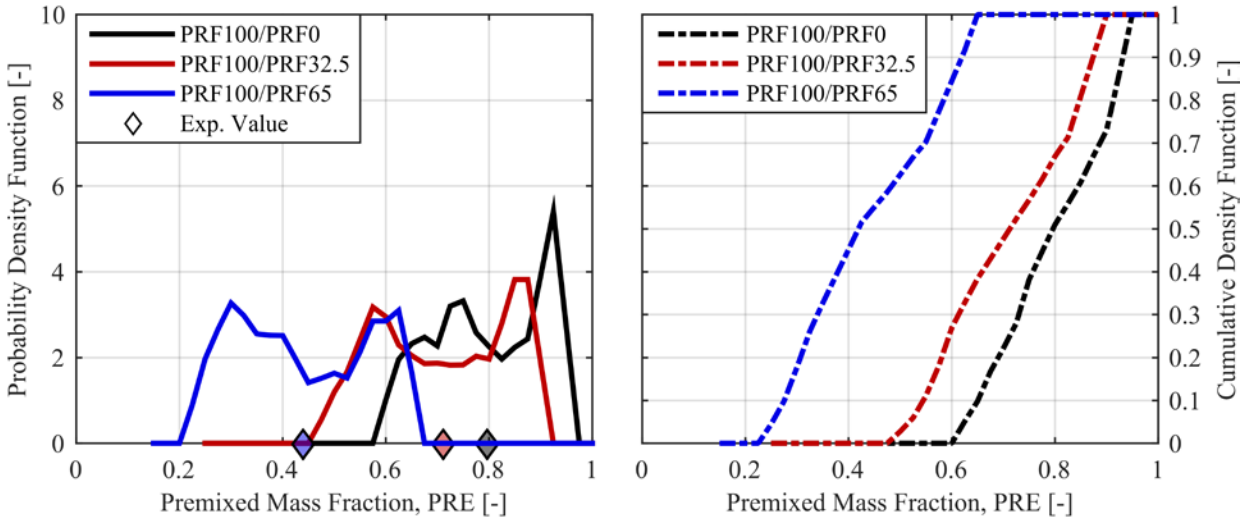

Figure 6.18: FSA predicted PDF (left), and CDF (right) of fuel distribution, for a Gaussian HRR shape with CA50 = 0°CA, and CA10-90 = 8°CA for three different DI PRF mixtures (0, 32.5, 65), with premixed isooctane (PRF100)

It is clear from Figure 6.19 that the distributions are actually significantly different. The least reactive case (PRF100/PRF65) requires a large stratification of equivalence ratio in order to produce the desired heat release phasing and duration, primarily due to the relatively small difference in reactivity between the premixed and DI fuels. This equivalence ratio stratification effectively replaces the reactivity stratification missing from the fuel mixture compared to the baseline PRF100/PRF0 case. The reason the relatively small difference in the premixed mass fraction leads to a very large difference in the equivalence ratio distribution is that the relationship between the two parameters is non-linear, as discussed and shown in Section 5.2.1.

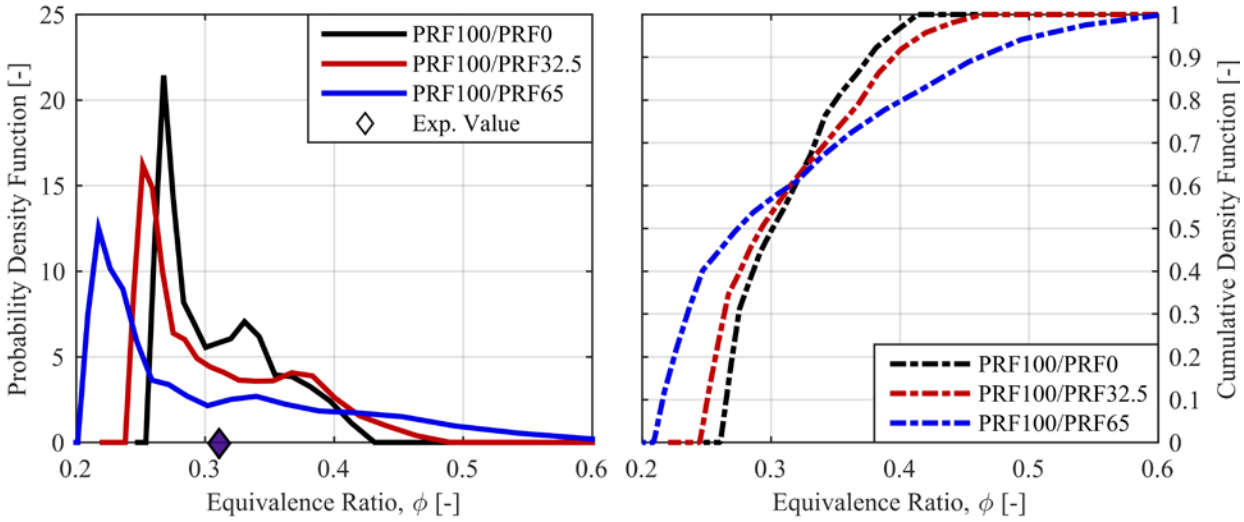

Figure 6.19: FSA predicted PDF (left), and CDF (right) of equivalence ratio, for a Gaussian HRR shape with CA50 = 0ºCA, and CA10-90 = 8ºCA for three different DI PRF mixtures (0, 32.5, 65), with premixed isooctane (PRF100)

The fuel combinations were next tested on the maximum gross efficiency Gaussian heat release rate profiles constrained by PPRR shown in Figure 6.5. Figure 6.20 shows the FSA predicted fuel distributions for the three PPRR constrained Gaussian HRRs, for each of the premixed PRF mixtures with direct-injected n-heptane. For a given heat release, again the more reactive premixed fuels unsurprisingly require less DI fuel. For the highest PPRR constraint considered (15bar/deg), the fuel distributions resemble HCCI type combustion events, where there is very little fuel stratification (<0.1 premixed mass fraction). The fuel distributions for the 15bar/deg cases are merely shifted to the right by the difference in PRF number between the baseline PRF100 case and the fuel of interest. As the PPRR constraint is decreased, the required fuel stratification increases and the global premixed fraction also increases for all the fuel combinations, as shown previously. Figure 6.21 shows the predicted equivalence ratio distributions for these cases. It is obvious that the 15bar/deg case converges on what approximates a homogeneous fuel distribution for all three fuel combinations, having only a spread in local equivalence ratio of about 0.30 to 0.33. As the PPRR constraint was decreased, and the combustion duration necessarily increased, the required equivalence ratio stratification increased significantly, particularly for the PRF100/PRF0 case.

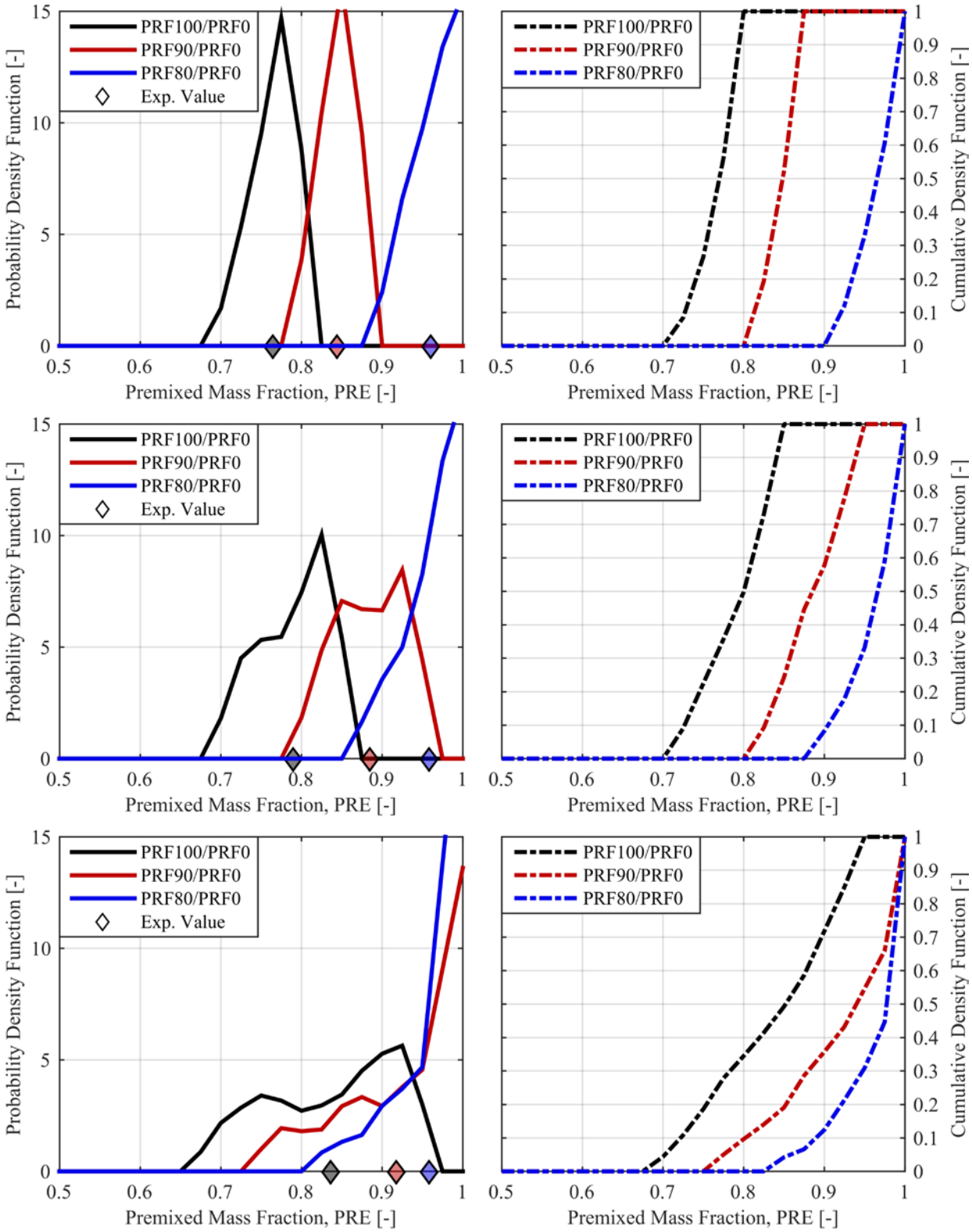

Figure 6.20: FSA predicted PDF (left), and CDF (right) of fuel distribution, for the maximum η_g Gaussian shaped HRRs with PPRR constraints of 15bar/deg (top), 10bar/deg (middle), and 5bar/deg (bottom), for three different premixed PRF mixtures (100, 90, 80), with DI n-heptane (PRF0)

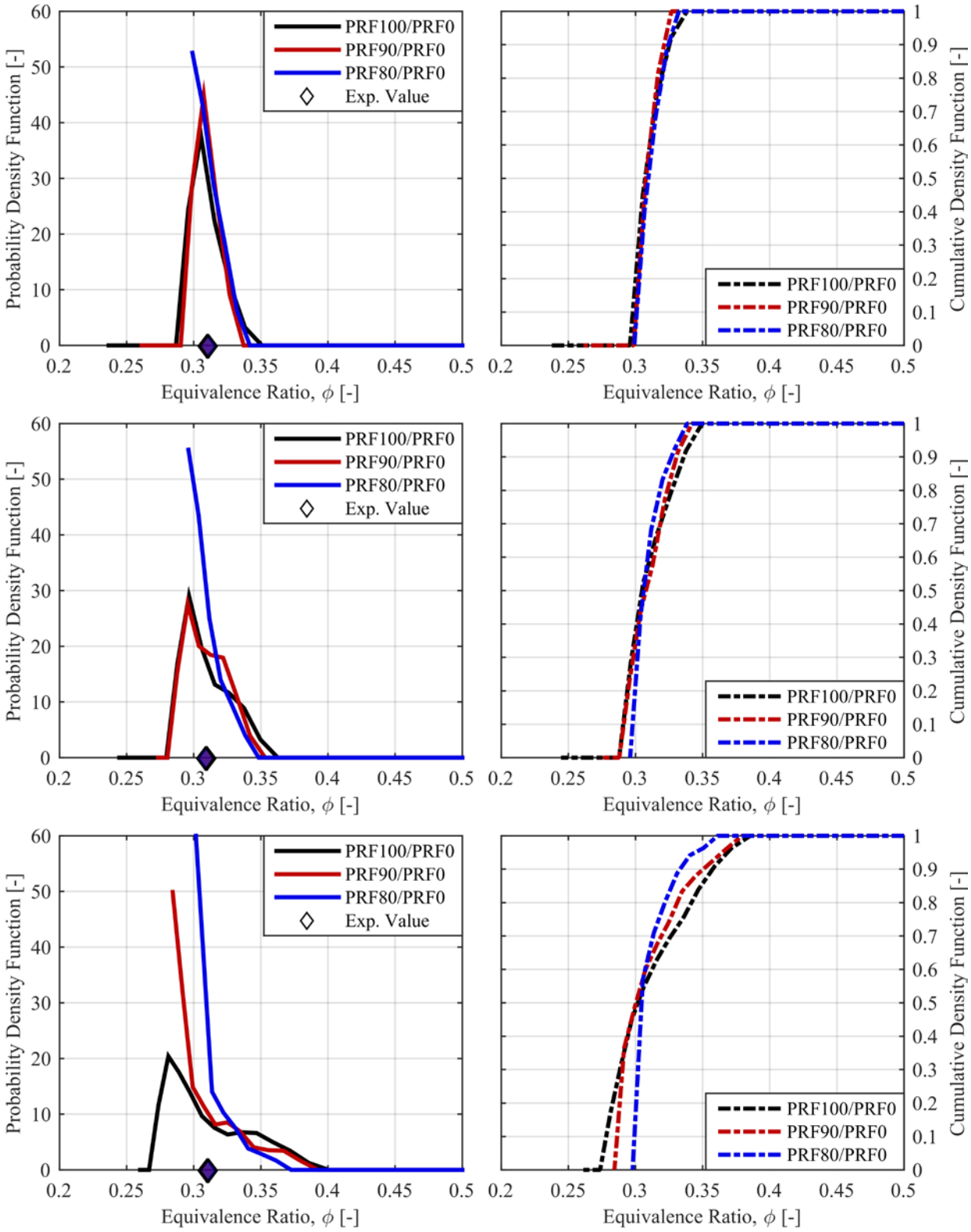

Figure 6.21: FSA predicted PDF (left), and CDF (right) of equivalence ratio, for the maximum η_g Gaussian shaped HRRs with PPRR constraints of 15bar/deg (top), 10bar/deg (middle), and 5bar/deg (bottom), for three different premixed PRF mixtures (100, 90, 80), with DI n-heptane (PRF0)

The effects of the variable DI fuel chemistry were then studied with the same Gaussian-shaped max efficiency HRRs. Figure 6.22 shows the FSA predicted fuel distributions for the varying DI PRF mixture cases with premixed isooctane (PRF100), for the three PPRR-constrained Gaussian heat release rates. Here it is again seen that for a less reactive DI fuel mixture, significantly more DI fuel mass is required to match the combustion phasing. The 15bar/deg case again exhibits a nearly homogeneous required fuel distribution for all three fuel combinations, and the global premixed mass fraction was found to be a strong function of the DI fuel reactivity for this case. The required premixed fraction, and required fuel stratification again increased as the PPRR constraint was decreased, due to the increased combustion duration required.

Figure 6.23 shows the predicted equivalence ratio distributions for the DI fuel chemistry cases for each PPRR constraint. For all three PPRR constrained cases, the required equivalence ratio stratification increased with decreasing DI fuel reactivity. This increased equivalence ratio stratification makes up for the decrease in in-cylinder reactivity gradients due to the increased DI PRF number. The difference between the premixed fuel reactivity and direct-injected fuel reactivity defines the required equivalence ratio stratification in the cylinder to achieve some arbitrary heat release event. Decreasing the difference in reactivity (e.g., ΔPRF) between the two fuels requires an increase in the equivalence ratio stratification to maintain combustion phasing and duration, and increasing the reactivity difference between the two fuels requires decreased equivalence ratio stratification.

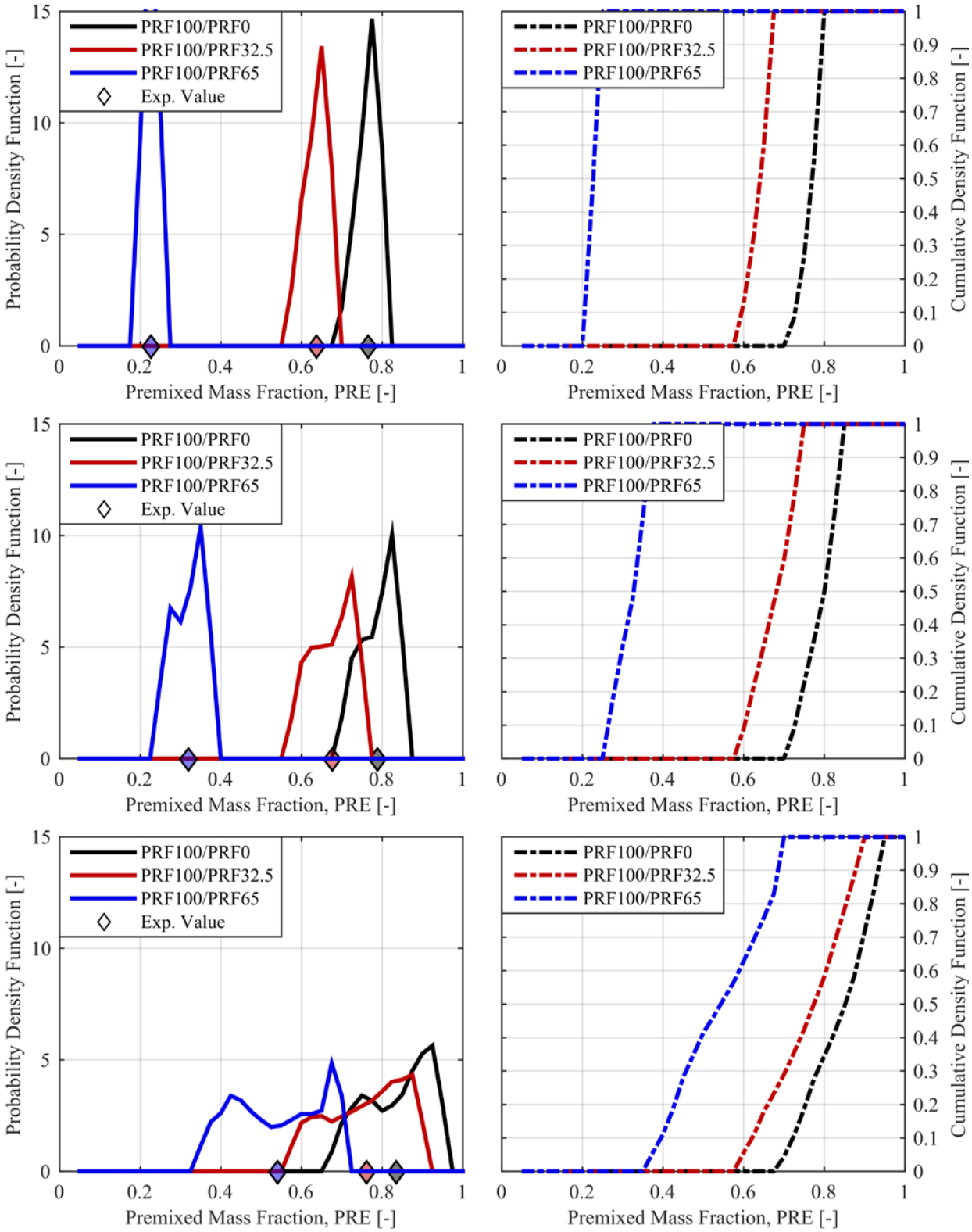

Figure 6.22: FSA predicted PDF (left), and CDF (right) of fuel distribution, for the maximum η_g Gaussian shaped HRRs with PPRR constraints of 15bar/deg (top), 10bar/deg (middle), and 5bar/deg (bottom), for three different DI PRF mixtures (0, 32.5, 65), with premixed isooctane (PRF100)

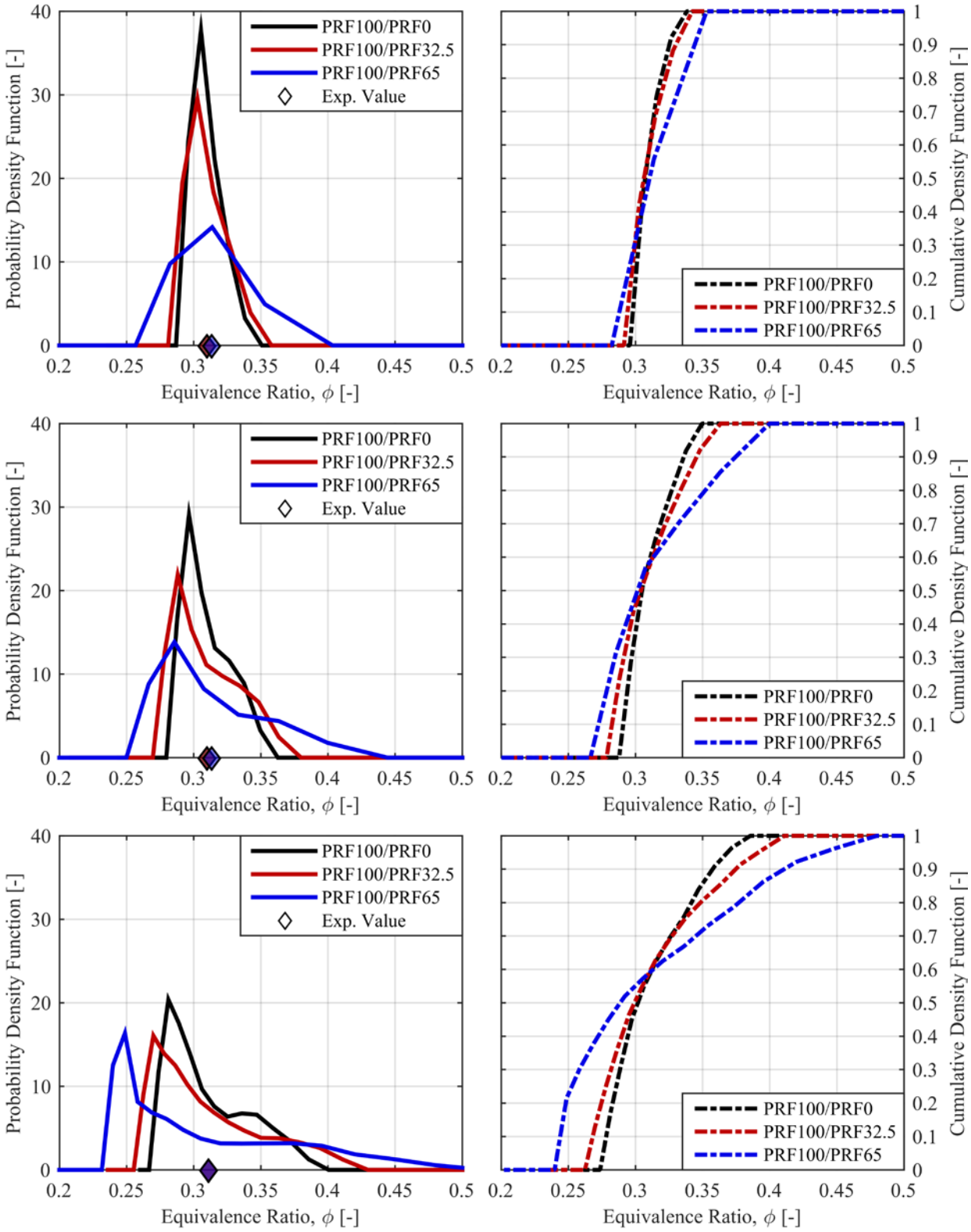

Figure 6.23: FSA predicted PDF (left), and CDF (right) of equivalence ratio, for the maximum η_g Gaussian shaped HRRs with PPRR constraints of 15bar/deg (top), 10bar/deg (middle), and 5bar/deg (bottom), for three different DI PRF mixtures (0, 32.5, 65), with premixed isooctane (PRF100)

6.2.2 Stratification Requirements for Alternative Premixed Fuels

The FSA methodology can be used to predict fuel stratification for any premixed and direct-injected fuel combination of interest. In order to further explore the FSA methodology, the alternative premixed fuels tested in Chapter 3 (syngas composed of 50%$_{mol}$ H_2 + 50%$_{mol}$ CO_2, and methane) were compared to isooctane for a variety of heat release shapes. The DI fuel for all the cases in this section was n-heptane. The ignition delay matrices for each fuel combination were populated with Cantera according to the method discussed in Section 4.1.2, using the same reduced mechanism by Wang et al. [99] that has been used throughout the present work.

As discussed in Section 6.1.3, the process of predicting the fuel stratification for a given heat release rate for each fuel combination again required an iterative approach. An initial guess value for the global premixed mass percentage was arbitrarily chosen as 90% premixed. The FSA method was initialized with the guess value, and the fuel distribution was predicted. If the calculated average value from the distribution was not within ±0.25% of the global premixed percentage, then the initial premixed fuel mass percentage was adjusted in the appropriate direction. This process continued until the two values converged, which typically required between 3 and 5 iterations.

The three fuel combinations were tested on the max gross efficiency Gaussian heat release rate profiles constrained by PPRR shown in Figure 6.5. Figure 6.24 shows the FSA predicted fuel and equivalence ratio distributions for the Gaussian HRR constrained to a maximum PPRR of 15bar/deg for the three premixed fuels. The three fuels all exhibit a similarly narrow required fuel and equivalence ratio distribution, indicative of HCCI combustion. The fuels require different premixed fuel percentages, however, demonstrating the differences in reactivity between the fuel sources. Due to the differences in the LHV and AFR_{stoich} of syngas compared to isooctane and

methane, these plots can be somewhat difficult to interpret. For example, for the same pressure, temperature, fuel energy input, etc., the global equivalence ratio of the SYN/PRF0 case is lower than the PRF100/PRF0 and CH4/PRF0 cases. This is an artifact of the difference in the stoichiometric AFRs of the fuels (15.09 for PRF100, 17.19 for CH4, 4.59 for Syngas), combined with the difference in heating values (44.33MJ/kg for PRF100, 50.009 MJ/kg for CH4, 17.48 MJ/kg for Syngas). The two properties actually work in opposite directions, as the low AFR_{stoich} decreases φ, while the low LHV requires more fuel mass, which would increase φ.

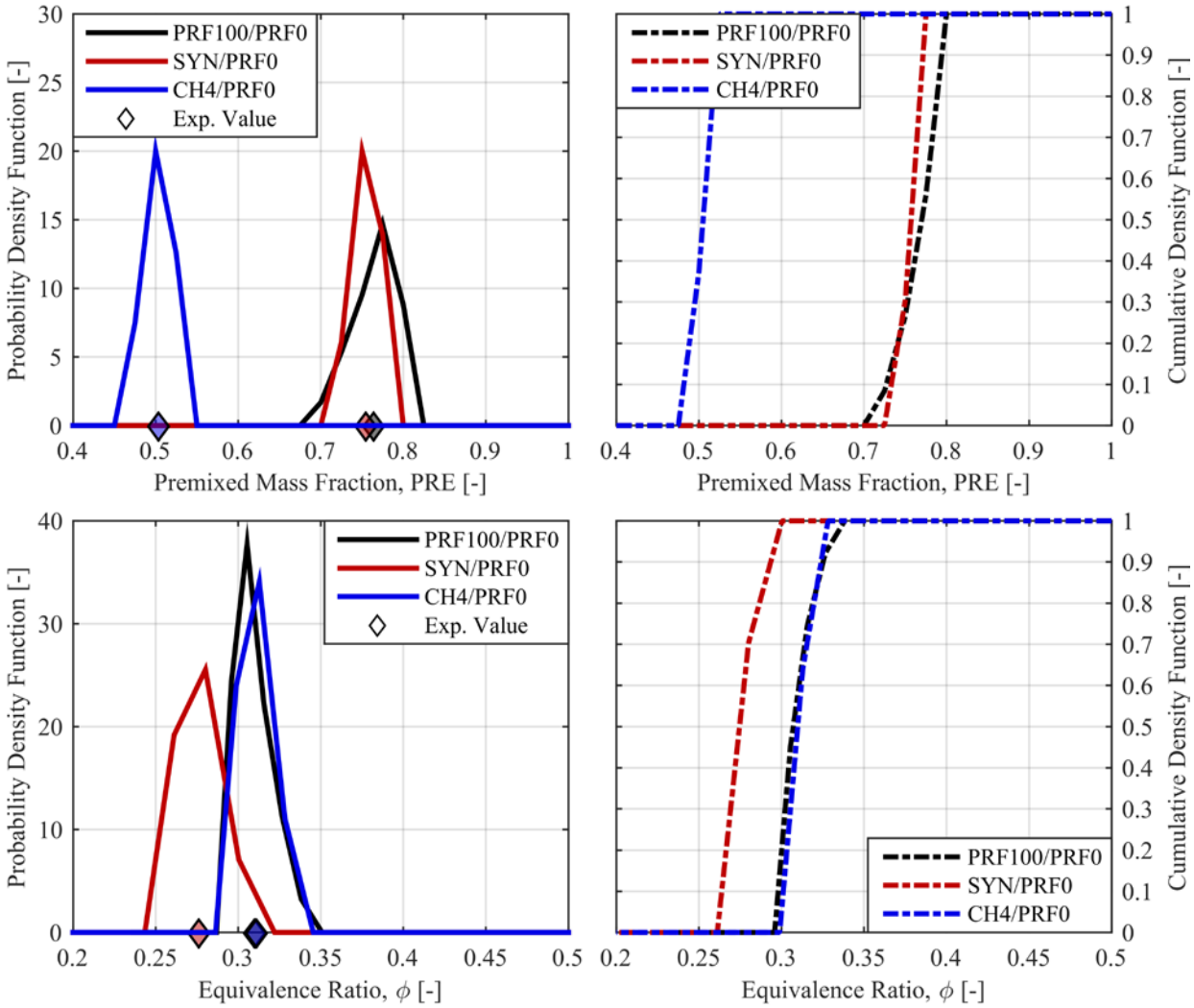

Figure 6.24: FSA predicted PDF (left), and CDF (right) of fuel distribution (top) and equivalence ratio (bottom), for the maximum η_g Gaussian shaped HRR with PPRR constraints of 15bar/deg, for three different premixed fuels, PRF100 (black), 50/50 syngas (red), and CH_4 (blue) with DI n-heptane (PRF0)

Despite the large differences in premixed fuel requirement for the CH4 and PRF100 cases, the equivalence ratio distributions are nearly identical in both range and magnitude. The syngas equivalence ratio distribution appears slightly wider, while the fuel distribution for syngas is actually shorter than the PRF100 case. This may be an artifact of the difference in fuel properties. The cases were also tested at the maximum efficiency, Gaussian-shaped heat release rate cases constrained to 10bar/deg and 5bar/deg. The predicted distributions for these two cases can be seen in Figure 6.25 and Figure 6.26, respectively.

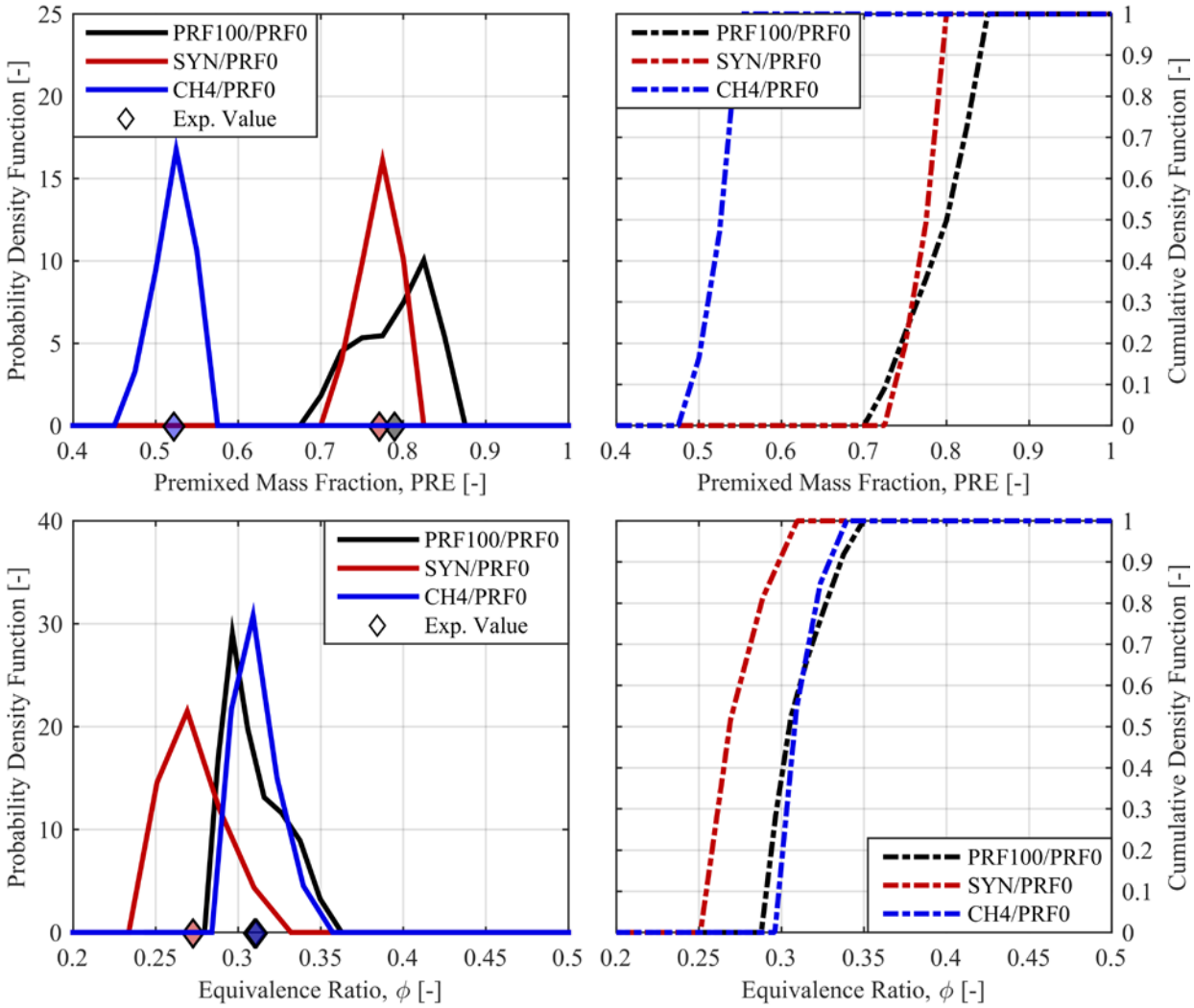

Figure 6.25: FSA predicted PDF (left), and CDF (right) of fuel distribution (top) and equivalence ratio (bottom), for the maximum η_g Gaussian shaped HRR with PPRR constraints of 10bar/deg, for three different premixed fuels, PRF100 (black), 50/50 syngas (red), and CH_4 (blue) with DI n-heptane (PRF0)

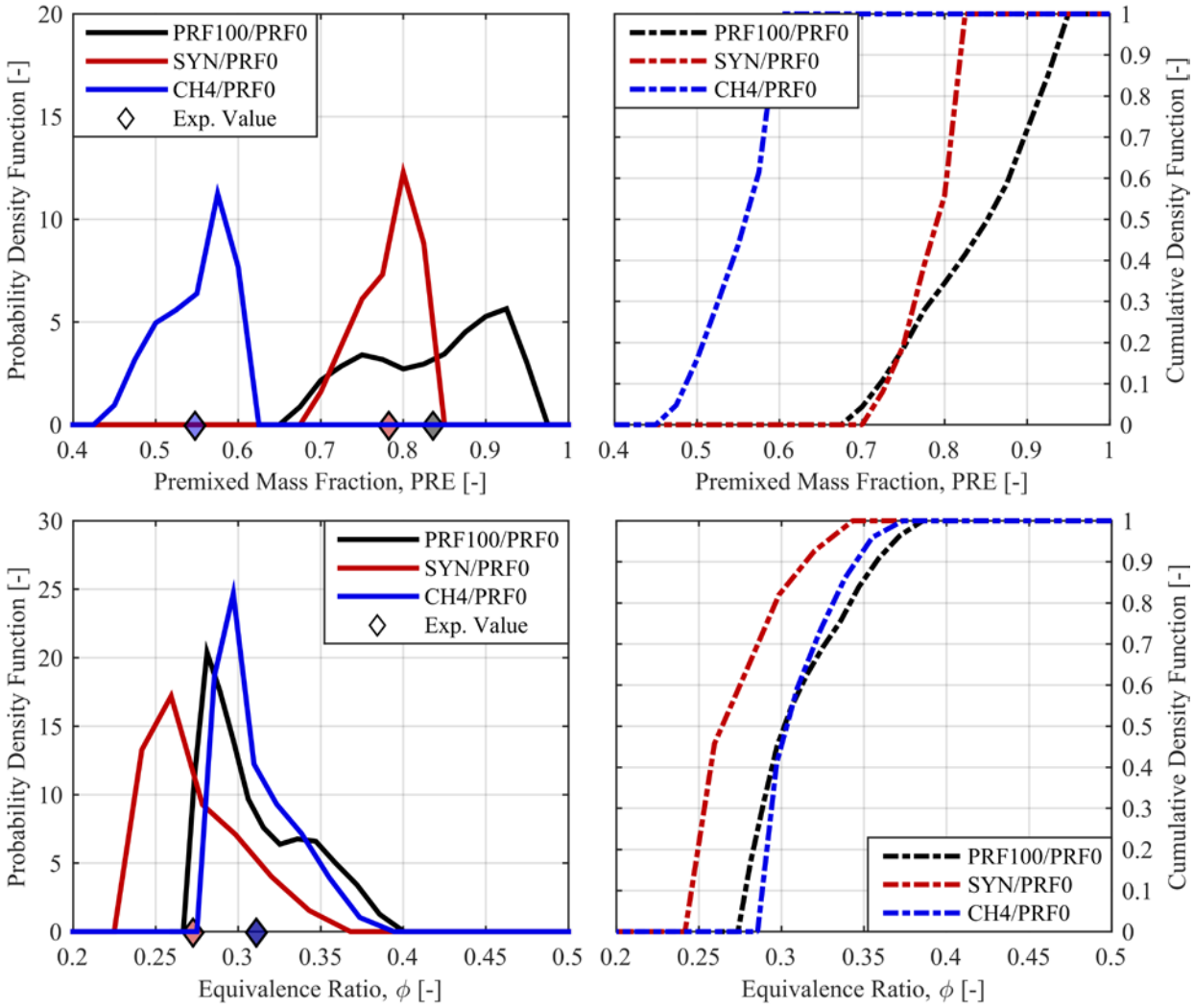

Figure 6.26: FSA predicted PDF (left), and CDF (right) of fuel distribution (top) and equivalence ratio (bottom), for the maximum η_g Gaussian shaped HRR with PPRR constraints of 5bar/deg, for three different premixed fuels, PRF100 (black), 50/50 syngas (red), and CH_4 (blue) with DI n-heptane (PRF0)

Similar behavior is seen in the fuel stratification requirements for the two lower PPRR cases, though the trends are significantly more pronounced for the 5bar/deg case. The less reactive premixed fuels (CH_4 and syngas) show reduced fuel stratification requirements for the same heat release. This is likely due to the greater sensitivity in ignition delay to premixed fuel percent due to the larger reactivity gradient between the premixed and DI fuels. Again, the difference in fuel properties between syngas and PRF100 makes the trends difficult to interpret. Syngas requires less stratification of fuel mass between the DI and premixed fuels, yet this small gradient in fuel mass

induces larger gradients in equivalence ratio because of the differences in stoichiometric AFR for the various mixtures of premixed and DI fuels. When examining fuels with very different physical and/or chemical properties, it is important to keep this in mind.

Finally, the FSA method was used to evaluate a portion of the experimental results shown in Chapter 3. It was shown that matching combustion phasing with different premixed fuels was insufficient to retain the performance and emissions from some arbitrary baseline fuel combination (in this case PRF100/PRF0), but that if the entire heat release rate could be matched, then the efficiency and emissions would approach the baseline results. Therefore, the approach taken here was to analyze the same baseline PRF100/PRF0 cases, and predict the fuel stratification required to match the PRF100 heat release rates with syngas and CH_4 as the premixed fuel.

Table 6.5: Experimental operating conditions of PRF100/PRF0 experiments and FSA predictions

SOI [°ATDC]	Q_{fuel} [J/cyc]	φ [-]	η_{comb} [%]	P_{IVC} [kPa]	Exp. T_{IVC} [K]	FSA T_{IVC} [K]
-140	2602	0.307	97.8	127.4	364	359
-50	2603	0.307	97.5	126.1	349	360
-40	2601	0.307	97.2	126.6	362	363

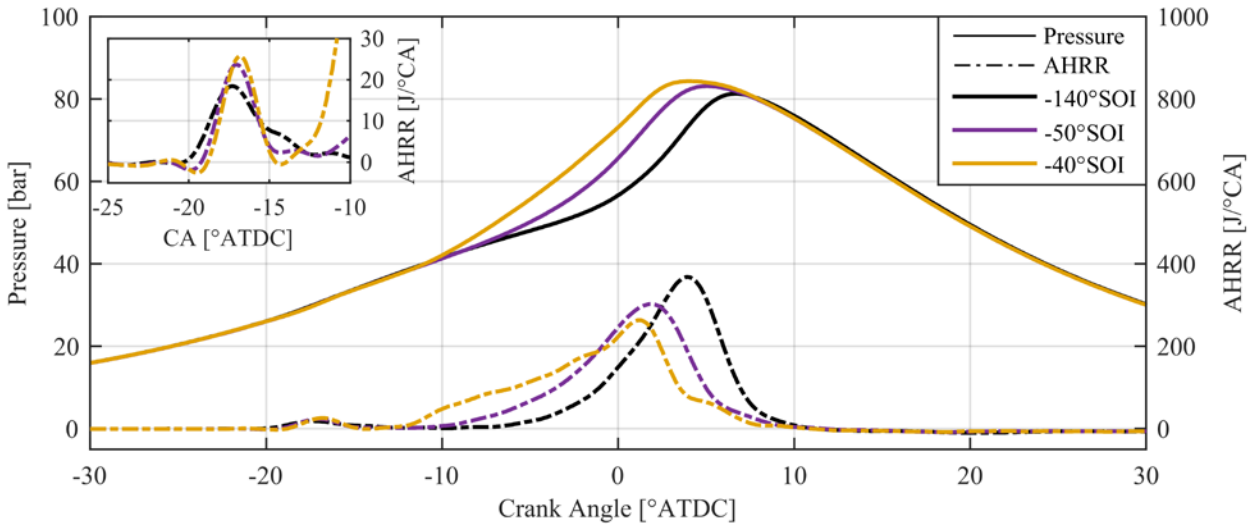

Figure 6.27: Pressure and HRR of experimental RCCI data with PRF fuels for various SOI timings at φ = 0.30, T_{in} = 40°C, P_{in} = 114.5kPa, and a fixed global PRF of 88.0

Table 6.5 shows the experimental operating conditions of the baseline PRF100/PRF0 cases examined in this section, and Figure 6.27 shows the baseline experimental pressure and heat release rates for the three SOI timings for PRF100/PRF0. The approach taken was: adjust the IVC temperature for the PRF100/PRF0 case until the FSA method predicted the experimental premixed fuel percentage within ±0.25%, resulting in FSA T_{IVC} shown in the table. Next, the FSA method was used for the two other fuel combinations by iterating the global premixed mass percentage until the predicted value and the global value converged.

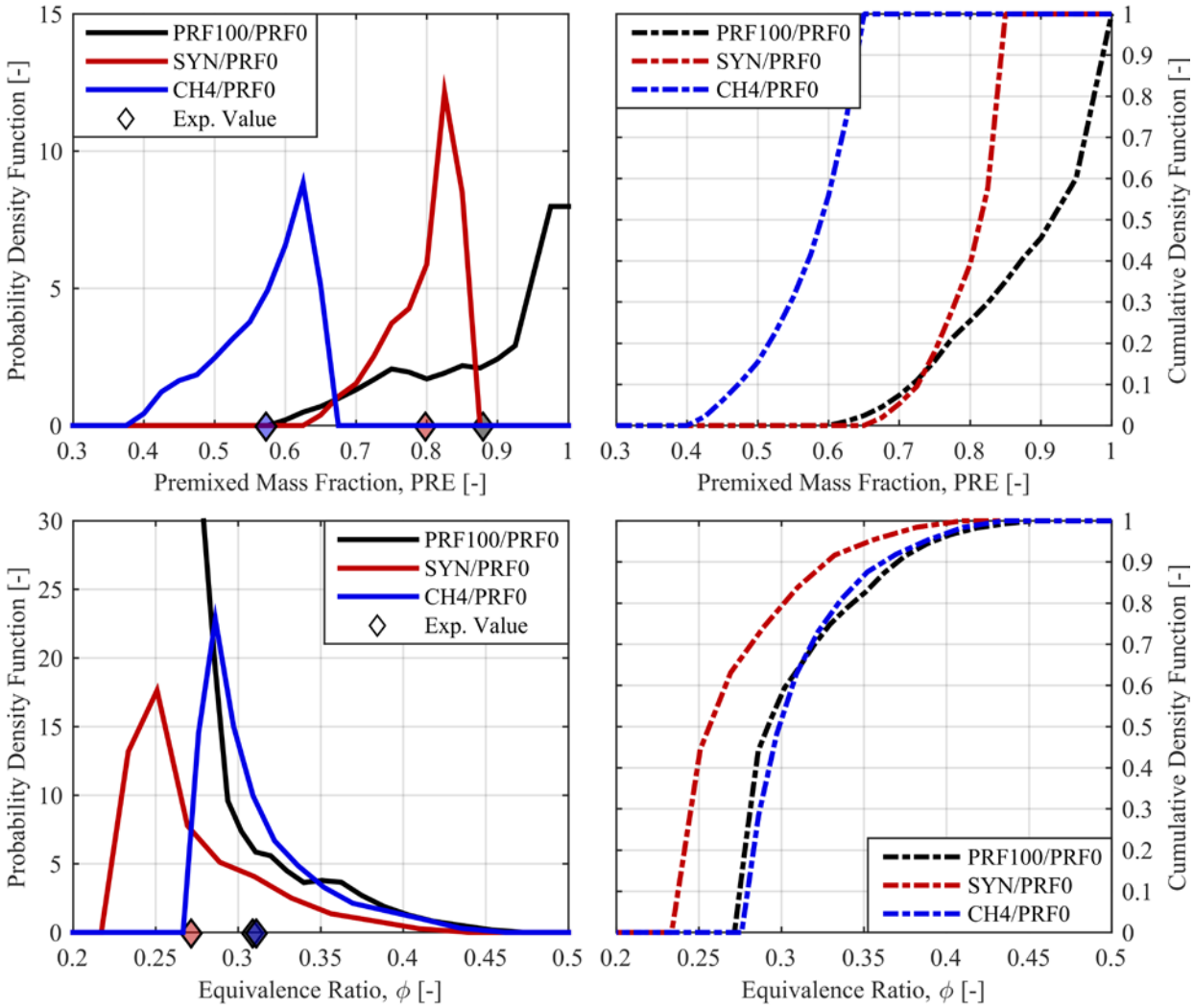

Figure 6.28: FSA predicted PDF (left), and CDF (right) of fuel distribution (top) and equivalence ratio (bottom), for the -50°SOI matched HRR case, for three different premixed fuels, PRF100 (black), 50/50 syngas (red), and CH_4 (blue) with DI n-heptane (PRF0)

Figure 6.28 shows the FSA predicted fuel and equivalence ratio distributions for the three different fuel combinations at the -50°SOI baseline case. The FSA method converged on ~80%$_m$ syngas, and about ~58%$_m$ CH_4, compared to the baseline 88%$_m$ PRF100. The equivalence ratio distributions for the CH_4/PRF0 and PRF100/PRF0 baseline case are very similar in terms of range and magnitudes. This result indicates that the quantity of stratified fuel between the two cases is similar, despite the ratio of the two fuels being quite different. These factors indicate that a large portion of DI fuel would have to be premixed, while the stratified portion of the fuel should be similar between the PRF100/PRF0 and CH4/PRF0 cases. The heat release matching was accomplished experimentally by doing exactly this, i.e., premixing n-heptane with a valve overlap injection at -320°SOI, while maintaining the duration and timing of the DI event from the PRF100 baseline case. The experimental pressure and heat release rate for the matched HRR cases for the -50°SOI baseline can be seen in Figure 6.29, where the mass percentage of low reactivity fuel is indicated in the legend for each case. This value is equivalent to the global premixed percentage from the FSA method results.

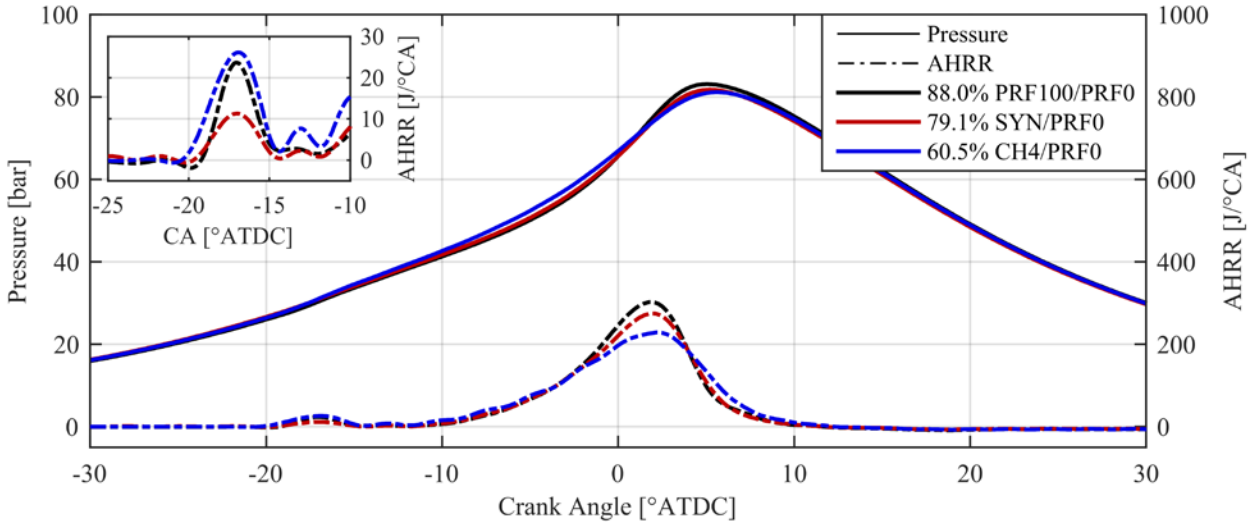

Figure 6.29: Pressure and HRR for three matched HRR cases with different premixed fuels and DI n-heptane. PRF100 case with an SOI of timing -50°, Syngas and CH_4 with injections at -320° and -50°. The percentage in the legend corresponds to the low reactivity fuel mass percent

The FSA method result predicts very similar global fuel ratios compared to the experimental data for the matched HRR conditions (58% vs. 60.5% for CH_4, and 80% vs. 79.1% for syngas). This agreement between the experimental results and the FSA method further validates the methodology; however, significant interpretation is required to relate the results of the FSA method with any specific injection strategy, which is the inherent limitation of the methodology. Figure 6.30 shows the FSA predicted fuel and equivalence ratio distributions for the three fuel combinations at the -40°SOI baseline case.

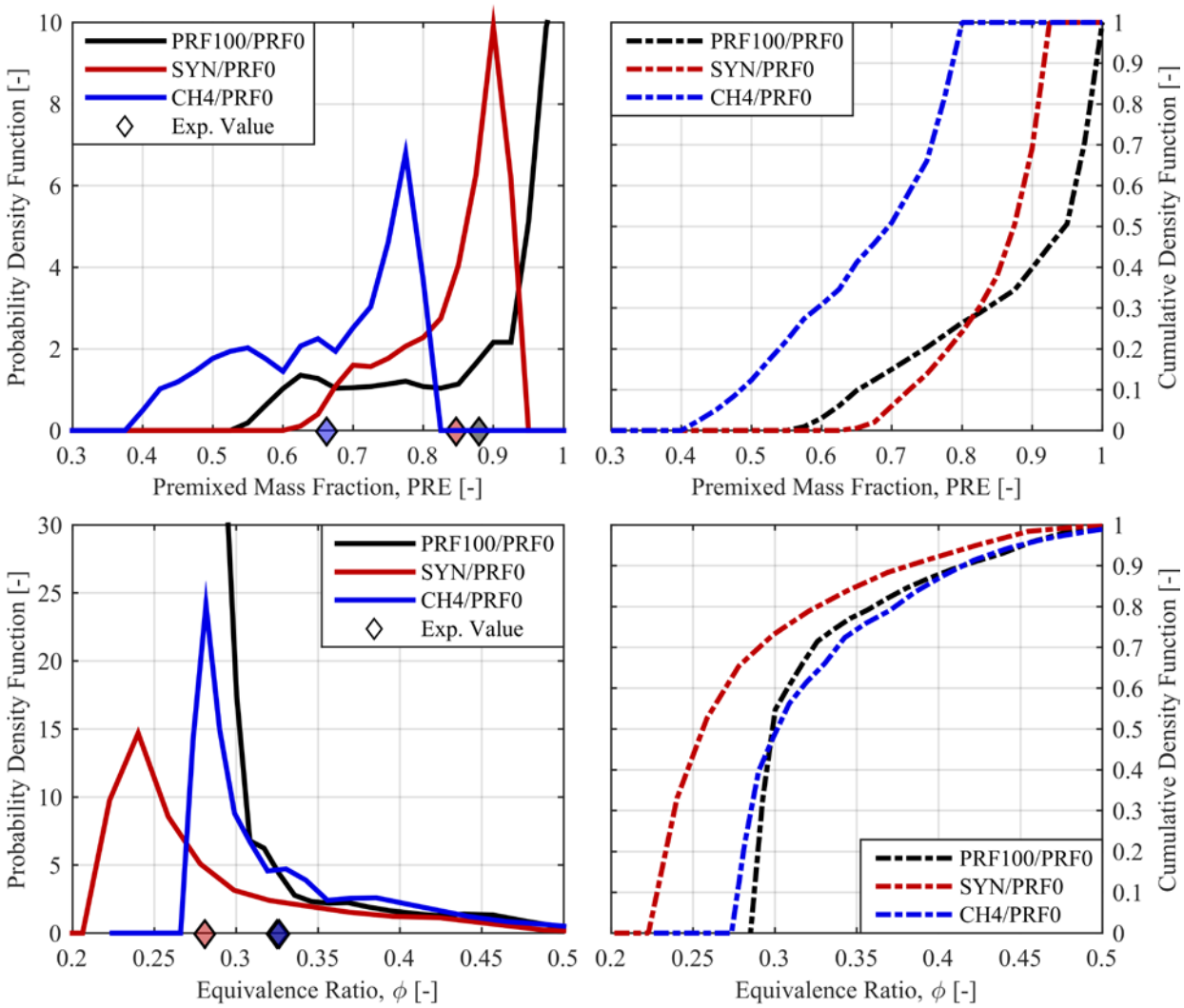

Figure 6.30: FSA predicted PDF (left), and CDF (right) of fuel distribution (top) and equivalence ratio (bottom), for the -40°SOI matched HRR case, for three different premixed fuels, PRF100 (black), 50/50 syngas (red), and CH_4 (blue) with DI n-heptane (PRF0)

For the -40°SOI case, the FSA method converged on a premixed percentage for CH_4 of about 66%, and about 85% for syngas, compared to the baseline 88% for PRF100. The syngas case was not tested experimentally at the -40°SOI timing; however, the CH_4 case was tested, and is shown along with the baseline PRF100 case in Figure 6.31. The experimental data required a CH_4 percentage of 61.7%, compared to the FSA predicted 66%. This difference is greater than the -50°SOI case; however, it would provide a reasonable starting point for future experimental efforts. The FSA predicted equivalence ratio distributions for the PRF100 and CH_4 cases show relatively similar trends; however, there is some deviation at the lower equivalence ratio end. Again, the syngas case demonstrates a narrower distribution in terms of fuel mixture, but with a wider distribution of equivalence ratio resulting from the difference in AFR_{stoich}.

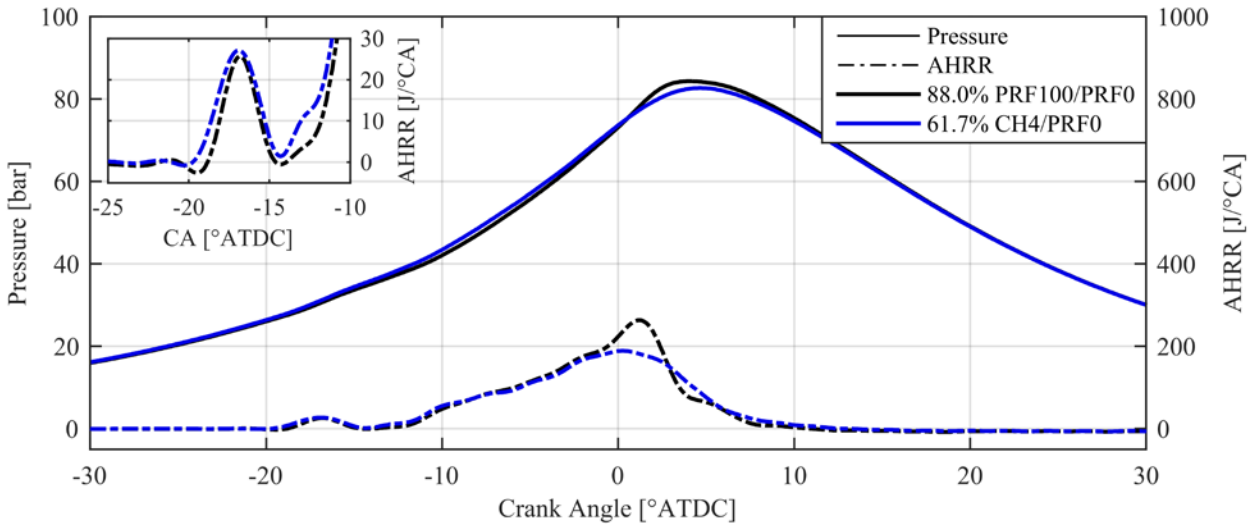

Figure 6.31: Pressure and HRR for two matched HRR cases with different premixed fuels and DI n-heptane. PRF100 case with an SOI of timing -40°, CH_4 with injections at -320° and -40°. The percentage in the legend corresponds to the low reactivity fuel mass percent

The final condition tested was the -140°SOI baseline case. This condition was not tested experimentally for CH_4 or syngas; however, it can still provide useful information regarding the stratification and global fuel requirements for this condition. The experimental pressure and heat release rate for the baseline PRF100/PRF0 case are shown in Figure 6.32.

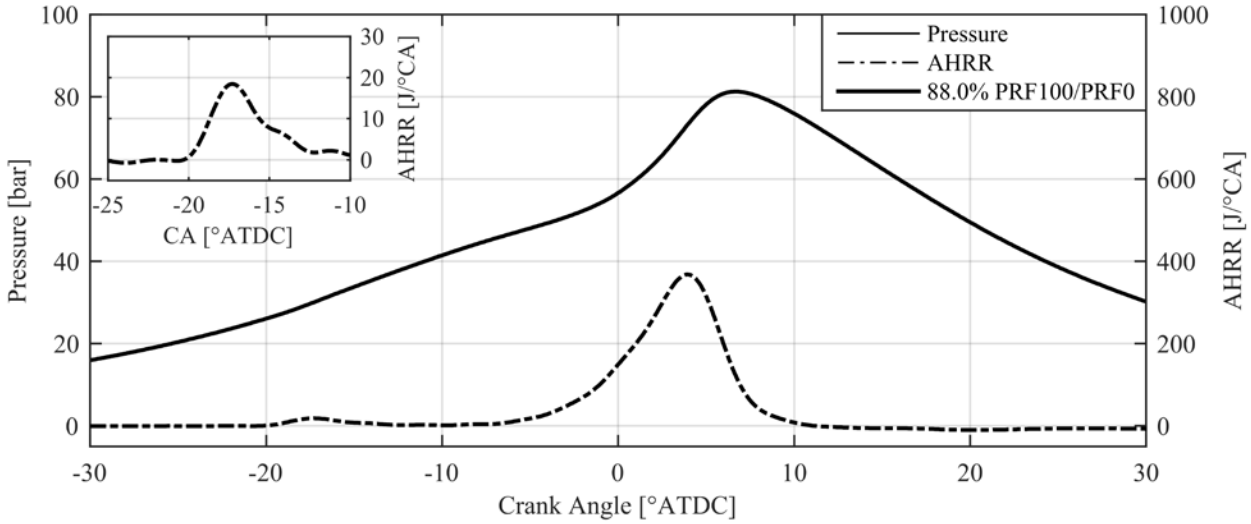

Figure 6.32: Pressure and HRR for the PRF100/PRF0 experimental case with an SOI of timing -140°. The percentage in the legend corresponds to the low reactivity fuel mass percent

The FSA predicted fuel and equivalence ratio distributions for this case can be seen in Figure 6.33. The global predicted fuel ratios for the -140°SOI case were nearly identical to the -50°SOI case. The FSA method predicted a global CH_4 mass percentage of about 58%, and about 80% for syngas. It would therefore be expected that, experimentally, these conditions would likely require CH_4 and syngas percentages very similar to the -50°SOI experimental results (60.5%$_m$ and 79.1%$_m$, respectively). The equivalence ratio distributions for the CH_4 and PRF100 cases are nearly identical in magnitude across the entire distribution. This indicates that, like the -50°SOI case, the injection strategy would require a premixed injection of n-heptane, and the same quantity of stratified fuel for the PRF100 and CH_4 cases.

Due to the similarity of the PRF100 and CH_4 cases and the fact that the experimental results for the -50°SOI case agreed very well with this strategy, it is likely that the Syngas/PRF0 case would require a very similar injection strategy. Owing to the differences in fuel properties between Syngas and PRF100, this is not explicitly obvious from the predicted fuel distributions, as the differences in AFR_{stoich} tend to stretch the equivalence ratio distributions more than expected.

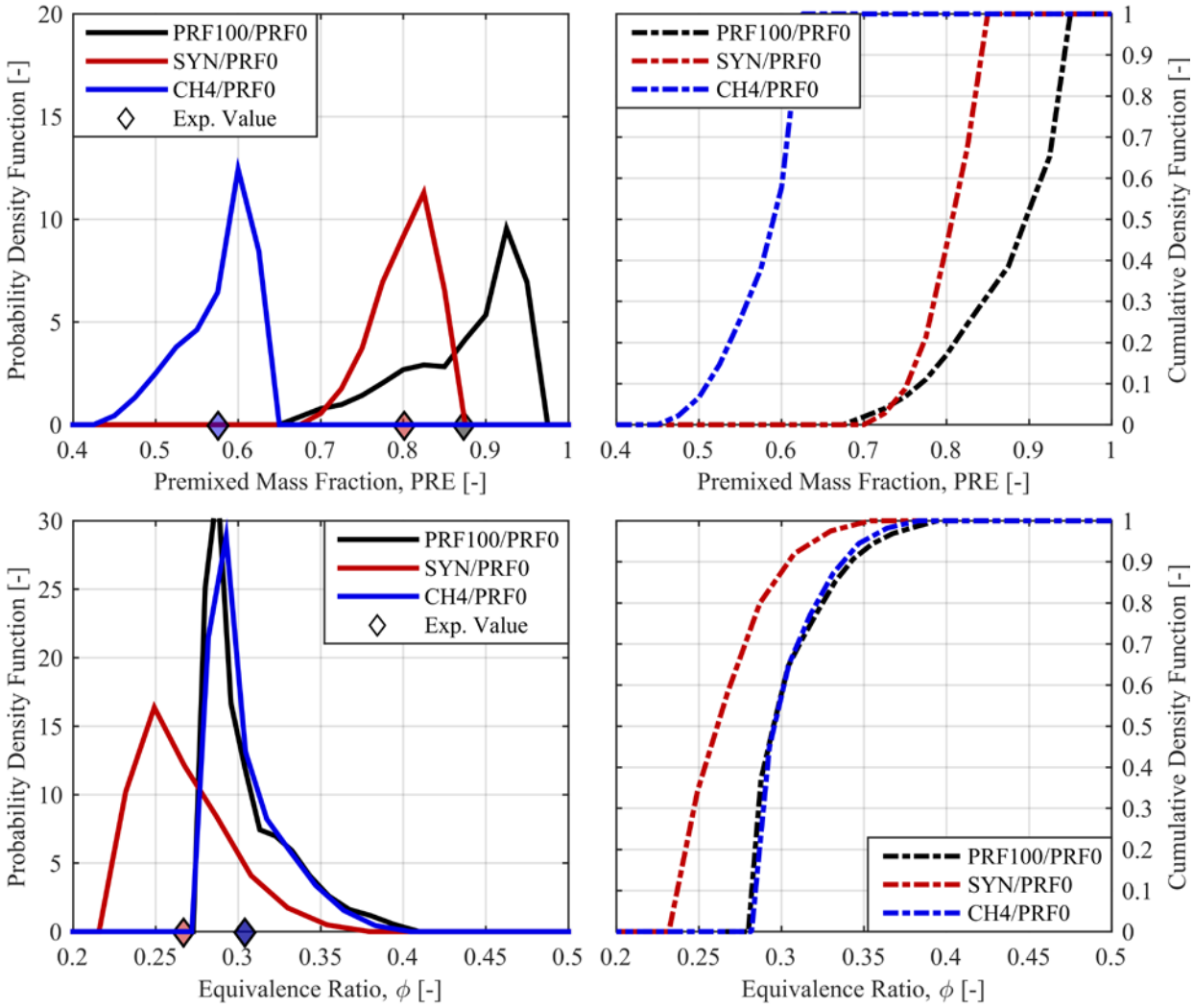

Figure 6.33: FSA predicted PDF (left), and CDF (right) of fuel distribution (top) and equivalence ratio (bottom), for the -140°SOI matched HRR case, for three different premixed fuels, PRF100 (black), 50/50 syngas (red), and CH_4 (blue) with DI n-heptane (PRF0)

7 SUMMARY AND CONCLUSIONS

The main conclusions and findings of the present work are summarized in the following section. The work utilized heavy-duty engine experiments operating under HCCI and RCCI combustion modes, with various premixed fuels including isooctane, methane, and syngas. The HCCI experiments also utilized premixed injections of n-heptane, accommodated by a new intake runner design which houses four separate fuel injectors, and the RCCI experiments used direct-injections of n-heptane with a high pressure common-rail system, and the addition of a small amount of lubricity improver. The engine experiments with PRF fuels were validated with 3-D CFD performed using KIVA-3Vr2, coupled with a reduced chemical mechanism.

A 0-D post-processing methodology developed in MATLAB to predict fuel stratification requirements in kinetically-controlled, stratified-charge combustion strategies was proposed and validated with non-reacting and reacting CFD data. The method was then used to analyze various simulated heat release rate events for various premixed and direct-injected fuels to study the effects of heat release shape and fuel chemistry on the fuel stratification requirements.

7.1 HCCI Engine Experiments

HCCI engine experiments were conducted using separate port fuel injections of isooctane and n-heptane. The engine speed and total fuel energy were held constant, and the blend of the PRF fuels was varied at two intake temperatures (40^{o}C, and 60^{o}C) and three global equivalence ratios (0.25, 0.28, 0.30), which was set by adjusting the intake pressure. It was shown that the PRF number does not linearly adjust combustion phasing (defined by CA50), and that the sensitivity of CA50

to PRF number was greater at 0.30 then 0.25 and constant T_{in}, but was similar between 40°C and 60°C intake temperatures at a constant φ.

For decreasing global equivalence ratio, the combustion phasing advanced. This occurred because the constraints of the experiment required an increase in intake pressure to achieve a decrease in equivalence ratio. The higher cylinder pressure was assumed to be responsible for the acceleration of the kinetics for the leaner cases. For a given combustion phasing, there exist many combinations of PRF mixture and intake conditions which could achieve such a phasing. A change in intake temperature of 20°C was found to require an increase in PRF number of 3 to match combustion phasing at φ = 0.30. For a fixed PRF, the same 20°C increase in intake temperature required an increase in φ from 0.25 to 0.30, along with a corresponding decrease in intake pressure of 17.9kPa.

HCCI experiments were also performed with various mixtures of PRF fuels and syngas (composed of 50% CO, and 50% H_2). The experiments were performed at two operating conditions, and fixed combustion phasing of 3.75°±0.25. This phasing corresponded to the combustion phasing of PRF91 at the two operating conditions (T_{in} = 40°C, φ = 0.25, and T_{in} = 60°C, φ = 0.30). The results showed that syngas was significantly less reactive than isooctane (indicating an octane number > 100), because the quantity of n-heptane required to match combustion phasing was much greater for syngas/n-heptane than for isooctane/n-heptane (~25%$_m$ vs. ~9%$_m$). At low syngas percentages (<50%$_m$), the two intake conditions required a nearly identical PRF mixture to match combustion phasing. At higher syngas percentages (>50%$_m$) the two trends deviated slightly, potentially indicated differences in either the pressure or φ sensitivities between syngas and PRF fuels.

The syngas was shown to suppress the LTHR event compared to the pure PRF cases at both intake conditions, and demonstrated slightly reduced peak heat release rates. These differences were

relatively minor compared to the cycle-to-cycle variability in the HCCI cases, however. The syngas cases tended to exhibit greater cyclic variability compared to the cases without syngas, potentially due to higher variability in the shot-to-shot mass of fuel injected by the gaseous PFI.

7.2 Experimental RCCI Results with Primary Reference Fuels

RCCI experiments were conducted with PRF fuels at similar operating conditions to the HCCI experiments presented in this work. The first set of experiments assessed the effect of injection timing and global equivalence ratio on RCCI performance and emissions with a fixed premixed mass fraction of 88.1±0.2%. Three global equivalence ratios (0.28, 0.30, and 0.35) were studied, and SOI timing was swept from -140^{o} to -17^{o}ATDC. As SOI timing was retarded between -140^{o} and -35^{o}ATDC, combustion phasing advanced, but as SOI timing was further retarded, CA50 also retarded, potentially indicating a transition from a kinetically-controlled combustion regime to a mixing-controlled regime. The combustion phasing of the three global φ cases converged around an SOI of about -30^{o}ATDC, and followed the same path as SOI further retarded. This result indicated a decrease in the sensitivity of combustion phasing to intake pressure, supporting the notion of a change in combustion regime.

Peak gross efficiency was achieved between SOI timings of -60^{o} and -45^{o}ATDC for all three global φ's, potentially due to an optimization of combustion phasing, duration, and heat transfer effects. Combustion efficiency was relatively constant at about 98% until late SOI timings, where it decreased rapidly. NO_x emissions increased dramatically at SOI timings later than -40^{o}ATDC, peaking around -25^{o}SOI. The combination of combustion phasing, and high local equivalence ratios caused by retarded SOI timing was to blame for the high NO_x emissions in this region.

To eliminate the influence of combustion phasing on the performance and emissions results, a separate test was conducted where combustion phasing was held constant at the peak efficiency location (CA50~1^{o}CA), and the premixed percentage was adjusted as SOI was swept to match phasing. Initially, as injection timing was retarded, the required PRF was increased to match combustion phasing. After -25^{o}SOI, the required PRF decreased rapidly as the combustion process became less sensitive to the global fuel kinetics, and more sensitive to the mixing process. Gross efficiency again peaked between -60^{o} and -45^{o}ATDC SOI timings, and the NO_x emissions increased as SOI retarded beyond -35^{o}ATDC due to high local equivalence ratios. Whether fixing global fuel reactivity or combustion phasing, it was found that the optimal cases in terms of both gross efficiency and PPRR were in mid-range SOI timings around -50^{o}ATDC at these conditions. Late injection timings resulted in decrease η_g, decreased combustion efficiency, and high NO_x emissions due to the overly stratified mixture. Very early SOI timings, including HCCI, suffered from high PPRR, resulting in increased combustion noise and decreased η_g.

7.3 Experimental RCCI Results with Methane and Syngas

In order to assess the performance of syngas and methane as premixed fuels in RCCI combustion, the best case from the PRF data set, corresponding to an SOI timing of -50^{o}ATDC at T_{in} = 40^{o}C, and φ = 0.30 was used as a baseline reference condition, and isooctane was replaced as the premixed fuel. For the syngas cases, the combustion phasing of the baseline PRF case was matched by adjusting the DI SOI timing at a matched premixed mass percentage, and by adjusting the premixed mass percentage with a matched SOI timing, separately. For the methane cases, the SOI timing alone did not provide sufficient control to match the combustion phasing, so this case was omitted. The HRR of the baseline condition was also match for the two alternate premixed fuels

by maintaining the SOI timing and duration of the baseline direct injection event, and adding a direct injection of n-heptane at -320°ATDC to increase the background reactivity of the premixed fuel to a mixture that approximated the reactivity of isooctane. This insured that the in-cylinder gradients of reactivity and equivalence ratio, which define the heat release shape and phasing, were matched. For both premixed fuels, matching CA50 alone resulted in decreased η_g, and drastically increased NO_x emissions due to the high DI fuel requirements necessary to overcome the less reactive premixed fuels. Matching the bulk heat release characteristics was shown to regain most of the lost efficiency, while decreasing NO_x emissions close to the baseline level.

7.4 FSA Method Development

A 0-D methodology was developed to predict the fuel stratification necessary to achieve a certain heat release in stratified-charge, kinetically-controlled combustion strategies. The model was inspired by the Thermal Stratification Analysis (TSA) tool developed by Lawler et al. [15, 20], which predicts in-cylinder thermal stratification in HCCI combustion events at the start of combustion, based on autoignition predictions, and experimental mass fraction burned data. The FSA method utilizes a similar approach to predict the distribution of fuel in the cylinder at the start of combustion. Autoignition predictions are performed with the Livengood-Wu autoignition integral for various possible fuel mixtures, and associated equivalence ratios, for many possible thermal pathways in the cylinder. These autoignition predictions are then related to the energy released during specific crank angle windows, and probability density functions of the fuel distribution are calculated. The implicit and explicit assumptions associated with the FSA method are as follows:

- The pressure is uniform in the cylinder.

- The premixed fuel, air, residuals, and EGR are completely mixed at IVC.
- Chemical reaction rates are very fast relative to engine time scales, and therefore when a zone autoignites it does so instantaneously.
- There is no heat or mass transfer between zones, implying that the hot burned gases do not mix with cold unburned gases, and in turn, accelerate the autoignition events.
- There is no flame propagation in the combustion chamber, which would cause zones to burn prior to the autoignition integral prediction.
- Fuel instantaneous vaporizes at the end of injection.

7.5 Validation of 3-D CFD Modeling using KIVA

3-D CFD simulations were performed with KIVA3Vr2 combined with several improved submodels developed at the ERC. A reduced chemical mechanism by Wang et al. [99] was used for all reacting CFD simulations, and ignition delay predictions in this work. A relatively coarse sector mesh with ~10,800 cells and periodic boundary conditions was used for the reacting and non-reacting 3-D CFD simulations.

The CFD model was first validated against HCCI engine data with PRF fuels, and showed good agreement with the experimental pressure and heat release traces with minimal adjustments to the IVC temperature calculated in the experimental results. Some minor discrepancies were seen in the peak heat release rates predicted by the CFD simulations at the very lean cases ($\varphi = 0.25$), which tended to under-predict the peak values, while over-predicting the combustion duration. All the cases required IVC temperature adjustments that were within the range of uncertainty of the experimental IVC temperature calculation.

CFD simulations were then performed on the RCCI combustion cases with fixed global PRF number, and fixed combustion phasing with swept SOI timing. The CFD predictions demonstrated excellent agreement between SOI timings of -90^{o} and -30^{o}ATDC, which is the range of interest in typical RCCI combustion. The earliest injection timings of -140^{o}SOI over-predicted the mixing of the DI fuel, and therefore resulted in a shorter combustion duration than observed in the experiment. Late injection timing cases did not capture the two stage combustion behavior seen in the experimental results particularly well, and the general trends in combustion for the late injection timings were not as well captured as the earlier injection timing cases.

7.6 FSA Method Validation with 3-D CFD Results

The FSA method was validated using reacting CFD pressure and heat release results as inputs to the analysis, and compared to non-reacting simulations which were used to generate the distribution of fuel in the CFD simulations. Various SOI timings, along with an HCCI case with PRF fuels were used as validation for the methodology. In general, good agreement was seen between the non-reacting CFD fuel distributions and the FSA method results between SOI timings of -140^{o} and about -35^{o}ATDC. After this point, the FSA predications and CFD results began to deviate significantly, indicating a violation of one or more of the inherent assumptions of the FSA methodology. Even the HCCI case with no fuel stratification showed reasonable agreement when the FSA method was applied. The results of the validation showed that the FSA method was able to provide relatively good agreement between the predicted and actual fuel distributions from CFD simulations within the range of SOI timings of interest in RCCI combustion (from about -140^{o} to -35^{o}ATDC). Beyond this SOI timing, the FSA predictions are relatively poor, potentially

indicating a transition into a regime where significant flame propagation exists, or a mixing-limited combustion regime.

7.7 Heat Release Shaping

In order to explore the performance and fuel stratification requirements for various arbitrary heat release shapes, a methodology was employed by which the heat release and pressure trace could be calculated based on an arbitrary mass fraction burned profile at some initial IVC conditions (temperature, pressure, fuel energy). Using MATLAB, various Gaussian-shaped heat releases were calculated to explore the effects of combustion phasing and duration on gross efficiency. The fminsearch function was used in MATLAB to determine the optimum combustion phasing and duration for a Gaussian-shaped HRR. Using this approach, and a constraint on the maximum PPRR, the function converged on minimum combustion duration which did not exceed the PPRR constraint. The maximum efficiency occurred with combustion phasing between 2-3^{o}ATDC due to tradeoffs between the effective compression ratio, which is maximized at TDC phasing with minimum combustion duration (i.e., constant volume, ideal Otto cycle combustion), and heat transfer, which increases with advancing CA50.

A representative low temperature heat release was added to a Gaussian HTHR event to explore the effects of the LTHR on the efficiency of the heat release event. A Gaussian LTHR composing 3.5% of the total fuel energy was used, the phasing and magnitude of which was approximated from experimental data at similar global conditions. The introduction of this LTHR resulted in a decrease in calculated gross efficiency of 0.2 points, half of which was a result of an increase in heat transfer due to the increase in temperature and pressure caused by the early heat release. While

this difference is very small, if the maximum gross efficiency is desired, then fuels that do not exhibit NTC behavior, such as ethanol, should be used.

7.8 FSA Predicted Fuel Distributions for Various HRR Shapes

The FSA method was used to calculate the required fuel distribution for a variety of Gaussian-shaped heat release rates for premixed isooctane with direct injected n-heptane. For a constant combustion duration of 8^{o}CA with varying CA50, significant differences in the global premixed fuel percentage and magnitude of the fuel stratification were required. To result in an advanced combustion phasing with a fixed duration, a more stratified mixture was required, along with a more globally reactive mixture. Typically as combustion phasing is advanced, combustion duration decreases. In order to maintain duration with advanced phasing, greater stratification in reactivity and equivalence ratio is required.

For cases with fixed combustion phasing and varying combustion duration, the FSA method predicted a less stratified mixture required for shorter combustion duration, while simultaneously requiring a more globally reactive mixture. Because of the earlier start of combustion of the longer combustion duration cases, the temperature and pressure is increased earlier in the cycle, requiring a less reactive global mixture in order to maintain the same combustion phasing.

Instead of matching CA50 with varying duration, Gaussian heat release rates matching CA10 and CA90 with varying duration were also considered. The FSA method results suggested that the end of combustion (or CA90) fixes the global premixed percentage, while the duration (CA10-90) defines the magnitude of fuel stratification required. For fixed CA10, there was a translational shift of the fuel distribution towards a more reactive global mixture with decreasing combustion duration, along with a rotational shift in the distribution towards less stratified mixtures. For the

fixed CA90 cases, there was a purely rotational shift about a common global premixed percentage that was representative of a decrease in the required fuel stratification for decreasing combustion duration without a significant change in the global reactivity of the mixture.

For the maximum efficiency Gaussian-shaped heat release rates, the lower the PPRR constraint, the greater the combustion duration, and therefore the greater required fuel stratification. Again it was seen that the more homogeneous the mixture was, the more globally reactive the mixture must be. The limiting case of HCCI combustion requires the most reactive global mixture to achieve some desired combustion phasing, and any induced fuel stratification reduces the global reactivity required to achieve the combustion phasing. The introduction of a LTHR event, accounting for 3.5% of the total fuel energy, resulted in an increase in the temperature and pressure prior to combustion. This resulted in a shift in the global PRF required to achieve the prescribed heat release from 80 to 86. This result indicates that it is important to consider the potential for NTC behavior when considering prospective heat release events.

7.9 Varying Premixed and DI Chemistry

In order to explore the effects of varying fuel chemistry on fuel stratification requirements, the FSA method was employed with various premixed and DI fuels. For a Gaussian-shaped HRR with TDC phasing, and CA10-90 of 8^{o}CA, three premixed PRF mixtures (100, 90, and 80), with direct-injected n-heptane were compared. As expected, the more reactive the premixed fuel, the less DI fuel was required to achieve the heat release rate. For less reactive premixed fuels, less fuel stratification was required.

The same heat release rate was tested with various DI PRF mixtures including PRF0, PRF32.5, and PRF65, with PRF100 as the premixed fuel. Again, as expected, decreasing the difference in

reactivity between the DI and premixed fuel necessitated a shift towards greater DI fuel percentage to match combustion phasing. The least reactive mixture (PRF100/PRF65) required a large stratification of equivalence ratio in order to reproduce the desired heat release rate, primarily due to the relatively small difference in reactivity between the premixed and DI fuels (i.e., 35PRF vs. 100PRF for PRF100/PRF0). The equivalence ratio stratification effectively replaced the decrease in reactivity stratification.

The FSA method was used to predict the fuel stratification requirements for alternative premixed fuels, including syngas and methane. The fuels were first compared with the Gaussian HRRs constrained by PPRR. For the 15bar/deg PPRR constraint, the three premixed fuels exhibited similarly narrow required fuel and equivalence ratio distributions, indicative of HCCI combustion. The fuels each required a different premixed fuel percentage, demonstrating the differences in reactivity between the three fuels (~76%$_m$ PRF100, ~75%$_m$ syngas, ~50%$_m$ CH_4). The less reactive premixed fuels (CH_4 and syngas) required reduced fuel stratification for the 10bar/deg and 5bar/deg PPRR constrained cases compared to the PRF100 baseline.

The FSA method was then used to validate a portion of the experiments results presented with methane and syngas. The approach taken was to analyze the baseline PRF100/PRF0 cases, and predict the fuel stratification required to match the PRF100 heat release rates with syngas and CH_4 as the premixed fuel. The FSA method result predicted very similar global fuel ratios compared to the experimental data for the matched HRR conditions with an SOI of -50^{o}ATDC (58% vs. 60.5% for CH_4, and 80% vs. 79.1% for syngas). This agreement between the experimental results and the FSA method further validated the FSA methodology.

8 *FUTURE WORK*

The methodology developed in this work has a number of applications that, due to time and the scope of the work, were unable to be explored in detail. The following section proposes a number of areas for improvement in the methodology, as well as a number of applications of the model that could provide significant insight into the development of kinetically controlled combustion strategies such as RCCI, PFS, PPC, and GCI.

8.1 Improvement and Expansion of FSA method

While the methodology proposed in this work demonstrated good agreement with CFD predicted fuel distributions for the range of SOI timings of interest in RCCI combustion, a number of limitations and assumptions of the methodology still exist, and should be addressed in future iterations of the method. A number of these improvements are listed in this section.

8.1.1 Incorporation of a Multi-Zone Thermal Model

The greatest room for improvement, and the most significant source of uncertainty in the model, is related to the magnitude and influence of the in-cylinder thermal stratification on the autoignition predictions for the various fuel mixture zones. A multi-zone thermal model which includes the effects of heat transfer, such as those proposed in references [22, 110, 111], could provide a much better representation of the in-cylinder temperature as a function of crank angle. This would improve the autoignition predictions, and could provide better agreement between the FSA predictions and the CFD and experimental results shown in this work.

8.1.2 Incorporation of a Two-Stage Autoignition Integral Approach

The use of two-stage fuels such as n-heptane and iso-octane, or any other fuel that presents NTC behavior, pose challenges to the prediction of autoignition. The FSA methodology would benefit from the incorporation of a two-stage autoignition approach such as those proposed in references [112, 113], in terms of both autoignition prediction, as well as predicting the onset and magnitude of the LTHR event. As shown in the present work, the presence of a LTHR event can have a relatively large impact on the global fuel blend required for a given heat release, so predicting the magnitude and timing of the LTHR event is an important consideration for the FSA method.

8.1.3 Predictions of NO_x, and PM Formation and Emissions

With the FSA predicted fuel distributions, efforts could be made to predict the formation of pollutant emissions such as NO_x, and PM for specific heat release events, based on the fuel distribution required to achieve the heat release of interest. The mass distribution of equivalence ratio predicted by the FSA analysis could be combined with estimates of the adiabatic flame temperature of the fuel-air mixture to predict the formation of these molecules. The results would then have to be compared to engine-out emissions measurements, and CFD predicted emissions to validate the methodology. This analysis would provide significant insight into the emissions profiles of various heat release shapes, given some IVC conditions, and provide another parameter by which the heat release rate shape and phasing could be constrained (e.g., maximum gross efficiency HRR with less than the EPA limit for NO_x and PM emissions).

8.2 Explore the effects of Bore Size on Fuel Stratification

Using size-scaling relationships such as those proposed in references [114-117], the effect of varying engine bore size can be isolated. Assuming a constant engine speed scaling approach, the

primary mechanism that differentiates small-bore engines from large-bore engines is the volume to surface area ratio of the combustion chamber. This parameter effects the heat transfer to the piston walls (i.e., larger V/A leads to less heat transfer), therefore influencing the natural thermal stratification. If the thermal stratification for each bore size of interest can be approximated, then the FSA method could be used to predict the differences in fuel stratification requirements for varying bore-sizes. Even without the use of scaling relationships, the FSA method could be used to predict the fuel stratification necessary for a desired heat release as a function of engine speed, load, or varying engine geometry.

8.3 Exploring Simulated Engine Transients

The experimental data presented in this work was all taken at steady-state operating conditions. Real engines, however, frequently operate across speed and load transients. The biggest challenge for a kinetically controlled combustion strategy is transient operation, and the FSA method provides a mechanism by which the stratification requirements during transients can be predicted.

During an engine transient, the fuel flowrate can be adjusted nearly instantaneously as the commanded fuel quantity is delivered “next cycle”. Due to the nature of the air-handling system, there exists a significant time-lag in the ability of the air-handling system to deliver the desired quantity of diluent to match the desired quantity of fuel. Therefore, an engine transient can be approximated as a step-change in the fuel energy input at a fixed intake pressure, or airflow rate, until the desired load (or fuel energy) condition is met. At this point, the air-handling system begins to catch up at the new fuel energy condition, until the desired equivalence ratio is met. This process is illustrated in Figure 8.1, where the fuel energy exhibits a step change, while the global

equivalence ratio initially increases with no change in the IVC pressure, and then recovers to the initial equivalence ratio set-point.

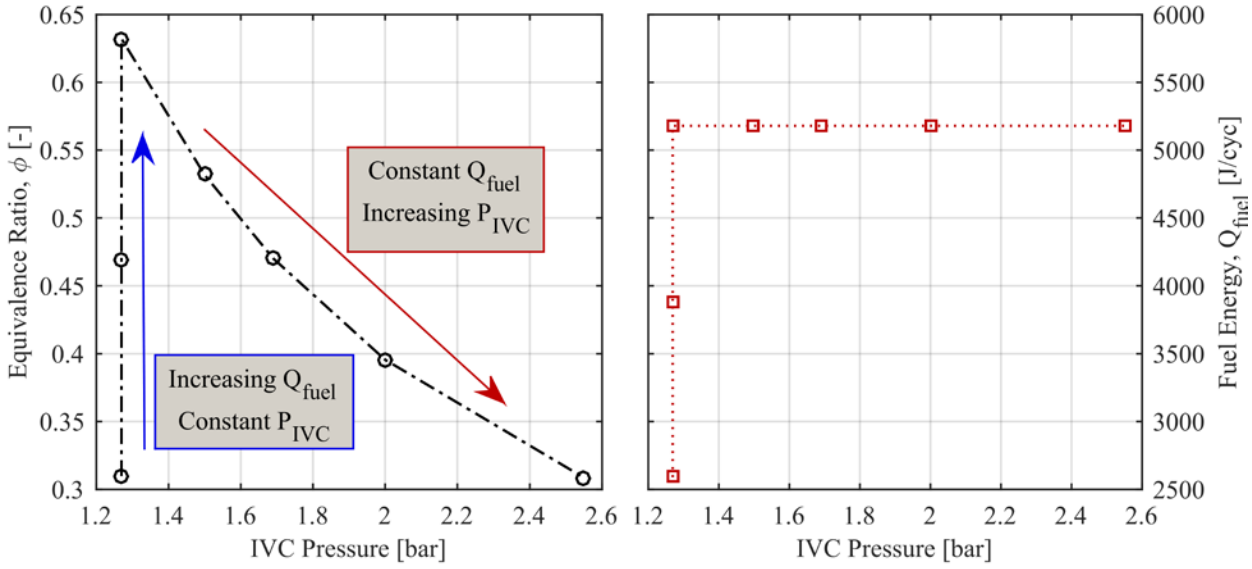

Figure 8.1: An illustration of the process of a simulated transient. The fuel energy is increased essentially instantaneously, with a delay in the air-handling system response

Figure 8.2 shows the maximum gross efficiency, Gaussian-shaped heat release rates at selected steps along the simulated engine transient as an example. These pressure and heat release traces could be used with the FSA method to predict the necessary fuel stratification for the load transient.

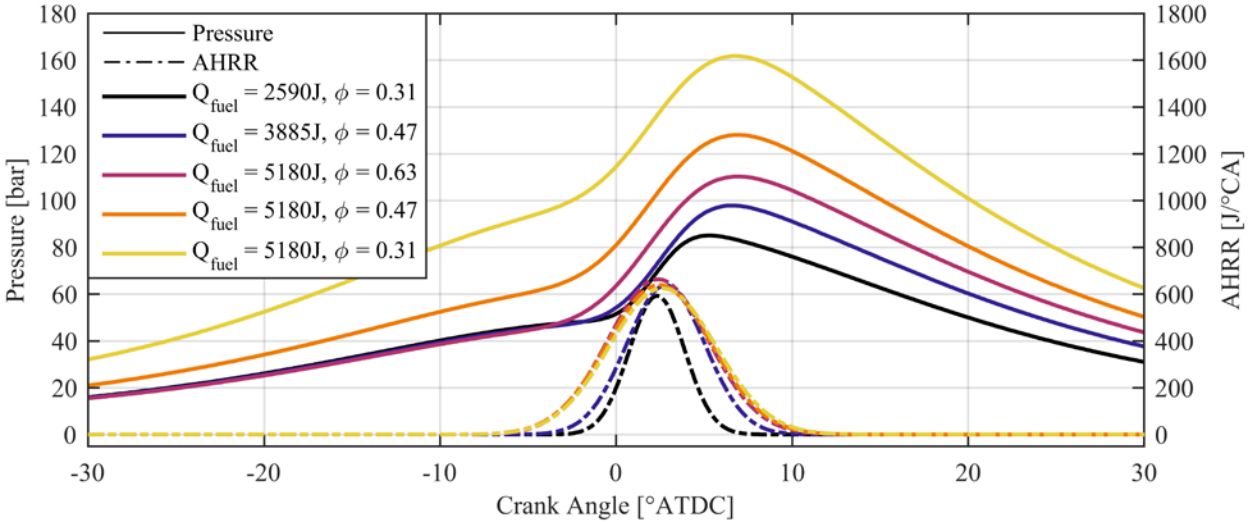

Figure 8.2: Maximum gross efficiency pressure and heat release rate for a Gaussian-shaped HRR constrained to 10bar/deg PPRR, at various intake conditions for a simulated transient from Q_{fuel} = 2590J to 5180J

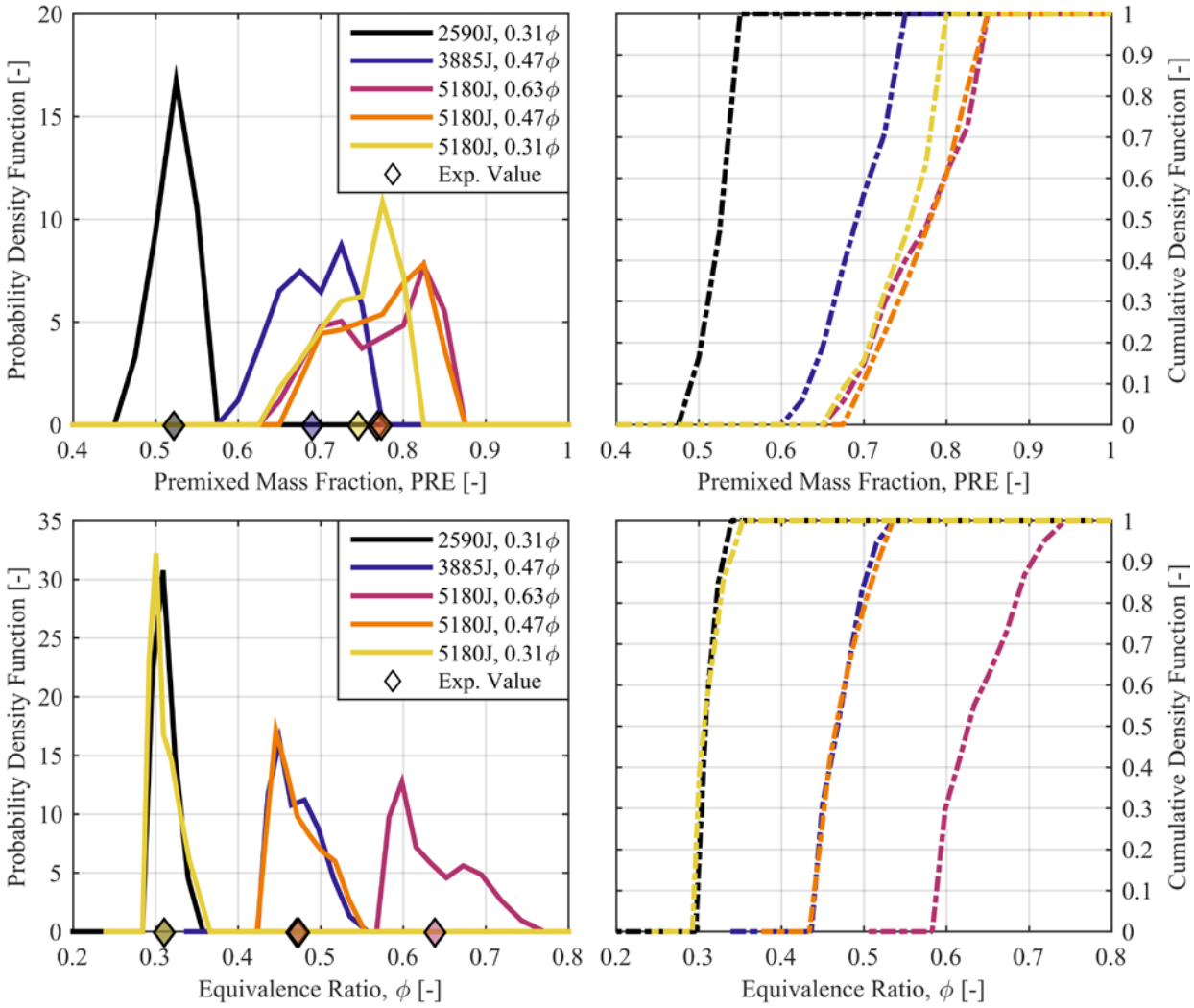

Figure 8.3: FSA predicted fuel mass distributions (top), and equivalence ratio distributions (bottom), for a simulated transient event with CH_4/PRF0 as the fuel combination from Q_{fuel} = 2590J to 5180J, with Gaussian-shaped HRRs constrained to 10bar/deg PPRR

Figure 8.3 shows the FSA predicted fuel and equivalence ratio distributions for the simulated transient shown in this section using premixed CH_4 and direct-injected n-heptane. For the first portion of the transient event (i.e., the instantaneous increase in fueling), the methane percentage increases significantly, from about 52%$_m$ to 78%$_m$, responding to the increase in global φ, with a simultaneous increase in the stratification of the DI fuel to match the increasing combustion duration. For the second transient phase (i.e., the boost pressure recovery stage), the global methane percentage actually decreases slightly from about 78%$_m$ to 75%$_m$ as the global φ

decreases, and the fuel mixture becomes less stratified due to the increasing sensitivity of ignition delay to equivalence ratio, and the constant combustion duration of the second phase heat releases. This example demonstrates the method by which an engine load transient may be simulated at constant engine speed. Assuming the user could model the air-handling system response, an actual transient event could be captured using this methodology as well. This could be especially useful if the emissions can be predicted using the FSA method as discussed previously, allowing the user to develop an operation pathway through transient events, which optimizes the tradeoffs between efficiency, pollutant emissions, and combustion noise.

8.4 Analyzing Cycle-to-Cycle Variations with FSA Method

A significant challenge of kinetically controlled combustion strategies is cyclic variability due to variations in the premixed charge composition, temperature, fuel mass, and variations in the turbulent mixing processes. Kinetically controlled strategies are inherently susceptible to cyclic variability due to the sensitivity of the fuel kinetics to these parameters. The FSA method could be used to analyze the potential sources of these cycle-to-cycle variations in combustion phasing and performance. The potential sources that could be analyzed with the FSA method include IVC temperature, percentage of premixed fuel, and distribution of direct-injected fuel. Figure 8.4 shows an example of the cyclic variability present in an HCCI combustion event with a global PRF of 88.8, and an RCCI combustion case with an SOI of -50^{o}, and 88.2% premixed PRF100 with direct injected PRF0. The input parameters required to match the individual cycle heat release events, such as IVC temperature, premixed percentage, and fuel distribution could be independently calculated for each cycle in order to explore the potential cycle variations of these inputs.

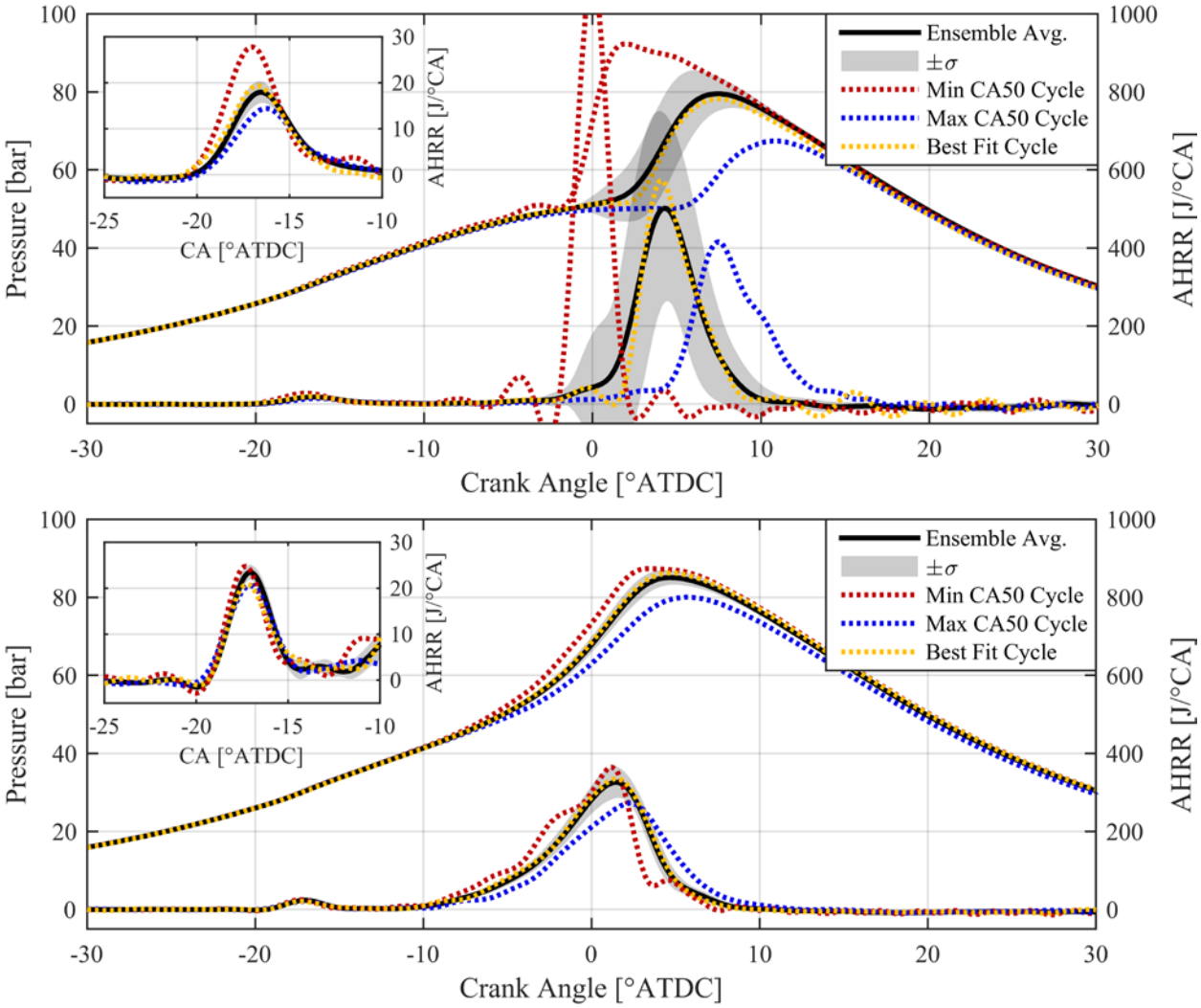

Figure 8.4: Ensemble averaged pressure and heat release rate (black lines) of 250 cycles with standard deviation range (grey region) and cycles representing the minimum CA50 (red dotted), maximum CA50 (blue dotted), and best fit with the ensemble averaged (yellow dotted) for HCCI (top), -50°SOI (bottom)

8.5 Coupling a Genetic Algorithm Targeting Fuel Distributions

While the FSA method is able to predict a probability density function of the fuel distribution, this distribution on its own says nothing about the direct injection strategy required to achieve this distribution. Once a favorable heat release rate has been defined, and the fuel distribution required to achieve such a heat release is calculated with the FSA method, non-reacting CFD simulations could be coupled with a genetic algorithm (GA) to develop the injection strategy required to recreate the fuel distribution. The GA would have to vary injection parameters including number

of injections, injection timings, quantity of mass in each injection, and injection pressure. The calculated fuel distribution at each iteration of the GA could then be compared to the desired fuel distribution to determine its fitness. This process would continue until the GA converged on an injection strategy which best approximated the desired fuel distribution. This method would allow the coupling of the fuel distribution to the injection strategy, thus providing all the inputs necessary to achieve some optimal heat release rate.

8.6 Coupling FSA Method with 1-D Spray Model

While the use of non-reacting 3-D CFD, coupled with a genetic algorithm, could provide the injection strategy for a given fuel distribution, this method is relatively computationally expensive. A simplified spray model such as the 1-D model proposed by Pastor et al. [118], and further developed by Musculus and Kattke [119], could be used to generate fuel distributions for various injection strategies, which could again be coupled to a GA in order to optimize the injection strategy for a targeted fuel distribution. This method provides a more computationally efficient solution than using 3-D CFD due to the model's relative simplicity.

8.7 Comparisons of Real and Reference Fuels

The work presented here only examined pure and reference fuels because of the extensively studied chemistry of these fuels, and the availability of chemical mechanisms which adequately predict their performance. Real fuels such as gasoline, diesel, and natural gas are blends of many different chemical components, and can vary widely in composition. The performance of these fuels can vary significantly from their reference fuel counterparts under modern engine conditions, and thus require robust chemical surrogates in order to model their performance.

REFERENCES

[1] Heywood, J. B., 1988, Internal Combustion Engine Fundamentals, McGraw-Hill.

[2] EIA, 2015, "Nonpetroleum Share of Transportation Energy at Highest Level since 1954."

[3] BP, 2015, "BP Statistical Review of World Energy June 2015," www.bp.com/statisticalreview.

[4] BP, 2016, "BP Energy Outlook 2016 Edition: Outlook to 2035," www.bp.com/energyoutlook.

[5] Wissink, M. L., 2015, "Direct injection for dual fuel stratification (DDFS) : improving the control of heat release in advanced IC engine combustion strategies," Ph.D., University of Wisconsin-Madison, Madison, Wis.

[6] (EPA), U. S. E. P. A., 2016, "Heavy-Duty Highway Compression-Ignition Engines and Urban Buses: Exhaust Emission Standards," Office of Transportation and Air Quality, https://www.epa.gov/sites/production/files/2016-03/documents/420b16018.pdf.

[7] 2012, "2017 and Later Model Year Light-Duty Vehicle Greenhouse Gas Emissions and Corporate Average Fuel Economy Standards," Federal Register, 77(199), pp. 62624--63200.

[8] Neely, G. D., Sasaki, S., Huang, Y., Leet, J. A., and Stewart, D. W., 2005, "New Diesel Emission Control Strategy to Meet US Tier 2 Emissions Regulations," SAE Technical Paper 2005-01-1091.

[9] Kim, D., Ekoto, I., Colban, W. F., and Miles, P. C., 2008, "In-cylinder CO and UHC Imaging in a Light-Duty Diesel Engine during PPCI Low-Temperature Combustion," SAE Int. J. Fuels Lubr. 2008-01-1602, 1(1), pp. 933-956.

[10] Wagner, R., Curran, S., Dempsey, A., Sluder, S., Splitter, D., Szybist, J., and West, B., 2014, "ORNL Advanced Combustion Research and Future Fuel Opportunities."

[11] Najt, P. M., and Foster, D. E., 1983, "Compression-Ignited Homogeneous Charge Combustion," SAE Technical Paper 830264.

[12] Dec, J. E., and Sjöberg, M., 2004, "Isolating the Effects of Fuel Chemistry on Combustion Phasing in an HCCI Engine and the Potential of Fuel Stratification for Ignition Control," SAE Technical Paper 2004-01-0557.

[13] Dec, J. E., Hwang, W., and Sjöberg, M., 2006, "An Investigation of Thermal Stratification in HCCI Engines Using Chemiluminescence Imaging," SAE Technical Paper 2006-01-1518.

[14] Dec, J. E., and Hwang, W., 2009, "Characterizing the Development of Thermal Stratification in an HCCI Engine Using Planar-Imaging Thermometry," SAE Int. J. Engines, 2(1), pp. 421--438.

[15] Lawler, B., Lacey, J., Dronniou, N., Dernotte, J., Dec, J. E., Guralp, O., Najt, P., and Filipi, Z., 2014, "Refinement and Validation of the Thermal Stratification Analysis: A post-processing methodology for determining temperature distributions in an experimental HCCI engine," SAE Technical Paper 2014-01-1276.

[16] Sjöberg, M., Dec, J. E., Babajimopoulos, A., and Assanis, D. N., 2004, "Comparing Enhanced Natural Thermal Stratification Against Retarded Combustion Phasing for Smoothing of HCCI Heat-Release Rates," SAE Technical Paper 2004-01-2994.

[17] Sjöberg, M., and Dec, J. E., 2005, "Effects of Engine Speed, Fueling Rate, and Combustion Phasing on the Thermal Stratification Required to Limit HCCI Knocking Intensity," SAE Technical Paper 2005-01-2125.

[18] Sjöberg, M., Dec, J. E., and Cernansky, N. P., 2005, "Potential of Thermal Stratification and Combustion Retard for Reducing Pressure-Rise Rates in HCCI Engines, Based on Multi-Zone Modeling and Experiments," SAE Technical Paper 2005-01-0113.

[19] Snyder, J., Dronniou, N., Dec, J. E., and Hanson, R., 2011, "PLIF Measurements of Thermal Stratification in an HCCI Engine under Fired Operation," SAE Int. J. Engines, 4(1), pp. 1669-1688.

[20] Lawler, B., Hoffman, M., Filipi, Z., Güralp, O., and Najt, P., 2012, "Development of a Postprocessing Methodology for Studying Thermal Stratification in an HCCI Engine," ASME J. Eng. Gas Turbines Power, 134(10), pp. 102801: 102801-102807.

[21] Lawler, B., Joshi, S., Lacey, J., Guralp, O., Najt, P., and Filipi, Z., "Understanding the Effect of Wall Conditions and Engine Geometry on Thermal Stratification and HCCI Combustion," Proc. ASME 2014 Internal Combustion Engine Division Fall Technical Conference.

[22] Fiveland, S. B., and Assanis, D. N., 2001, "Development of a Two-Zone HCCI Combustion Model Accounting for Boundary Layer Effects," SAE Technical Paper 2001-01-1028.

[23] Bessonette, P. W., Schleyer, C. H., P., D. K., L., H. W., and P., L. M., 2007, "Effects of Fuel Property Changes on Heavy-Duty HCCI Combustion," SAE Technical Paper 2007-01-0191.

[24] Dec, J., Yang, Y., and Dronniou, N., 2011, "Boosted HCCI - Controlling Pressure-Rise Rates for Performance Improvements using Partial Fuel Stratification with Conventional Gasoline," SAE Int. J. Engines, 4(1), pp. 1169-1189.

[25] Hwang, W., Dec, J. E., and Sjoberg, M., 2007, "Fuel Stratification for Low-Load HCCI Combustion: Performance & Fuel-PLIF Measurements," SAE Technical Paper 2007-01-4130.

[26] Sjöberg, M., and Dec, J. E., 2006, "Smoothing HCCI Heat-Release Rates Using Partial Fuel Stratification with Two-Stage Ignition Fuels," SAE Technical Paper 2006-01-0629.

[27] Sjoberg, M., and Dec, J. E., 2011, "Smoothing HCCI Heat Release with Vaporization-Cooling-Induced Thermal Stratification using Ethanol," SAE Int. J. Fuels Lubr., 5(1), pp. 7-27.

[28] Yang, Y., Dec, J. E., Dronniou, N., Sjöberg, M., and Cannella, W., 2011, "Partial Fuel Stratification to Control HCCI Heat Release Rates: Fuel Composition and Other Factors Affecting Pre-Ignition Reactions of Two-Stage Ignition Fuels," SAE Int. J. Engines, 4(1), pp. 1903-1920.

[29] Yang, Y., Dec, J. E., Dronniou, N., and Cannella, W., 2012, "Boosted HCCI Combustion Using Low-Octane Gasoline with Fully Premixed and Partially Stratified Charges," SAE Int. J. Engines, 5(3), pp. 1075-1088.

[30] Bakker, P. C., De Abreu Goes, J. E., Somers, L. M. T., and Johansson, B. H., 2014, "Characterization of Low Load PPC Operation using RON70 Fuels," SAE Technical Paper 2014-01-1304.

[31] Manente, V., Zander, C.-G., Johansson, B., Per, T., and Cannella, W., 2010, "An Advanced Internal Combustion Engine Concept for Low Emissions and High Efficiency from Idle to Max Load Using Gasoline Partially Premixed Combustion," SAE Technical Paper 2010-01-2198.

[32] Dec, J. E., Yang, Y., and Dronniou, N., 2012, "Improving Efficiency and Using E10 for Higher Loads in Boosted HCCI Engines," SAE Int. J. Engines, 5(3), pp. 1009-1032.

[33] Lewander, C. M., Johansson, B., and Tunestål, P., 2011, "Extending the Operating Region of Multi-Cylinder Partially Premixed Combustion using High Octane Number Fuel," SAE Technical Paper 2011-01-1394.

[34] Manente, V., Johansson, B., Per, T., and Cannella, W. J., 2010, "Influence of Inlet Pressure, EGR, Combustion Phasing, Speed and Pilot Ratio on High Load Gasoline Partially Premixed Combustion," SAE Technical Paper 2010-01-1471.

[35] Inagaki, K., Fuyuto, T., Nishikawa, K., Nakakita, K., and Sakata, I., 2006, "Dual-Fuel PCI Combustion Controlled by In-Cylinder Stratification of Ignitability," SAE Technical Paper 2006-01-0028.

[36] Kokjohn, S. L., Hanson, R. M., Splitter, D. A., and Reitz, R. D., 2009, "Experiments and Modeling of Dual-Fuel HCCI and PCCI Combustion Using In-Cylinder Fuel Blending," SAE Int. J. Engines, 2(2), pp. 24-39.

[37] Splitter, D., Hanson, R., Kokjohn, S., and Reitz, R. D., 2011, "Reactivity Controlled Compression Ignition (RCCI) Heavy-Duty Engine Operation at Mid-and High-Loads with Conventional and Alternative Fuels," SAE Technical Paper 2011-01-0363.

[38] Splitter, D. A., Wissink, M. L., Hendricks, T. L., Ghandhi, J. B., and Reitz, R. D., 2012, "Comparison of RCCI, HCCI, and CDC Operation from Low to Full Load," THIESEL 2012 ConferenceValencia, Spain.

[39] Splitter, D., 2012, "High Efficiency RCCI Combustion," PhD, University of Wisconsin-Madison, Madison, WI.

[40] Splitter, D., Wissink, M., DelVescovo, D., and Reitz, R. D., 2013, "RCCI Engine Operation Towards 60% Thermal Efficiency," SAE Technical Paper 2013-01-0279.

[41] Hanson, R. M., Kokjohn, S. L., Splitter, D. A., and Reitz, R. D., 2010, "An Experimental Investigation of Fuel Reactivity Controlled PCCI Combustion in a Heavy-Duty Engine," SAE Int. J. Engines, 3(1), pp. 700--716.

[42] Hanson, R., Kokjohn, S., Splitter, D., and Reitz, R. D., 2011, "Fuel Effects on Reactivity Controlled Compression Ignition (RCCI) Combustion at Low Load," SAE Int. J. Engines, 4(1), pp. 394--411.

[43] Hanson, R., Curran, S., Wagner, R., and Reitz, R. D., 2013, "Effects of Biofuel Blends on RCCI Combustion in a Light-Duty, Multi-Cylinder Diesel Engine," SAE Int. J. Engines, 6(1), pp. 488--503.

[44] Curran, S., Prikhodko, V., Cho, K., Sluder, C. S., Parks, J., Wagner, R., Kokjohn, S., and Reitz, R. D., 2010, "In-Cylinder Fuel Blending of Gasoline/Diesel for Improved Efficiency and Lowest Possible Emissions on a Multi-Cylinder Light-Duty Diesel Engine," SAE Technical Paper 2010-01-2206.

[45] Curran, S., Hanson, R., and Wagner, R., 2012, "Effect of E85 on RCCI Performance and Emissions on a Multi-Cylinder Light-Duty Diesel Engine," SAE Technical Paper 2012-01-0376.

[46] Curran, S., Hanson, R., Wagner, R., and Reitz, R., 2013, "Efficiency and Emissions Mapping of RCCI in a Light-Duty Diesel Engine," SAE Technical Paper 2013-01-0289.

[47] Curran, S., Gao, Z., and Wagner, R., 2014, "Reactivity Controlled Compression Ignition Drive Cycle Emissions and Fuel Economy Estimations Using Vehicle Systems Simulations with E30 and ULSD," SAE Int. J. Engines, 7(2), pp. 902--912.

[48] Kokjohn, S. L., D., R. R., A., S. D., and Musculus, M., 2012, "Investigation of Fuel Reactivity Stratification for Controlling PCI Heat-Release Rates Using High-Speed Chemiluminescence Imaging and Fuel Tracer Fluorescence," SAE Int. J. Engines, 5(2), pp. 248-269.

[49] Christensen, M., Hultqvist, A., and Johansson, B., 1999, "Demonstrating the Multi Fuel Capability of a Homogeneous Charge Compression Ignition Engine with Variable Compression Ratio," SAE Technical Paper 1999-01-3679.

[50] Shen, M., Tuner, M., and Johansson, B., 2013, "Close to Stoichiometric Partially Premixed Combustion -The Benefit of Ethanol in Comparison to Conventional Fuels," SAE Technical Paper 2013-01-0277.

[51] Chang, J., Kalghatgi, G., Amer, A., and Viollet, Y., 2012, "Enabling High Efficiency Direct Injection Engine with Naphtha Fuel through Partially Premixed Charge Compression Ignition Combustion," SAE Technical Paper 2012-01-0677.

[52] Nieman, D. E., Dempsey, A. B., and Reitz, R. D., 2012, "Heavy-Duty RCCI Operation Using Natural Gas and Diesel," SAE Int. J. Engines, 5(2), pp. 270-285.

[53] Hanson, R., Ickes, A., and Wallner, T., 2016, "Comparison of RCCI Operation with and without EGR over the Full Operating Map of a Heavy-Duty Diesel Engine," SAE Technical Paper 2016-01-0794.

[54] DelVescovo, D., Wang, H., Wissink, M., and Reitz, R. D., 2015, "Isobutanol as Both Low Reactivity and High Reactivity Fuels with Addition of Di-Tert Butyl Peroxide (DTBP) in RCCI Combustion," SAE Int. J. Fuels Lubr., 8(2), pp. 329-343.

[55] Splitter, D. A., Wissink, M. L., DelVescovo, D. A., and Reitz, R. D., 2014, "Improving the Understanding of Intake and Charge Effects for Increasing RCCI Engine Efficiency," SAE Int. J. Engines, 7(2), pp. 913-927.

[56] Wissink, M. L., Lim, J. H., Splitter, D. A., Hanson, R. M., and Reitz, R. D., 2012, "Investigation of Injection Strategies to Improve High Efficiency RCCI Combustion With Diesel and Gasoline Direct Injection," Internal Combustion Engine Division Fall Technical Conference, ASME, Vancouver, BC, Canada, pp. 327-338.

[57] Sung, K., 2011, "Private Communication,"University of Wisconsin-Madison.

[58] Wissink, M., 2013-2015, "Private Communication,"University of Wisconsin-Madison.

[59] Ku, H. H., 1966, "Notes on the use of propagation of error formulas," Journal of Research of the National Bureau of Standards, Section C: Engineering and Instrumentation, 70C(4), pp. 263--273.

[60] Eng, J. A., 2002, "Characterization of Pressure Waves in HCCI Combustion," SAE Technical Paper 2002-01-2859.

[61] Gatowski, J. A., Balles, E. N., Chun, K. M., Nelson, F. E., Ekchian, J. A., and Heywood, J. B., 1984, "Heat Release Analysis of Engine Pressure Data," SAE Technical Paper 841359.

[62] Klein, M., and Eriksson, L., 2004, "A Specific Heat Ratio Model for Single-Zone Heat Release Models," SAE Technical Paper 2004-01-1464.

[63] Chang, J., Güralp, O., Filipi, Z., Assanis, D. N., Kuo, T.-W., Najt, P., and Rask, R., 2004, "New Heat Transfer Correlation for an HCCI Engine Derived from Measurements of Instantaneous Surface Heat Flux," SAE Technical Paper 2004-01-2996.

[64] Krieger, R. B., and Borman, G. L., 1966, "The computation of apparent heat release for internal combustion engines," Diesel and Gas Engine Power Division at the Winter Annual Meeting and Energy Systems Exposition, ASME, New York, NY.

[65] Brunt, M. F. J., Rai, H., and Emtage, A. L., 1998, "The Calculation of Heat Release Energy from Engine Cylinder Pressure Data," SAE Technical Paper 981052.

[66] DelVescovo, D., Kokjohn, S., and Reitz, R., 2016, "The Development of an Ignition Delay Correlation for PRF Fuel Blends from PRF0 (n-Heptane) to PRF100 (iso-Octane)," SAE Int. J. Engines, 9(1), pp. 520-535.

[67] 2015, "ASTM D2699-15a, Standard Test Method for Research Octane Number of Spark-Ignition Engine Fuel," ASTM International, West Conshohocken, PA.

[68] 2016, "ASTM D2700-16, Standard Test Method for Motor Octane Number of Spark-Ignition Engine Fuel," ASTM International, West Conshohocken, PA.

[69] Chang, J., Filipi, Z., Assanis, D., Kuo, T. W., Najt, P., and Rask, R., 2005, "Characterizing the thermal sensitivity of a gasoline homogeneous charge compression ignition engine with measurements of instantaneous wall temperature and heat flux," International Journal of Engine Research, 6(4), pp. 289-310.

[70] Curran, H. J., Gaffuri, P., Pitz, W. J., and Westbrook, C. K., 1998, "A Comprehensive Modeling Study of n-Heptane Oxidation," Combustion and Flame, 114(1–2), pp. 149-177.

[71] Curran, H. J., Gaffuri, P., Pitz, W. J., and Westbrook, C. K., 2002, "A comprehensive modeling study of iso-octane oxidation," Combustion and Flame, 129(3), pp. 253-280.

[72] Walker, N. R., Wissink, M. L., DelVescovo, D. A., and Reitz, R. D., 2015, "Use of Natural Gas for Load Extension of Dual-Fuel Reactivity Controlled Compression Ignition Heavy-Duty Engine Operation," Journal of Energy Resources Technology, JERT-15-1031.

[73] Goldsborough, S. S., 2009, "- A chemical kinetically based ignition delay correlation for iso-octane covering a wide range of conditions including the NTC region," Combustion and Flame, 156(- 6), pp. 1248-1262.

[74] Kozarac, D., Tomic, R., Taritas, I., Chen, J.-Y., and Dibble, R. W., 2015, "A Model for Prediction of Knock in the Cycle Simulation by Detail Characterization of Fuel and Temperature Stratification," SAE Int. J. Engines, 8(4), pp. 1520-1534.

[75] Davidson, D. F., and Hanson, R. K., 2003, "Interpreting Shock Tube Ignition Data," Stanford University, University of California at Los Angeles.

[76] Ohashi, T., Yang, X., Takabayashi, T., Urata, Y., Kubota, S., and Katsuyama, H., 2006, "Ignition and Combustion Simulation in HCCI Engines," SAE Technical Paper 2006-01-1522.

[77] He, X., Donovan, M. T., Zigler, B. T., Palmer, T. R., Walton, S. M., Wooldridge, M. S., and Atreya, A., 2005, "An experimental and modeling study of iso-octane ignition delay times under homogeneous charge compression ignition conditions," Combustion and Flame, 142, pp. 266-275.

[78] Horning, D. C., Davidson, D. F., and Hanson, R. K., 2002, "Study of the High-Temperature Autoignition of n-Alkane/O/Ar Mixtures," Journal of Propulsion and Power, 18(2), pp. 363-371.

[79] Goldsborough, S. S., Smith, T. A., Johnson, M. V., and McConnell, S. S., 2012, "Evaluation of Ignition Timing Predictions Using Control-Oriented Models in Kinetically-Modulated Combustion Regimes," SAE Technical Paper 2012-01-1136.

[80] Shahbakhti, M., Lupul, R., and Koch, C. R., 2007, "Predicting HCCI Auto-Ignition Timing by Extending a Modified Knock-Integral Method," SAE Technical Paper 2007-01-0222.

[81] Swan, K., Shahbakhti, M., and Koch, C. R., 2006, "Predicting Start of Combustion Using a Modified Knock Integral Method for an HCCI Engine," SAE Technical Paper 2006-01-1086.

[82] Mehl, M., Chen, J. Y., Pitz, W. J., Sarathy, S. M., and Westbrook, C. K., 2011, "An Approach for Formulating Surrogates for Gasoline with Application toward a Reduced Surrogate Mechanism for CFD Engine Modeling," Energy & Fuels, 25(11), pp. 5215-5223.

[83] Livengood, J., and Wu, P., 1954, "Correlation of Autoignition Phenomena in Internal Combustion Engines and Rapid Compression Machines," Proceedings of the Fifth International Symposium on Combustion, Reinhold, New York, Pittsburgh, PA, pp. 347-356.

[84] Wolk, B., Chen, J.-Y., and Dec, J. E., 2015, "Computational study of the pressure dependence of sequential auto-ignition for partial fuel stratification with gasoline," Proceedings of the Combustion Institute, 35(3), pp. 2993-3000.

[85] Kokjohn, S. L., 2012, "Reactivity Controlled Compression Ignition (RCCI) Combustion," Ph.D., University of Wisconsin-Madison.

[86] Kokjohn, S. L., Musculus, M. P. B., and Reitz, R. D., 2015, "Evaluating temperature and fuel stratification for heat-release rate control in a reactivity-controlled compression-ignition engine using optical diagnostics and chemical kinetics modeling," Combustion and Flame, 162(6), pp. 2729-2742.

[87] Kalghatgi, G., Babiker, H., and Badra, J., 2015, "A Simple Method to Predict Knock Using Toluene, N-Heptane and Iso-Octane Blends (TPRF) as Gasoline Surrogates," SAE Int. J. Engines, 8(2), pp. 505-519.

[88] Amsden, A. A., 1999, "KIVA-3V, Release 2. Improvements to KIVA-3V," LA-UR-99-915.

[89] Dempsey, A. B., 2013, "Dual-Fuel Reactivity Controlled Compression Ignition (RCCI) with Alternative Fuels," Ph.D, University of Wisconsin-Madison.

[90] Reitz, R. D., 1987, "Modeling Atomization Processes in High-Pressure Vaporizing Sprays," Atomization & Spray Technology, 3, pp. 309-337.

[91] Patterson, M. A., and Reitz, R. D., 1998, "Modeling the Effects of Fuel Spray Characteristics on Diesel Engine Combustion and Emission," SAE Technical Paper 980131.

[92] Ra, Y., and Reitz, R. D., 2009, "A vaporization model for discrete multi-component fuel sprays," International Journal of Multiphase Flow, 35(2), pp. 101-117.

[93] Han, Z., and Reitz, R. D., 1995, "Turbulence Modeling of Internal Combustion Engines Using RNG κ-ε Models," Combustion Science and Technology, 106(4-6), pp. 267-295.

[94] Perini, F., Galligani, E., and Reitz, R. D., 2012, "An Analytical Jacobian Approach to Sparse Reaction Kinetics for Computationally Efficient Combustion Modeling with Large Reaction Mechanisms," Energy & Fuels, 26(8), pp. 4804-4822.

[95] Reitz, R. D., and Munnannur, A., 2009, "Comprehensive Collision Model for Multidimensional Engine Spray Computations," Atomization and Sprays, 19(7), pp. 597-619.

[96] Abani, N., and Reitz, R. D., 2007, "Unsteady turbulent round jets and vortex motion," Physics of Fluids, 19(12), p. 125102.

[97] Abani, N., Kokjohn, S., Park, S. W., Bergin, M., Munnannur, A., Ning, W., Sun, Y., and Reitz, R. D., 2008, "An Improved Spray Model for Reducing Numerical Parameter Dependencies in Diesel Engine CFD Simulations," SAE Technical Paper 2008-01-0970.

[98] Kee, R. J., Rupley, F. M., and Miller, J. A., 1989, "CHEMKIN-II: A FORTRAN chemical kinetics package for the analysis of gas phase chemical kinetics," Sandia Report SAND 89-8009.

[99] Wang, H., Jiao, Q., Yao, M., Yang, B., Qiu, L., and Reitz, R. D., 2013, "Development of an n-heptane/toluene/polyaromatic hydrocarbon mechanism and its application for combustion and soot prediction," International Journal of Engine Research, 14(5), pp. 434-451.

[100] Ra, Y., and Reitz, R. D., 2008, "A reduced chemical kinetic model for IC engine combustion simulations with primary reference fuels," 155(4), pp. 713-738.

[101] Yun, H. J., and Mirsky, W., 1974, "Schlieren-Streak Measurements of Instantaneous Exhaust Gas Velocities from a Spark-Ignition Engine," SAE Technical Paper 741015.

[102] Komninos, N. P., Hountalas, D. T., and Kouremenos, D. A., 2004, "Development of a New Multi-Zone Model for the Description of Physical Processes in HCCI Engines," SAE Technical Paper 2004-01-0562.

[103] Woschni, G., 1967, "A Universally Applicable Equation for the Instantaneous Heat Transfer Coefficient in the Internal Combustion Engine," SAE Technical Paper 670931.

[104] Northrop, W. F., Fang, W., and Huang, B., 2013, "Combustion Phasing Effect on Cycle Efficiency of a Diesel Engine Using Advanced Gasoline Fumigation," J. Eng. Gas Turbines Power, 135(3), pp. 032801-032801.

[105] Lu, J. H., Ezekoye, D., Iiyama, A., Greif, R., and Sawyer, R. F., 1989, "Effect of Knock on Time-Resolved Engine Heat Transfer," SAE Technical Paper 890158.

[106] Syrimis, M., Shigahara, K., and Assanis, D. N., 1996, "Correlation Between Knock Intensity and Heat Transfer Under Light and Heavy Knocking Conditions in a Spark Ignition Engine," SAE Technical Paper 960495.

[107] Grandin, B., Denbratt, I., Bood, J., Brackmann, C., and Bengtsson, P.-E., 2000, "The Effect of Knock on the Heat Transfer in an SI Engine: Thermal Boundary Layer Investigation using CARS Temperature Measurements and Heat Flux Measurements," SAE Technical Paper 2000-01-2831.

[108] Grandin, B., and Denbratt, I., 2002, "The Effect of Knock on Heat Transfer in SI Engines," SAE Technical Paper 2002-01-0238.

[109] Kalghatgi, G. T., 2005, "Auto-Ignition Quality of Practical Fuels and Implications for Fuel Requirements of Future SI and HCCI Engines," SAE Technical Paper 2005-01-0239.

[110] Aceves, S. M., Flowers, D. L., Westbrook, C. K., Smith, J. R., Pitz, W., Dibble, R., Christensen, M., and Johansson, B., 2000, "A Multi-Zone Model for Prediction of HCCI Combustion and Emissions," SAE Technical Paper 2000-01-0327.

[111] Bissoli, M., Cuoci, A., Frassoldati, A., Faravelli, T., Ranzi, E., Lucchini, T., D'Errico, G., and Contino, F., 2013, "Detailed Kinetic Analysis of HCCI Combustion Using a New Multi-Zone Model and CFD Simulations," SAE Int. J. Engines, 6(3), pp. 1594-1609.

[112] Hernández, J. J., Lapuerta, M., and Sanz-Argent, J., 2014, "Autoignition prediction capability of the Livengood–Wu correlation applied to fuels of commercial interest," International Journal of Engine Research, 15(7), pp. 817-829.

[113] Pan, J., Zhao, P., Law, C. K., and Wei, H., 2015, "A predictive Livengood–Wu correlation for two-stage ignition," International Journal of Engine Research.

[114] Stager, L. A., and Reitz, R. D., 2007, "Assessment of Diesel Engine Size-Scaling Relationships," SAE Technical Paper 2007-01-0127.

[115] Tess, M. J., Lee, C.-W., and Reitz, R. D., 2011, "Diesel Engine Size Scaling at Medium Load without EGR," SAE Int. J. Engines, 4(1), pp. 1993-2009.

[116] Ge, H.-W., Lee, C.-W., Shi, Y., Reitz, R. D., and Willems, W., 2011, "Coupling of Scaling Laws and Computational Optimization to Develop Guidelines for Diesel Engine Down-sizing," SAE Technical Paper 2011-01-0836.

[117] Shi, Y., and Reitz, R. D., 2008, "Study of Diesel Engine Size-Scaling Relationships Based on Turbulence and Chemistry Scales," SAE Technical Paper 2008-01-0955.

[118] Pastor, J. V., Lopez, J. J., Garcia, J. M., and Pastor, J. M., 2008, "A 1D model for the description of mixing-controlled inert diesel sprays," Fuel, 87, pp. 2871-2885.

[119] Musculus, M., and Kattke, K., 2009, "Entrainment Waves in Diesel Jets," SAE Int. J. Engines, 2(1), pp. 1170-1193.

A INJECTOR INFORMATION AND FUEL PROPERTIES

A.1 AFS Injector Details

Fuel Injector

Gs Series

The AFS Gs series injector offers cost effective, precision metering of gaseous fuels, coupling fast response and high flow to allow the use of fewer injectors per engine. Other key advantages include inherent self-cleaning design and low-wear components, which provide exceptional service life.

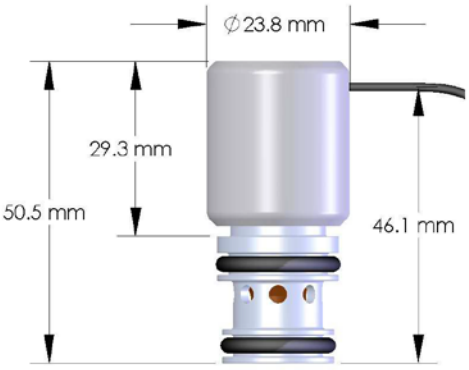

Key Features

- Compatible for use with gaseous hydrocarbon fuels such as: **CNG/LCNG/LPG**
- Usable in **port or throttle body injection** configurations
- Designed to operate in the temperature range of **-40˚C to 120˚C**
- Compatible with **12 VDC and 24 VDC** systems
- Injector response time **less than 2 ms** with 8:2 Amp peak and hold driver
- **Custom polymer sealing surface** provides exceptional sealing and reduced wear in dry gas applications
- **Custom** flow calibrations available
- Cartridge style design allows for **easy drop-in installation**
- **Side feed-bottom discharge** allows for simpler port design and better tolerance to gas contamination
- Custom **Hydrogen** version is available

AFS 2004
Alternative Fuel Systems (2004) Inc.
Unit 1, 4321 – 14th Street NE, Calgary, Alberta, Canada T2E 7A9
Phone: +1 (403) 262-1833 Fax: +1 (403) 237-7441 E-mail: sales@afsglobal.com Web: www.afsglobal.com

50-01123-0

A.2 Lubricity Additive Specification Sheet

Infineum R655

Description

Infineum R655 is an additive designed to improve distillate fuel lubricity, thus reducing wear of moving parts in contact with the fuel (particularly fuel injector pumps).

Normal treat rates are 50-200 ppm.

Typical Inspections

Property:	Value	Unit:	Method
Appearance	Yellow Clear Liquid		Visual
Density at 15°C	960	Kg/m³	ASTM D 4052
Flash Point (PMCC)	>210	°C	ASTM D 93
Pour Point	-15	°C	ASTM D 97
Viscosity at 20°C	192	cSt	ASTM D 445
Viscosity at 40°C	65	cSt	ASTM D 445
Viscosity at 60°C	29	cSt	ASTM D 445
Viscosity at 100°C	9	cSt	ASTM D 445
Total Acid Number	<1	mg KOH/g	ASTM D 974
Coefficient of Thermal Expansion	0.00080	1/°C	ITM 50-020

Handling / Precautions

Infineum R655 requires no special handling above that which is normal for petroleum products.

The recommended additive storage temperature range is from 20°C to 40°C.

Where LP steam coils are used for heating purposes, agitation is recommended to prevent excessive local skin temperatures.

Note that the product has a Pour Point of -15°C, but that under prolonged unheated storage, the product may solidify at temperatures up to +10°C.

Further Information

For further information please contact your local Infineum affiliate or representative.

B *CALIBRATION CURVES*

The calibrations presented here were performed with the entire measurement chain including the transmission, amplification, analog to digital conversion, and all other intermediate steps in the experimental apparatus in-situ. A reference value was supplied to the particular instrument, and the signal was measured by LabVIEW until the measurement was steady. For each reference value 30 data points were acquired at each reference value, however, due to the relative scaling of the plots shown below, these values often appear as single point. The emissions calibrations were performed with a gas divider and known gas concentrations of the specific emissions species diluted with zero-grade nitrogen at every 10% interval between 0 and 100%. For all type-K thermocouples, the reported standard measurement error was used which is the greater of 2.2°C or 0.75% of the measured value. For PM measurements with the AVL 415S smoke meter, the error calculations were performed based on the 5 measured samples and the reported accuracy.

B.1 Emissions Calibrations

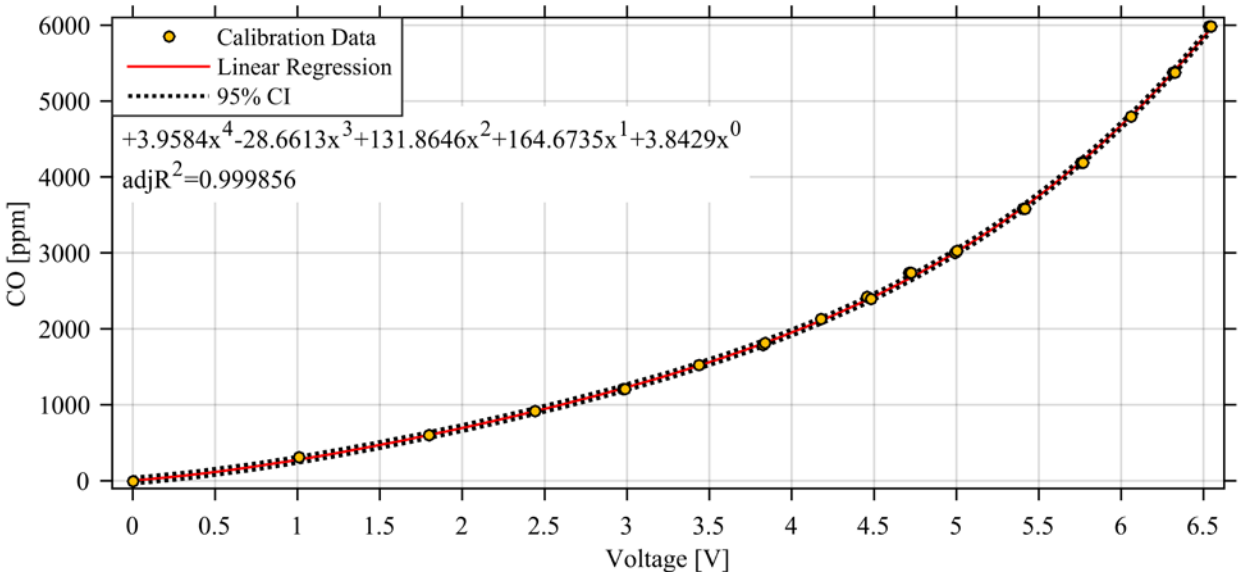

Figure B.1: Calibration curve for exhaust CO

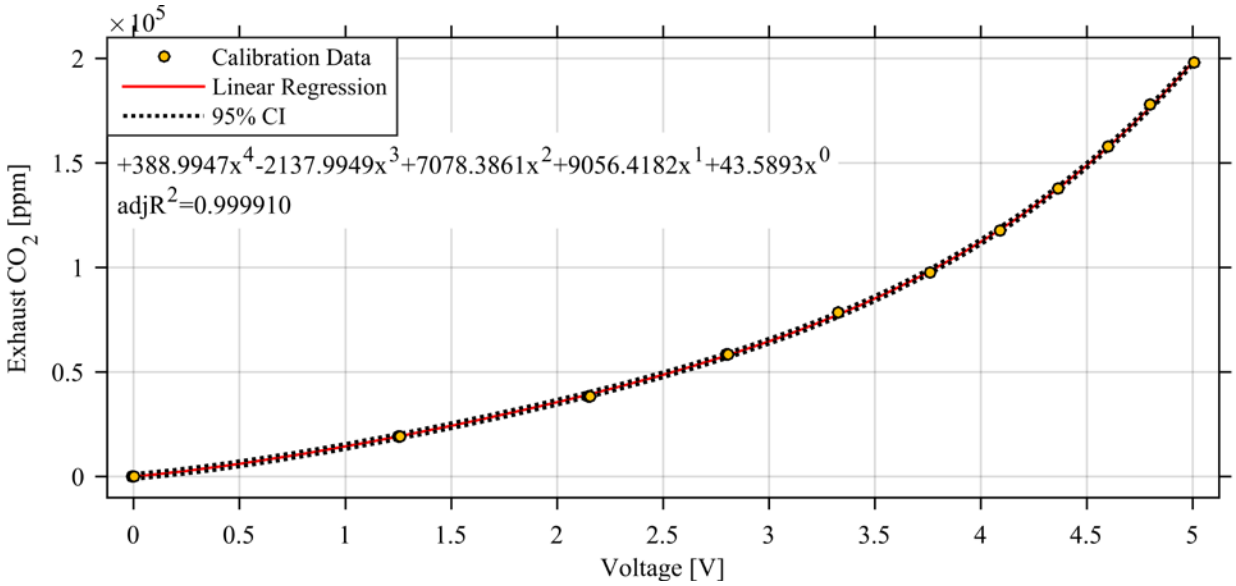

Figure B.2: Calibration curve for exhaust CO_2

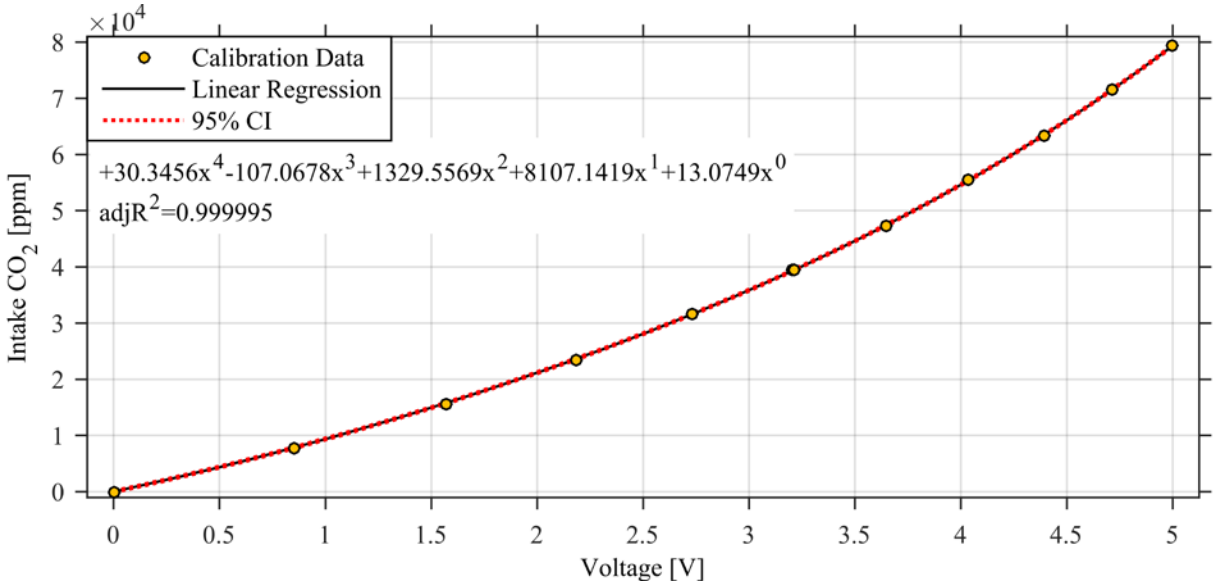

Figure B.3: Calibration curve for intake CO_2

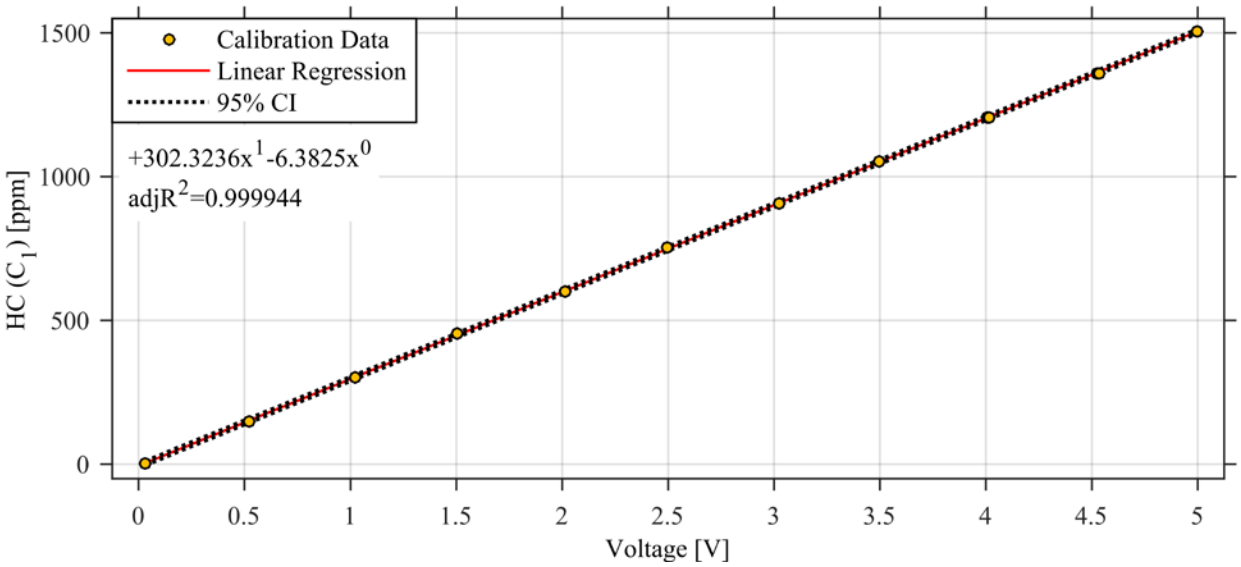

Figure B.4: Calibration curve for exhaust HC

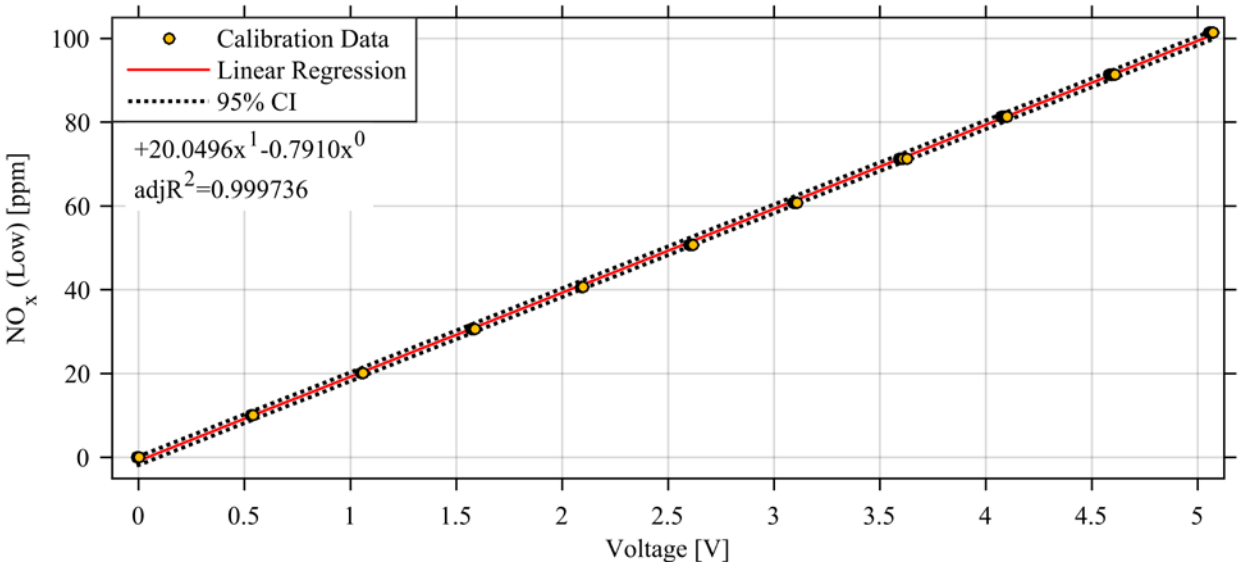

Figure B.5: Calibration curve for exhaust NO_x (low span value)

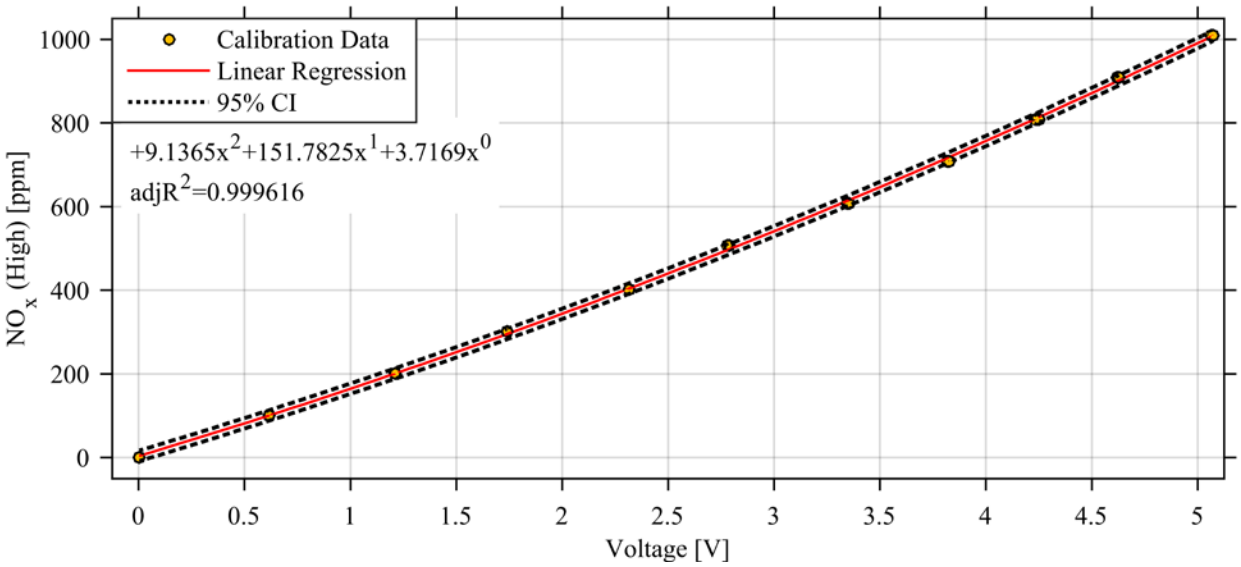

Figure B.6: Calibration curve for exhaust NO_x (high span value)

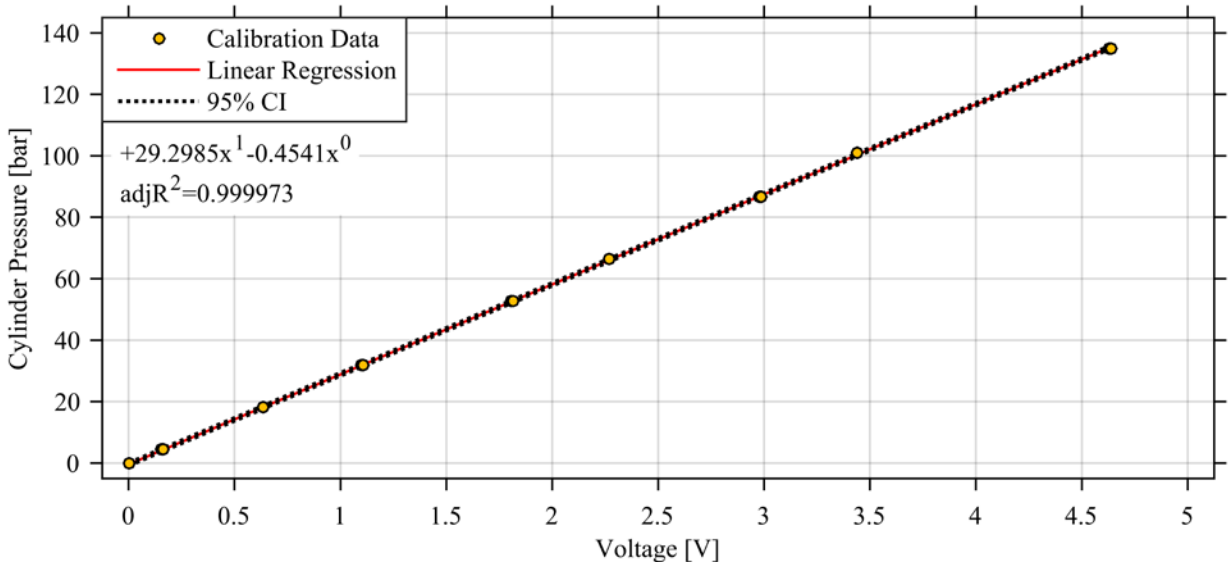

Figure B.7: Calibration curve for the in-cylinder pressure transducer with the charge amplifier set to 30MU/Volt

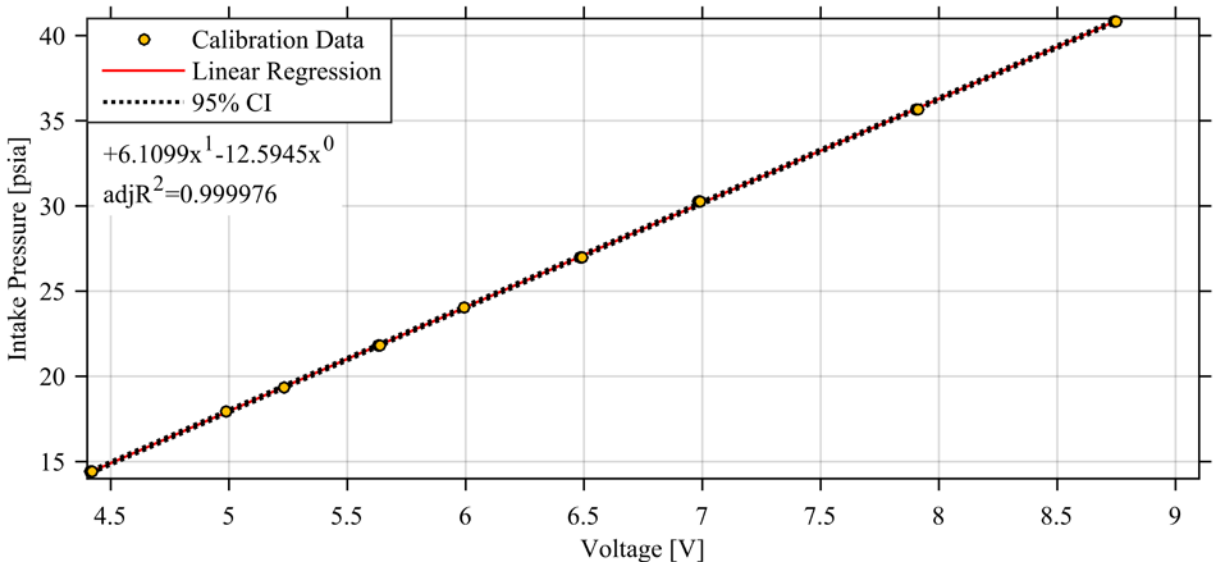

Figure B.8: Calibration curve for the intake surge tank pressure transducer

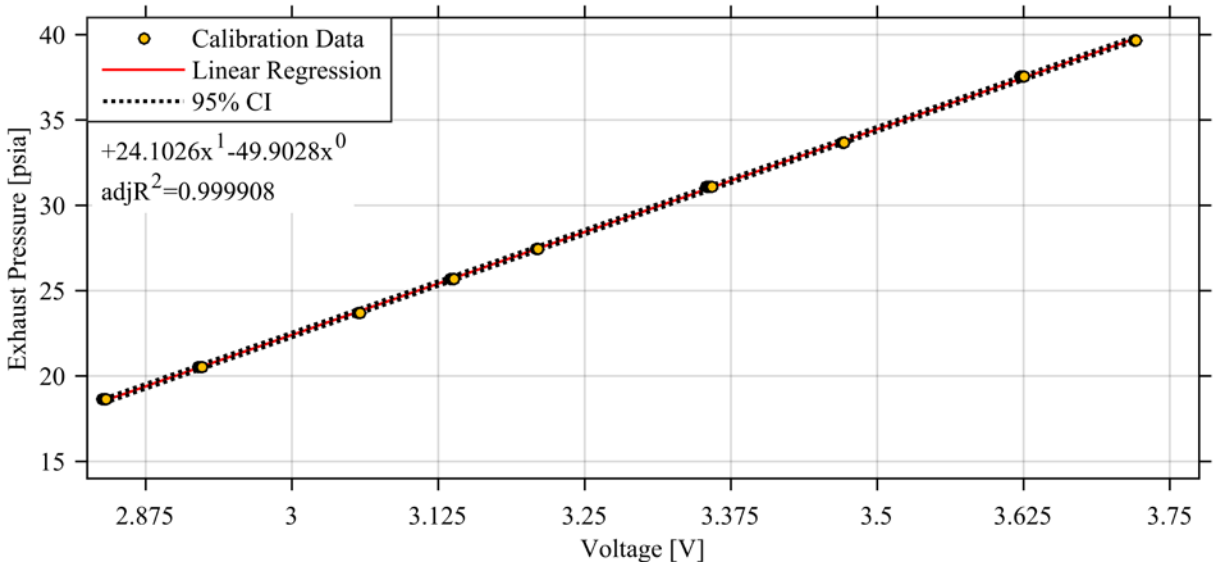

Figure B.9: Calibration curve for the exhaust surge tank pressure transducer

B.2 Fuel Flowrate Calibrations

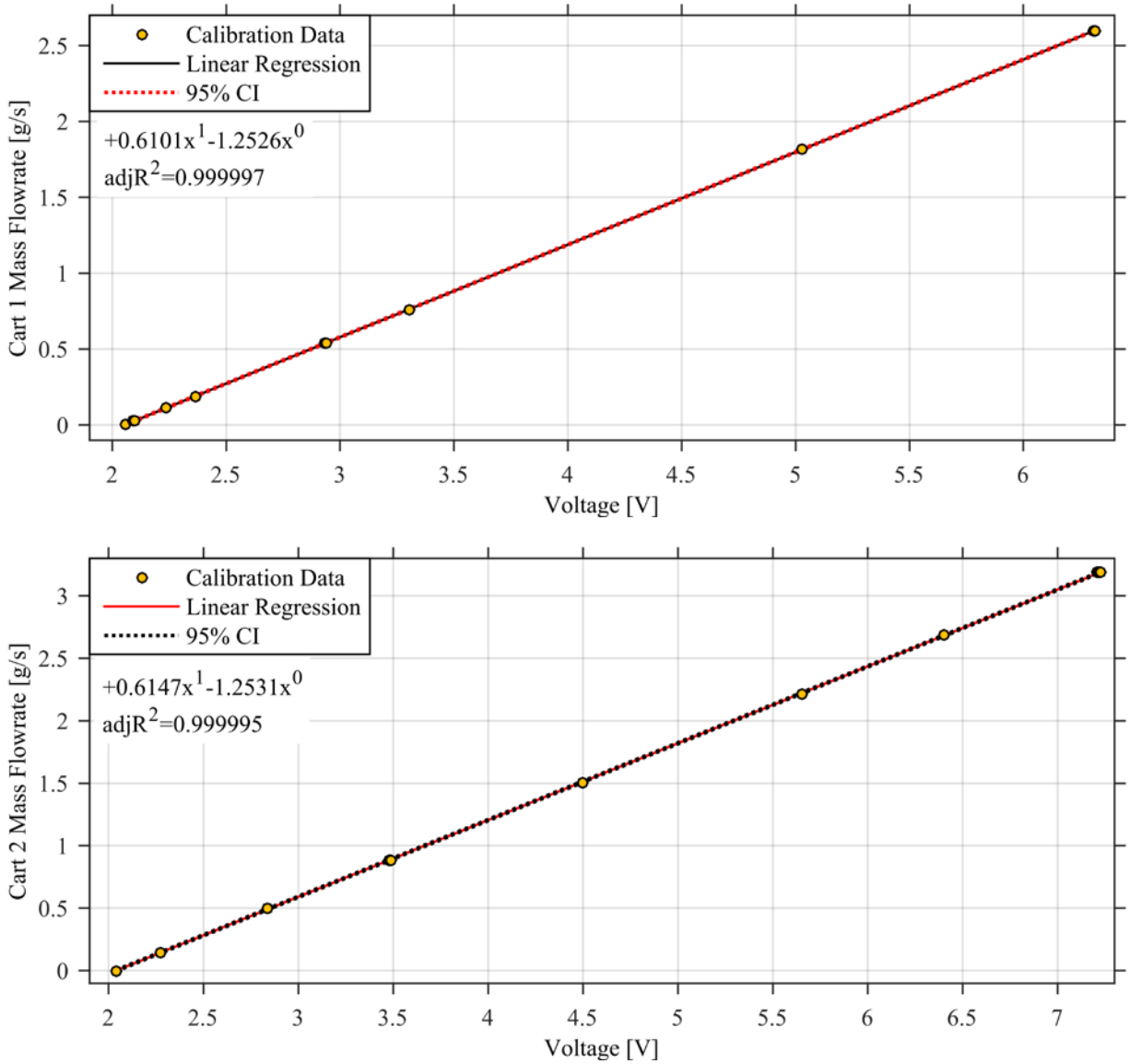

Figure B.10: Calibration curves for fuel cart 1 (top) and fuel cart 2 (bottom)

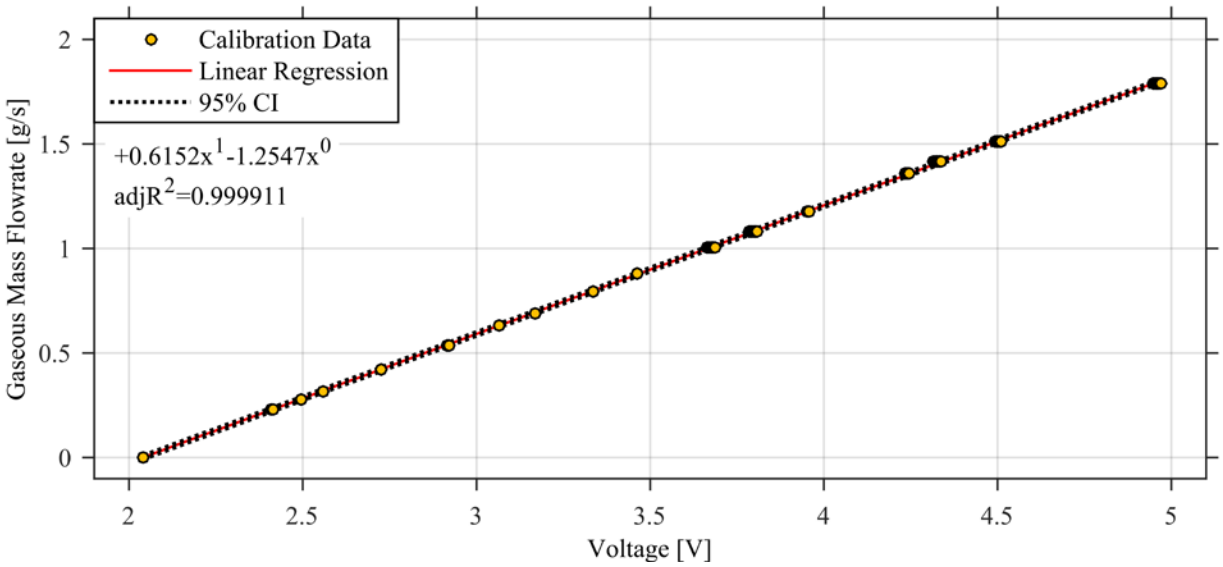

Figure B.11: Calibration curve for gaseous fuel flowrate

C *Further Experimental Results*

C.1 CH_4/PRF0 RCCI Experiments

This section shows additional results of the RCCI engine experiments discussed in Section 3.10, which compared the performance and emissions of methane as the premixed fuel to the baseline PRF100 cases. Shown here are additional SOI timing cases (-40° and -30°ATDC), showing the injection schedules employed in Figure C. for the -40°SOI case, and Figure C.15 for the -30°SOI case, along with the performance and emissions of the two cases in Figure C.17, and Figure C.20, respectively. Also shown are the pressure and heat release traces for each injection strategy and intake conditions in Figure C.18 and Figure C.21, respectively.

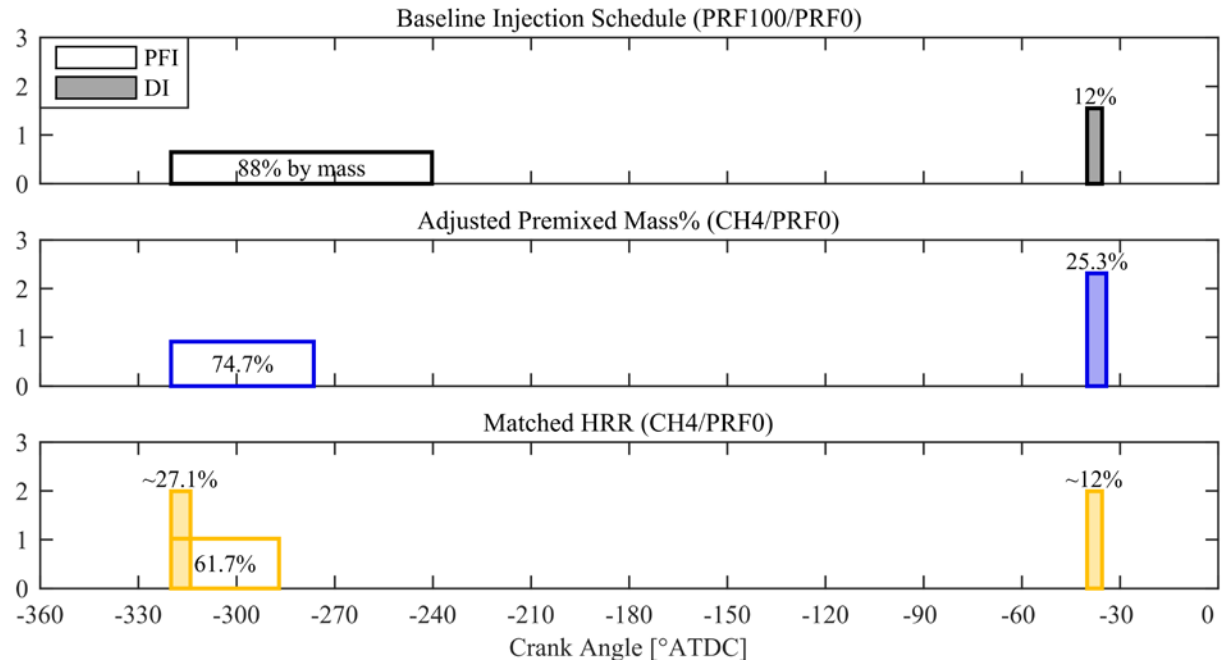

Figure C.12: Injection schedule used for baseline PRF100/PRF0 case at -40° SOI (top in black), matched CA50 with premixed % only (middle in blue), and matched HRR (bottom in yellow) for a fixed intake pressure of P_{in} = 114.5kPa. Area of rectangles is equal to the injected mass

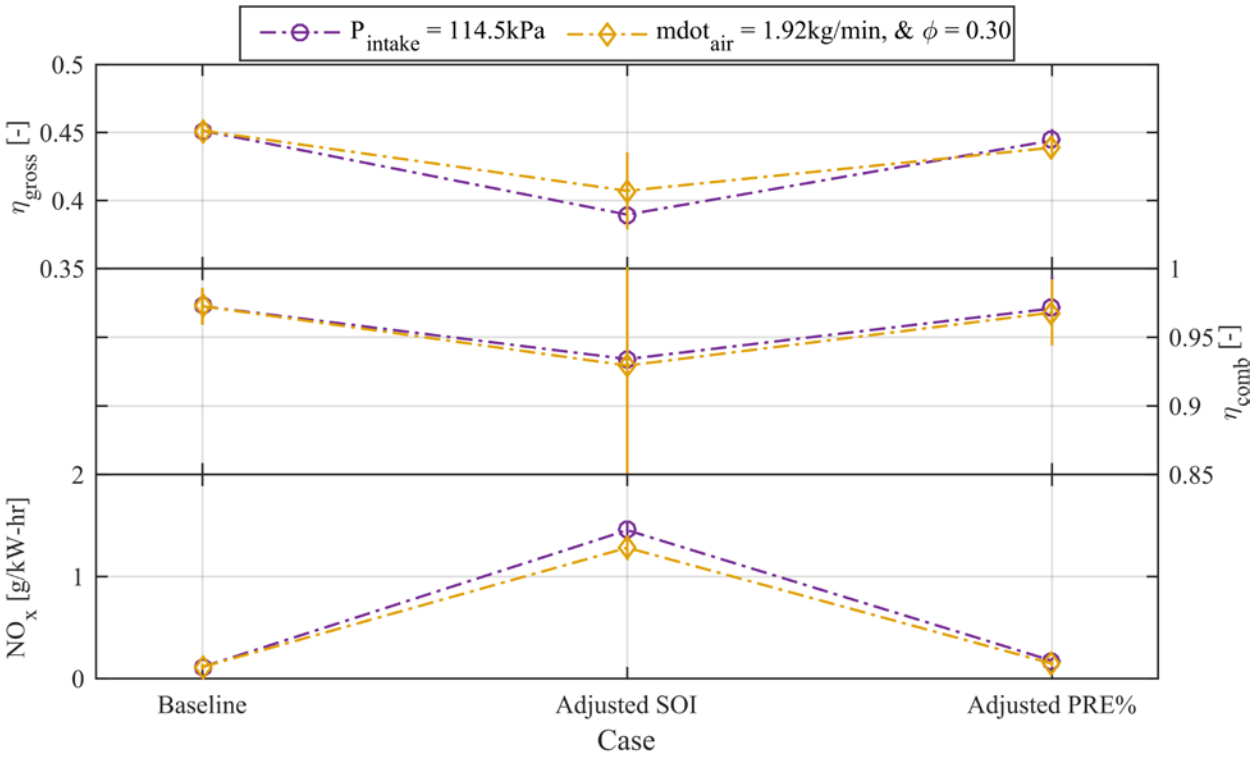

Figure C.13: Gross efficiency (top), combustion efficiency (middle), and NOx (bottom) for the baseline case at -40° SOI with PRF100/PRF0, and the matched CA50 case and the matched HRR case with CH_4/PRF0 for each of the two fixed intake parameters (P_{in} in purple, $\dot{m}_{air}$ and φ in yellow)

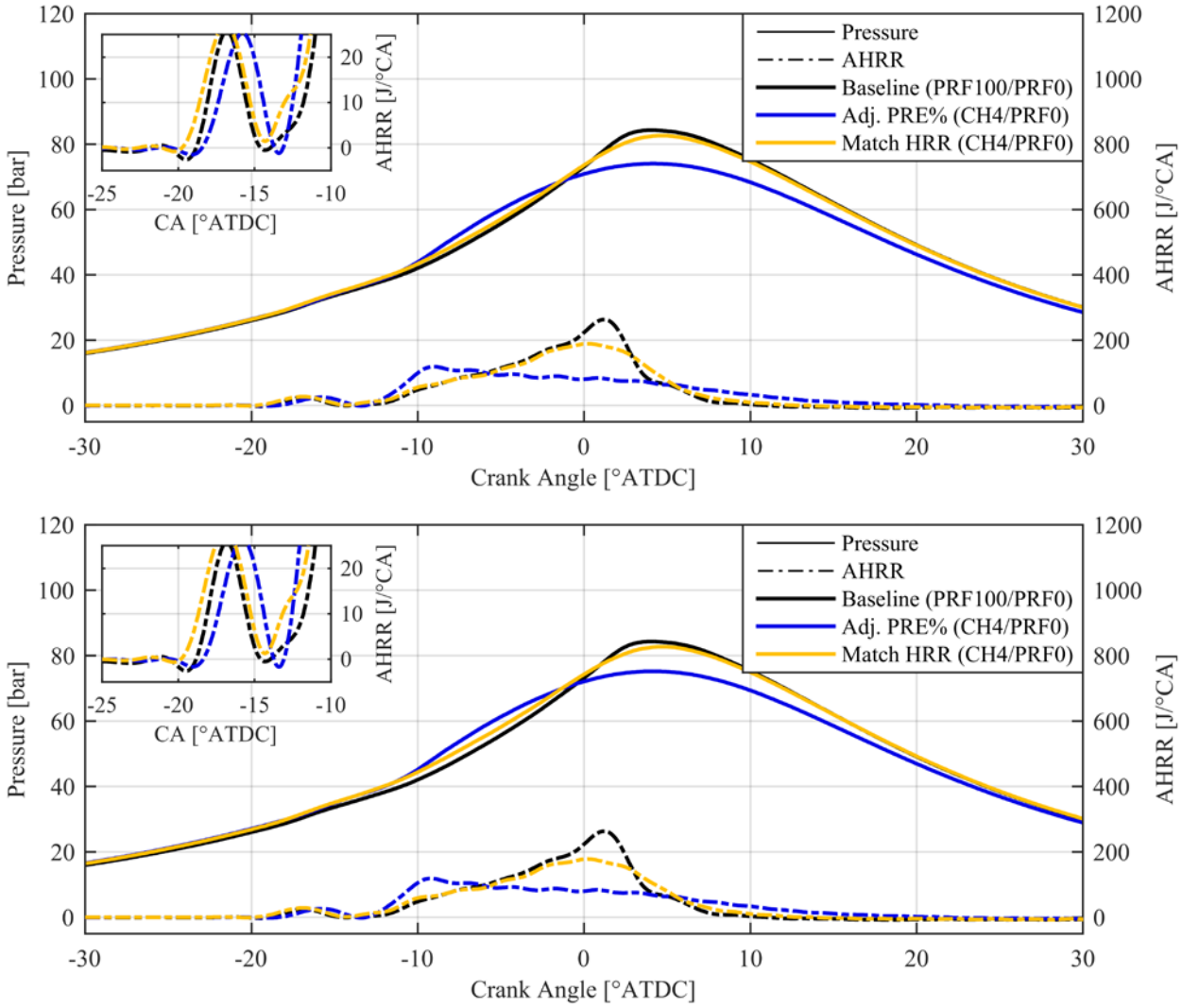

Figure C.14: Pressure and HRR for CH4/PRF0 RCCI cases (adjusted premixed mass percent in blue, and matched HRR in yellow) compared to the baseline PRF100/PRF0 case at -40º SOI (black), for Pin = 114.5kPa (top), and $\dot{m}_{air}$ = 1.92kg/min and φ = 0.30 (bottom)

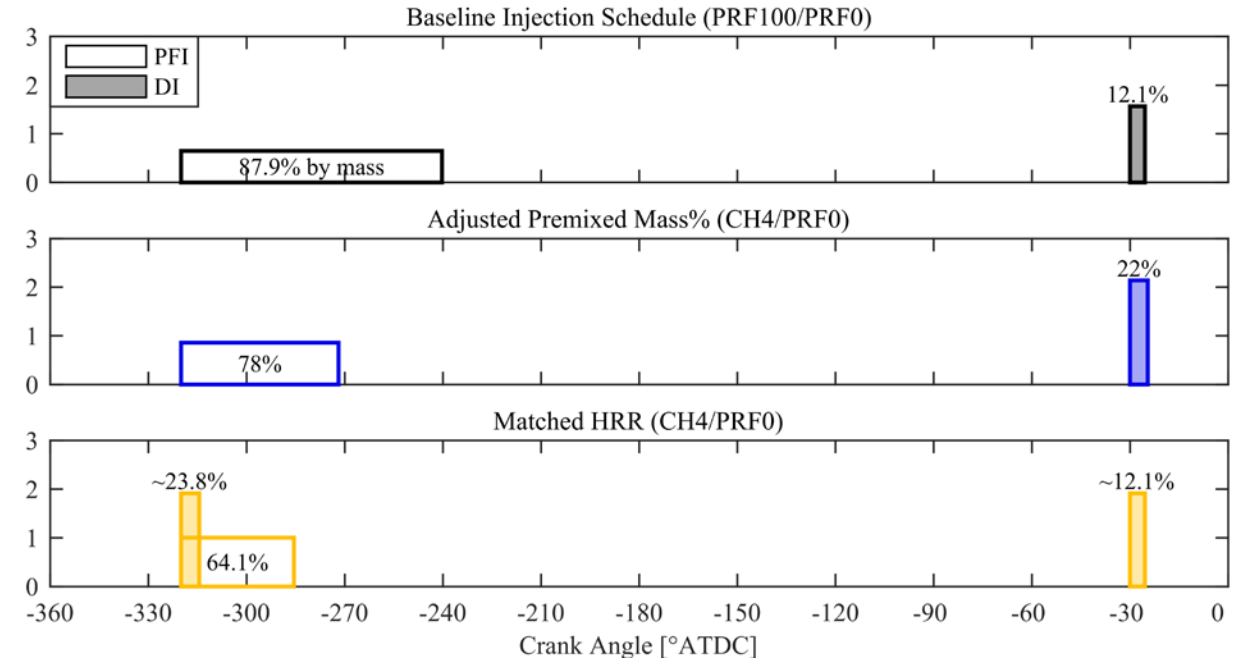

Figure C.15: Injection schedule used for baseline PRF100/PRF0 case at -30° SOI (top in black), matched CA50 with premixed % only (middle in blue), and matched HRR (bottom in yellow) for a fixed intake pressure of P_{in} = 114.5kPa. Area of rectangles is equal to the injected mass

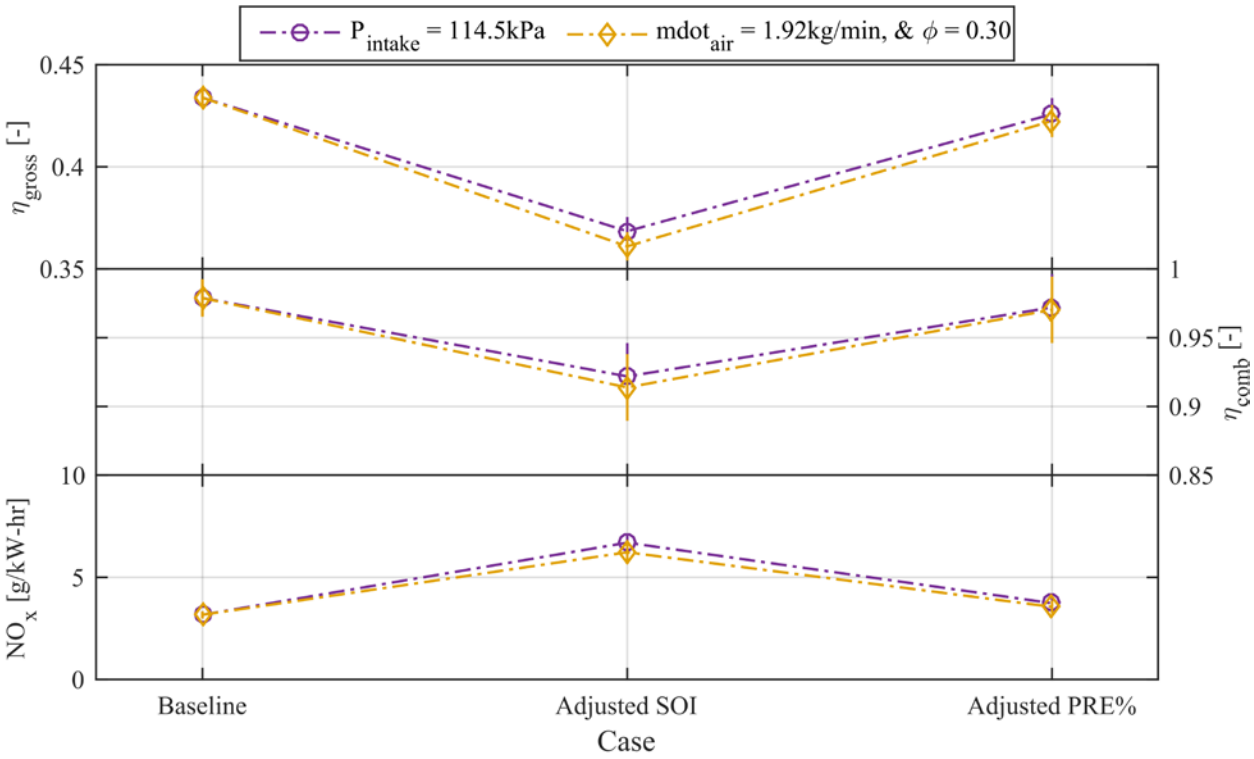

Figure C.16: Gross efficiency (top), combustion efficiency (middle), and NOx (bottom) for the baseline case at -30° SOI with PRF100/PRF0, and the matched CA50 case and the matched HRR case with CH_4/PRF0 for each of the two fixed intake parameters (P_{in} in purple, $\dot{m}_{air}$ and φ in yellow)

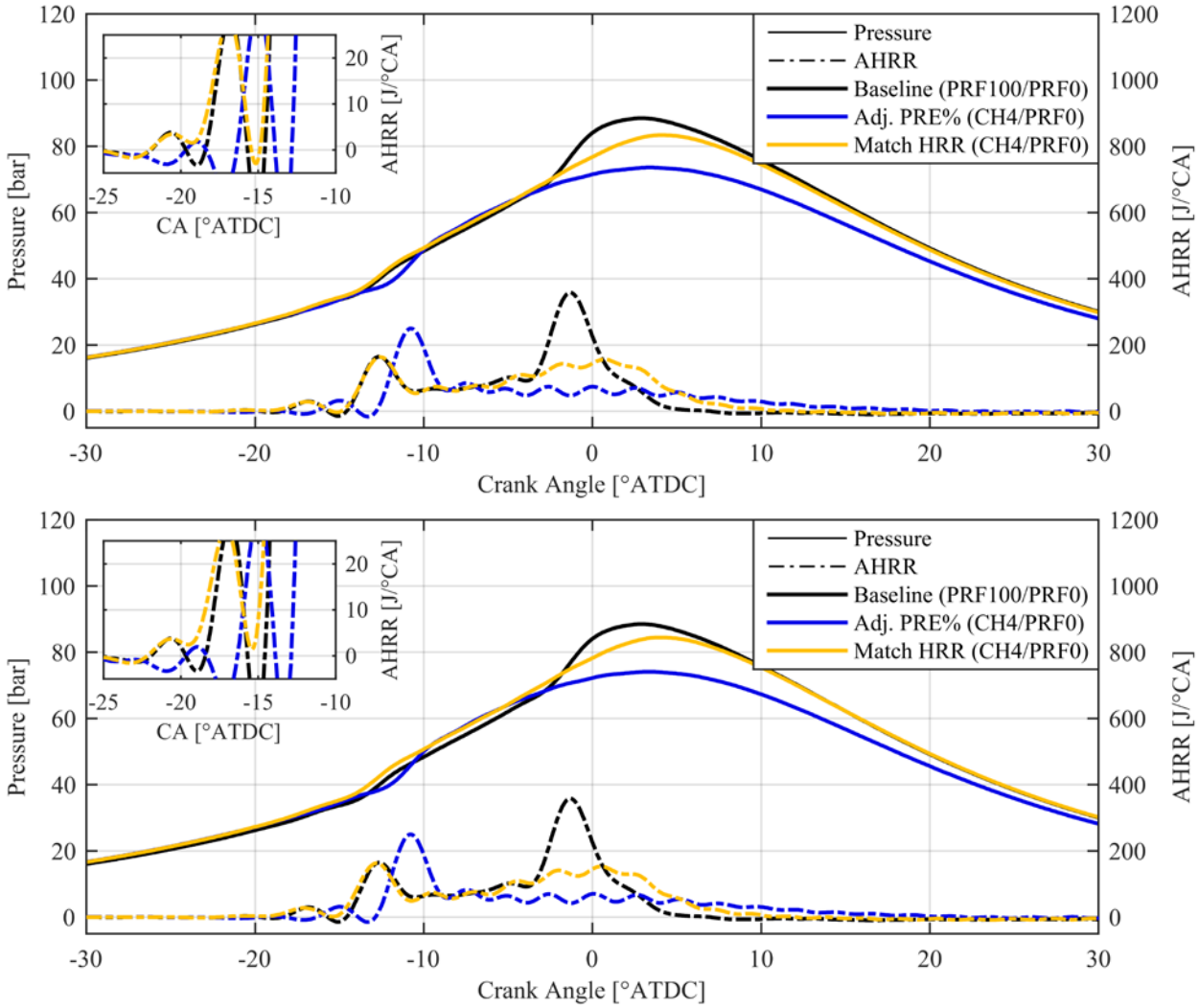

Figure C.17: Pressure and HRR for CH_4/PRF0 RCCI cases (adjusted premixed mass percent in blue, and matched HRR in yellow) compared to the baseline PRF100/PRF0 case at -30° SOI (black) for P_{in} = 114.5kPa (top), and $\dot{m}_{air}$ = 1.92kg/min and φ = 0.30 (bottom)

D *Experimental Data, Simulation Data, and Post Processing Codes*

To obtain copies of the raw and processed experimental or simulation data, or the MATLAB scripts used to post-process the raw data, please contact Profess Rolf Reitz: reitz@wisc.edu

E *CFD VALIDATION*

E.1 HCCI Engine Cases

The initial conditions for the T_{in} = 60ºC HCCI validation cases for equivalence ratios of 0.25, and 0.28 and 0.30 are summarized in Table E.1 and Table E.2, and the comparisons between the experimental data and the simulated pressure and heat release profiles can be seen in Figure E.18 and Figure E.19 respectively.

Table E.1: Initial conditions of HCCI validation simulations (T_{in} = 60ºC, φ = 0.25)

Condition	Fuel Mass [mg/cyc]	PRF [-]	P_{IVC} [kPa]	Exp. T_{IVC} [K]	Sim. T_{IVC} [K]
1	57.79	90.3	163.2	383	380
2	58.24	92.1	163.2	384	378
3	27.95	93.0	162.4	380	378
4	58.30	93.8	162.4	381	376
5	57.82	95.8	161.6	378	372
6	57.97	96.8	160.5	377	370

Table E.2: Initial conditions of HCCI validation simulations (T_{in} = 60ºC, φ = 0.28 and φ = 0.30)

Condition	φ [-]	Fuel Mass [mg/cyc]	PRF [-]	P_{IVC} [kPa]	Exp. T_{IVC} [K]	Sim. T_{IVC} [K]
1		57.98	90.3	144.2	374	372
2	0.28	57.89	91.9	143.2	373	370
3		57.84	93.1	143.5	371	368
1		58.13	90.5	133.1	375	366
2	0.30	57.88	91.8	132.6	375	364
3		58.39	92.8	133.0	374	360

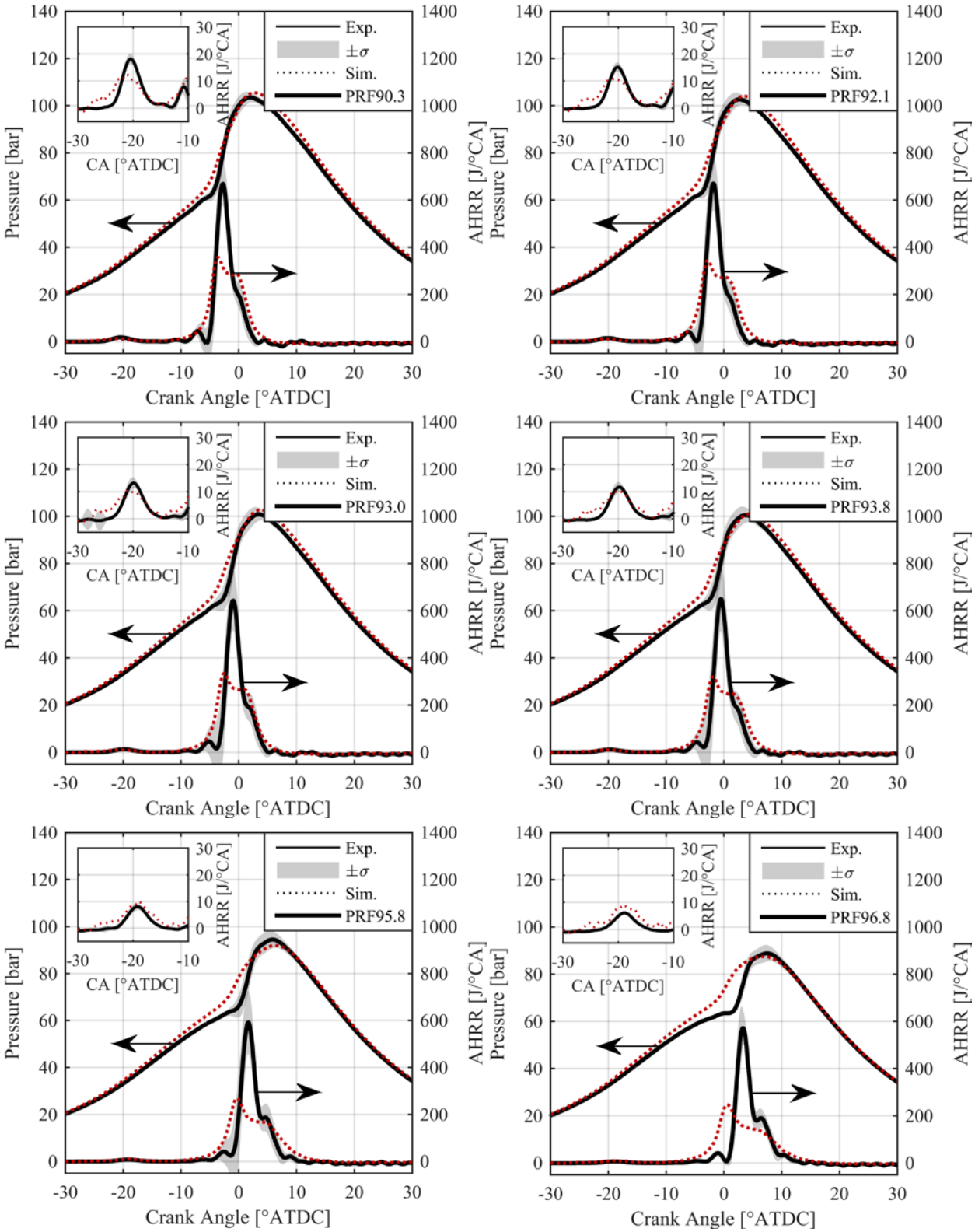

Figure E.18: Comparison of experimental HCCI pressure and heat release rate data (black lines), including standard deviation (grey region) with simulated pressure and heat release rate (red dotted lines) at T_{in} = 60ºC, φ = 0.25 and specified PRF mixture.

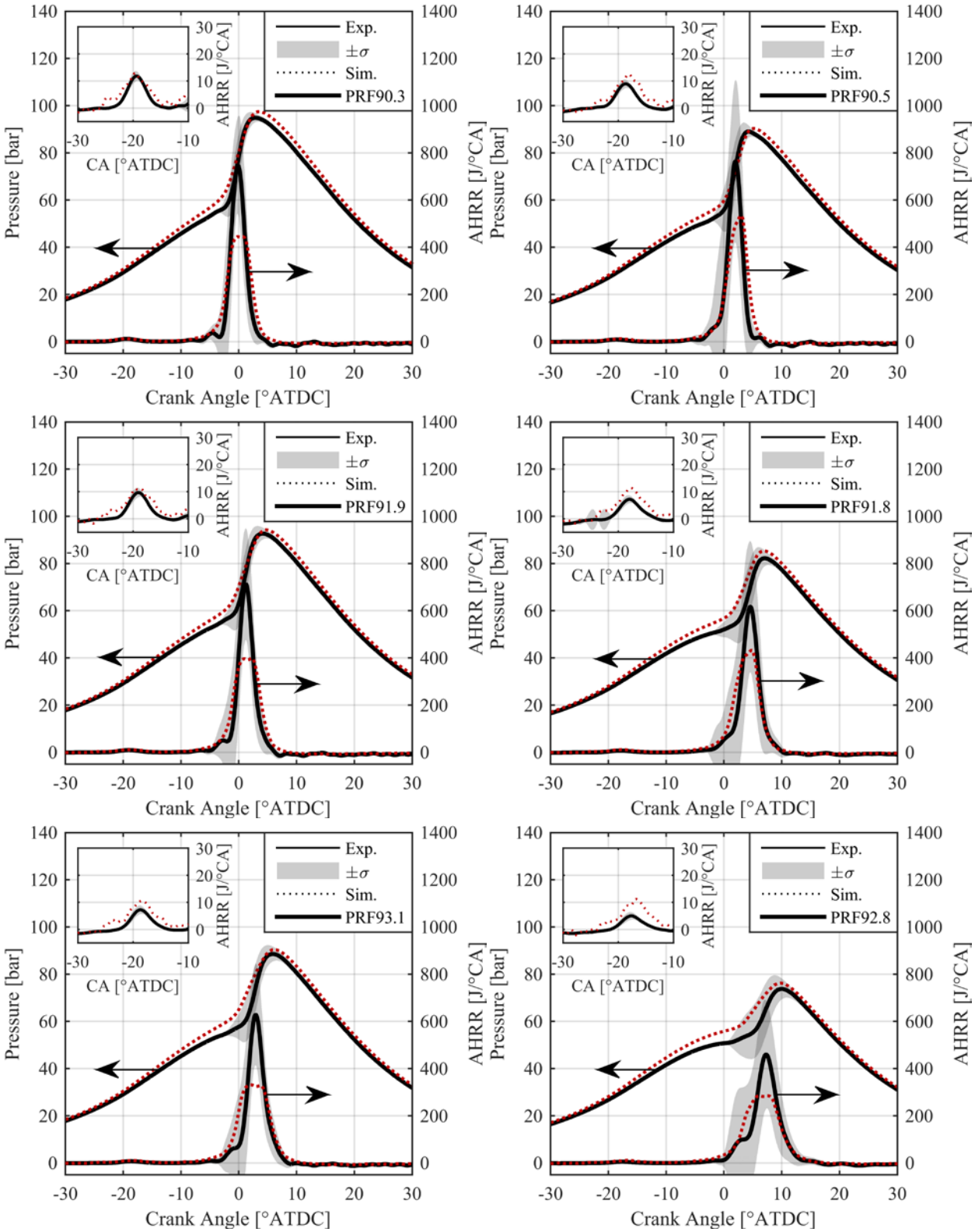

Figure E.19: Comparison of experimental HCCI pressure and heat release rate data (black lines), including standard deviation (grey region) with simulated pressure and heat release rate (red dotted lines) at T_{in} = 60ºC, φ = 0.28 (left), φ = 0.30 (right), and specified PRF mixture.

E.2 RCCI Engine Cases

A number of injection timing sweeps were conducted that were not included in the body of the present work due to space limitations. These cases were simulated in KIVA to validate the CFD models, and provided generally very good agreement in the range of SOI timings of interest in RCCI combustion (-140° to about -30°ATDC), with only minor adjustments from the calculated IVC temperature from the experiments. The constant operating conditions for the sweeps are shown in Table E.3, and the CFD IVC conditions can be seen in the subsequent tables for each sweep. The parameter of interest in each case is highlighted in red text.

Table E.3: Nominal operating conditions held constant in all PRF RCCI sweeps

Engine speed [rev/min]	1300
Fuel Energy, (Q_{fuel}) [J/cyc]	2590 (±20)
Nominal Load ($IMEP_n$) [bar]	4.3-4.75
EGR [%]	0
PFI Fuel	iso-octane (PRF100)
DI Fuel	n-heptane (PRF0)

Table E.4: Initial conditions simulations with constant PRF (T_{in} = 60°C, φ = 0.30, P_{rail} = 500bar, PRF = 88.0±0.2)

SOI [°ATDC]	Fuel Mass [mg/cyc]	PRF [-]	P_{IVC} [kPa]	Exp. T_{IVC} [K]	Sim. T_{IVC} [K]
-140	58.32	88.1	133.9	383	375
-90	58.36	87.9	133.7	382	373
-60	58.29	88.2	132.5	379	371
-50	58.44	87.9	132.6	378	371
-40	58.44	88.0	133.6	384	373
-35	58.36	88.1	133.9	385	375
-30	58.57	87.8	134.2	386	373
-25	58.56	87.8	134.6	388	371
-20	58.55	87.7	133.8	385	363
-17	58.62	87.6	133.5	382	363

Table E.5: Initial conditions with constant CA50 (T_{in} = 60ºC, φ = 0.30, P_{rail} = 500bar, CA50 = 0.75º ATDC)

SOI [ºATDC]	Fuel Mass [mg/cyc]	PRF [-]	P_{IVC} [kPa]	Exp. T_{IVC} [K]	Sim. T_{IVC} [K]
-140	58.36	91.1	133.5	373	371
-90	58.19	90.8	133.0	368	369
-60	58.46	92.0	132.0	368	367
-50	58.12	93.0	132.4	369	367
-45	58.55	93.7	132.8	370	367
-35	58.41	94.2	133.1	371	365
-30	58.51	94.7	133.1	372	365
-25	58.32	94.7	133.6	374	365
-20	58.24	92.0	133.7	374	365
-19.5	58.40	91.7	134.0	376	365
-18	58.41	88.0	133.6	373	363
-17	58.22	71.8	132.8	371	361

Table E.6: Initial conditions simulations with constant PRF (T_{in} = 40ºC, φ = 0.35, P_{rail} = 500bar, PRF = 88.1±0.2)

SOI [ºATDC]	Fuel Mass [mg/cyc]	PRF [-]	P_{IVC} [kPa]	Exp. T_{IVC} [K]	Sim. T_{IVC} [K]
-140	58.46	87.9	111.0	364	357
-90	58.44	87.9	110.9	363	357
-60	58.47	87.9	110.4	362	353
-50	58.44	87.9	110.2	360	353
-45	58.51	87.9	110.4	361	353
-40	58.56	87.9	111.4	365	355
-35	58.26	88.1	112.4	370	359
-30	58.20	88.3	113.3	374	361
-25	58.45	88.0	112.8	371	353
-20	58.46	88.0	112.0	367	349
-17	58.58	87.8	111.3	364	345

Figure E.20 and Figure E.21 show the comparisons between experimental and simulated pressure and HRR for the fixed PRF SOI sweep with T_{in} = 60ºC, while Figure E.22 and Figure E.23 show the fixed CA50 sweep at T_{in} = 60ºC. Figure E.24 and Figure E.25 show the fixed global PRF case at an equivalence ratio of 0.35.

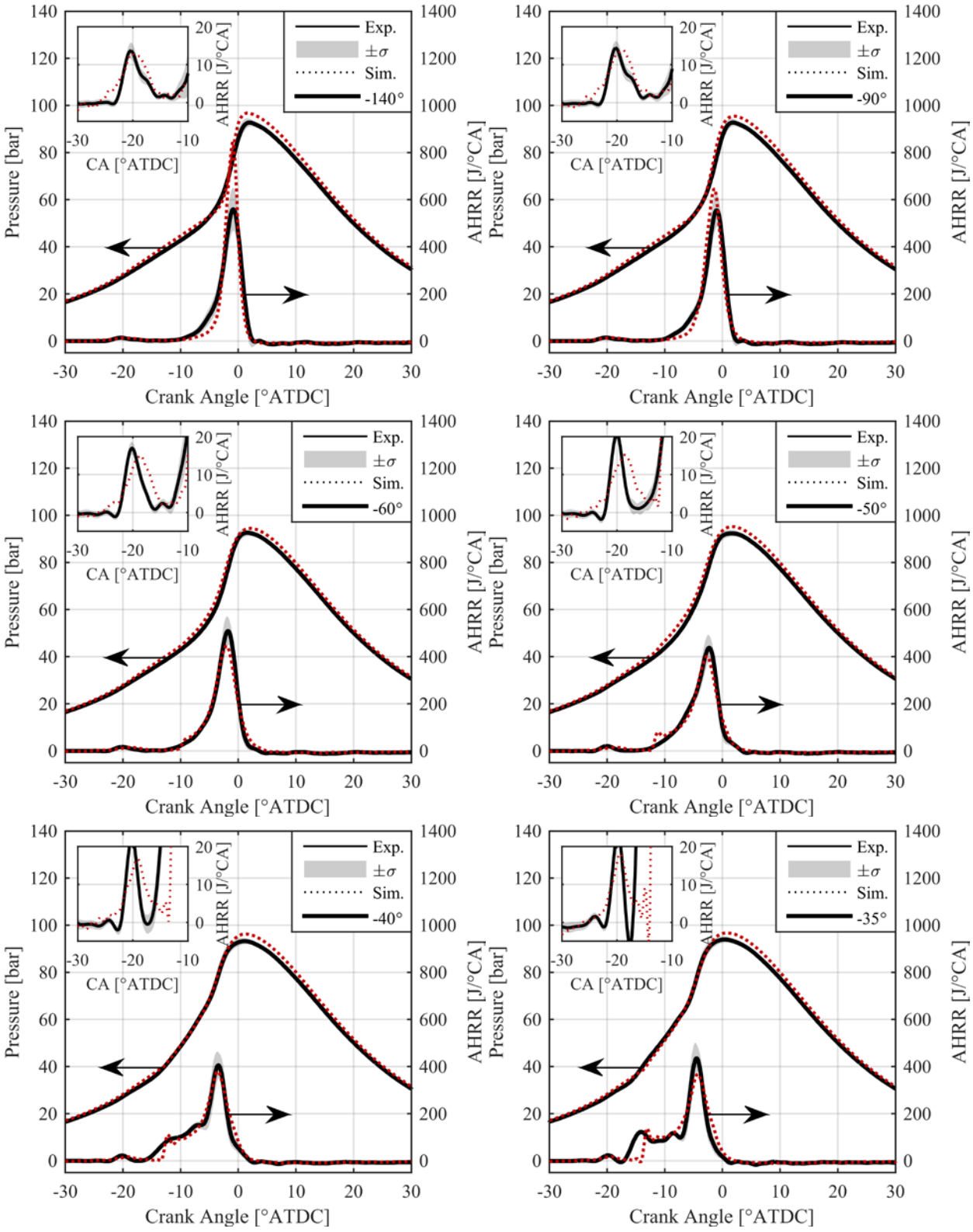

Figure E.20: Comparison of experimental RCCI pressure and heat release rate data (black lines) including standard deviation (grey region) with simulated pressure and heat release rate (red dotted lines) at T_{in} = 60°C, φ = 0.30, PRF = 88.0±0.2, P_{rail} = 500bar, and SOI timing specified in legend

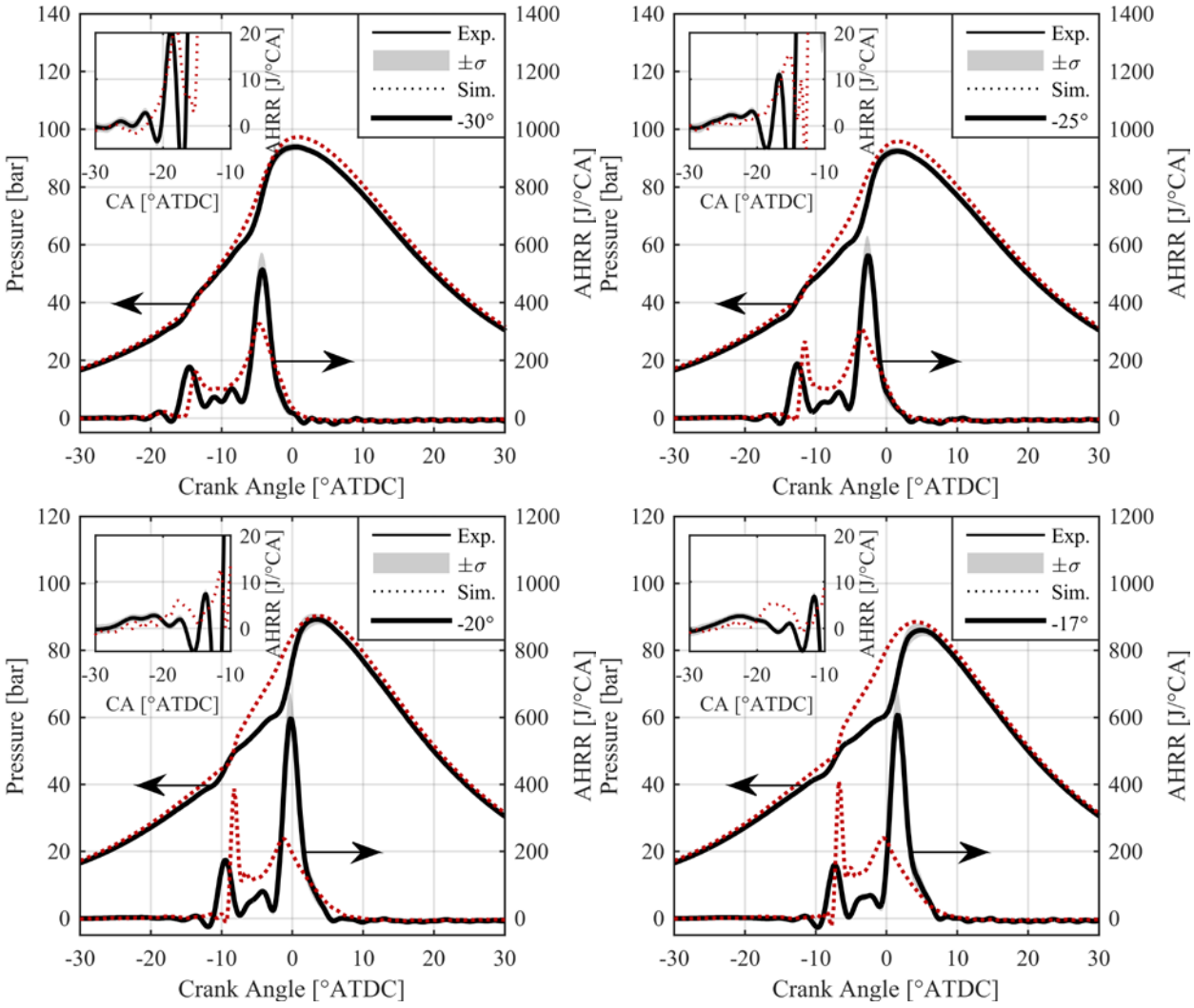

Figure E.21: Comparison of experimental RCCI pressure and heat release rate data (black lines) including standard deviation (grey region) with simulated pressure and heat release rate (red dotted lines) at T_{in} = 60°C, φ = 0.30, PRF = 88.0±0.2, P_{rail} = 500bar, and SOI timing specified in legend

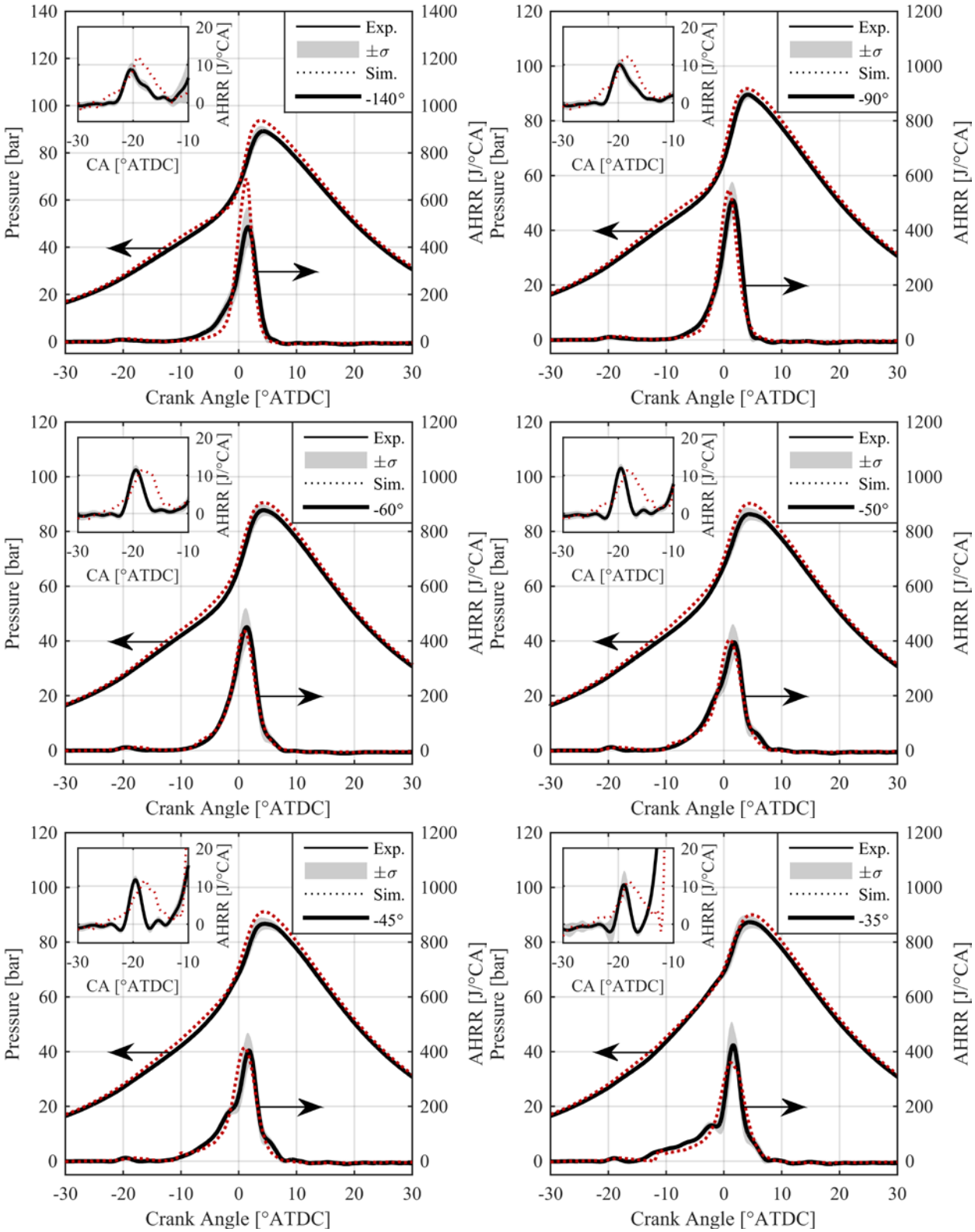

Figure E.22: Comparison of experimental RCCI pressure and heat release rate data (black lines), including standard deviation (grey region) with simulated pressure and heat release rate (red dotted lines) at T_{in} = 60°C, φ = 0.30, CA50 = 0.75±0.25, P_{rail} = 500bar, varying PRF blends, and SOI timing specified in legend

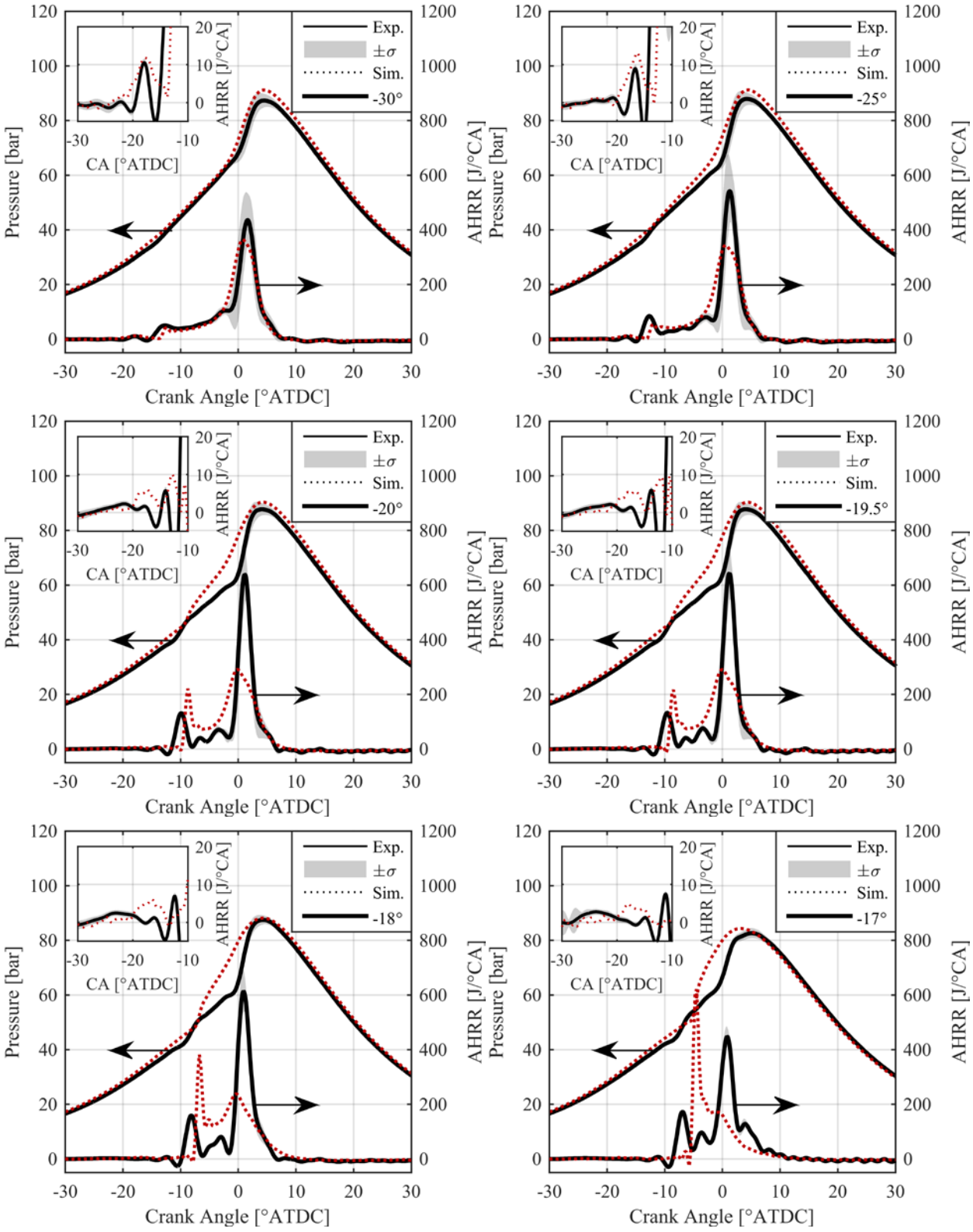

Figure E.23: Comparison of experimental RCCI pressure and heat release rate data (black lines), including standard deviation (grey region) with simulated pressure and heat release rate (red dotted lines) at T_{in} = 60°C, φ = 0.30, CA50 = 0.75±0.25, P_{rail} = 500bar, varying PRF blends, and SOI timing specified in legend

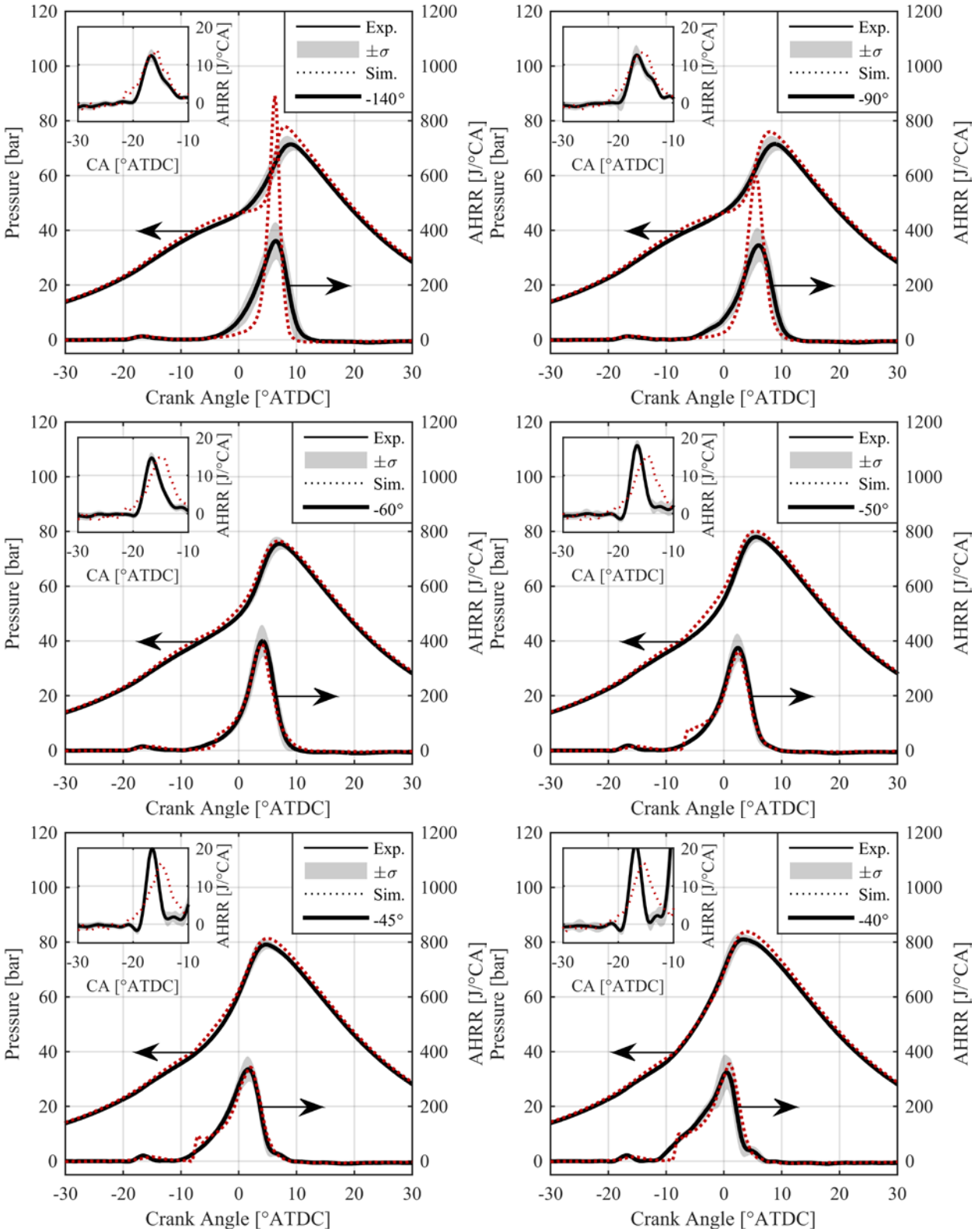

Figure E.24: Comparison of experimental RCCI pressure and heat release rate data (black lines) including standard deviation (grey region) with simulated pressure and heat release rate (red dotted lines) at T_{in} = 40ºC, φ = 0.35, PRF = 88.1±0.2, P_{rail} = 500bar, and SOI timing specified in legend

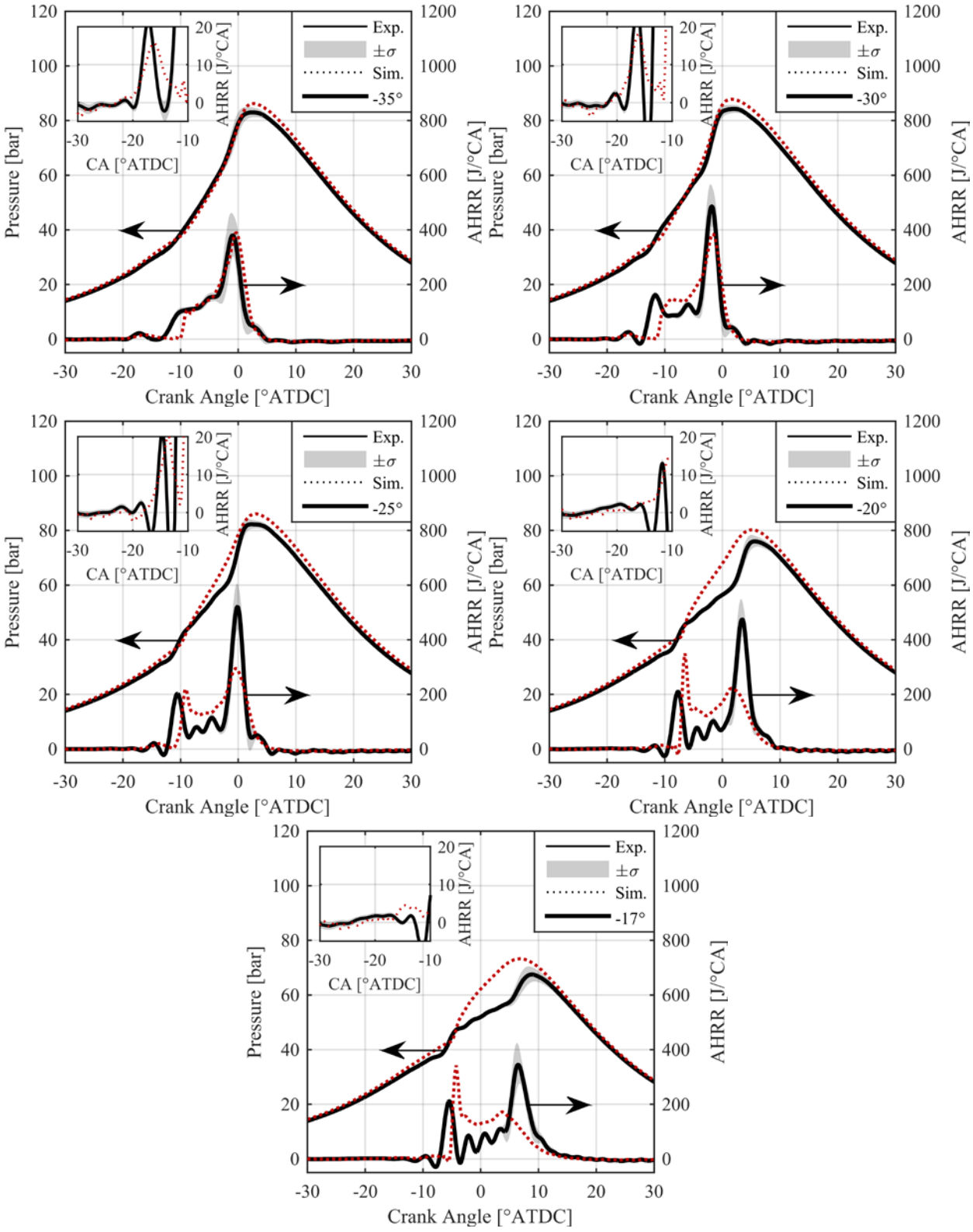

Figure E.25: Comparison of experimental RCCI pressure and heat release rate data (black lines) including standard deviation (grey region) with simulated pressure and heat release rate (red dotted lines) at T_{in} = 40ºC, φ = 0.35, PRF = 88.1±0.2, P_{rail} = 500bar, and SOI timing specified in legend

Table E.7 and Table E.8 show the fixed PRF SOI sweeps at 300bar rail pressure, and 1000bar rail pressure, respectively. Figure E.26 and Figure E.27 show the experimental and simulated pressure and HRRs for each of the SOI timings at 300bar rail pressure, while Figure E.28 and Figure E.29 show the pressure and heat release rates for the 1000bar rail pressure sweep.

Table E.7: Initial conditions simulations with constant PRF (T_{in} = 40ºC, φ = 0.30, P_{rail} = 300bar, PRF = 88.0±0.2)

SOI [ºATDC]	Fuel Mass [mg/cyc]	PRF [-]	P_{IVC} [kPa]	Exp. T_{IVC} [K]	Sim. T_{IVC} [K]
-140	58.26	88.5	126.5	350	357
-90	58.39	88.2	126.4	350	355
-60	58.15	88.4	125.8	349	355
-50	58.33	88.2	125.8	349	355
-40	58.38	88.2	126.4	351	355
-35	58.40	88.1	127.2	354	357
-30	58.49	87.9	127.3	354	357
-25	58.57	88.0	127.1	353	351
-20	58.70	87.8	125.8	347	343

Table E.8: Initial conditions simulations with constant PRF (T_{in} = 40ºC, φ = 0.30, P_{rail} = 1000bar, PRF = 88.0±0.2)

SOI [ºATDC]	Fuel Mass [mg/cyc]	PRF [-]	P_{IVC} [kPa]	Exp. T_{IVC} [K]	Sim. T_{IVC} [K]
-140	58.57	87.9	126.9	352	359
-90	58.69	87.8	126.5	351	357
-60	58.69	87.9	126.2	350	353
-50	58.52	88.0	125.8	349	353
-40	58.61	87.9	125.7	349	353
-35	58.58	88.0	126.2	350	353
-30	58.49	88.1	126.4	351	353
-25	58.58	87.7	127.1	353	351
-20	58.64	87.8	127.7	355	351
-17	58.44	87.7	127.4	354	347
-15	58.53	87.9	126.8	352	345

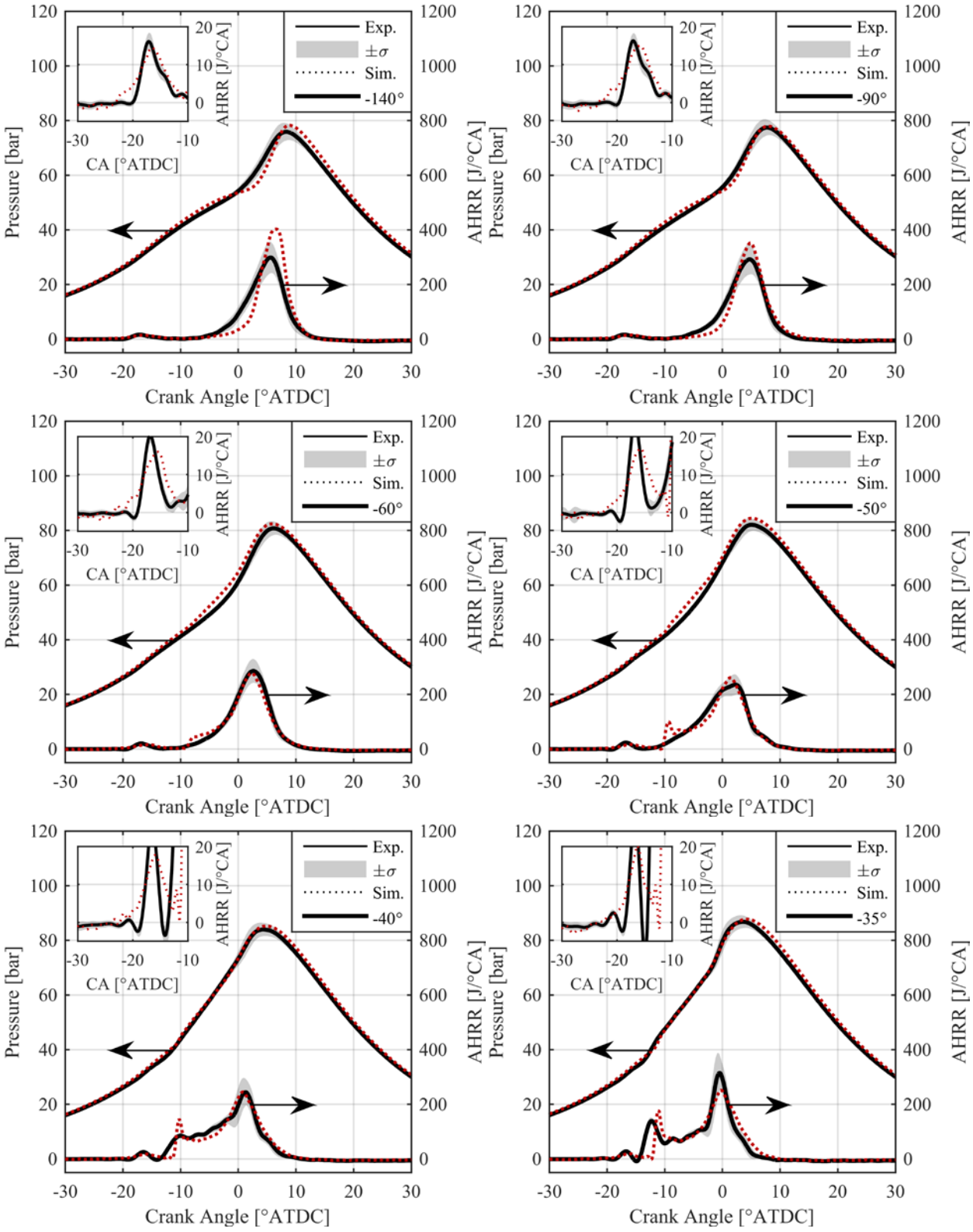

Figure E.26: Comparison of experimental RCCI pressure and heat release rate data (black lines) including standard deviation (grey region) with simulated pressure and heat release rate (red dotted lines) at Tin = 40ºC, φ = 0.30, PRF = 88.0±0.2, P_{rail} = 300bar, and SOI timing specified in legend

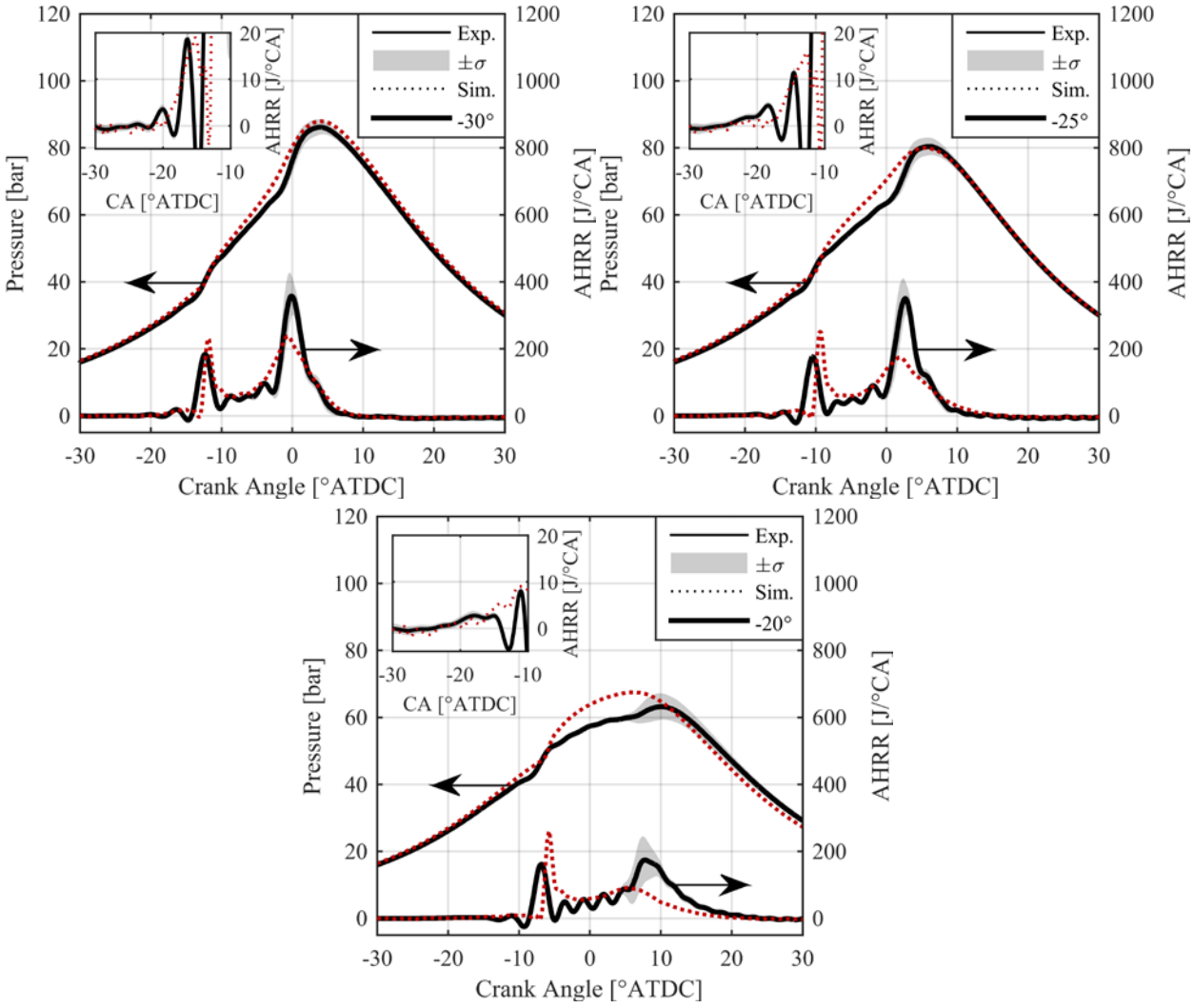

Figure E.27: Comparison of experimental RCCI pressure and heat release rate data (black lines) including standard deviation (grey region) with simulated pressure and heat release rate (red dotted lines) at Tin = 40ºC, φ = 0.30, PRF = 88.0±0.2, P_{rail} = 300bar, and SOI timing specified in legend

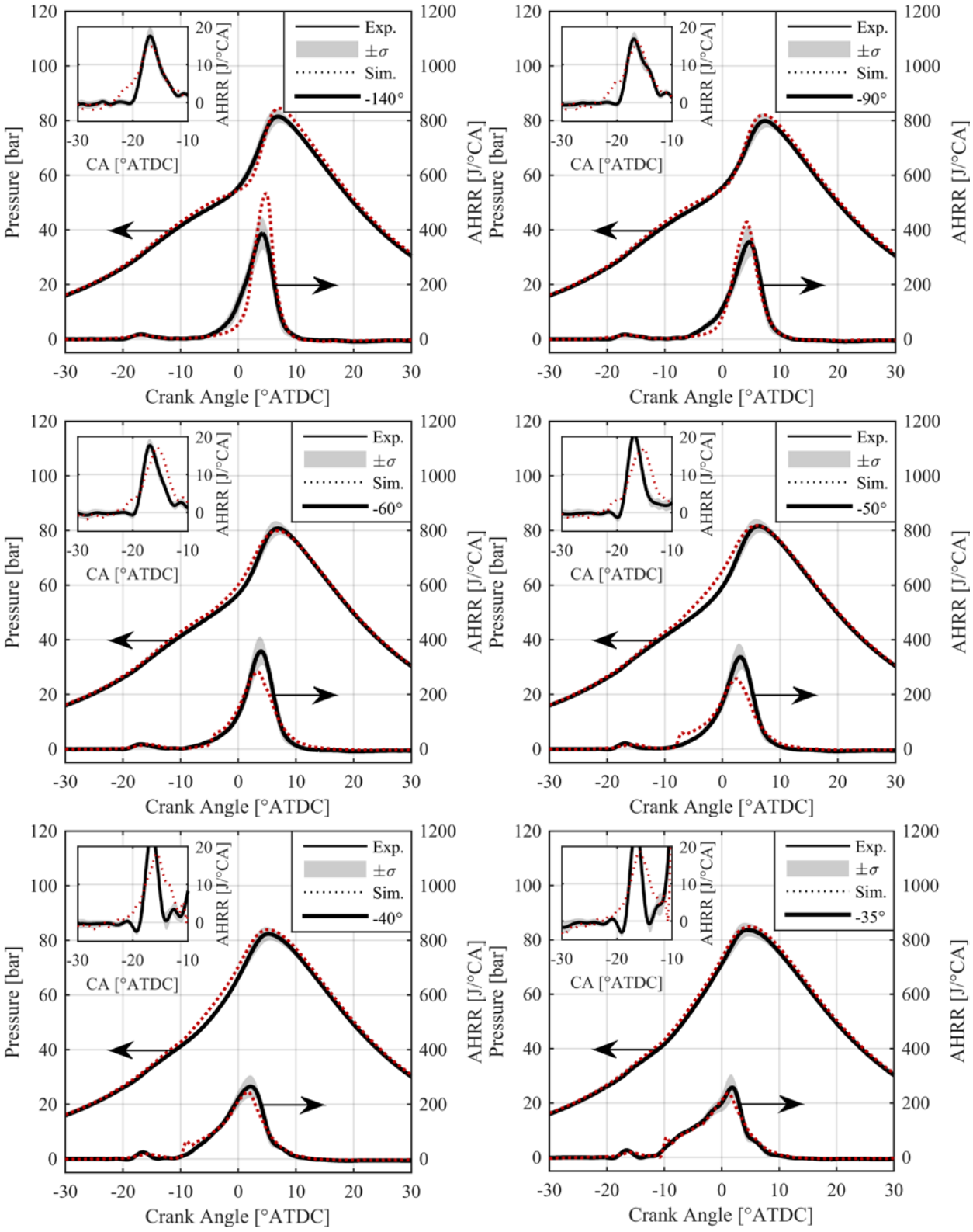

Figure E.28: Comparison of experimental RCCI pressure and heat release rate data (black lines) including standard deviation (grey region) with simulated pressure and heat release rate (red dotted lines) at Tin = 40ºC, φ = 0.30, PRF = 88.0±0.2, P_{rail} = 1000bar, and SOI timing specified in legend

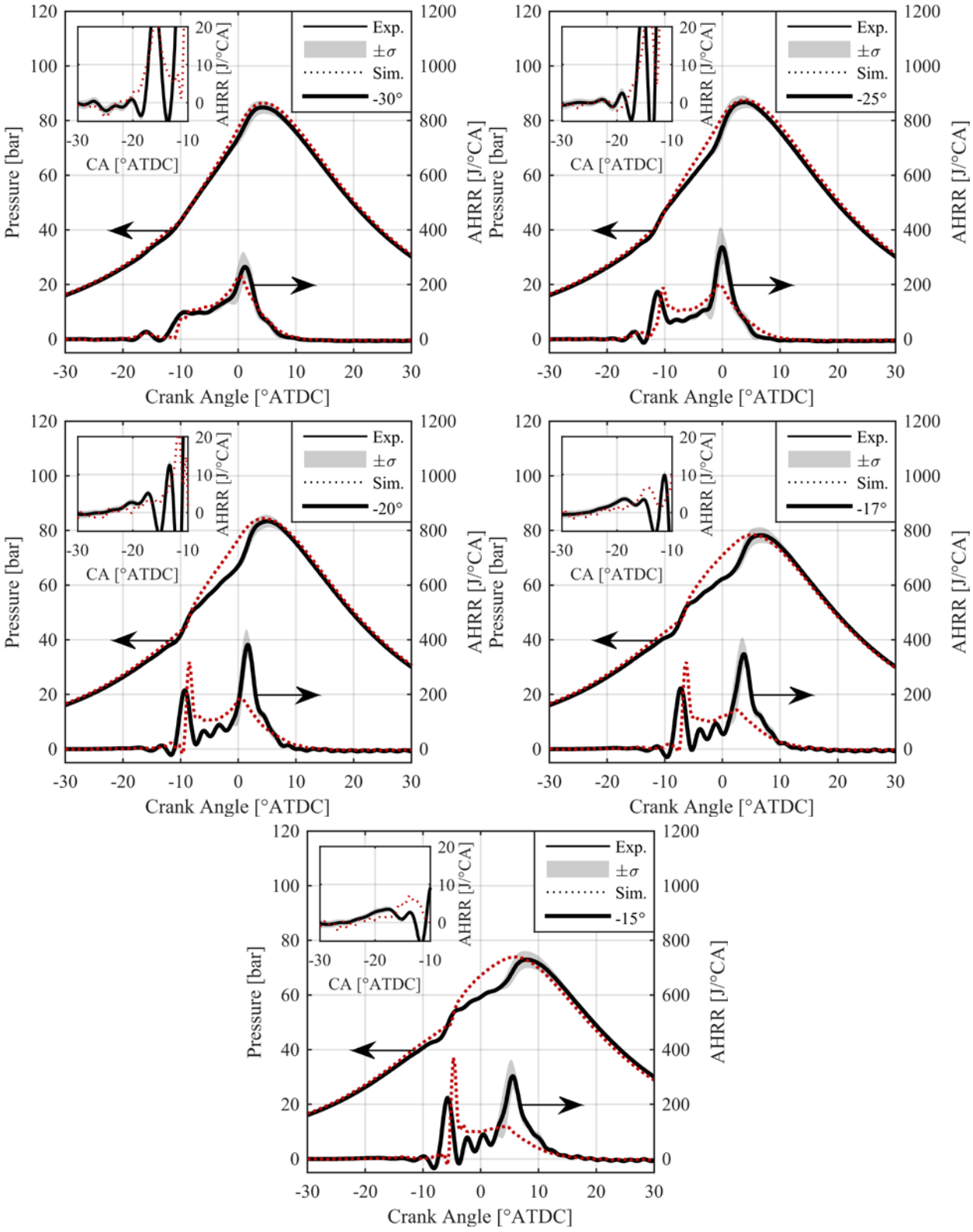

Figure E.29: Comparison of experimental RCCI pressure and heat release rate data (black lines) including standard deviation (grey region) with simulated pressure and heat release rate (red dotted lines) at Tin = 40ºC, φ = 0.30, PRF = 88.0±0.2, P_{rail} = 1000bar, and SOI timing specified in legend